



Editor, **YOGESH JALURIA** (2010)
Assistant to the Editor, **S. PATEL**

Associate Editors

Yutaka Asako, Tokyo Metropolitan University, Japan (2010)
Gautam Biswas, Indian Inst. of Tech., Kanpur (2009)
Louis C. Burmeister, Univ. of Kansas (2008)
Cho Lik Chan, The University of Arizona (2010)
Louis C. Chow, University of Central Florida (2010)
Minking Chyu, Univ. of Pittsburgh (2009)
A. Haji-Sheikh, Univ. of Texas at Arlington (2008)
Anthony M. Jacobi, Univ. of Illinois (2008)
Yogendra Joshi, Georgia Inst. of Tech. (2008)
Satish G. Kandlikar, Rochester Inst. of Tech. (2010)
SunJ Jin Kim, Korea Adv. Inst. Sci. Technol., Korea (2010)
Sai C. Lau, Texas A&M Univ. (2009)
Ben Q. Li, Univ. of Michigan, Dearborn (2009)
Raj M. Manglik, Univ. of Cincinnati (2009)
Jayanthi Y. Murthy, Purdue University (2010)
Roger R. Schmidt, IBM Corporation (2010)
Jamal Seyed-Yagoobi, Illinois Inst. of Tech. (2009)
S. A. Sherif, University of Florida (2010)
Bengt Sundén, Lund Inst. of Tech., Sweden (2008)
Peter Vadasz, Northern Arizona University (2010)
Walter W. Yuen, Univ. of California-Santa Barbara (2008)

Past Editors

V. DHIR
J. R. HOWELL
R. VISKANTA
G. M. FAETH
K. T. YANG
E. M. SPARROW

HEAT TRANSFER DIVISION
Chair, **T. W. TONG**
Vice Chair, **C. H. OH**
Past Chair, **R. W. DOUGLASS**

PUBLICATIONS COMMITTEE
Chair, **BAHRAM RAVANI**

OFFICERS OF THE ASME
President, **SAM Y. ZAMRIK**
Executive Director,
VIRGIL R. CARTER
Treasurer,
THOMAS D. PESTORIUS

PUBLISHING STAFF
Managing Director, Publishing
PHILIP DI VIETRO
Manager, Journals
COLIN McATEER
Production Coordinator
JUDITH SIERANT

Transactions of the ASME, Journal of Heat Transfer (ISSN 0022-1481) is published monthly by The American Society of Mechanical Engineers, Three Park Avenue, New York, NY 10016. Periodicals postage paid at New York, NY and additional mailing offices.
POSTMASTER: Send address changes to Transactions of the ASME, Journal of Heat Transfer, c/o THE AMERICAN SOCIETY OF MECHANICAL ENGINEERS, 22 Law Drive, Box 2300, Fairfield, NJ 07007-2300.
CHANGES OF ADDRESS must be received at Society headquarters seven weeks before they are to be effective.
Please send old label and new address.

STATEMENT from By-Laws. The Society shall not be responsible for statements or opinions advanced in papers or ... printed in its publications (B7.1, Para. 3).

COPYRIGHT © 2008 by The American Society of Mechanical Engineers. For authorization to photocopy material for internal or personal use under those circumstances not falling within the fair use provisions of the Copyright Act, contact the Copyright Clearance Center (CCC), 222 Rosewood Drive, Danvers, MA 01923, tel: 978-750-8400, www.copyright.com.
Request for special permission or bulk copying should be addressed to Reprints/Permission Department.
Canadian Goods & Services Tax Registration #126148048

Journal of Heat Transfer

Published Monthly by ASME

VOLUME 130 • NUMBER 1 • JANUARY 2008(pp.011301-015501)

RESEARCH PAPERS

Conduction

011301 Heat Conduction Through Heat Exchanger Tubes of Noncircular Cross Section
Manoj Ku. Moharana and Prasanta Ku. Das

Electronic Cooling

011401 Genetic Algorithm Based Optimization of PCM Based Heat Sinks and Effect of Heat Sink Parameters on Operational Time
Atul Nagose, Ankit Somani, Aviral Shrot, and Arunn Narasimhan

Evaporation, Boiling, and Condensation

011501 Subcooled Boiling Flow Heat Transfer From Plain and Enhanced Surfaces in Automotive Applications
Franz Ramstorfer, Helfried Steiner, Günter Brenn, Claudius Kormann, and Franz Rammer

Heat Exchangers

011801 Dynamic Behavior of Three-Fluid Crossflow Heat Exchangers
Manish Mishra, P. K. Das, and Sunil Sarangi

Jets, Wakes, and Impingement Cooling

012201 Film Cooling and Heat Transfer on Two Cutback Trailing Edge Models With Internal Perforated Blockages
Jung-ho Choi, Shantanu Mhetras, Je-Chin Han, Sai C. Lau, and Ron Rudolph
012202 Heat Transfer in the Flow of a Cold, Axisymmetric Vertical Liquid Jet Against a Hot, Horizontal Plate
Jian-Jun Shu and Graham Wilks

Natural and Mixed Convection

012501 Heatline Visualization of Natural Convection in a Porous Cavity Occupied by a Fluid With Temperature-Dependent Viscosity
K. Hooman and H. Gurgenci

Porous Media

012601 Moving Boundary-Moving Mesh Analysis of Freezing Process in Water-Saturated Porous Media Using a Combined Transfinite Interpolation and PDE Mapping Methods
P. Rattanadecho and S. Wongwises
012602 Numerical Investigation of Thermofluid Flow Characteristics With Phase Change Against High Heat Flux in Porous Media
Kazuhisa Yuki, Jun Abei, Hidetoshi Hashizume, and Saburo Toda

Two-Phase Flow and Heat Transfer

012901 The Critical Heat Flux Condition With Water in a Uniformly Heated Microtube
A. P. Roday, T. Borca-Tasçiuç, and M. K. Jensen

TECHNICAL BRIEFS

014501 Numerical Analysis of Wooden Porous Media Effects on Heat Transfer From a Staggered Tube Bundle
Mohammad Layeghi

(Contents continued on inside back cover)

This journal is printed on acid-free paper, which exceeds the ANSI Z39.48-1992 specification for permanence of paper and library materials. ©™
♻️ 85% recycled content, including 10% post-consumer fibers.

- 014502 **Impact of Interface Resistance on Pulsed Thermoelectric Cooling**
Y. Sungtaek Ju
- 014503 **A Light Transmission Based Liquid Crystal Thermography System**
Timothy B. Roth and Ann M. Anderson
- 014504 **Discussion of Boundary Conditions of Transpiration Cooling Problems Using Analytical Solution of LTNE Model**
Jianhua Wang and Junxiang Shi
- 014505 **Heat Transfer From a Rotating Disk to Fluids for a Wide Range of Prandtl Numbers Using the Asymptotic Model**
M. M. Awad

DISCUSSIONS

- 015501 **Discussion "Pressure Drop During Refrigerant Condensation Inside Horizontal Smooth, Helical Microfin, and Herringbone Microfin Tubes"** (Olivier, J. A., Liebenberg, L., Kedzierski, M. A., and Meyer, J. P., 2004, *J. Heat Transfer*, 126(5), pp. 687–696)
M. M. Awad

The ASME Journal of Heat Transfer is abstracted and indexed in the following:

Applied Science and Technology Index, Chemical Abstracts, Chemical Engineering and Biotechnology Abstracts (Electronic equivalent of Process and Chemical Engineering), Civil Engineering Abstracts, Compendex (The electronic equivalent of Engineering Index), Corrosion Abstracts, Current Contents, E & P Health, Safety, and Environment, Ei EncompassLit, Engineered Materials Abstracts, Engineering Index, Enviroline (The electronic equivalent of Environment Abstracts), Environment Abstracts, Environmental Engineering Abstracts, Environmental Science and Pollution Management, Fluidex, Fuel and Energy Abstracts, Index to Scientific Reviews, INSPEC, International Building Services Abstracts, Mechanical & Transportation Engineering Abstracts, Mechanical Engineering Abstracts, METADEX (The electronic equivalent of Metals Abstracts and Alloys Index), Petroleum Abstracts, Process and Chemical Engineering, Referativnyi Zhurnal, Science Citation Index, SciSearch (The electronic equivalent of Science Citation Index), Theoretical Chemical Engineering

Heat Conduction Through Heat Exchanger Tubes of Noncircular Cross Section

Manoj Ku. Moharana

Research Scholar
Department of Mechanical Engineering,
Indian Institute of Technology Kanpur,
Kanpur, Uttar Pradesh 208016,
India
e-mail: manoj.moharana@rediffmail.com

Prasanta Ku. Das

Professor
Department of Mechanical Engineering,
Indian Institute of Technology Kharagpur,
Kharagpur, West Bengal 721302,
India
e-mail: pkd@mech.iitkgp.ernet.in

Conduction through shaped tubes with circular inner surface and hydrodynamically shaped outer surface has been analyzed by two different techniques. A two-dimensional analysis has been made by a semianalytical technique using boundary collocation at the outer periphery. A one-dimensional approximate technique called sector method shows a closed agreement with the two-dimensional analysis. The present work gives an improvement on the analysis of Li et al. (2004, "Heat Transfer Enhancement Using Shaped Polymer Tubes: Fin Analysis," ASME J. Heat Transfer, 126, pp. 211–218) who solved the same problem using a one-dimensional approximation following the methodology of fin analysis. Both the present methods relax some of the approximations taken by Li et al. Further, the suggested one-dimensional sector method is simple and requires limited computational effort. [DOI: 10.1115/1.2780176]

Keywords: heat conduction, shaped tubes, noncircular, boundary collocation method, sector method, efficiency, fin

1 Introduction

Circular tubes are most commonly used in the design of various heat exchangers. However, conduits with a noncircular outer profile have specific advantages over the circular tubes. In cross flow, the aerodynamically shaped tubes can reduce the pressure drop of the external fluid to a great extent in the subcritical range. In general, the tubes are given an elongated shape with their major axis oriented toward the direction of flow. Such a design also increases the area of the outer surface, thus improving the overall heat transfer. This has promoted heat transfer and hydrodynamic studies on noncircular tubes and tube banks. Mainly two types of noncircular shapes, elliptic and lenticular, have been considered. Studies of heat transfer from and fluid flow over oval or elliptic tubes have been taken up by a number of researchers [1–4]. Performance of heat exchangers with oval tube banks [5–9] has also been studied elaborately. These investigations have established the potential of using elliptic tubes in the design of various heat exchangers. Efforts [10] have also been made to use lenticular tubes in the construction of heat exchangers. The superiority of the lenticular shape in drag reduction has been established [11,12] by theoretical analysis. With the development of polymeric materials, construction of heat exchangers with small tubes of innovative shape has become a reality [13]. It is envisaged that such heat exchangers will have superior performance compared to conventional heat exchangers with circular metallic tubes.

Reduction of fouling on the external surface of tubes is another reason for selecting noncircular geometry. Bouris et al. [14] postulated and established by numerical modeling that elliptic tubes will have a reduced rate of fouling due to its lower frontal area and small wake region.

Besides, during filmwise condensation, effective drainage of the condensate film from the external surface of the tube increases the rate of heat transfer. Dutta et al. [15] proposed different noncircular geometries of heat exchanger tubes where the force of gravity

can be exploited to reduce the thickness of condensate film. The authors have also analyzed the augmentation in heat transfer due to the use of such tubes.

In spite of a number of advantages of noncircular tubes for heat exchanger applications, not much effort has been made to analyze conduction through such geometry. Two-dimensional shells, where the inner and outer boundaries are described by regular curves and are maintained at different isotherms, are often encountered in various engineering applications. Determining the conductive resistance of such shells is a challenging task. Frequently, the concept of conduction shape factor [16,17] is used for this purpose. Different analytical [18] and semianalytical techniques [19] were adopted in the past for determining shape factors. However, the conduction through shaped tubes used in heat exchangers is not subjected to identical boundary conditions. The inner boundary can be assumed to be at isothermal condition as liquid is most likely to flow through the tubes. Due to high thermal resistance in gas flow, a specified heat transfer coefficient and a given ambient temperature could be most appropriate conditions for the outer boundary. However, no rigorous analysis has been reported for the tubes with nonuniform thickness to the best of the knowledge of the authors.

Recently, Li et al. [13] proposed different designs of shaped polymeric tubes. These tubes have two unique features. The inner flow passage is kept circular for the pressure capability, while the outer surface is given an aerodynamic shape to reduce form drag. The authors have proposed three different shapes, namely, teardrop, lenticular, and oval, as shown in Fig. 1. They further presented a method of characterizing the thermal performance of these tubes of nonlinear cross section in a way similar to that adopted for fins. In Fig. 1, a base circular tube is also shown. The outer surface of the base tube is considered to be isothermal, and the additional materials of the other three tubes are considered as fins added to a circular base. Assuming fins of variable cross section, as shown in Fig. 2, Li et al. [13] formulated the following one-dimensional conduction equation:

$$d \left[r_s \theta(r_s) k_t \frac{dT(r_s)}{dr_s} \right] = h_0(r_s) [T(r_s) - T_\infty] ds(r_s) \quad (1)$$

In the above equation, θ and ds are nonlinear functions of the corresponding radius r_s . For different geometries, these functional

Contributed by the Heat Transfer Division of ASME for publication in the JOURNAL OF HEAT TRANSFER. Manuscript received May 25, 2006; final manuscript received May 5, 2007; published online January 25, 2008. Review conducted by A. Haji-Sheikh.

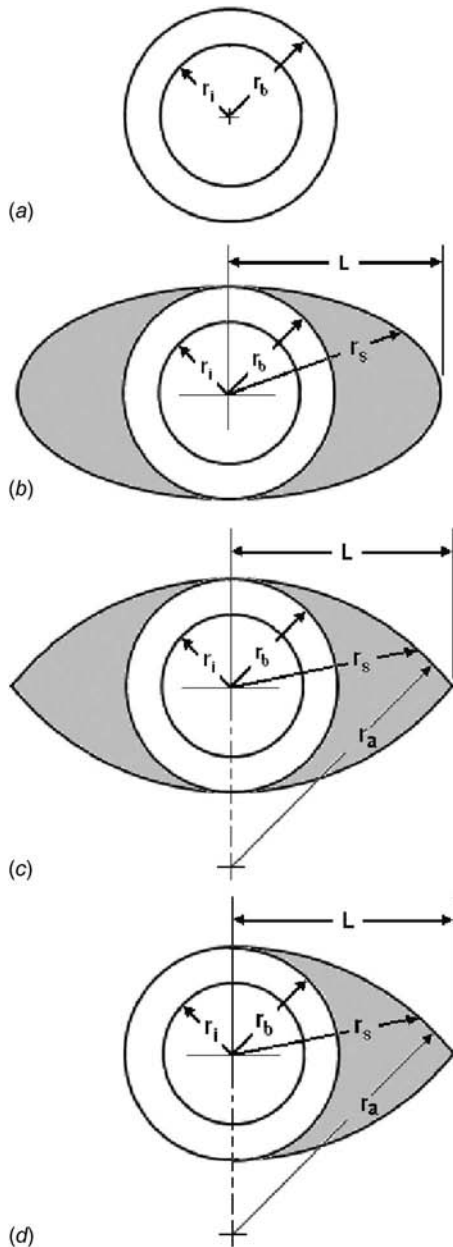


Fig. 1 Different types of shaped tubes: (a) circular, (b) oval, (c) lenticular, and (d) teardrop

relationships are given in Table 1 of Ref. [13]. The authors solved the above equation numerically to find out the efficiency of the shaped tubes. Though this is a unique attempt, the analysis is based on some simplified assumptions and has a scope of improvement. Firstly, the assumption of isothermal condition at the outer surface of the base circle is not strictly valid. Secondly, the analysis ignores any angular variation of temperature along a radius. Based on the above background, the present investigation has been taken up to provide an improved analysis of conduction in shaped tubes. A semianalytical technique based on boundary collocation method (BCM) has been proposed to solve the two-dimensional conduction problem in these typical geometry. Next a simple approximate technique has been elaborated to solve the same problem assuming one-dimensional conduction, but implicitly taking the azimuthal variation in temperature.

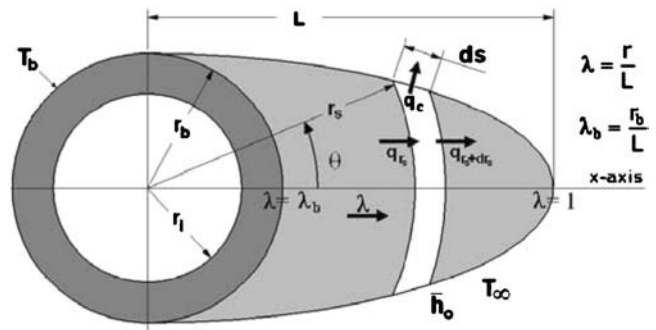


Fig. 2 Differential elements for a one-dimensional energy balance for a single sided fin on an oval shaped tube

2 Boundary Collocation Method

2.1 Assumptions. The problem has been analyzed with the following prior assumptions.

- The heat transfer through the shaped tube is at steady state, and there is no heat generation in the tube material.
- Temperature is uniform and constant over the inner surface.
- The local heat transfer coefficient over the outer surface of the tube may vary, particularly if the tube is subjected to a cross flow. This variation cannot be taken into consideration unless it is known a priori or a conjugate analysis is done. For the present work, uniform heat transfer coefficient on the outer periphery has been assumed. Further, the analysis has been made assuming uniform ambient temperature. The shaped tube material is of constant thermal conductivity.
- There is no heat transfer in the axial direction of the tube.

2.2 Mathematical Formulation. In this section, the mathematical formulation for oval shaped tube is presented. Following the same procedure, one can determine the temperature profile for both the lenticular and teardrop shaped tubes. Some difference in the final expression will appear due to the change in geometry, as given in Table 1 at the end of this section.

The following nondimensional parameters are introduced for generalizing the analysis:

$$\Theta = \frac{T - T_\infty}{T_i - T_\infty} \quad R = \frac{r}{r_i} \quad E_{cp} = \frac{r_b}{r_i} \quad \bar{R} = \frac{r_s(\theta)}{r_i} \quad (2)$$

Based on the assumptions stated above, the conduction through the shaped tubes can be modeled by a nondimensional equation in a cylindrical polar coordinate (Fig. 3),

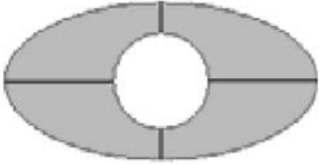
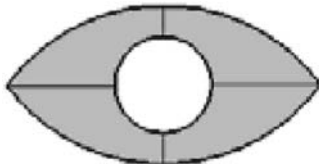
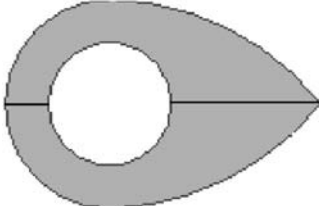
$$\frac{\partial^2 \Theta}{\partial R^2} + \frac{1}{R} \frac{\partial \Theta}{\partial R} + \frac{1}{R^2} \frac{\partial^2 \Theta}{\partial \theta^2} = 0 \quad (3)$$

Taking the queue from Ref. [19], the generalized variation of temperature in the r - θ coordinate is given by

$$\begin{aligned} \Theta(R, \theta) = & A + B \ln R + C\theta + D\theta \ln R \\ & + \sum_{k=1}^{\infty} (A_k R^{\lambda_k} + B_k R^{-\lambda_k}) \cos(\lambda_k \theta) \\ & + \sum_{k=1}^{\infty} (C_k R^{\lambda_k} + D_k R^{-\lambda_k}) \sin(\lambda_k \theta) \end{aligned} \quad (4)$$

where $A, B, C, D, A_k, B_k, C_k, D_k$, and λ_k are unknown constants. The boundary conditions in nondimensional form are as follows:

Table 1 Temperature profile in different shaped tubes (Note: \bar{R} value plays a role in evaluating values of Y_k)

Shape of tubes	Angle of symmetric segment in degree	Outer radius (in nondimensional form) $\bar{R} = \frac{r_s(\theta)}{r_i}$	Temperature profile $\Theta(R, \theta)$
 Oval	90	$E_{cp}[(\lambda_b \cos \theta)^2 + (\sin \theta)^2]^{-1/2}$ where $\lambda_b = \frac{r_b}{L}$	$1 + Y_1 \ln R + \sum_{k=2}^N Y_k (R^{2(k-1)} + R^{-2(k-1)})$
 Lenticular	90	$\left[\frac{\sqrt{[(R_a - 1) \sin \theta]^2 + (2R_a - 1)}}{-(R_a - 1) \sin \theta} \right] E_{cp}$ where $R_a = \frac{1}{2} \left(1 + \frac{1}{\lambda_b^2} \right)$	Same as oval
 Teardrop	180	For $0 < \theta < \frac{\pi}{2}$, \bar{R} is the same as lenticular For $\frac{\pi}{2} < \theta < \pi$, $\bar{R} = E_{cp}$	for $(0 < \theta < \pi)$ $1 + Y_1 \ln R + \sum_{k=2}^N Y_k (R^{(k-1)} - R^{-(k-1)}) \cdot Z$ where $Z = \cos[(k-1)\theta]$

$$\frac{\partial \Theta}{\partial \theta} = 0 \quad \text{for } \theta = 0 \quad (5a)$$

$$\frac{\partial \Theta}{\partial \theta} = 0 \quad \text{for } \theta = \frac{\pi}{2} \quad (5b)$$

$$\Theta = 1 \quad \text{for } R = 1 \quad (5c)$$

$$\frac{\partial \Theta}{\partial R} + \text{Bi}^* \Theta = 0 \quad \text{for } R = \bar{R} \quad (5d)$$

where

$$\text{Bi}^* = \frac{h_0 r_i}{k_t} = \left(\frac{h_0 r_b}{k_t} \right) \left(\frac{r_i}{r_b} \right) = \frac{\text{Bi}}{E_{cp}} \quad \text{Bi} = \frac{h_0 r_b}{k_t}$$

It is important to note that Eq. (5d) is responsible for equating convection and conduction at the tube's outer surface. Equation (5a) will be fulfilled if

$$C = D = C_k = D_k = 0 \quad \text{for } k = 1, 2, 3, \dots \quad (6)$$

An application of Eq. (5b) gives

$$\lambda_k = 2k \quad (7)$$

Substituting Eqs. (6) and (7) in Eq. (4) one gets

$$\Theta(R, \theta) = A + B \ln R + \sum_{k=1}^{\infty} (A_k R^{2k} + B_k R^{-2k}) \cos(2k\theta) \quad (8)$$

From Eqs. (5c) and (8),

$$A = 1 \quad (9a)$$

and

$$B_k = -A_k \quad (9b)$$

Now, from Eqs. (8), (9a), and (9b),

$$\Theta(R, \theta) = 1 + B \ln R + \sum_{k=1}^{\infty} A_k (R^{2k} - R^{-2k}) \cos(2k\theta) \quad (10)$$

Introducing new symbols,

$$Y_1 = B \quad Y_2 = A_1 \quad Y_3 = A_2 \quad \text{and so on} \quad (11)$$

We have Eq. (10) as

$$\Theta(R, \theta) = 1 + Y_1 \ln R + \sum_{k=2}^{\infty} Y_k (R^{2(k-1)} - R^{-2(k-1)}) \cos[2(k-1)\theta] \quad (12)$$

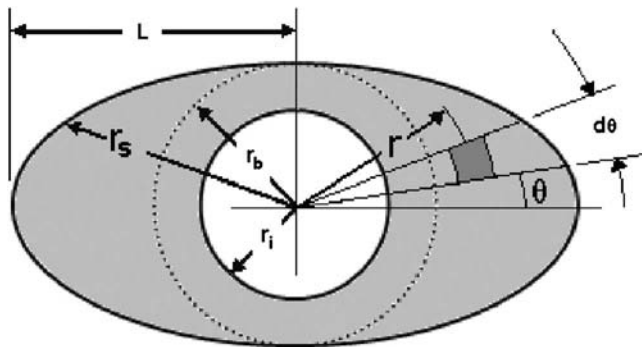


Fig. 3 Coordinate system of a typical shaped tube for two-dimensional analysis

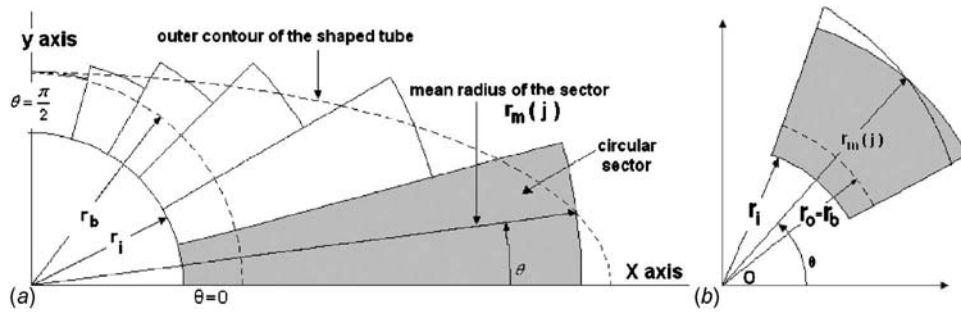


Fig. 4 (a) Division of shaped tube into sectors. (b) A single sector (j th in anticlockwise direction) from the domain of the shaped tube.

This is the temperature profile in the domain of the problem with Y_1, Y_2, Y_3, \dots as the unknowns. Finally, the boundary condition in Eq. (5d) is applied in Eq. (12) to get

$$Y_1 \left(\frac{1}{\bar{R}} + \text{Bi}^* \ln \bar{R} \right) + \sum_{k=2}^{\infty} Y_k \left[\frac{2(k-1)}{\bar{R}} (\bar{R}^{2(k-1)} + \bar{R}^{-2(k-1)}) + \text{Bi}^* (\bar{R}^{2(k-1)} - \bar{R}^{-2(k-1)}) \right] \cos[2(k-1)\theta] = -\text{Bi}^* \quad (13)$$

However, the expression given in Eq. (13) cannot be evaluated explicitly due to the unique geometry of the outer periphery of the shaped tubes. At this point, BCM as used in Ref. [19] is applied. This is done by truncating the infinite series in Eq. (13) to first N terms, and taking N number of points on the boundary (outer surface of the domain), N values of angle θ are given by the formula

$$\theta(j) = \frac{\pi}{2} \left(\frac{j-1}{N-1} \right) \quad j = 1, 2, 3, \dots, N \quad (14)$$

Equation (13) can be written as a system of linear equations, with Y_k as the unknown constants

$$\sum_{k=1}^N \mathbf{G}_{jk} Y_k = \mathbf{F}_j \quad j = 1, 2, 3, \dots, N \quad (15)$$

where

$$\mathbf{G}_{j1} = \frac{1}{\bar{R}} + \text{Bi}^* \ln \bar{R} \quad (16)$$

and for $k \geq 2$,

$$\mathbf{G}_{jk} = \left[\frac{2(k-1)}{\bar{R}} (\bar{R}^{2(k-1)} + \bar{R}^{-2(k-1)}) + \text{Bi}^* (\bar{R}^{2(k-1)} - \bar{R}^{-2(k-1)}) \right] \times \cos[2(k-1)\theta] \quad (17)$$

$$\mathbf{F}_j = -\text{Bi}^* \quad (18)$$

The system of linear equations in Eq. (15) on solving gives values of unknown constants Y_k . The nondimensional temperature profile of the oval tube can be found from Eq. (12) using calculated values of Y_k . It may be noted that though some approximation is involved in the above technique, the accuracy of prediction can be increased by increasing the number of the collocation points. This gives the temperature profile as

$$\Theta(R, \theta) = 1 + Y_1 \ln R + \sum_{k=2}^N Y_k (R^{2(k-1)} - R^{-2(k-1)}) \cos[2(k-1)\theta] \quad (19)$$

The number of collocation points N is selected such that further

increase in N does not increase the accuracy of the prediction.

It has been mentioned earlier that Li et al. [13] considered the outer surface of the base circular tube (at radius r_o of Fig. 1(a)) as the isothermal surface. With this consideration, the expression of temperature changes as follows:

$$\Theta(R, \theta) = 1 + Y_1 \ln \frac{R}{E_{cp}} + \sum_{k=2}^N Y_k (R^{2(k-1)} - E_{cp}^{4(k-1)} R^{-2(k-1)}) \times \cos[2(k-1)\theta] \quad (20)$$

3 Sector Method

In the previous section, a rigorous two-dimensional technique has been elaborated for the estimation of the temperature field. This requires solution of a system of simultaneous equations. In the present section, an approximate method called *sector method* (SM), is used for a one-dimensional heat conduction analysis of the domain of this problem. The method presently used is similar to that used [20] for the analysis of circumferential plate fins of noncircular geometry. This method takes care of the variation of temperature in two directions, with the assumption that temperature remains constant in the angular direction for a small angle only. Further, no numerical technique is essential for the evaluation of temperature profile along a sector.

In this approach, the shaped tube is divided into a number of sectors, as shown in Fig. 4. It is assumed that each sector subtending a small angle at the center is separated from its neighboring sectors by imaginary insulating radial lines. The distance from the center of the tube to the point on the outer contour along the angle bisector of a particular sector is treated as the mean outer radius for that part. Considering radial conduction between two radii, the nondimensional temperature profile is given by

$$\Theta = \frac{1 - \text{Bi}^* D_{cp}(j) \ln[R/D_{cp}(j)]}{1 - \text{Bi}^* D_{cp}(j) \ln[1/D_{cp}(j)]} \quad (21)$$

where

$$\text{Bi}^* = \frac{h_0 r_i}{k_t} = \left(\frac{h_0 r_b}{k_t} \right) \left(\frac{r_i}{r_b} \right) = \frac{\text{Bi}}{E_{cp}} \quad \text{Bi} = \frac{h_0 r_b}{k_t} \quad (22)$$

$$\Theta = \frac{T - T_{\infty}}{T_i - T_{\infty}} \quad R = \frac{r}{r_i} \quad E_{cp} = \frac{r_b}{r_i} \quad D_{cp}(j) = \frac{r_m(j)}{r_i} \quad (23)$$

For constant wall temperature boundary condition at the surface of the circular tube (i.e., the fin base), the temperature profile can be derived as

$$\Theta = \frac{1 - \text{Bi}^* D_{cp}(j) \ln[R/D_{cp}(j)]}{1 - \text{Bi}^* D_{cp}(j) \ln[E_{cp}/D_{cp}(j)]} \quad (24)$$

The accuracy of predicting the rate of heat transfer depends on the

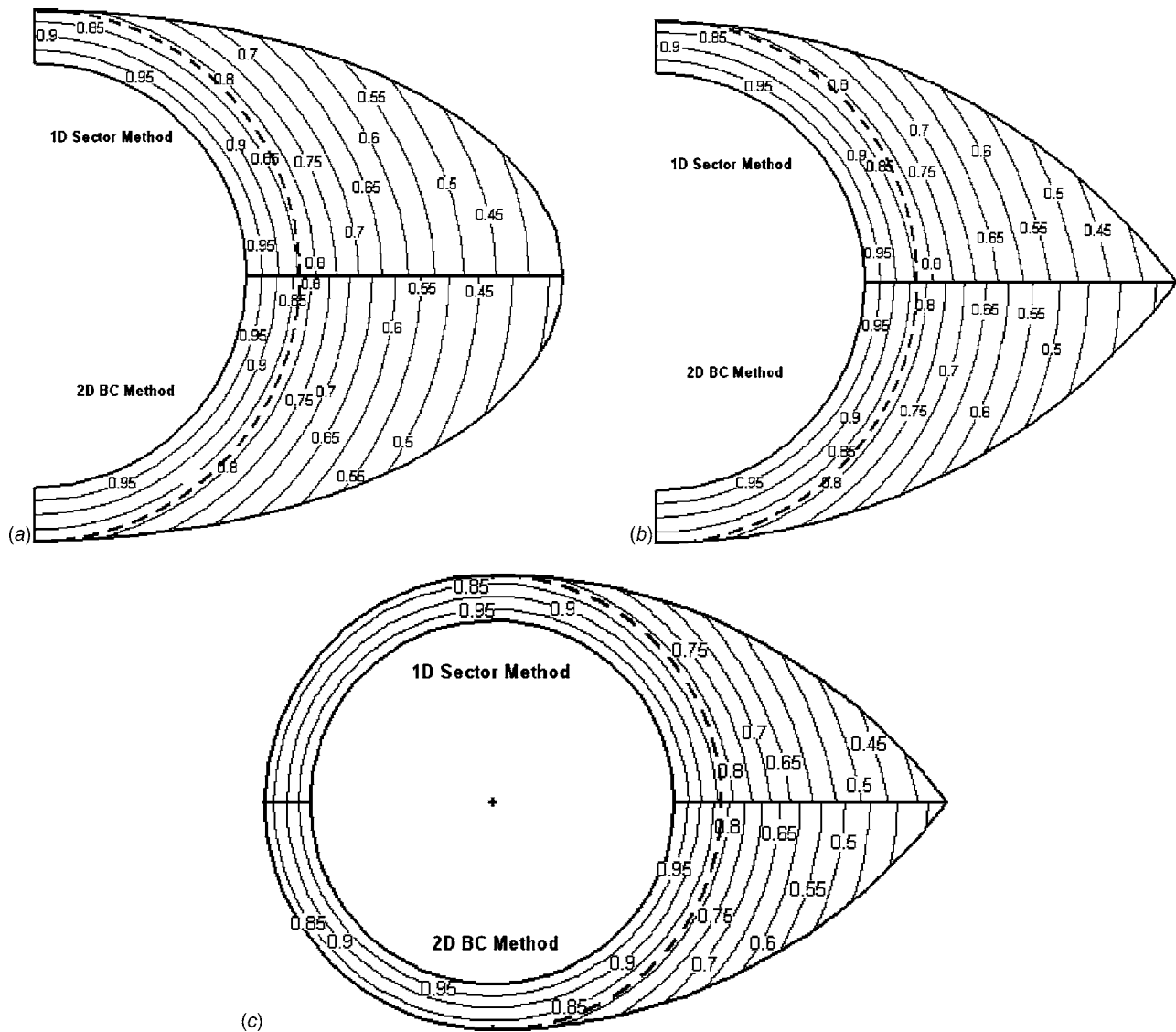


Fig. 5 Isothermal curves shown in (a) oval, (b) lenticular, and (c) teardrop shaped tubes with isothermal inner wall

number of sectors. The number is increased until there is no change in the result within the numerical tolerance.

4 Results and Discussion

From the solution of Eq. (19) or (21), the isotherms for the shaped tubes may be obtained. Figure 5 depicts the isotherms obtained by both of these techniques in three different shaped tubes. One may note that the difference between the predictions from these two methods is minimal. Interestingly, it may be observed that when the inner periphery of the tubes is assumed to be at constant temperature, the isothermal curves do not coincide with the circumference of the base circle. This shows that the assumption of isothermal condition at the outer surface of the base circle [13] is not strictly valid.

For a comparison of the present techniques with that of Li et al. [13], results in the following sections are presented for isothermal condition at the outer surface of the base tube.

4.1 Temperature Distribution. Figures 6(a) and 6(b) present a variation of temperature for an oval shaped tube in angular and radial directions respectively, for $\lambda_b=0.5$, $Bi=1.0$. The results are presented introducing a nondimensional term Ω used to define temperature,

$$\Omega = \frac{T_\lambda - T_\infty}{T_{x\lambda} - T_\infty} \quad (25)$$

where T_λ is the temperature at any angular position for a certain value of λ and $T_{x\lambda}$ is the temperature on the x axis for that value of λ .

In Fig. 6(a), the horizontal line at $\Omega=1$ represents a temperature profile as obtained by Li et al. [13] for any value of radial position λ . This is due to the assumption of no variation of temperature in the angular direction. The horizontal line at $\Omega=1$ also presents a variation of temperature at $\lambda=\lambda_b$ (base radius) in the angular direction for the one-dimensional SM and two-dimensional BCM due to the assumption that temperature at base radius is constant. All the remaining curves present a variation of temperature in angular direction for certain values of λ , as given in the graph. From Fig. 6(a), temperature decreases in angular direction away from the x axis and the rate of decrease increases as the radius increases. This is due to the increase in the surface area of the fin as the length of the fin increases. Similarly, Fig. 6(b) presents a variation of temperature along the radial direction at different angular positions for an oval shaped tube with $\lambda_b=0.5$, $Bi=1.0$. At a certain angular position, the temperature decreases in the angular direction, and the rate of decrease increases

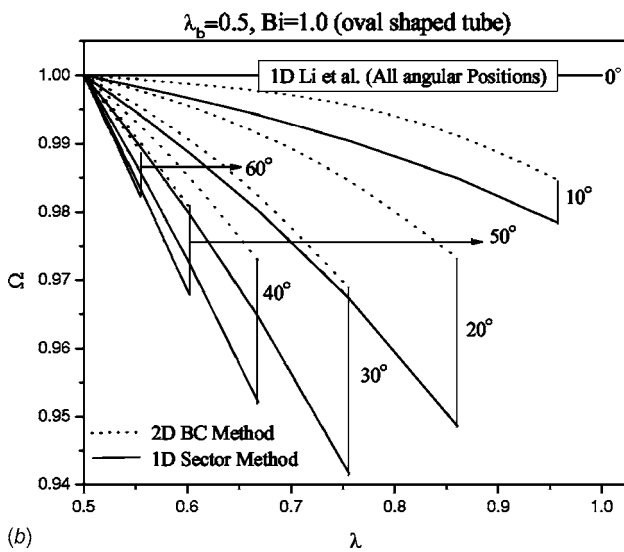
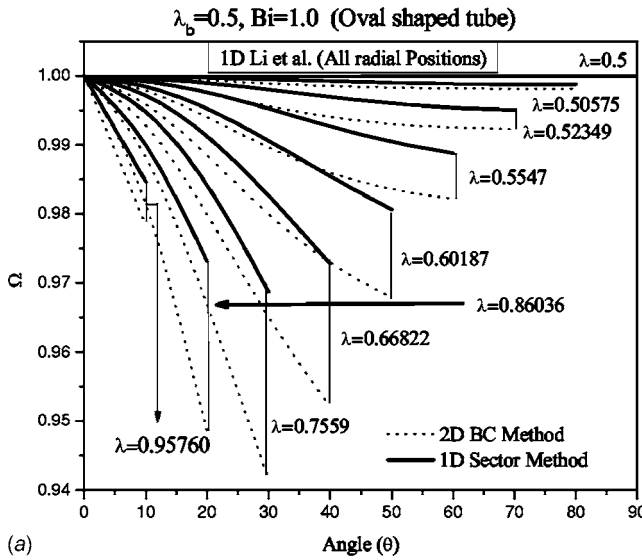


Fig. 6 Variation of temperature along (a) radial direction at different angles, (b) angular positions at different radial positions for an oval shaped tube with $\lambda_b=0.5$, $Bi=1.0$

for higher values of angles, i.e., away from the x axis.

From Fig. 6(a), it may be noted that the temperature values for the one-dimensional SM at every point are marginally higher than those for the two-dimensional BCM, while in Fig. 6(b), the temperature values for the one-dimensional SM at every point are marginally less than those for the two-dimensional BCM. This trend occurs as we assume the temperature to be constant in the angular direction in a particular sector.

Further comparison with the analysis of Li et al. [13] can be made considering temperature distribution along the x axis. The dimensionless temperature is plotted along the x axis (Fig. 2) in Figs. 7(a) and 7(b) against the dimensionless coordinate $\lambda=r/L$ for oval and lenticular shaped tubes, respectively. Results are presented for the shaped tubes with tube shape factor $\lambda_b=0.5$ and $Bi=1.0$ and 0.1 .

The fin for each tube extends from $\lambda=\lambda_b$ (tube shape factor $\lambda_b=r_b/L$) to $\lambda=1$. So, the vertical lines in Figs. 7(a) and 7(b) indicate the location of the base of the fin for the corresponding value of λ_b . The higher the value of λ_b , the shorter the fin is. There is a sharp decrease in the nondimensional temperature profile for $Bi=1.0$ than at $Bi=0.1$. At $Bi=0.1$, the nondimensional

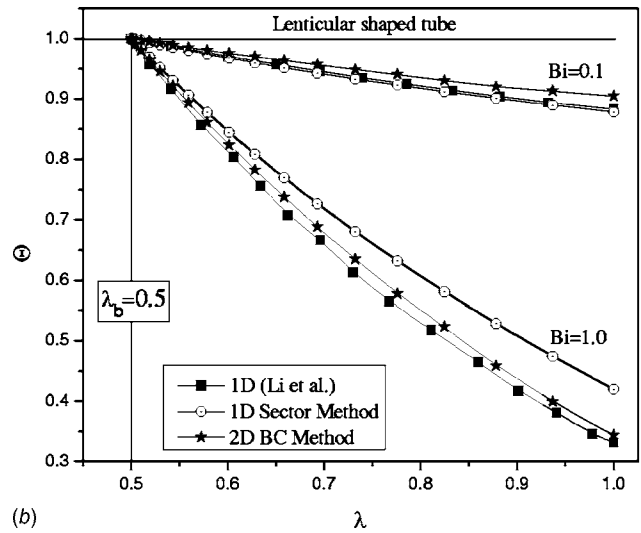
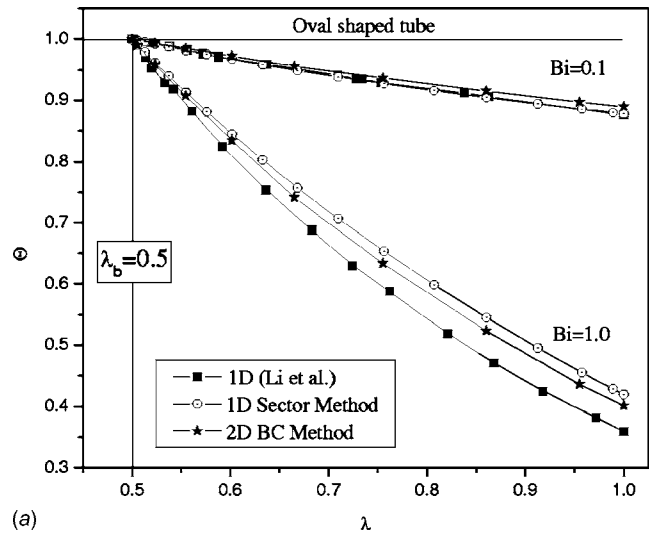


Fig. 7 Dimensionless temperature plotted as a function of Biot number and the dimensionless coordinate $\lambda=r/L$ for (a) oval and (b) lenticular shaped tubes

temperatures by the two-dimensional BCM, one-dimensional SM, and one-dimensional solution by Li et al. [13] are almost the same. They are further very close to each other for $\lambda_b=0.5$ at $Bi=0.1$. When $Bi=1.0$, there is some difference in values of dimensionless temperature for $\lambda_b=0.5$. The nondimensional temperature at a particular point on the x axis is more for the one-dimensional SM than for the one-dimensional solution by Li et al. [13]. The corresponding nondimensional temperature for the two-dimensional BCM lies in between values by the one-dimensional SM and one-dimensional solution by Li et al. [13].

4.2 Shaped Tube Efficiency. As Li et al. [13] analyzed the performance of shaped tubes similar to fins attached to a circular tube, they have defined the efficiency for these tubes as

$$\chi \equiv \frac{q}{q_{\max}} = \frac{\bar{T}_0 - T_{\infty}}{T_b - T_{\infty}} \quad (26)$$

where q is the actual heat transfer rate of the shaped tube and q_{\max} is the heat transfer rate that would be achieved if the spatially average temperature of the surface of the shaped tube, \bar{T}_0 , were equal to the temperature of the base of the fin, T_b , at $r=r_b$.

For symmetrical shaped tubes such as the oval and lenticular ones, the shaped tube efficiency is equal to the fin efficiency. The

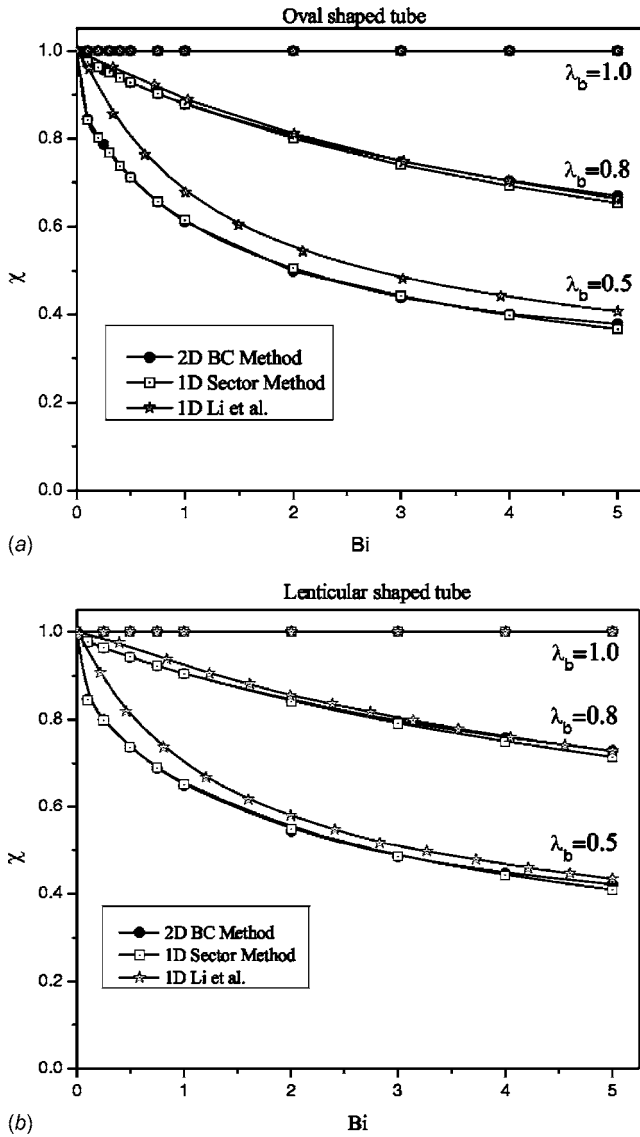


Fig. 8 Shaped tube efficiency plotted as a function of Biot number and λ_b for (a) oval shaped tube and (b) lenticular shaped tube

shaped tube efficiencies for oval and lenticular shaped tubes (χ) are plotted against Biot number in Figs. 8(a) and 8(b), respectively. All the results are presented for $Bi \leq 5$. Curves are shown for the two-dimensional BCM, one-dimensional SM, and one-dimensional method by Li et al. [13] for values of $\lambda_b = 0.5, 0.8$, and 1.0. The base line circular tube is represented by $\lambda_b = 1$, corresponding to $\chi = 1$. For a certain value of Biot number (Bi), the effect of the addition of material to the base circular tube on the fin efficiency can be estimated by decreasing values of λ_b .

From Figs. 8(a) and 8(b), the shaped tube efficiency (χ) decreases with increasing Bi and with the addition of material to the base circular tube, i.e., decreasing value of λ_b . The rate of decrease of the shaped tube efficiency with increasing Bi is higher for $Bi \leq 0.5$.

From Figs. 8(a) and 8(b), in the case of all the methods, the shaped tube efficiency for $\lambda_b = 1.0$ is equal to 1.0 as $\lambda_b = 1.0$ denotes a circular tube. As the value of λ_b decreases, the fin length increases. For $\lambda_b = 0.8$, i.e., smaller fin length, the shaped tube efficiencies of the two-dimensional BCM, one-dimensional SM, and one-dimensional method by Li et al. [13] are almost equal.

At $\lambda_b = 0.5$, the shaped tube efficiencies of the two-dimensional

BCM and one-dimensional SM are equal, but the one-dimensional solution by Li et al. [13] is marginally higher than the two.

5 Conclusion

Tubular structures are most common in the construction of heat exchangers. A circular inner passage of tubular elements is preferred as it is superior in withstanding the internal pressure. On the other hand, the outer profile of the tubes can be innovatively shaped to improve the hydrodynamic and/or the thermal design. In the present work, the conduction through such shaped tubes has been analyzed. Three different outer profiles, namely, elliptic, lenticular, and teardrop, have been considered. A two-dimensional analysis through a boundary collocation based semianalytical technique and a one-dimensional approximate method have been suggested. The prediction from both these methods agrees closely. Recently, Li et al. [13] solved the same problem considering the temperature variation only in the radial direction where the shaped tubes are idealized as one-dimensional fins attached to the outer periphery of a base cylinder. While Li et al. [13] neglected the conductive resistance of the base cylinder, the present methods are more accurate. Further, the one-dimensional SM does not require any numerical solution and can be employed with a minimum computational effort. It also takes care of the angular temperature variation partially. Therefore, the one-dimensional SM is a definite improvement over the one-dimensional method proposed by Li et al. [13].

Nomenclature

ds = width of the strip on the surface of the shaped tube as shown in Fig. 2, m

h_0 = convective heat transfer coefficient, $W/m^2 K$

q = heat transfer rate, W

q_{max} = maximum heat transfer rate, W

r = radial coordinate, m

r_a = radius of surface arc of the lenticular shaped tube as in Fig. 1, m

r_b = tube radius at the fin base, m

r_i = tube inner radius, m

$r_m(j)$ = mean outer radius of the j th sector, m

r_o = outer radius of the circular tube, m

$r_s(\theta)$ = surface distance from the center of the tube, m

$A, B, C, D, A_k, B_k, C_k, D_k$ = integral constants in a general solution (Eq. (4))

Bi = Biot number ($=h_0 r_b / k_t$), dimensionless

Bi^* = ratio of Bi and E_{cp} , dimensionless

$D_{cp}(j)$ = ratio of $r_m(j)$ and r_i , dimensionless

E_{cp} = ratio of inner radius r_i and base radius, dimensionless

F_j = right-hand vector in a system of linear equations resulting from a simple collocation

G_{jk} = matrix in a system of linear equation resulting from a simple collocation

k_t = material thermal conductivity, $W/m K$

L = length of the fin, m

N = number of collocation points

R = ratio of r and r_i , dimensionless

\bar{R} = ratio of $r_s(\theta)$ and r_i , dimensionless

R_a = ratio of r_a and r_i , dimensionless

T = temperature, K

T_b = temperature at the base of the fin, K

T_i = temperature of the inner surface, K

T_∞ = temperature of the surrounding fluid, K
 T_λ = temperature at any angular position for a certain value of λ , K
 $T_{x\lambda}$ = temperature at the 0 deg angular position (on the x axis) for a certain value of λ , K
 \bar{T}_0 = spatially average temperature of the surface of the shaped tube, K
 Y_k = unknowns in linear systems

Greek

Θ = dimensionless temperature
 θ = angle between horizontal axis and radius $r_s(\theta)$
 λ = dimensionless coordinate ($=r/L$)
 λ_b = tube shape factor ($=r_b/L$)
 λ_k = integral constants in a general solution (Eq. (4))
 χ = shaped tube efficiency as defined in Eq. (26)
 Ω = dimensionless temperature

References

- [1] Ota, T., Aiba, S., Tsuruta, T., and Kaga, M., 1983, "Forced Convection Heat Transfer From an Elliptic Cylinder," *Bull. JSME*, **26**(212), pp. 262–267.
- [2] Ota, T., and Nishiyama, H., 1984, "Heat Transfer and Flow Around an Elliptic Cylinder," *Int. J. Heat Mass Transfer*, **27**(10), pp. 1771–1779.
- [3] Nishiyama, H., Ota, T., and Matsumoto, T., 1988, "Forced Convection Heat Transfer From Two Elliptic Cylinders in a Tandem Arrangement," *Heat Transfer-Jpn. Res.*, **17**, pp. 19–31.
- [4] Badr, H. M., Dennis, S. C. R., and Kocabiyik, S., 2001, "Numerical Simulation of the Unsteady Flow Over an Elliptic Cylinder at Different Orientations," *Int. J. Numer. Methods Fluids*, **37**(8), pp. 905–931.
- [5] Merker, G. P., and Hanke, H., 1986, "Heat Transfer and Pressure Drop on the Shell-Side of Tube-Banks Having Oval-Shaped Tubes," *Int. J. Heat Mass Transfer*, **29**(12), pp. 1903–1909.
- [6] Merker, G. P., Hanke, H., and Bähr, M., 1987, "Analogy Between Momentum and Heat-Transport in Cross-Flow Tube Banks With Oval-Shaped Tubes," *Wärme und Stoffübertragung (Heat Mass Transfer)*, **21**(2–3), pp. 95–102.
- [7] Jin, J., Feng, M., Zhang, M., and Qiu, L., 1996, "Experimental Investigation of a New Kind of Heat Exchanger Tube Bank," *Proceedings of the International Conference on Energy and Environment*, Begell House Inc., New York, pp. 417–421.
- [8] Matos, R. S., Vargas, J. V. C., Laursen, T. A., and Saboya, F. E. M., 2001, "Optimization Study and Heat Transfer Comparison of Staggered Circular and Elliptic Tubes in Forced Convection," *Int. J. Heat Mass Transfer*, **44**(20), pp. 53–61.
- [9] Jang, J., and Li, B., 1996, "A Numerical Analysis of Two-Dimensional Laminar Flow Over an Elliptic Tube Bank," *Proceedings of the Fourth International Symposium on Heat Transfer*, Beijing, R.O.C, pp. 547–552.
- [10] Ruth, E. K., 1983, "Experiments on a Crossflow Heat Exchanger With Tubes of Lenticular Shape," *ASME J. Heat Transfer*, **105**, pp. 571–575.
- [11] Rühlich, I., and Quack, H., 1998, "New Regenerator Design for Cryocoolers," *17th International Cryogenic Engineering Conference*, Bournemouth, UK, pp. 291–294.
- [12] Rühlich, I., and Quack, H., 1999, "Investigations on Regenerative Heat Exchangers," *Tenth International Cryocooler Conference*, Monterey, CA, pp. 265–274.
- [13] Li, Z., Davidson, J. H., and Mantell, S. C., 2004, "Heat Transfer Enhancement Using Shaped Polymer Tubes: Fin Analysis," *ASME J. Heat Transfer*, **126**, pp. 211–218.
- [14] Bouris, D., Papadakis, G., and Bergeles, G., 2001, "Numerical Evaluation of Alternate Tube Configurations for Particle Deposition Rate Reduction in Heat Exchanger Tube Bundles," *Int. J. Heat Fluid Flow*, **22**, pp. 525–536.
- [15] Dutta, A., Som, S. K., and Das, P. K., 2004, "Film Condensation of Saturated Vapor Over Horizontal Noncircular Tubes With Progressively Increasing Radius of Curvature Drawn in the Direction of Gravity," *ASME J. Heat Transfer*, **126**, pp. 906–914.
- [16] Incropera, F. P., and DeWitt, D. P., 2002, *Fundamentals of Heat and Mass Transfer* 5th ed. Wiley, New Delhi, Chap. 4, pp. 192–194.
- [17] Ozisik, M., N., 1985, *Heat Transfer: A Basic Approach* International ed., McGraw-Hill, Singapore, pp. Chap. 4, 130–134.
- [18] Eckert, E. R. G., and Drake, R. M., 1972, *Analysis of Heat and Mass Transfer*, McGraw-Hill, Tokyo, Japan.
- [19] Kolodziej, J. A., and Streck, T., 2001, "Analytical Approximations of the Shape Factors for Conductive Heat Flow Incircular and Regular Polygonal Cross-Sections," *Int. J. Heat Mass Transfer*, **44**, pp. 999–1012.
- [20] Kundu, B., and Das, P. K., 1999, "Performance Analysis and Optimization of Eccentric Annular Disk Fins," *ASME J. Heat Transfer*, **121**, pp. 128–135.

Genetic Algorithm Based Optimization of PCM Based Heat Sinks and Effect of Heat Sink Parameters on Operational Time

Atul Nagose

Ankit Somani

Aviral Shrot

Arunn Narasimhan¹

Assistant Professor
e-mail: arunn@iitm.ac.in

Heat Transfer and Thermal Power Laboratory,
Department of Mechanical Engineering,
Indian Institute of Technology Madras,
Chennai 600 036, India

Using an approach that couples genetic algorithm (GA) with conventional numerical simulations, optimization of the geometric configuration of a phase-change material based heat sink (PBHS) is performed in this paper. The optimization is done to maximize the sink operational time (SOT), which is the time for the top surface temperature of the PBHS to reach the critical electronics temperature (CET). An optimal solution for this complex multiparameter problem is sought using GA, with the standard numerical simulation seeking the SOT forming a crucial step in the algorithm. For constant heat dissipation from the electronics (constant heat flux) and for three typical PBHS depths (A), predictive empirical relations are deduced from the GA based simulation results. These correlations relate the SOT to the amount of phase change material to be used in the PBHS (ϕ), the PBHS depth (A), and the heat-spreader thickness (s), a hitherto unconsidered variable in such designs, to the best of the authors' knowledge. The results show that for all of the typical PBHS depths considered, the optimal heat-spreader thickness is 2.5% of the PBHS depth. The developed correlations predict the simulated results within 4.6% for SOT and 0.32% for ϕ and empowers one to design a PBHS configuration with maximum SOT for a given space restriction or the most compact PBHS design for a given SOT. [DOI: 10.1115/1.2780182]

Keywords: phase change material, genetic algorithm, heat spreader, composite heat sink, electronics cooling, optimization

Introduction

Thermal management of high heat flux dissipating electronic components is a pertinent research need of our present times [1]. A promising heat sink design for cooling electronics with reliable operating temperature of 90°C is the composite heat sink [2] that utilizes a phase-change material (PCM) along with a base material (BM) in a judicious combination such that the heat is taken away quickly from the potential hot spots by the BM and to be sunk in the PCM in the form of its latent heat storage. The passive nature of such a PBHS makes it useful in space applications [3] also. Chow and Zhong [4] were amongst the earliest researchers working on such composite heat sinks, which focused on a metal/phase-change material (M/PCM) composite giving high performance. Pal and Joshi [5] predicted that PCM are an effective option for passive cooling of high-density electronic modules for transient periods. Bujage [6] also worked on paraffin wax storage fins. He compared star shaped matrices and internal fins and found internal fins giving better results. Krishnan and Garimella [7] have studied transient response of PCM based heat sinks that uses a rectangular enclosure made using copper and aluminum with PCM (Eicosane) in it, to short pulses in power dissipation by multiple discrete sources. The PCM unit with heat sources on the bottom wall gave the best performance. Krishnan et al. [8] have also worked on a hybrid heat sink, which is designed to have a PCM bath externally at the BM fin tip as a buffer heat sink, while the BM fins can also be cooled by external air convection. The improved performance of hybrid heat sinks is quantified and a

one-dimensional fin equation, which takes into account both convective heat transfer and PCM melting, is formulated. An alternate PBHS design involves the impregnation of PCM in metal foam, serving as the BM, thus combining the thermal energy storage concept with the thermal conductivity enhancement [9].

Stritih and Novak [10] found that the distance between the BM fins is an important parameter influencing the sink operational time (SOT) of a PBHS. Zheng and Wirtz [11,12] have worked on the design optimization of PBHS. They use VISUALDOC, which calls its optimizer for varying the design variables and design parameters which are stabilization time and hot side temperature-transition temperature difference. Best design is determined subject to the geometric and heat loading constraints. Shatikian et al. [13] have simulated various geometries of PBHS by varying the fin thickness and PCM layer thickness keeping the ratio constant. They considered in their analysis the convection heat transfer at the surfaces of the PBHS that are not in contact with the electronics. Recently, Akhilesh et al. [14] analyzed a PBHS and showed through analysis and simulations that the maximization of SOT can be achieved when the PBHS geometry is designed such that complete melting of all of the PCM used happens when the PBHS reaches the set-point criterion. They came up with the concept of critical fin thickness, which ensures complete melting and presented a correlation for the same. Nayak et al. [15] have experimentally analyzed the composite heat sinks using plate type and rod type metal fins, also concluding that the rod type fins perform the best. All of these analyses have not considered the heat-spreader design and the possibility of multiple design solutions for the PBHS.

It is evident from the above literature survey that the performance of a PBHS is characterized by the SOT, which is dependent on the PBHS geometry [14]. Thus, the objective of this paper is to maximize the SOT by optimizing the configuration of the PBHS

¹Corresponding author.

Contributed by the Heat Transfer Committee of ASME for publication in the JOURNAL OF HEAT TRANSFER. Manuscript received January 12, 2007; final manuscript received May 7, 2007; published online January 28, 2008. Review conducted by Sung Jin Kim.

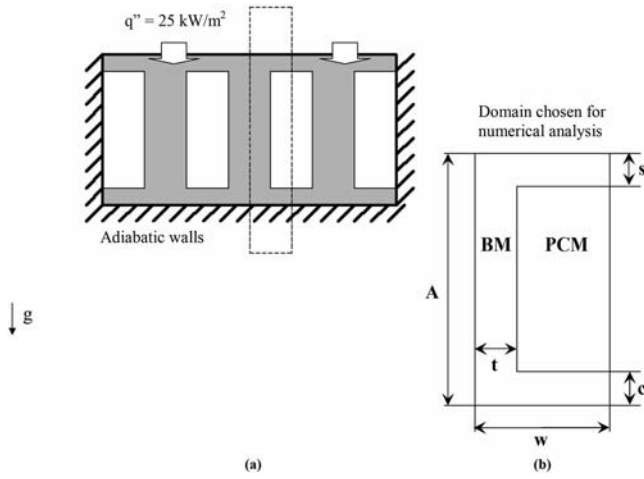


Fig. 1 (a) Schematic representation of PBHS; (b) domain chosen for analysis (E-PBHS)

using genetic algorithms. In order to choose an optimal PBHS design that maximizes the SOT for a given set of parameters and constraints, in this paper we have used a genetic algorithm (GA) based solution procedure that utilizes the numerical simulation of typical PBHS geometry to estimate the SOT. The GA approach is a stochastic search mechanisms inspired by the Darwinian natural selection and genetics [16–19] and has an advantage over other methods in obtaining multiple solutions and considerable computational savings compared to an exhaustive search. From a multiple solution space of geometrical design of the PBHS, combining several geometric parameters such as heat-spreader thickness, PBHS depth, and BM fin size, PCM quantity used, the GA solution technique used in this paper selects at each intermediate step of the solution procedure, a better geometrical design of the PBHS that maximizes SOT.

2 Phase Change Material-Base Heat Sink

Figure 1(a) shows the schematic representation of the PCM-BM heat sink (PBHS) analyzed in this study. It consists of a fin array of uniform thickness ($2t$) and depth equivalent to the sink height (A) made of a BM, which protrudes in a PCM bath. This typical PBHS design [14] is considered to enhance the BM/PCM heat transfer contact surface area, resulting in a judicious use of high thermal conductivity BM carrying the heat away from the source and sinking it into the high latent heat capacity PCM. In such a design, owing to the low thermal conductivity, the PCM is kept away from the electronics (heat source), to avoid local hot spots on the surface where the electronics directly come into contact with PCM. Thus the portion between the BM-PCM array and the electronic component has a layer of “heat spreader” [14] made of the BM. The purpose is to assimilate the heat flux available from the top and distribute it uniformly to the lower portion of the PBHS. The bottom-most layer of PCM has the least melt front progression rate [14,20]. Therefore, to ensure complete melting of this layer, we propose to have an auxiliary heat spreader (c) at the bottom of the sink. The elemental PBHS (E-PBHS) chosen in Fig. 1(b) repeats itself symmetrically in the model and it is assumed that there is no lateral heat transfer between such E-PBHS's. The sidewalls of PBHS are assumed to be adiabatic. As the width of the box is fixed, the width of the half fin (w) in turn decides the number of fins present in the PBHS.

The sidewalls and the bottom surface of the sink are insulated from surroundings, an assumption undertaken since the natural convective losses from the sides are minimal and radiation losses can be neglected at the involved temperatures [14]. Also, the above design becomes conservative even when such losses be-

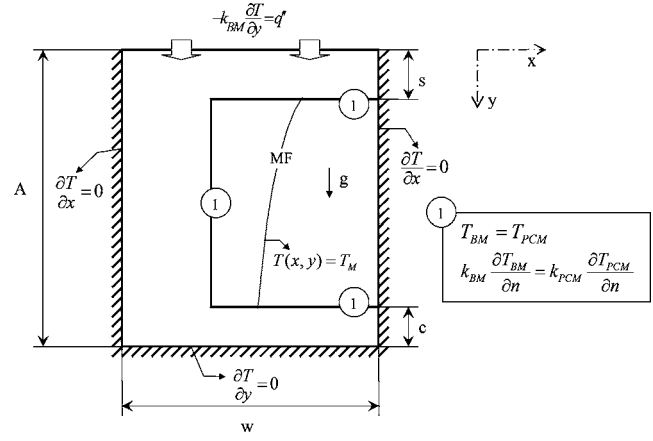


Fig. 2 E-PBHS with boundary conditions

come significant. Natural convection in the liquid PCM is not considered [2,14]. Thus, the domain considered in Fig. 1(b), an E-PBHS of arbitrary dimensions, is chosen for numerical analysis.

3 Modeling Procedure and Numerical Method

Figure 2 gives the E-PBHS domain with the imposed boundary conditions. Both the BM and PCM regions are governed by the two-dimensional transient energy conduction equations. Thus, the temperature at any point in the domain is presented as $T \equiv T(x, y, t)$. The governing differential equation on the BM side can be written as

$$k_{BM} \left[\frac{\partial^2 T}{\partial x^2} + \frac{\partial^2 T}{\partial y^2} \right] = (\rho c)_{BM} \frac{\partial T}{\partial t} \quad (1)$$

For the PCM region, when it is in either liquid or solid state at a point, the governing equation is

$$k_{PCM} \left[\frac{\partial^2 T}{\partial x^2} + \frac{\partial^2 T}{\partial y^2} \right] = (\rho c)_{PCM} \frac{\partial T}{\partial t} \quad (2)$$

Taking corroboration from Refs. [3,7], the $k_{PCM}, (\rho c)_{PCM}$ values are assumed to be identical for both the solid and liquid phases. Change of phase of PCM is compensated through an enthalpy balance scheme [13–15], in the grid points surrounding PCM, ensuring that the net energy flux balances the latent heat of melting of the PCM for that control volume. The boundary conditions existing at the left and right boundaries of the PCM domain, in Fig. 2, are

$$\left. \frac{\partial T}{\partial x} \right|_{x=0,w} = 0 \quad (3a)$$

$$\left. \frac{\partial T}{\partial y} \right|_{y=A} = 0 \quad (3b)$$

The heat flux received by the top BM surface of Fig. 2 is received into the E-PBHS through the boundary condition

$$-k_{BM} \left. \frac{\partial T}{\partial y} \right|_{y=0} = q'' \quad (4)$$

Equations (1) and (2), along with the boundary conditions (3) and (4), are solved numerically using the finite volume method (FVM) [21] involving implicit time marching scheme [22]. Owing to the FVM formulation of the numerical solution procedure, the BM-PCM interface automatically satisfies the temperature continuity term, assumed with zero contact resistance,

$$T_{BM} = T_{PCM} \quad (5a)$$

along with an energy flux balance continuity equation of the form

Table 1 Thermophysical properties of the BM (aluminum) and PCM (Eicosane) used

Parameters	Symbol	Values used in simulation
BM properties [22]	ρ (kg m ⁻³)	2702
	k (W m ⁻¹ K ⁻¹)	237
	c (kJ kg ⁻¹ K ⁻¹)	0.9
PCM properties [25]	ρ (kg m ⁻³)	800
	k (W m ⁻¹ K ⁻¹)	0.24
	c (kJ kg ⁻¹ K ⁻¹)	2.5
	L (kJ kg ⁻¹)	266
	T_M (K)	310

$$k_{BM} \frac{\partial T_{BM}}{\partial n} = k_{PCM} \frac{\partial T_{PCM}}{\partial n} \quad (5b)$$

where n is the direction of the normal vector to the interface. Since the temperatures are available only at the nodes of each cell control volume, the equations in FVM have incorporated this interface condition using the harmonic mean approach while calculating the effective interface thermal conductivity. The required initial condition of the E-PBHS is assumed to be at the ambient temperature

$$T(x, y, 0) = T_{amb} \quad (6)$$

Aluminum is chosen as the BM for analysis because of its high thermal conductivity. The PCM material chosen is n -Eicosane, which is a standard PCM used in such electronics cooling applications [2,8,14] due to its high latent heat of melting (see Table 1 for properties) and the melting temperature, which, being closer to the ambient, leads to maximum utilization of its melting capacity

Table 2 Validation of the numerical scheme and grid independence study

$q'' = 25 \text{ kW/m}^2; A = 0.05 \text{ m}; \Phi = 0.5; t^* = 0.06; w^* = 0.12$				
Δt (s)	40×40 grid points time taken (s)	60×60 grid points time taken (s)	20×20 grid points [14]	40×40 grid points [14]
1.0	453	453	—	—
0.1	452.7	452.5	421.8	—
0.005	452.635	452.445	455.2	452.5
0.0025	—	—	455.8	455.1

for the given critical electronics temperature (CET), which is about 363 K [2,14].

The numerical simulation is validated by an analysis similar to that performed in Refs. [14,23]. The numerical domain, which was used in Ref. [14], was simulated for 40×40 grid and 60×60 grid for two different time steps: $\Delta t = 1 \text{ s}$ and $\Delta t = 0.1 \text{ s}$. From Table 2, it can be seen that the error involved in SOT due to the use of coarser grid is 0.2 s (0.044%) for $\Delta t = 0.1 \text{ s}$, and 0 when $\Delta t = 1 \text{ s}$ is used. Neglecting the small error, 40×40 grid can be used without any loss of accuracy. The results in Table 2 also show that for a 40×40 grid varying Δt from 0.1 s to 1 s introduces an error of 0.3 s (0.066%) in SOT, which can be safely neglected. Thus, 40×40 grid with $\Delta t = 1 \text{ s}$ is used for all subsequent simulations. These results are also compared with those obtained in Ref. [14] where $\Delta t = 0.0025 \text{ s}$ is assumed to give minimal error. The simulation used in this paper predicts SOT value within 0.6% error to the corresponding values in Ref. [14].

Further melting solver is validated for the one-dimensional melting, i.e., Stefan's problem as done in Ref. [14]. The sidewalls and the bottom surface of a PCM domain are insulated for this problem. The top surface is held at a constant temperature, which is higher than the melting point of PCM. Initially, all the PCM is in the solid state at the melting temperature. For the numerical solution, 40×40 grid was used along with a time step $\Delta t = 1 \text{ s}$. In Fig. 3, melt front progression with time has been plotted along with the theoretical solution for Stefan's problem [24]. The numerical method adopted involves the discrete space melt front tracking and thus the steps in the graph can be seen. At any instant of time, maximum deviation in melt front position of numerical solution from the theoretical solution is found to be 0.04 mm and the error is 4%.

Additionally the numerical simulation yields perfect energy balance, as energy entering PBHS as flux is equivalent to energy stored in BM and PCM at the end of operation. Thus, the same numerical code can be safely used for simulations.

4 Temperature Profiles in Phase Change Material Based Heat Sink

The motivation for using GA is described in this section by enunciating the complexity of the problem with corroborative results. Three arbitrarily chosen E-PBHS designs with specified geometry in Table 3 were numerically simulated under transient conditions for their top surface to reach CET. Obviously for identical A and w , variations in s , c , and t would exist with the variations in quantity of PCM used in the E-PBHS. This implies under usage of PCM even when the PBHS has reached CET, beyond which time

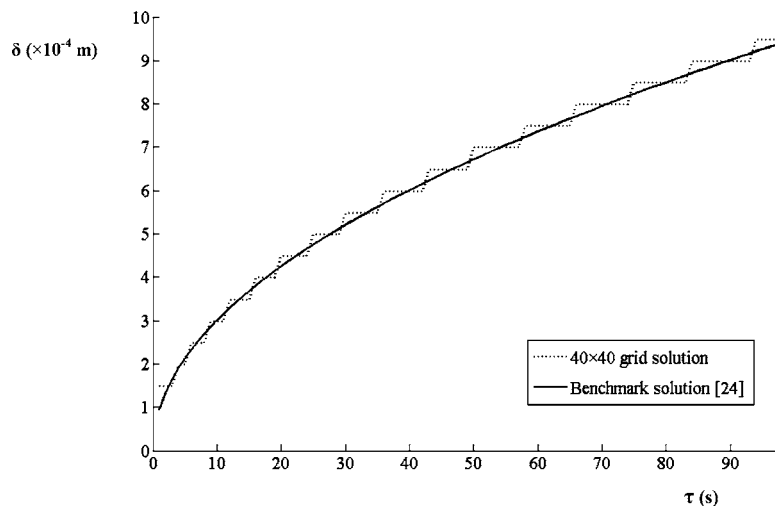


Fig. 3 Comparison of melt front solver with benchmark solution

Table 3 Dimensions for three arbitrary E-PBHS designs chosen for comparison (Fig. 4)

$q''=25 \text{ kW/m}^2; \Delta t=1 \text{ s}; 40 \times 40 \text{ grid points}; A=0.06 \text{ m}; w^*=0.0667$				
	s^*	c^*	t^*	Time (s)
(a)	0.025	0.000	0.0067	600
(b)	0.125	0.075	0.0167	575
(c)	0.025	0.000	0.0167	620

instant, it is rendered useless. Isotherms thus obtained when CET is reached by the E-PBHS at the end of SOT are shown in Fig. 4. Design (c) is the best among the three. Decrease in t from Designs (c) to (a) results in a drop of SOT by 20 s. In terms of the time of operation of the designs, Design (c) is better than the other two. Further, it is evident from the designs that when compared to (a) all of the PCM has melted in (c), realizing the capability of the design. An arbitrary decrease in t from Design (c) to (a) would result in SOT getting decreased by 30 s even though $\phi(a) > \phi(c)$. In fact, increase in ϕ has rendered (a) underutilized. Variation in s and c values, on the other hand, from Designs (c) to (b) leads to a drop of SOT by 55 s. Thus, it is evident that maximizing SOT, a strong function of the PBHS geometrical parameters, requires proper geometry that ensures complete melting of PCM. This requires a detailed analysis of the dependence of SOT on the E-PBHS geometrical parameters in order to optimize the PBHS configuration for maximum SOT for the constraint of complete melting.

5 Dependence of Sink Operational Time on Geometrical Parameters

For a fixed s and c value of the E-PBHS at a given q'' and A , Fig. 5 depicts the SOT and time for complete melting in an E-PBHS. From Fig. 5, the sensitivity of SOT and complete melting time due to variation in ϕ and w can be seen. It can be observed that the SOT increases with increasing ϕ until a maximum is reached after which it starts decreasing. However, the time for complete melting increases with the increase in ϕ and for a critical value of ϕ meets the SOT line. This critical value of ϕ depends on the geometric parameters (A , w , s , and c) that are held constant in this graph. Increasing ϕ further will lead to incomplete melting of PCM. Another salient feature of Fig. 5 is that the ϕ representing maximum SOT is not the same as the critical ϕ value for complete melting. Similar variations in critical ϕ value and ϕ for maximum SOT are obtained for $w=0.002 \text{ m}$ with higher SOT values for each ϕ .

The above analysis proves that PBHS design is both a multiparameter problem and a multiobjective problem. The objectives are maximizing SOT and ensuring complete melting of PCM. This necessitates the employment of an optimization technique, which can handle and sift through a large solution space in terms of the

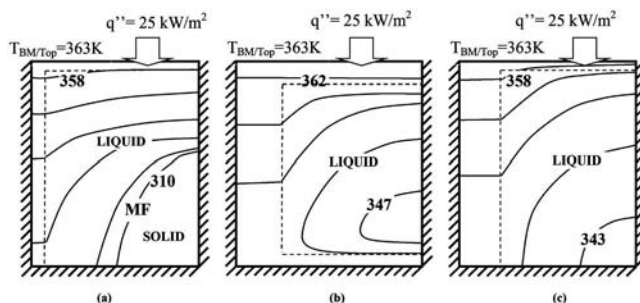


Fig. 4 Isotherms for three arbitrary E-PBHS designs (see Table 3 for specific values) at the end of SOT

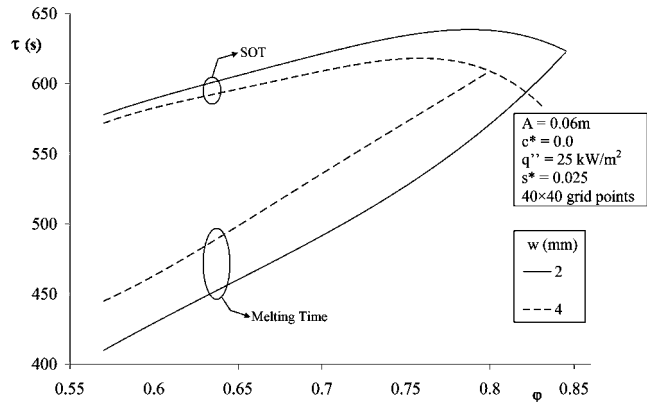


Fig. 5 SOT and melt time versus ϕ for $w=2 \text{ mm}$ and $w=4 \text{ mm}$

combinations of A , w , s , c , and t to achieve the required ϕ value to optimize SOT and gives best design based on all objectives. One such optimization technique is the GA, which has been employed to find the optimized solution for the present problem.

Genetic Algorithm and Fitness Function

GAs involve an “explorative logic,” which ensures that a large number of solutions, marginally better or worse, are considered while avoiding convergence on local maxima [25,26].

The algorithm involved in GA is delineated in Fig. 6 as a flow-chart. Every possible solution to the problem, every possible E-PBHS design in this case, is said to be an individual in the total population. An “individual” is represented by a binary string or a set of floating numbers, which specifies all the independent parameters considered in the problem. A set of such individuals at any simulation instant forms a population. An example of such a string for the individual out of the population of possible E-PBHS combination is given in Fig. 7. As seen earlier, since ϕ depends on A , w , s , c , and t , the parameter space is large. Every possible design in the range has to be represented completely and uniquely by a binary number. Here, a 16 bit number is used as a signature for a particular design specifying all the variables. As shown in Fig. 7 for each value of A , first 3 bits give the value of s , the next 5 bits for w , the next 5 bits for t , and the final 3 bits for c .

Even though all the variables can be theoretically varied from a minimum of 0 to the maximum when the heat sink is completely filled with BM, values used here (Fig. 7) are representative of the practical range of such heat sinks used to cool electronics [13,14,27] and practical limitations restrict the feasible range of values. Additionally, the ranges considered for simulation are chosen keeping in mind the ease of representation in GA. The initial population is randomly generated.

To evaluate the “fitness” of an individual, or in other words, to evaluate the suitability of a particular E-PBHS design, a fitness function is introduced. The fitness function for each individual is evaluated using the parameters determined by the “standard numerical simulation” block of the algorithm, as depicted in Fig. 6. Depending on the fitness values, pairs of individuals called parents are chosen for breeding using operators borrowed from natural genetics. The level of fitness of an individual dictates its chances of reproducing and surviving through generations. Thus, GA starts with a randomly chosen population and refines them over generations. The fitness function should take into account SOT and α . Both of these are combined into one function as

$$F = \text{SOT}^{0.7} \alpha^{1.4} \quad (7)$$

As the primary objective is to ensure full utilization of PCM, effect of α (the percentage of PCM to be melted) is pronounced by choosing its exponent n_2 greater than 1 in Eq. (7). Also, n_2

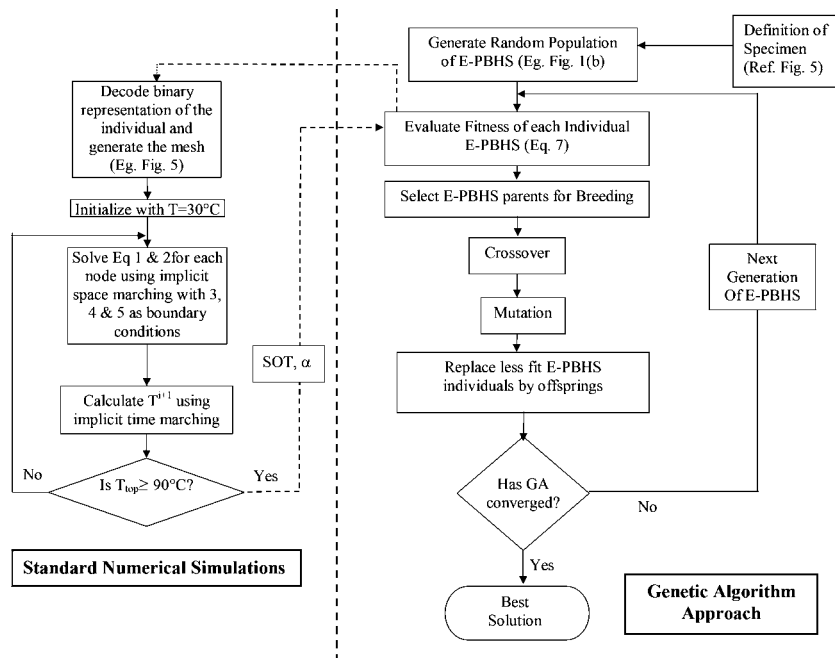


Fig. 6 Flowchart of the GA solution procedure

$=2n_1$ where n_1 is the exponent of SOT and n_2 that of α . This has been done to increase the dominance of α over SOT. The fitness function F , Eq. (7), is a positive number and as an optimizing constraint we seek maximum SOT and $\alpha=1$, higher F value will indicate a better (optimal) design.

The individuals created as a result of selecting with the fitness function are called offspring. Breeding is achieved by implementing crossover and mutation operators. Crossover involves swapping of the bits of the two selected parents from a specified bit position. Mutation randomly alters a bit in the representation of the offspring depending on mutation probability thus aiding the “explorative logic.” A new population is created, which retains the best individuals of the previous generation and replaces the rest of the individuals by the offspring.

Performance of GA is dependent on the choice of various GA parameters such as crossover probability, mutation probability, etc., and hence, prediction of the choice of parameters for ensuring best results is seldom possible. The set specified in Refs. [18], and used in this study (Table 4), is shown to work well with most of the standard optimization problems such as design of heat exchangers and the traveling salesman problem.

Genetic Algorithm Results

Using the algorithm listed in Fig. 6, separate GA codes were executed for $A=0.02$ m, 0.04 m, 0.06 m, 0.08 m, and 0.10 m [28]. The variation of the maximum F with generation has been plotted in Figs. 8(a) and 8(b) for the GA codes of $A=0.02$ m and

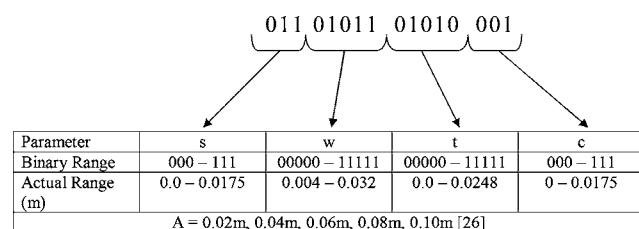


Fig. 7 Binary representation of the “individual” E-PBHS considered in the GA solution procedure

0.06 m, respectively. An increase in F with generations can be observed. Thus, the performance of the design improves with each generation and GA approaches the best solution.

After a few generations, GA converges to the best solution. At this simulation instant, almost all the individuals in the population represent the same design; thus it is unlikely to evolve further. For instance, in Fig. 8(a) for $A=0.02$ m, the F value saturates at a maximum value after about ten generations of mutated simulations. Similarly, for $A=0.06$ m, the F value saturates at a maximum after about 15 generations. Similar invariance of F is checked for other A values considered, before rendering the design as the optimized one. As a conservative estimate, all the simulations have run for at least 25 generations to ensure proper convergence and invariance of F value.

The best designs arrived at after different runs of GA along with their performance have been listed in Table 5. It can be observed that except for $A=0.02$ m, the best design for the rest of the PBHS heights (A) have $c^*=0$. The auxiliary heat spreader provides only a low resistance path for the heat to reach the bottommost layer of PCM. The resistance of the BM increases with increasing PBHS heights, which renders the auxiliary heat spreader ineffective at higher PBHS depths.

Further, from Table 5, it can be seen that out of the range of w values given (0.004 – 0.032 m, see Fig. 7), the best design generated by the GA uniformly chooses $w=0.004$ m. This lowest value of w corroborates the reasoning that for maximizing SOT of a PBHS, it should comprise of E-PBHS of infinitesimal thickness to facilitate complete melting of the PCM used.

In Fig. 9, the heat-spreader size (s) for best designs have been plotted for several values of A . From these data, the equation governing the variation of s is found to be

Table 4 Details of the GA scheme applied

Population size	80
Selection method	Roulette wheel method
Crossover	1 point
Crossover probability	0.90
Mutation probability	0.02

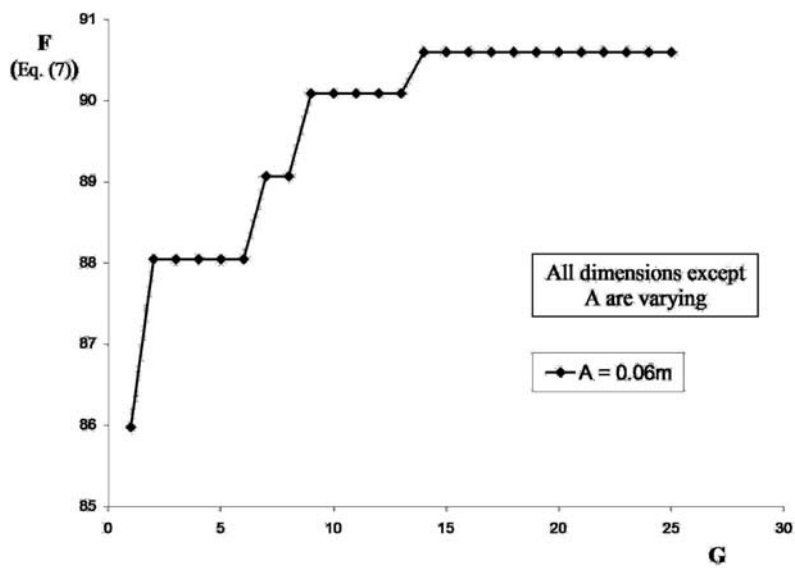
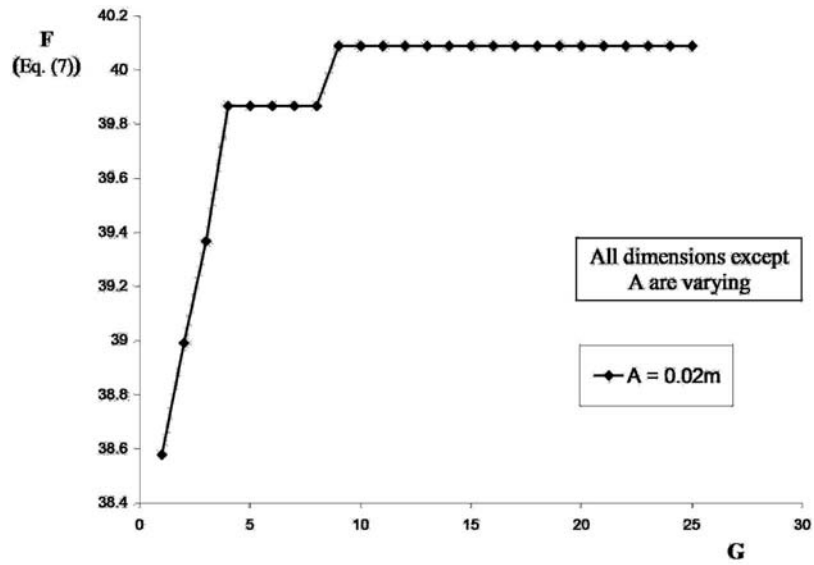


Fig. 8 Fitness function, Eq. (7), evolution with generations for $A=(a)$ 0.02 m; (b) 0.06 m

$$s = 0.025A \quad (8)$$

Thus, an E-PBHS with $A=0.06$ m should have a heat-spreader thickness of 0.0015 m for maximum fitness and SOT. Thus, it is observed from Table 5 that the designs have $s^*=0.025$. Thin heat spreaders distribute heat efficiently along with allowing more PCM proportion in the heat sink and thus increasing the latent heat storage capacity of the PBHS.

Table 5 Best designs of the E-PBHS obtained by GA for different E-PBHS depths (A)

s^*	w^*	A (m)	t^*	c^*	φ	Time (s)	F (Eq. (7))
0.025	0.2	0.02	0.06	0.025	0.66	196	40.23
0.025	0.1	0.04	0.02	0	0.78	421	68.70
0.025	0.067	0.06	0.0134	0	0.78	625	90.59
0.025	0.05	0.08	0.01125	0	0.75	814	109.00
0.025	0.04	0.1	0.01	0	0.73	995	125.45

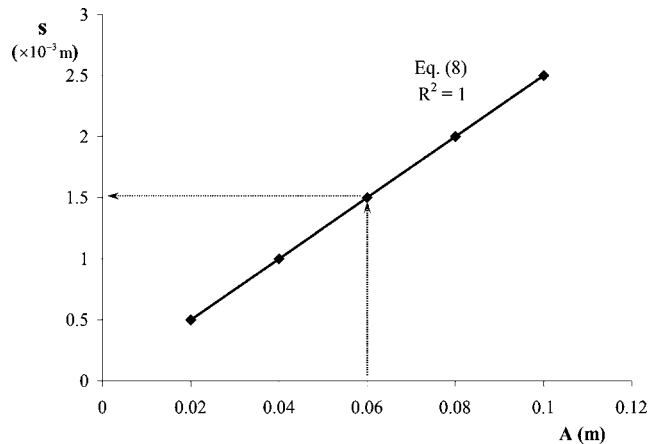


Fig. 9 Values of s for optimal designs determined by the GA procedure

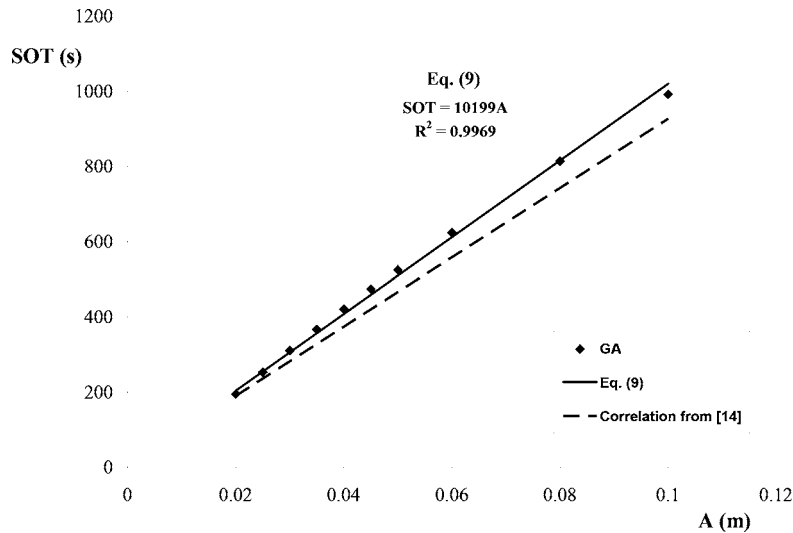


Fig. 10 SOT values for different A for optimal designs determined by the GA procedure

Figure 10 shows the variation of maximum SOT obtainable corresponding to the best designs with respect to A . A linear fit is used to correlate the data with a variance of 0.9969. The governing equation is

$$SOT = 10,199A \quad (9)$$

Figure 11 shows the variation of φ for best designs with respect to the corresponding A . The variation is divided in three ranges. The general form of the correlation equation is proposed to be

$$\varphi = B_1A^2 + B_2A + B_3 \quad (10)$$

Table 6 lists the values for B_1 , B_2 , and B_3 for all three ranges along with the variances related to the respective fits. The correlation predicts the data within 0.5% error.

Figures 9, 10(a), and 10(b) in combination with Eqs. (8)–(10) can be used to determine the optimized PBHS design for a particular requirement, within limited constraints. For instance, for a particular electronic package cooling requirement, there is a constraint in the maximum depth of the PBHS (A) due to space restrictions, while maximizing the SOT. According to Eq. (9), A will be kept maximum, to maximize SOT. Equations (10) and (8) pre-

dict the required optimal φ and s for the chosen A , while from Table 5, it is clear that for the optimized designs, $w=0.004$ m and $c=0$ for the PBHS design.

On the other hand, if the constraint on SOT is fixed, through Eq. (9), A can be back calculated using s and φ , which can be determined by Eqs. (8) and (10), respectively.

Conclusions

Using an approach that couples GA with conventional numerical simulations, optimization of the geometric configuration of a PBHS is performed in this paper. The optimization is done to maximize the SOT, which is the time for the top temperature of the PBHS to reach the CET. First, using numerical simulations of the governing equations of energy balance with change of phase, an E-PBHS for analysis is considered owing to the symmetry of the design, to establish the dependence of SOT on various PBHS geometrical parameters. An optimal solution for this complex multiparameter problem is then sought using GA with the numerical simulation seeking the SOT forming a crucial step in the algorithm. This multistep procedure varies each design parameter within its chosen range to “mutate” into successful PBHS designs that meet the constraint of maximizing SOT. For constant heat dissipation from the electronics (constant heat flux) and for three typical PBHS depths (A), predictive empirical relations are deduced from the GA based simulation results. These correlations relate the SOT to the amount of PCM to be used in the PBHS (φ), the PBHS depth (A), and the heat-spreader thickness (s), a hitherto unconsidered variable in such designs, to the best of the authors’ knowledge. The results show that for all of the typical PBHS depths considered, the optimal heat-spreader thickness is 2.5% of the PBHS depth.

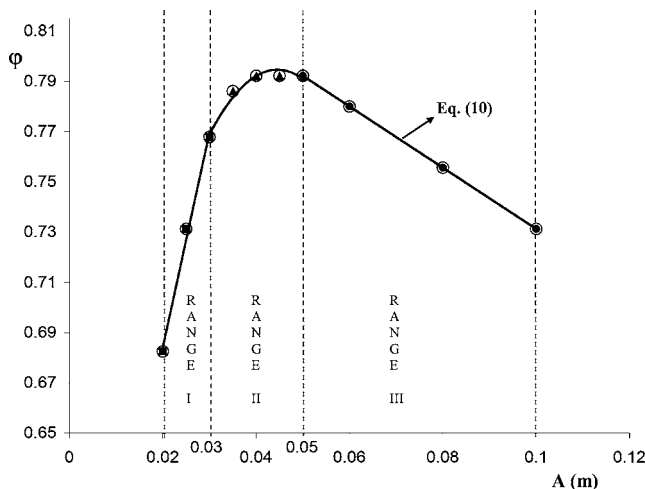


Fig. 11 Φ values for different A for optimal designs determined by the GA procedure

Table 6 Correlation of φ versus A for best designs of E-PBHS (Eq. (10))

Eq. (10)				
Range	B_1	B_2	B_3	R^2
$0.02 \leq A \leq 0.03$	0	8.53	0.5139	0.9933
$0.03 \leq A \leq 0.05$	-122	10.858	0.5531	0.9667
$0.05 \leq A \leq 0.10$	0	-1.22	0.8352	1

Two predictive correlations are proposed based on the outcome of the GA and simulations, to find the optimized configuration of the E-PBHS for maximizing the time of operation of the sink. The correlation, Eq. (9), predicts SOT with a maximum 4.6% error and Eq. (10) predicts φ with a 0.32% error.

Nomenclature

A	= height of the PBHS, m, Fig. 1
BM	= base material, Table 1
c	= auxiliary heat-spreader thickness, m, Fig. 1(b)
CET	= critical electronics temperature, K
F	= fitness value, in Eq. (7), in Figs. 8(a) and 8(b)
G	= number of generations in GA, Figs. 8(a) and 8(b)
g	= acceleration due to gravity, in Fig. 2
GA	= genetic algorithm
k	= thermal conductivity, W/m K
L	= latent heat of PCM, kJ/kg
PBHS	= PCM-BM heat sink
PCM	= phase-change material, Table 1
q''	= heat flux, W/m ²
s	= heat-spreader thickness, m, Fig. 1
SOT	= sink operational time, Eq. (9), Figs. 4, 5, and 10(a)
t	= width of BM in half fin, m, Fig. 1
T	= temperature, °C and K
w	= width of half fin, m, Fig. 1
x, y	= Cartesian coordinates

Greek Symbols

α	= percentage of PCM melted
δ	= melt front, m, Fig. 3
ρ	= density, kg/m ³
φ	= percentage of PCM in PBHS, Eq. (10), Figs. 4, 5, and 10(b)
τ	= time, s

Miscellaneous

(ρc)	= heat capacity, kJ/m ³ K
Δt	= time step, s, Tables 2–4

Subscripts

AMB	= ambient
BM	= base material (here, aluminum, Table 1)
M	= melting point
MAX	= maximum
PCM	= phase-change material
TOP	= top surface of the PBHS

Superscript

*	= parameter nondimensionalized by A
---	---------------------------------------

References

- Joshi, Y. K., and Garimella, S. V., 2003, "Thermal Challenges in Next Generation Electronic Systems," *Microelectron. Eng.*, **34**(3), p. 169.
- Bass, J. C., Allen, D. T., Ghamaty, S., and Elsner, N. B., 2004, "New Technology for Thermoelectric Cooling," *20th IEEE SEMI-THERM Symposium*, pp. 18–20.
- Alawadhi, E. M., and Amon, C. H., 2002, "Thermal Analyses of a PCM Thermal Control Unit for Portable Electronic Devices: Experimental and Numerical Studies," *2002 Inter Society Conference on Thermal Phenomena*, pp. 466–475.
- Chow, L. C., and Zhong, J. K., 1996, "Thermal Conductivity Enhancement for Phase Change Storage Media," *Int. Commun. Heat Mass Transfer*, **23**(1), pp. 91–100.
- Pal, D., and Joshi, Y. K., 1997, "Application of Phase Change Materials to Thermal Control of Electronics Modules: A Computational Study," *ASME J. Electron. Packag.*, **119**, pp. 40–50.
- Bujage, I., 1997, "Enhancing Thermal Response of Latent Heat Storage Systems," *Int. J. Energy Res.*, **21**, pp. 759–766.
- Krishnan, S., and Garimella, S. V., 2004, "Analysis of a Phase Change Energy Storage System for Pulsed Power Dissipation," *IEEE Trans. Compon. Packag. Technol.*, **27**(1), pp. 191–199.
- Krishnan, S., Garimella, S. V., and Kang, S. S., 2004, "A Novel Hybrid Heat Sink Using Phase Change Materials for Transient Thermal Management of Electronics," *Proceedings of Inter Society Conference on Thermal Phenomena (ITHERM04)*, pp. 310–318.
- Krishnan, S., Murthy, J. Y., and Garimella, S. V., 2005, "A Two Temperature Model for Solid-Liquid Phase Change in Metal Foams," *ASME J. Heat Transfer*, **127**(9), pp. 995–1004.
- Striith, U., and Novak, P., 2000, "Heat Transfer Enhancement at Phase Change Processes," *Terrastock Eighth International Conference on Thermal Energy Storage*, Aug. 28–Sep. 1, Vol. 1, pp. 333–338.
- Zheng, N., and Wirtz, R. A., 2004, "A Hybrid Thermal Energy Storage Device, Part 1: Design Methodology," *ASME J. Electron. Packag.*, **126**, pp. 1–7.
- Zheng, N., and Wirtz, R. A., 2004, "A Hybrid Thermal Energy Storage Device, Part 2: Thermal Performance Figures of Merit," *ASME J. Electron. Packag.*, **126**, pp. 8–13.
- Shatikian, V., Ziskind, G., and Letan, R., 2005, "Numerical Investigation of a PCM-Based Heat Sink with Internal Fins," *Int. J. Heat Mass Transfer*, **48**(17), pp. 3689–3706.
- Akhilesh, R., Narasimhan, A., and Balaji, C., 2005, "Method to Improve Geometry for Heat Transfer Enhancement in PCM Composite Heat Sinks," *Int. J. Heat Mass Transfer*, **48**(13), pp. 2759–2770.
- Nayak, K. C., Saha, S. K., Srinivasan, K., and Dutta, P., 2006, "A Numerical Model for Heat Sinks With Phase Change Materials and Thermal Conductivity," *Int. J. Heat Mass Transfer*, **49**(11–12), pp. 1833–1844.
- Goldberg, D. E., 1989, *Genetic Algorithms in Search, Optimization, and Machine Learning*, Addison-Wesley, Reading, MA.
- Holland, J. H., 1992, *Adaption in Natural and Artificial Systems*, MIT Press, Cambridge, MA.
- Manish, C. T., Yan, F., and Urmila, M. D., 1999, "Optimal Design of Heat Exchangers: A Genetic Algorithm Framework," *Ind. Eng. Chem. Res.*, **38**, pp. 456–467.
- Hilbert, R., Janiga, G., Baron, R., and Thévenin, D., 2006, "Multi-Objective Shape Optimization of a Heat Exchanger Using Parallel Genetic Algorithms," *Int. J. Heat Mass Transfer*, **49**(15–16), pp. 2567–2577.
- Lamberg, P., and Siren, K., 2003, "Approximate Analytical Model for Solidification in a Finite PCM Storage With Internal Fins," *Appl. Math. Model.*, **27**, pp. 491–513.
- Cengel, Y. A., 2003, *Heat Transfer: A Practical Approach*, 2nd ed., McGraw-Hill, New York.
- Shamsundar, N., and Sparrow, E. M., 1975, "Analysis of Multidimensional Conduction Phase Change Via Enthalpy Model," *ASME J. Heat Transfer*, **97**, pp. 333–340.
- Krishnan, S., and Garimella, S. V., 2004, "Thermal Management of Transient Power Spikes in Electronics—Phase Change Energy Storage Or Copper Heat Sinks?," *ASME J. Electron. Packag.*, **126**, pp. 308–316.
- Bejan, A., 1993, *Heat Transfer*, Wiley, New York.
- Larranaga, P., Kuijpers, C. M. H., Murga, R. H., and Dizdarevic, S., 1999, "Genetic Algorithms for the Traveling Salesman Problem: A Review of Representations and Operators," *Artif. Intell. Rev.*, **13**(2), pp. 129–170.
- Michalewicz, Z., 1996, *Genetic Algorithms + Data Structures = Evolution Programs*, 3rd ed., Springer, Berlin.
- Haji-Sheikh, A., Eftekhar, J., and Lou, D., 1982, "Properties of Paraffin Wax as a Thermal Storage Medium," *Proceedings of AIAA/ASME Joint Thermo-Physics, Fluids, Plasma and Heat Transfer Conference*, AIAA.
- Leland, J., and Recktenwald, G., 2003, "Optimization of a Phase Change Heat Sink for Extreme Environments," *Proceedings of the 19th Annual IEEE Semiconductor Thermal Measurement and Management Symposium*, Mar. 11–13.

Franz Ramstorfer
The Virtual Vehicle Research Company,
Inffeldgasse 21A,
8010 Graz, Austria
e-mail: franz.ramstorfer.ext@siemens.com

Helfried Steiner
e-mail: steiner@fluidmech.tu-graz.ac.at

Günter Brenn
e-mail: brenn@fluidmech.tu-graz.ac.at

Institute of Fluid Mechanics and Heat Transfer,
Graz University of Technology,
Inffeldgasse 25F,
8010 Graz, Austria

Claudius Kormann
BASF AG, G-EVO/MI-J550,
67056 Ludwigshafen, Germany
e-mail: claudius.kormann@basf.com

Franz Rammer
MAN Nutzfahrzeuge Österreich AG,
Schönauerstraße 5,
4400 Steyr, Austria
e-mail: franz.rammer@at.man-mn.com

Subcooled Boiling Flow Heat Transfer From Plain and Enhanced Surfaces in Automotive Applications

The requirement for the highest possible heat transfer rates in compact, efficient cooling systems can often only be met by providing for a transition to subcooled boiling flow in strongly heated wall regions. The significantly higher heat transfer rates achievable with boiling can help keep the temperatures of the structure on an acceptable level. It has been shown in many experimental studies that special surface finish or porous coatings on the heated surfaces can intensify the nucleate boiling process markedly. Most of those experiments were carried out with water or refrigerants. The present work investigates the potential of this method to enhance the subcooled boiling heat transfer in automotive cooling systems using a mixture of ethylene-glycol and de-ionized water as the coolant. Subcooled boiling flow experiments were carried out in a vertical test channel considering two different types of coated surfaces and one uncoated surface as a reference. The experimental results of the present work clearly demonstrate that the concept of enhancing boiling by modifying the microstructure of the heated surface can be successfully applied to automotive cooling systems. The observed increase in the heat transfer rates differ markedly for the two considered porous coatings, though. Based on the experimental data, a heat transfer model for subcooled boiling flow using a power-additive superposition approach is proposed. The model assumes the total wall heat flux as a nonlinear combination of a convective and a nucleate boiling contribution, both obtained from well-established semiempirical correlations. The wall heat fluxes predicted by the proposed model are in very good agreement with the experimental data for all considered flow conditions and surface types. [DOI: 10.1115/1.2780178]

Keywords: subcooled boiling flow, heat transfer, boiling enhancement, enhanced surfaces

1 Introduction

In the modern design of highly efficient liquid cooling systems, increasing heat fluxes have to be transmitted through the wall structures of the devices. This tendency is specially evident in the development of today's internal combustion engines, where a continuous increase of specific power leads to ever higher thermal loads on limited heater surfaces associated with the compact design of the engines. Convective single-phase transport is often not sufficient to transfer the heat from the structure into the coolant. Hence, the wall temperature increases and boiling occurs. If the liquid bulk temperature remains below the saturation temperature, the process is called subcooled flow boiling. In this regime, the bubbles grow in the superheated zone near the wall and collapse in regions at a distance from the wall. Due to the phase change of the coolant, the heat flux from the structure into the liquid is increased significantly. In the layout of modern cooling devices, the transition to nucleate boiling has therefore become appreciated for its potential to keep the wall temperatures on acceptable levels. Thus, many cooling concepts deliberately provide for an onset of nucleate boiling in thermally highly loaded regions.

In the case of heterogeneous boiling, where bubble formation basically starts from inhomogeneities, typically cavities on the heated surface, there is a general consensus that only cavities that entrap a gaseous rest after bubble departure can act as stable

nucleation sites. The number density of these active cavities, generally termed nucleation site density, essentially determines the boiling heat transfer rates. The nucleation site density does not only depend on generally amenable parameters, such as pressure and wall heat flux, or the thermophysical properties of the working fluid (thermal conductivity, viscosity, latent heat, etc.). The bubble nucleation is also influenced by less amenable parameters related to the dynamics of the fluid-gas-solid interfaces, which strongly depend on the thermophysical properties and the microstructure of the surface. These highly complex effects, which are hard if not impossible to measure, have largely impaired a rigorous theoretical description of bubble nucleation so far. The process of bubble nucleation has been investigated in several experimental studies [1–3]. Aside from gaining a better understanding of the underlying physics, several studies were also focused on finding possibilities to enhance the nucleation process [4–8]. Providing more favorable conditions for bubble nucleation might finally shift the onset of nucleate boiling (ONB) to lower wall superheats and, beyond the ONB, might help sustain a highly intense and stable nucleate boiling activity. Using specially modified surfaces, commonly termed “enhanced surfaces,” turned out to be a promising approach to attain this objective.

Enhanced surfaces can be basically produced by special surface finishing techniques or by depositing (mostly porous) coatings on the ground body. All these techniques have in common that they generate a surface microstructure with a large number of cavities that can be easily activated and remain active because they are never flooded completely by the liquid phase. The boiling behavior of porous coated metal ground bodies was examined in several

Contributed by the Heat Transfer Division of ASME for publication in the JOURNAL OF HEAT TRANSFER. Manuscript received July 20, 2006; final manuscript received May 9, 2007; published online January 25, 2008. Review conducted by Chang Oh.

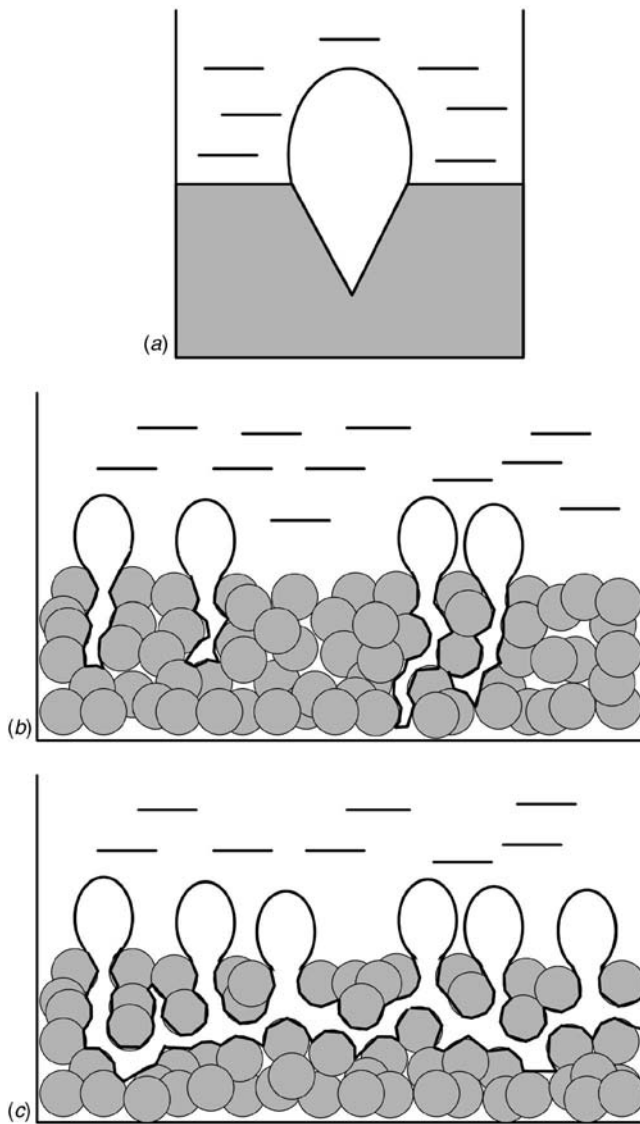


Fig. 1 The generation of vapor bubbles: (a) nucleation site on the smooth surface, (b) bubble nucleation from individual microchannels in the porous layer, and (c) formation of a continuous vapor film in the porous layer (adopted from Ref. [4])

studies. Afgan et al. [4] performed experiments on the pool boiling heat transfer on surfaces with porosities varying between 30% and 70%. They used water, freon-113, and ethanol as working fluids. It was found that boiling on a porous layer sets in already at very low wall superheats of 1–1.5 K, as compared to the wall superheat of about 20 K required for smooth surfaces. In their study, they distinguished three different types of bubble formation mechanisms in the pool boiling regime for smooth and porous coated surfaces, as schematically shown in Fig. 1. On technically smooth superheated surfaces, the vapor bubble formation occurs at small cavities, as sketched in Fig. 1(a). This case was first studied theoretically by Hsu [9], who developed an analytical expression for the critical radius of the mouth of the cavity that is required for the bubble formation at a given wall superheat. In porous coatings (Fig. 1(b)), vapor is produced inside the porous layer. The liquid enters through the channel-type dendritic cavities and evaporates on the superheated surface of the porous structure. With increasing heat flux, a continuous vapor film is formed inside the porous coating (Fig. 1(c)). Afgan et al. [4] assumed that these typical conditions, hypothesized for pool boiling, can also be extended to subcooled boiling flow on porous coated surfaces,

where the vapor bubbles condense after detachment, once they reach the subcooled bulk flow. A significant enhancement of the nucleate pool boiling heat transfer with saturated FC-72 using microporous coated surfaces was also reported by Kim et al. [5]. Rainey et al. [6] continued these experiments using the same type of microporous surface, especially investigating the effects of pressure, subcooling, and dissolved gas concentration. Later on, Rainey et al. [7] investigated subcooled boiling flow on a smooth (highly polished) and, alternatively, on a microporously coated heated surface using again pure FC-72 as the working fluid. These flow boiling experiments demonstrated that the porous surface exhibits a higher nucleation site density, which finally leads to a significant reduction of the wall superheat at a given heat flux compared to the smooth surface. However, the increase of the flow boiling heat flux with the wall superheat turned out to be lower for the enhanced surface than for the plain one.

The enhancement of the heat transfer into a liquid coolant is of great interest for the design of engine cooling systems as well. The ONB in regions subject to high wall heat fluxes inside the cooling jacket is a long known phenomenon. Having to provide always sufficient cooling power in these critical regions, it is therefore straightforward to use enhanced surfaces in order to achieve the locally highest possible nucleate boiling heat transfer rates. The boiling behavior of ethylene-glycol/water mixtures, which are typically used in automotive cooling systems, was investigated in several studies. Finlay et al. [10] performed boiling experiments with an ethylene-glycol/water mixture of 50 vol % / 50 vol % on copper, aluminum, and cast iron surfaces. They considered different velocities and pressures of the bulk liquid. Kandlikar and Bulut [11] carried out flow boiling heat transfer experiments in a rectangular channel heated from below using a circular heater surface. They varied the volume fraction of ethylene-glycol in the mixture within the range of 0–40%. Based on their measurements of the boiling heat transfer rate, they developed a boiling model for binary mixtures. Campbell et al. [12] carried out experiments in a short rectangular duct using copper and cast aluminum test heaters with a 50/50 mixture by volume of ethylene-glycol with additives and distilled water. Based on the experimental data obtained in the measurements, a heat transfer model for subcooled boiling flow was developed. While all these experimental studies considered boiling of automotive coolants on plain, technically smooth surfaces, the present work is focused on the subcooled boiling flow on enhanced surfaces. Using a mixture of 40 vol % of ethylene-glycol and 60 vol % of distilled water as the working fluid, two very different types of porous coated surfaces and one plain (uncoated) surface are considered. The investigations aim at two major goals. First, it shall be quantified to what extent the two different types of porous surfaces change the flow boiling characteristics, as compared to the case of a plain, uncoated reference surface. The fact that the investigated porous surfaces have completely different microstructures may also help identify those properties of the porous layer that are presumably most favorable for the boiling process. Second, our study attempts to provide a reliable model for the total wall heat flux in subcooled flow boiling on enhanced surfaces. Here, a well-established approach, which has been proposed and widely used for flow boiling on plain surfaces, shall be assessed on its applicability to the case of porous surfaces.

The present work is organized as follows. In Sec. 2, the experimental apparatus and the considered surfaces are described in detail. In Sec. 3, the obtained experimental results for subcooled boiling flow are discussed. The formulation of the wall heat flux model, as well as a comparison of its predictions against experimental data, is presented in Sec. 4. A conclusion is given in Sec. 5.

2 Experimental Apparatus and Heated Surface Types

Experimental Apparatus. The experimental facility, which is shown in Fig. 2, basically consists of a closed loop for the forced convective flow driven by a pump. The working fluid is preheated

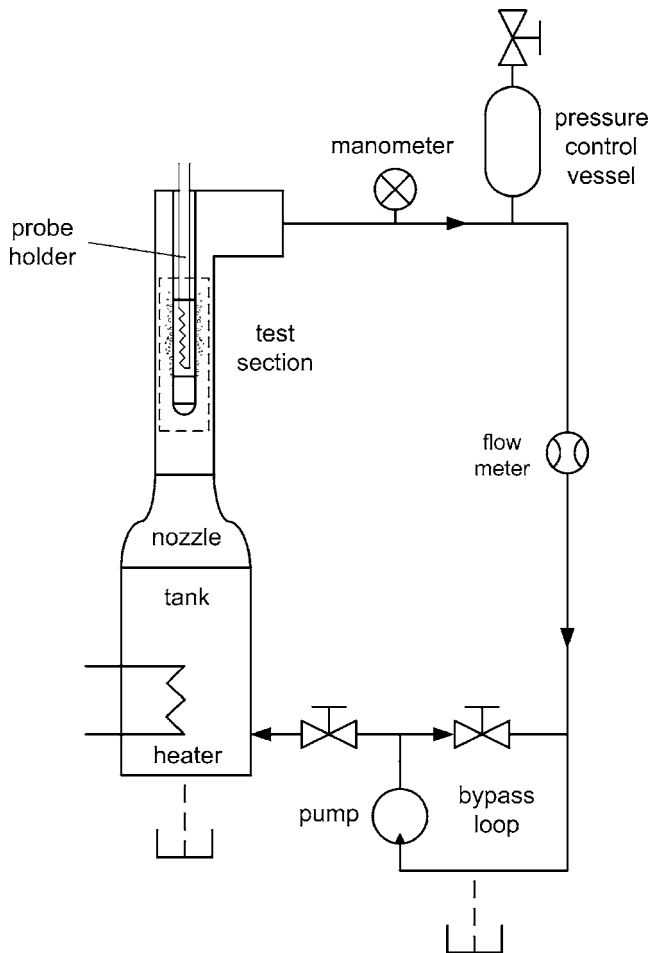


Fig. 2 Flow boiling test loop schematic

in a tank to provide a controlled bulk temperature in the test section. At the entrance into the test section, the fluid passes through a nozzle to ensure a uniform top-hat-like inlet velocity profile. The velocity, the temperature of the bulk liquid, and the operating pressure at the inlet of the test section are continuously controlled during the experiments. The velocity of the bulk flow is measured indirectly using an inductive flow meter. Its output is used to control the flow rate via the speed of the pump and/or the valves regulating the flow through the bypass loop. The relative uncertainty in the measured bulk velocity u_b is estimated as 5.5% at 0.1 m/s, 0.6% at 0.5 m/s, and 0.5% at 2.0 m/s. In the present configuration, the bulk velocity can be varied within the range of $0 \text{ m/s} \leq u_b < 2.0 \text{ m/s}$. The absolute liquid pressure can be set within the range $1.0 \text{ bar} \leq p \leq 3.5 \text{ bars}$. The relative uncertainty in the measured pressure was estimated as 0.6% at the pressure of 3.2 bars. The working fluid passes through a square test section with the side length $a_c = 56 \text{ mm}$. The upward flowing fluid is heated by a cylindrical heater made of cast iron, which is mounted on a probe holder aligned with the axis of the vertical channel, as shown in Fig. 3. The cylindrical heated surface has an axial extension of $L = 30 \text{ mm}$ and a diameter of $d = 12 \text{ mm}$. It is heated from the inside by a ceramic heating rod. The wall heat flux on the surface, q_w , is computed from the input of electrical power into the heating rod, which is measured with an accuracy of 0.5%. The surface temperature T_w is obtained from the temperatures, which are measured beneath the heated surface by the two thermocouples shown in Fig. 3. The axial positions of the temperature measurements are determined by the positions of the ends of the thermocouples, which are located approximately halfway down the heated surface in the streamwise direction ($\approx L/2$), as indi-

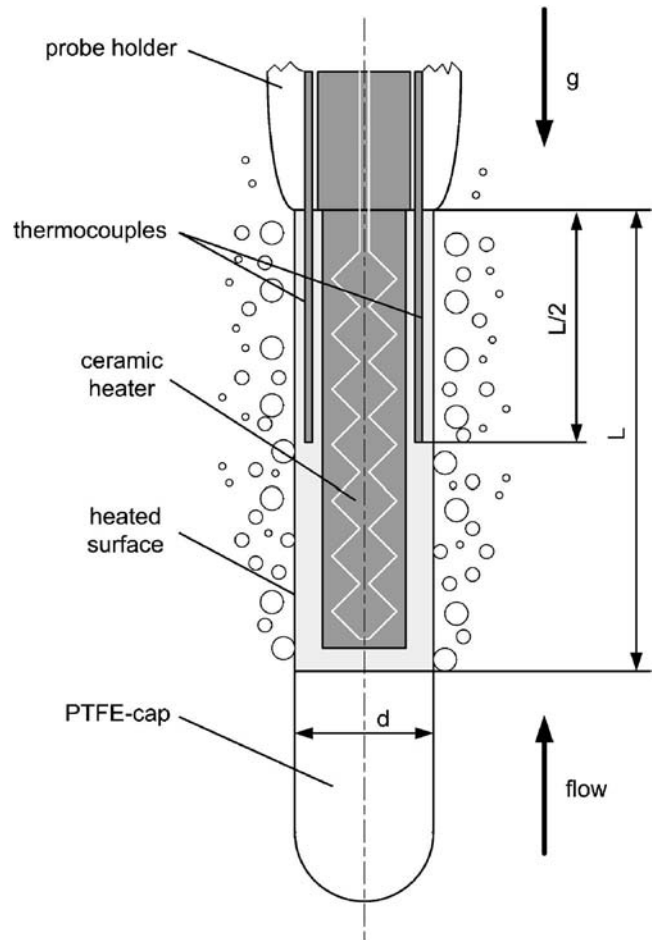


Fig. 3 Heated probe

cated in Fig. 3. The temperatures obtained at these subsurface positions are extrapolated radially outward to the radius of the heated surface, $r = d/2$, applying Fourier's law of heat conduction for axisymmetric geometry. The calibration error of the K-type thermocouples used for the temperature measurements was estimated as $\pm 0.1 \text{ K}$. The head of the heater is topped by a hemispherical cap to avoid separated flow on the cylindrical heater surface downstream. The cap is made of polytetrafluoroethylene (PTFE), whose low thermal conductivity should guarantee the lowest possible heat loss in the axial direction at the top of the heater.

Surface Types. Three different types of surfaces were considered in the experimental investigations of subcooled boiling flow. The unmodified cast iron surface shown in Fig. 4 represents the reference case. The experiments with this surface, which will be termed "S0" in the following, represent the conditions typically found in cylinder heads of internal combustion engines. As seen from Fig. 4, there are some dendritic segregations of carbides in the uppermost layers. Apart from these segregation inhomogeneities, the superficial microstructure contains no open cavities penetrating from the surface into deeper layers. The two other investigated surface types were produced by depositing special coatings on the cast iron ground surface of the reference case (S0). For the first type of coating (termed surface S1 in the following), mild steel was sprayed on the ground body using an electric arc spraying technology carried out at Bühler, Switzerland. The thickness of the deposited layer is approximately $200 \mu\text{m}$. As seen from Fig. 5, this coating technique does not produce a typical granular or capillary porous microstructure. The surface melt layer contains some microchannel-type stretched cavities with a thickness of

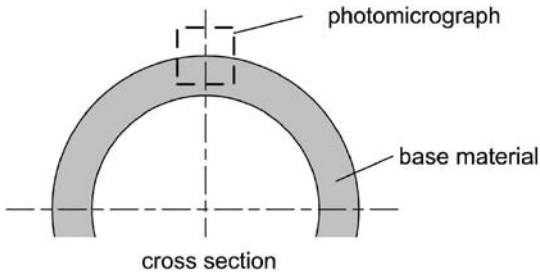
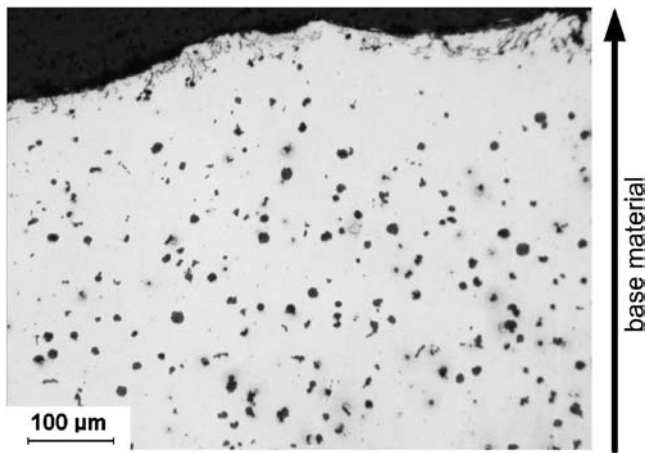


Fig. 4 Photomicrograph of the surface S0. The position of the frame of the micrograph is schematically marked by the dashed square in the sketch of the cross section of the heated probe below.

about 1–5 μm , while the remaining structure is very similar to that of the base material. Due to the big grains of solidified coat-

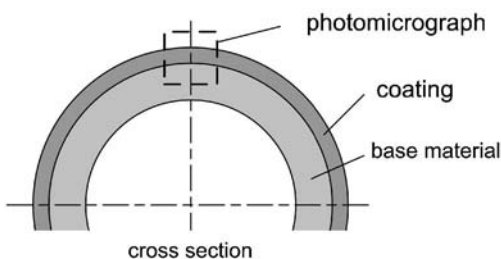
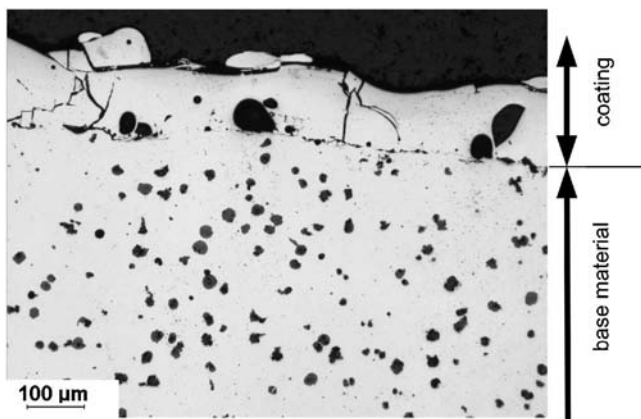


Fig. 5 Photomicrograph of the surface S1. The position of the frame of the micrograph is schematically marked by the dashed square in the sketch of the cross section of the heated probe below.

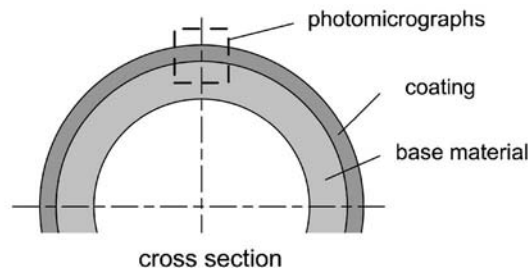
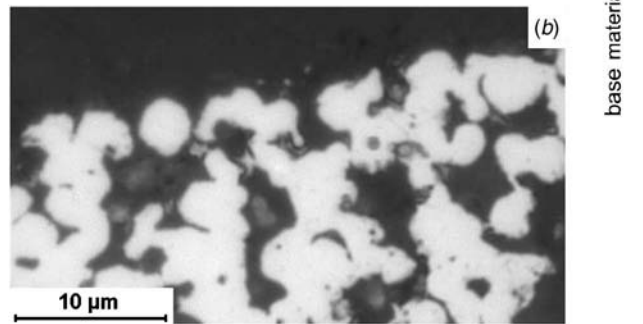
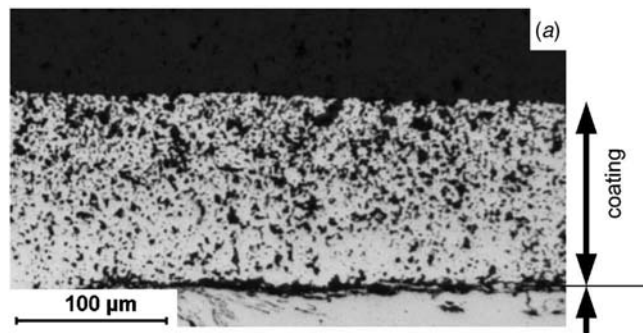


Fig. 6 Photomicrographs of the surface S2 at two different resolutions: (a) base material with superficial coating and (b) detailed view of the coating. The position of the frame of the micrographs is schematically marked by the dashed square in the sketch of the cross section of the heated probe below.

ing material on top of the surface, the macroscopic surface roughness is increased significantly. The higher macroscopic surface roughness can certainly have a strong dynamical effect on the liquid flow along the surface, such as an increased wall friction. Its impact on the boiling behavior can be regarded as low though. As it was also pointed out by Pioro et al. [13], macroscopic roughness is associated with comparatively large cavities. Except for the case of highly nonwetting fluids, these large macroscopic cavities are mostly flooded by the liquid and can therefore not act as effective nucleation sites. Thus, since active nucleation sites can only be provided by microgeometry elements, which remain unflooded due to wettability restrictions of the liquid, it can be argued that the nucleation site density is unaffected by a change in the macrostructure of the surface. In effect, the macroscopic roughness can be regarded as of minor importance for the nucleate boiling behavior. The second type of coating was produced by sintering metallic powder on the cast iron ground surface carried out at BASF AG, Germany. The sinter material was carbonyl-ultrapure iron powder with a grain size of 3–5 μm . The layer thickness of this coating, which shall be termed “S2” in the following, is approximately 200 μm . As seen in Fig. 6, this type of coating represents a typical granular porous layer. As such, its porosity is determined by the grain size and the packing density of the sinter particles. Here, it is estimated as about 40%. While the microstructure of the surface S2 has been changed completely by

the porous coating, its macroscopic surface roughness is almost the same as that of the plain surface S0. Judging from the high porosity of the surface S2, the large number of fine intergranular cavities is expected to provide a high density of potential nucleation sites.

3 Experimental Results

Using the experimental setup described above, several flow boiling curves for the reference surface S0 and the two enhanced surfaces S1 and S2 were measured. In all considered cases, the working fluid was a mixture of ethylene-glycol and water with a mixing ratio of 40 vol. %/60 vol. %. The bulk inlet temperature T_b was kept constant at 100°C. The system pressure was set to $p=3.2$ bars, which implies a subcooling of $\Delta T_{\text{sub}}=T_{\text{sat}}-T_b=43^\circ\text{C}$. By varying the electrical input power into the heater, a maximum wall superheat of $\Delta T_w=T_w-T_{\text{sat}}=30^\circ\text{C}$ was achievable. The bulk velocity was varied within the range of $0\text{ m/s} \leq u_b \leq 2.0\text{ m/s}$. This velocity range corresponds to the Reynolds number range from 0 to 137,910, which is based on the bulk flow conditions

$$\text{Re} = \frac{u_b d_{\text{hyd}} \rho_l}{\mu_l} \quad (1)$$

where the hydraulic diameter is defined as

$$d_{\text{hyd}} = \frac{4A}{s_w} = \frac{4(a_c^2 - d^2 \pi/4)}{4a_c + \pi d} = 46.2\text{ mm} \quad (2)$$

and involves the wetted perimeter s_w and the flow cross-sectional area A . Figure 7 shows the heat flux q_w as a function of the wall temperature T_w obtained from the measurements for the three types of surfaces at three different bulk velocities u_b . Below the saturation temperature, $T_w < T_{\text{sat}}$, the approximately linear sections of the curves indicate pure single-phase convection. In this nonboiling regime, the surface S1 exhibits the highest convective heat transfer rates, which becomes especially evident in the highest velocity case with $u_b=1\text{ m/s}$, where the linear part grows fastest for S1. This significant increase in the convective heat transfer can be attributed to the markedly higher macroscopic surface roughness of the coating S1. The large grain-type roughness elements observed with S1 (see Fig. 5) expectedly increase the near-wall turbulence, leading to an enhanced convective transport of heat. Above the saturation temperature $T_w > T_{\text{sat}}$, the curves start to deviate from the linearity associated with the single-phase convection, which marks the ONB. In this regime, the most outstanding difference between the uncoated surface S0 and the enhanced ones, S1 and S2, can be seen here in the levels of the superheat $\Delta T_w=T_w-T_{\text{sat}}$ at the ONB. The uncoated surface S0 requires much higher superheats for the ONB, and they also strongly depend on the velocity. As such, they increase from about $\Delta T_w=10\text{ K}$ for $u_b=0.1\text{ m/s}$ to about $\Delta T_w=20\text{ K}$ for $u_b=1\text{ m/s}$. In contrast, for both enhanced surfaces S1 and S2, the ONB already occurs once the wall temperature has reached the level of saturation, $T_w \approx T_{\text{sat}}$. This significant reduction in the minimum wall superheat required for all ONB is observed at all velocities. This effect can be explained by invoking the hypothesis of Afgan et al. [4] on the boiling process in porous layers shown in Fig. 1 above. Since the superheat in the deeper regions of the layer is effectively higher, the bubble nucleation can start in the remote subsurface microcavities, while the temperature on the upper surface is still too low for ONB. The incipience of bubble nucleation inside the deeper subsurface layers also explains the independence of the ONB of the velocity in comparison to the case with the uncoated surface S0. At the higher heat fluxes well above the ONB, the surface S1 provides the highest heat transfer rates. This can be clearly seen from the superheats ΔT_w being lowest for S1 at a given heat flux q_w . The most intense boiling activity observed for S1 also manifests itself in the steepest gradient of the boiling branch, especially in the two cases with the lower velocities. The

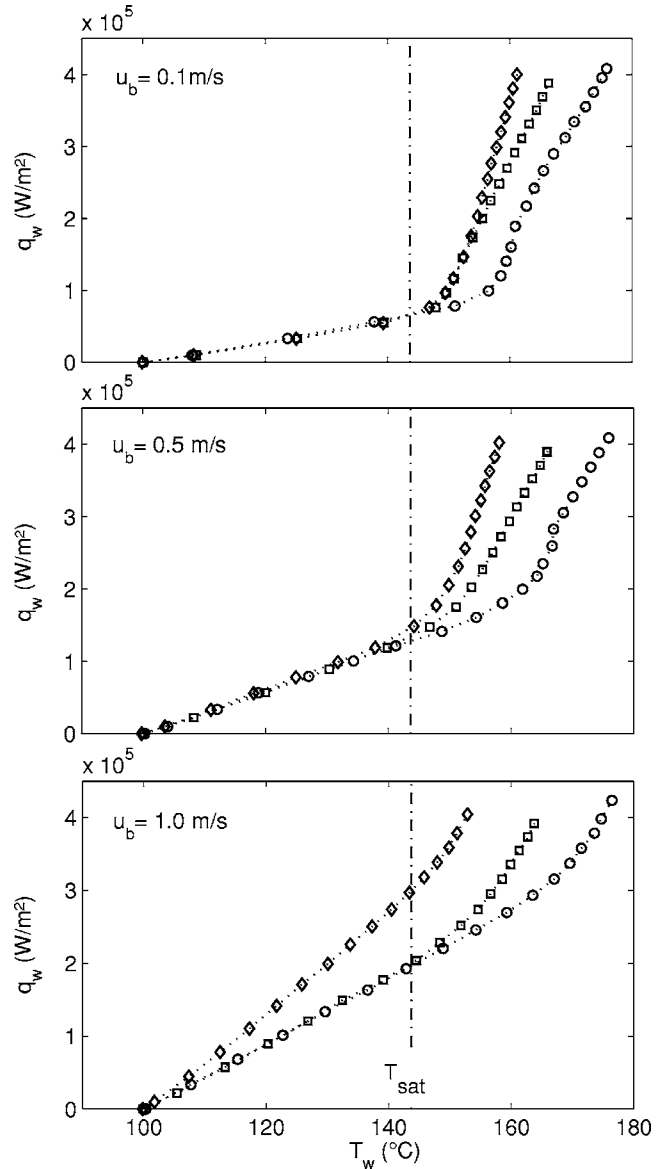


Fig. 7 Experimentally measured flow boiling curves using a mixture 40 vol % of ethylene-glycol and 60 vol % of distilled water as the working fluid at $p=3.2$ bars, $T_b=100^\circ\text{C}$, and three different velocities of the bulk flow: circles (\circ), surface S0; diamonds (\diamond), surface S1; squares (\square), surface S2

best boiling performance shown here for S1 is very remarkable in that the microstructure of S1 is not a typical porous layer, as seen from Fig. 5. The observed crack-type microchannels protruding from the surface into deeper layers evidently act as very effective nucleation sites. The comparison of the two enhanced surfaces, S1 and S2, against each other shows always lower boiling heat transfer rates for S2, although the number of the cavities is considerably higher in the porous layer S2, as shown in Figs. 5 and 6. It appears that a higher number of cavities does not automatically lead to a higher boiling heat transfer rate. It is further interesting to note that, approaching the higher heat fluxes, the flow boiling curves for the porous surface S2 and the plain surface S0 almost run parallel, which indicates a similar boiling activity on both surfaces in this region.

4 Modeling of the Wall Heat Flux

Due to the high complexity of the problem involving a great variety of thermophysical effects that are often hard or even im-

possible to measure, no rigorous analytical description of the nucleate boiling process has been developed yet. Therefore, most state-of-the-art models rely on a good deal of empiricism in terms of adjustable model parameters. Furthermore, most models do not explicitly account for the influence of any variation of the total wall heat flux in the streamwise direction, neglecting the influence of the thermally nondeveloped heated entrance region, nor for that of the bubble dynamics on the heat transfer conditions further downstream.

A large number of the various models proposed for the total wall heat flux fall into the category of the superposition approach. This widely used concept, which was introduced by Chen [14], assumes the total wall heat flux to be linearly composed of a macroscopic, convective component and a microscopic, nucleate boiling component, so that are may write

$$q_w = q_{\text{conv}} + q_{\text{nb}} \quad (3)$$

This linear decomposition is attractive for two reasons. First, it offers much freedom in choosing the most adequate submodels for each component. Secondly, it provides the correct asymptotics at the transition to the nonboiling regime, since the nucleate boiling component q_{nb} becomes zero once $T_w < T_{\text{sat}}$, and only the macroscopic, single-phase convection q_{conv} remains.

The macroscopic component is mostly obtained from widely used correlations for convective channel flow, such as the Dittus–Boelter correlation. The microscopic contribution is generally computed using well-established pool boiling models such as those proposed by Forster and Zuber [15], Cooper [16], Gorenflo [17], or Rohsenow [18]. Since the boiling activity can be strongly affected by the flow of the bulk liquid, especially at lower superheats, and hence the nucleate boiling contribution q_{nb} should be effectively smaller than the pool boiling heat flux, Chen [14] needed to introduce a flow-induced suppression factor S . The microscopic contribution is then rewritten as

$$q_{\text{nb}} = S \tilde{q}_{\text{nb}} \quad (4)$$

where \tilde{q}_{nb} is the wall heat flux for pool boiling and the suppression factor S varies from $S=1$ to $S=0$ for increasing flow rates. Chen's concept was adopted by many authors using different submodels for the pool boiling heat flux and/or different correlations for the suppression factor S (Campbell et al. [12], Wenzel and Müller-Steinhagen [19], Steiner et al. [20], and Liu and Winterton [21]).

Steiner and Taborek [22] extended Chen's linear superposition to a nonlinear or so-called asymptotic addition approach,

$$q_w = (q_{\text{conv}}^m + q_{\text{nb}}^m)^{1/m} \quad m \geq 1 \quad (5)$$

which was originally proposed by Kutateladze [23] using $m=2$. The higher the value of the exponent m , the more weight is put on the dominant contribution when approaching the asymptotic limit of the single-phase convection, where $q_w \rightarrow q_{\text{conv}}$, and the limit of fully developed boiling, where $q_w \rightarrow q_{\text{nb}}$. In contrast to Chen's linear superposition approach, no extra factor is basically needed here to account for the flow-induced suppression of nucleate boiling. This suppression is inherently provided by the asymptotic overweighting of the macroscopic (convective) component for $q_w \rightarrow q_{\text{conv}}$ depending on $m > 1$. Thus, an appropriate setting for the exponent m , which is obtained from a best fit to experimental data, enables one to capture fairly accurately the flow boiling characteristics near the two asymptotic limits ($q_w \rightarrow q_{\text{conv}}$ and $q_w \rightarrow q_{\text{nb}}$), as well as a smooth transition in between. For this obvious conceptual simplicity, the nonlinear addition approach is used in the present work as the base model.

Since the present study also considers cases with very low bulk flow rates, the modeling of the macroscopic (convective) contribution needed in Eq. (5) has to account for the natural convective heat transfer as well. In analogy to Eq. (5), the nonlinear addition concept is utilized here again, rewriting the local convective contribution as

$$q_{\text{conv}} = (q_{\text{nc}}^n + q_{\text{fc}}^n)^{1/n} \quad n \geq 1 \quad (6)$$

as suggested by Churchill [24]. The empirically obtained exponent n determines the transition of the mixed convective heat flux to the limits of pure natural convection and pure forced convection. The natural convective heat flux q_{nc} is calculated following an approach of Churchill and Chu [25] for vertical heated surfaces, who introduced the correlations

$$\text{Nu}_{\text{nc}} = \{0.825 + 0.387[\text{Gr Pr } f_1(\text{Pr})]^{1/6}\}^2 \quad (7)$$

where

$$f_1(\text{Pr}) = \left[1 + \left(\frac{0.492}{\text{Pr}} \right)^{9/16} \right]^{-16/9} \quad (8)$$

involving the Grashof, the Nusselt, and the Prandtl number of the liquid phase as

$$\text{Gr} = \frac{gL^3}{(\mu_l/\rho_l)^2} \beta_l (T_w - T_{\text{sys}}) \quad \text{Nu}_{\text{nc}} = \frac{q_{\text{nc}} L}{(T_w - T_{\text{sys}}) \lambda_l} \quad \text{Pr} = \frac{\mu_l c_{\text{pl}}}{\lambda_l}$$

with L the axial extension of the vertical cylindrical heated surface. The natural convective heat flux is finally obtained as

$$q_{\text{nc}} = \{0.825 + 0.387[\text{Gr Pr } f_1(\text{Pr})]^{1/6}\} \frac{\lambda_l}{L} (T_w - T_{\text{sys}}) \quad (9)$$

The heat transfer due to forced convection q_{fc} is computed from the Dittus–Boelter equation

$$\text{Nu}_{\text{fc}} = \frac{q_{\text{fc}}}{(T_w - T_{\text{sys}}) \lambda_l} \frac{d_{\text{hyd}}}{L} = a \text{Re}^b \text{Pr}^{0.4} \quad (10)$$

using modified model constants a and b determined from experimental results. The Reynolds number in Eq. (10) is based on the bulk flow quantities and the hydraulic diameter as defined in Eq. (1). The forced convective heat flux is then written as

$$q_{\text{fc}} = a \text{Re}^b \text{Pr}^{0.4} \frac{\lambda_l}{d_{\text{hyd}}} (T_w - T_b) \quad (11)$$

As already pointed out in the previous section, the coated surface S1 exhibits a much higher macroscopic roughness than S0 and S2. The latter can both be regarded as hydraulically smooth. The high roughness strongly enhances the near-wall turbulence, which leads to an increase in the convective heat transfer, as seen from the experimental results obtained for S1 (see Fig. 7). The enhanced single-phase convection due to the macroscopic roughness is considered in the present modeling by introducing a correction factor ξ into Eq. (6), which is rewritten as

$$q_{\text{conv}} = (q_{\text{nc}}^n + \xi q_{\text{fc}}^n)^{1/n} \quad (12)$$

The correction factor ξ is unity for the hydraulically smooth surfaces S0 and S2, while it assumes values greater than unity for the hydraulically rough surface S1 depending on the bulk flow velocity. The individual values $\xi > 1$, determined for the corresponding bulk velocities from a best fit to the experimental data for S1, are shown in Fig. 8. The exponent n remains 2.5 for all considered surfaces S0, S1, and S2.

The nucleate boiling contribution needed in Eq. (5) is obtained using the well-established pool boiling correlation due to Rohsenow [18],

$$q_{\text{nb}} = \left[\frac{C_{\text{pl}}}{h_v C_{\text{sf}}} \text{Pr}^{-(\delta+1)} \right]^{1/\gamma} \left[\frac{\sigma}{g(\rho_l - \rho_v)} \right]^{-1/2} h_v \mu_l (T_w - T_{\text{sat}})^{1/\gamma} \quad (13)$$

where C_{sf} is a model constant depending on the surface-fluid combination. For aqueous solutions, the model parameter δ is generally set to zero, which applies to the present working fluid as well. All other constants (m , n , a , b , C_{sf} , and γ) are obtained from a best fit of the total wall heat fluxes computed with the model equations (5)–(13) to the corresponding experimental results. The model pa-

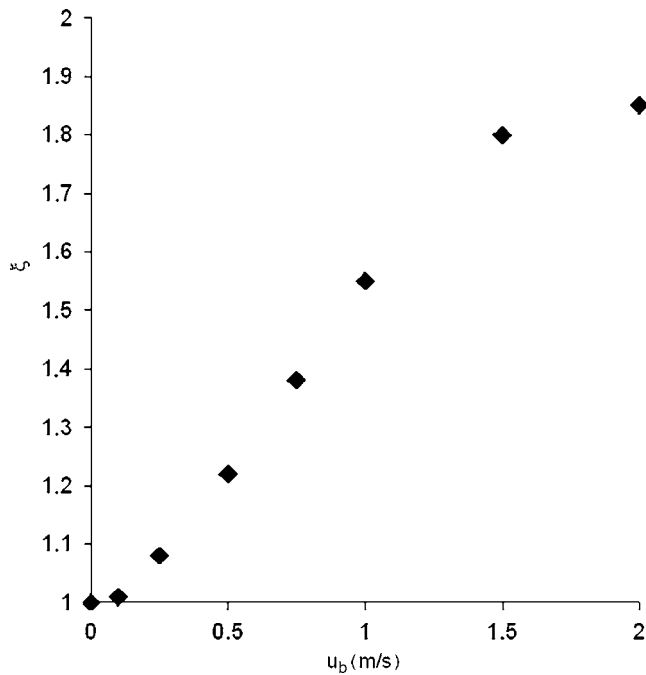


Fig. 8 Correction factor ξ representing the enhancement of the convective heat transfer due to the macroscopic surface roughness of S1 for different bulk velocities u_b

rameters obtained for the three considered surfaces (S0, S1, and S2) are summarized in Table 1.

Figures 9–11 show the boiling curves predicted by the model using the model parameters listed in Table 1, compared against the corresponding experimental data for all considered bulk velocities. The overall agreement is very good for all surfaces. The relative root mean square errors of the predicted heat fluxes are $\varepsilon_{rms}=0.81\%$, 0.58% , and 0.60% for the cases S0, S1, and S2, respectively. In the case of S0 at the lower velocities, the wall superheats in the ONB region exceed markedly the theoretical asymptotic limit of the pool boiling curve (denoted by the dashed line). This feature is not observed in the cases of the coated surfaces, where the wall superheats always lie below the asymptotic limit of pool boiling. The plain surface evidently requires considerably higher superheats for the activation of bubble nucleation sites at the incipience of boiling (ONB) than the coated surfaces. The exceeding of the asymptotic pool boiling limit can by definition not be reflected by the asymptotic superposition given in Eq. (5). The deviations observed in the region lead to a somewhat higher overall relative error for S0. Aside from that, the nonlinear, power-additive formulations used in Eqs. (5) and (6) obviously reflect very well the variety of flow boiling conditions occurring between the lower limit of natural convection (marked by the dash-dotted curve) and the upper limit of fully developed boiling,

Table 1 Parameter settings for the proposed model for the investigated surfaces

Parameter	Equation	Surface		
		S0	S1	S2
a	(10)	0.0447	0.0447	0.0447
b	(10)	0.75	0.75	0.75
m	(5)	10	1	1
n	(6)	2.5	2.5	2.5
C_{sf}	(13)	0.0172	0.0108	0.0130
γ	(13)	0.90	0.45	0.85

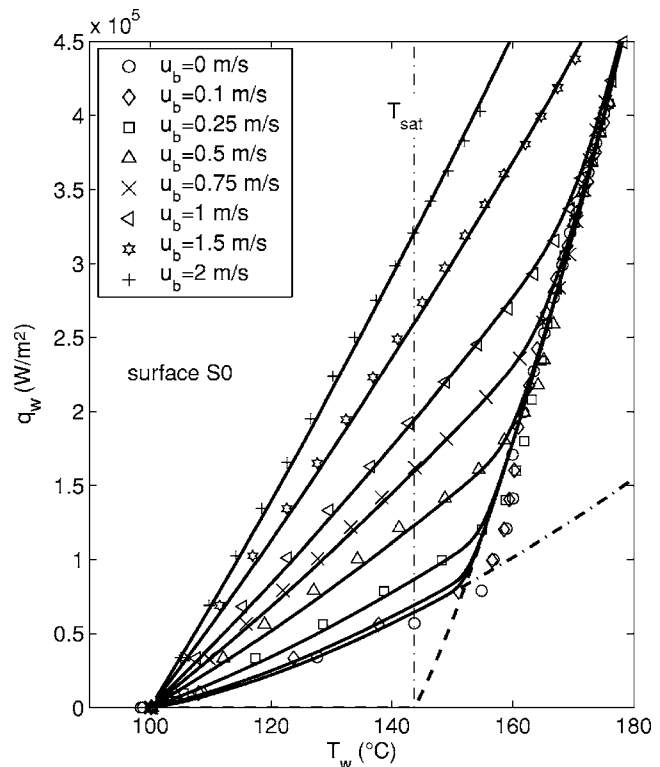


Fig. 9 Predicted flow boiling curves for the plain surface S0 at different velocities of the bulk flow. The symbols denote the measurements: full line (—), model prediction; dash-dotted line (---), natural convection; dashed line (---), pool boiling curve.

which resembles the pool boiling curve (plotted as dashed curve), considered here. In the case of the plain surface S0, the individual flow boiling curves strongly converge toward the fully developed boiling limit. This strong convergence indicates that for the surface S0, the influence of the flow rate decreases rapidly as the wall superheat increases, so that the boiling curves for the individual flow rates merge into one common pool boiling branch. In the power-additive modeling, this asymptotical behavior translates into a high value of the exponent $m=10$, which provides the observed dominance of the nucleate boiling contribution together with a strong reduction of the convective component. As seen from Fig. 10, the enhanced surface S1 shows very different asymptotic flow boiling characteristics. The boiling curves obtained for S1 do not merge into the limit of the pool boiling branch. In the considered range of wall heat fluxes, the convective mechanism obviously keeps contributing notably to the total heat transfer. At the same time, the nucleate boiling contributions appear to be largely unaffected by the flow rate, as seen from the individual boiling branches, which approximately run parallel to the pool boiling curve (dashed line). In the present modeling, this behavior is reflected best by setting the exponent $m=1$, which implies a simple linear (Chen-type) addition without any asymptotic weighting. As such, the formulation provides no flow-induced suppression of the boiling component at low wall superheats. Evidently from the lowest wall superheats, the microstructure of S1 promotes very robust and stable boiling conditions—basically resembling pool boiling heat transfer conditions—which are largely insensitive to flow of the bulk liquid. As seen from Fig. 11, the porous coated surface S2 exhibits a boiling behavior intermediate to that of S0 and S1. In contrast to S1, at lower superheats, the boiling curves show a notable influence of the velocity. At higher wall superheats, the boiling curves tend to converge toward the fully developed boiling curve, but less rapidly than for

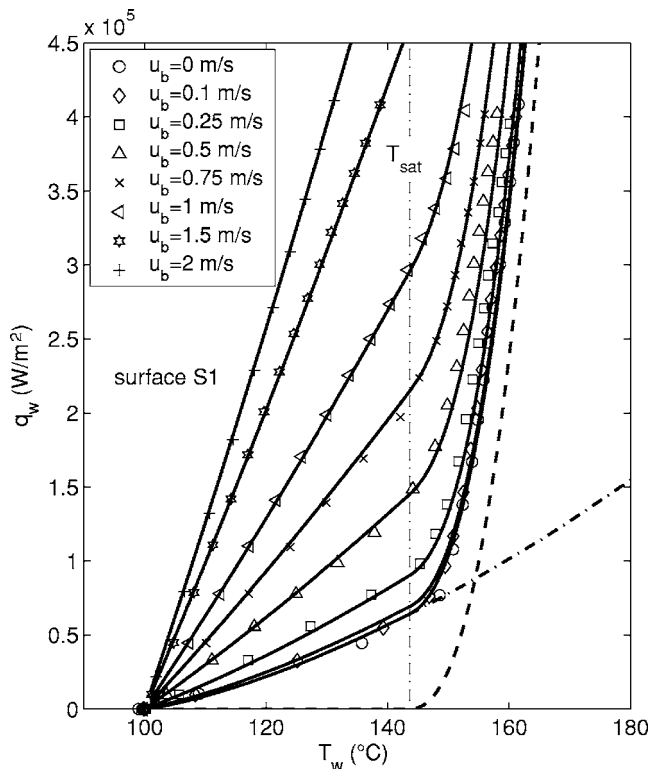


Fig. 10 Predicted flow boiling curves for the porous surface S1 at different velocities of the bulk flow. The symbols denote the measurements: full line (—), model prediction; dash-dotted line (-·-·-), natural convection; dashed line (---), pool boiling curve.

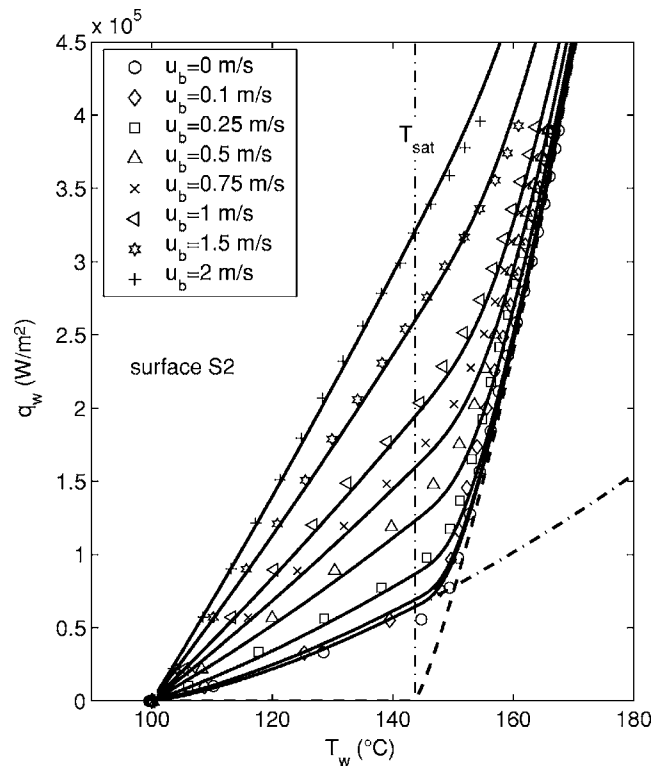


Fig. 11 Predicted flow boiling curves for the porous surface S2 at different velocities of the bulk flow. The symbols denote the measurements: full line (—), model prediction; dash-dotted line (-·-·-), natural convection; dashed line (---), pool boiling curve.

S0. The model exponent, which is determined for S2 as $m=3$, accordingly lies between the values for S0 and S1.

The authors are aware of the fact that the very good overall agreement of the predictions with the experimental data obtained with the present model strongly depends on the appropriate setting of the model parameters. Applying a more general type of model would certainly require a less case-dependent parameter setting. However, as demonstrated by Piro et al. [26], a wider applicability of a model and/or its parameters generally implies a lower accuracy of the predictions. This is especially to be expected in the case of porous coated surfaces, where the highly complex surface-liquid-vapor interactions have obstructed any detailed physical description to date. It appeared therefore conceivable to use the well-established pool boiling correlation due to Rohsenow [18], who represented all basically unknown surface-fluid effects by one empirical parameter C_{sf} . This modeling concept has been proven to be generally the most accurate when applied to plain metallic surfaces [26]. The present work demonstrated that using Rohsenow's correlation in the framework of the power-additive superposition concept is a very reliable modeling approach for the case of subcooled flow boiling with automotive coolants on porous coated surfaces as well.

5 Conclusions

Subcooled boiling flow experiments were carried out in a vertical test channel in order to investigate the potential of using special surface coatings to enhance nucleate boiling heat transfer rates in automotive engine cooling applications. A mixture of ethylene-glycol and water with a mixing ratio of 40 vol % / 60 vol % was used as the working fluid. Three different types of surfaces were considered in the experimental investigations. An unmodified cast iron surface, which can be typically found in cylinder heads of internal combustion engines, represents

the reference case. The two other investigated surface types were produced by depositing metallic coatings on the ground surface of the reference case using two completely different coating techniques, which generate very different microstructures. The first coating consists of a mostly homogeneous solid phase, which is penetrated by microchannel-type cavities starting from the surface. The second coating is a typical granular porous layer with a porosity of about 40%.

In comparison to the plain, uncoated surface, the enhanced surfaces showed a significant reduction in the minimum wall superheat required for the ONB. For both enhanced surfaces, the ONB already occurs once the wall temperature has reached the saturation level. At higher heat fluxes, the enhanced surface containing microchannellike cavities penetrating the otherwise mostly solid base phase exhibits higher heat transfer rates than the granular porous surface. Thus, the porosity, which is considerably higher in the granular porous layer, appears not to be the decisive criterion to enhance the boiling activity. With increasing heat fluxes, the flow boiling curves for the granular porous and the plain, unmodified surfaces become almost parallel, which indicates a similar boiling activity on both surfaces in this regime. The fact that both types of enhanced surfaces exhibit higher total heat transfer rates for all superheats compared to the plain reference surface clearly demonstrates that the concept to enhance the boiling heat transfer by modifying the microstructure of a heated surface represents a reliable and promising approach to increase the cooling power in automotive cooling systems.

In the modeling of the wall heat flux, a superposition approach, originally developed for flow boiling on plain surfaces, could be successfully extended to the case with porous coated surfaces. The nonlinear, power-additive superposition assumed in the present model was proven to reflect very well the wide range of different flow boiling conditions observed in the experiments. As such, the

proposed flow boiling model, which nonlinearly combines the convective and the nucleate boiling components computed from well-established correlations, yielded very accurate predictions for the wall heat flux on all considered surfaces.

Acknowledgment

Financial support of this work from the K plus Competence Center Program, initiated by the Austrian Federal Ministry of Transport, Innovation, and Technology (BMVIT) and funded by FFG, Land Steiermark, and Steirische Wirtschaftsförderung (SFG), is gratefully acknowledged.

Nomenclature

A	= flow cross-sectional area (m^2)
a	= model constant
a_c	= side length of the cross section of the test section (m)
b	= model constant
C_{sf}	= model constant
c_{pl}	= specific heat capacity at constant pressure (J/kg K)
d	= diameter of the heated surface (m)
d_{hyd}	= hydraulic diameter of the test section (m)
g	= gravitational acceleration (m/s^2)
h_b	= specific latent heat (J/kg)
L	= length of the heated surface (m)
m	= model constant
n	= model constant
p	= pressure (bar)
q	= heat flux (W/m^2)
\bar{q}	= heat flux (W/m^2)
r	= radius of the heated surface (m)
S	= suppression factor
s_w	= wetted perimeter (m)
T	= temperature ($^{\circ}\text{C}$)
u_b	= bulk velocity (m/s)

Greek Symbols

β	= coefficient of thermal expansion (K^{-1})
γ	= model constant
δ	= model constant
Δ	= difference
ε_{rms}	= relative root mean square error (%)
λ	= thermal conductivity (W/m K)
μ	= dynamic viscosity (kg/ms)
ξ	= correction factor
ρ	= density (kg/m^3)

Subscripts

b	= bulk
conv	= convection
fc	= forced convection
v	= vapor phase
l	= liquid phase
nb	= nucleate boiling
nc	= natural convection
sat	= saturation
sub	= subcooling
w	= wall

Characteristic Numbers

Gr	= Grashof number
----	------------------

Nu	= Nusselt number
Pr	= Prandtl number
Re	= Reynolds number

References

- [1] Bergles, A. E., and Rohsenow, W. M., 1964, "The Determination of Forced Convective Surface Boiling Heat Transfer," *ASME J. Heat Transfer*, **86**, pp. 365–372.
- [2] Wang, C. H., and Dhir, V. K., 1993, "Effect of Surface Wettability on Active Nucleation Site Density During Pool Boiling of Saturated Water," *ASME J. Heat Transfer*, **115**, pp. 659–669.
- [3] Basu, N., Warriar, G. R., and Dhir, V. K., 2002, "Onset of Nucleate Boiling and Active Nucleation Site Density During Subcooled Flow Boiling," *ASME J. Heat Transfer*, **124**, pp. 617–728.
- [4] Afgan, N. H., Jovic, L. A., Kovalev, S. A., and Levykov, V. A., 1985, "Boiling Heat Transfer From Surfaces With Porous Layers," *Int. J. Heat Mass Transfer*, **28**, pp. 415–422.
- [5] Kim, J. H., Rainey, K. N., You, S. M., and Pak, J. Y., 2002, "Mechanism of Nucleate Boiling Heat Transfer Enhancement From Microporous Surfaces in Saturated FC-72," *ASME J. Heat Transfer*, **124**, pp. 500–506.
- [6] Rainey, K. N., You, S. M., and Lee, S., 2003, "Effect of Pressure, Subcooling and Dissolved Gas on Pool Boiling Heat Transfer From Microporous Surfaces in FC-72," *ASME J. Heat Transfer*, **125**, pp. 75–83.
- [7] Rainey, K. N., Li, G., and You, S. M., 2001, "Flow Boiling Heat Transfer From Plain and Microporous Coated Surfaces in Subcooled FC-72," *ASME J. Heat Transfer*, **123**, pp. 918–925.
- [8] Memory, S. B., Sugiyama, D. C., and Marto, P. J., 1995, "Nucleate Pool Boiling of R-114 and R-114-Oil Mixtures From Smooth and Enhanced Surfaces—I. Single Tubes," *Int. J. Heat Mass Transfer*, **38**, pp. 1347–1361.
- [9] Hsu, Y. Y., 1962, "On the Size Range of Active Nucleation Cavities on a Heating Surface," *ASME J. Heat Transfer*, **84**, pp. 207–216.
- [10] Finlay, I. C., Boyle, R. J., Pirault, J. P., and Biddulph, T., 1987, "Nucleate and Film Boiling of Engine Coolants Flowing in a Uniformly Heated Duct of Small Cross Sections," *SAE Technical Paper No. 870032*.
- [11] Kandlikar, S. G., and Bulut, M., 2003, "An Experimental Investigation on Flow Boiling of Ethylene-Glycol/Water Mixtures," *ASME J. Heat Transfer*, **125**, pp. 317–325.
- [12] Campbell, N. A. F., Hawley, J. G., Robinson, K., Joyce, S., and Haigh, M., 2002, "Predictions for Nucleate Boiling—Results From a Thermal Bench Marking Exercise at Low Flows," *SAE Congress*, Detroit, MI, March 4–7, Paper No. 2002-01-1028.
- [13] Pioro, I. L., Rohsenow, W., and Doerffer, S. S., 2004, "Nucleate Pool-Boiling Heat Transfer. I: Review of Parametric Effects of Boiling Surface," *Int. J. Heat Mass Transfer*, **47**, pp. 5033–5044.
- [14] Chen, J. C., 1963, "A Correlation for Boiling Heat Transfer to Saturated Fluids in Convective Flow," *ASME Paper No. 63-HT-34*.
- [15] Forster, H. K., and Zuber, N., 1955, "Dynamics of Vapor Bubbles and Boiling Heat Transfer," *AICHE J.*, **1**, pp. 531–535.
- [16] Cooper, M. G., 1984, "Nucleate Pool Boiling Using Reduced Properties," *Adv. Heat Transfer*, **16**, pp. 157–239.
- [17] Gorenflo, D., 1988, *Behältersieden*, VDI, Düsseldorf.
- [18] Rohsenow, W. M., 1952, "A Method of Correlating Heat Transfer Data for Surface Boiling of Liquids," *Trans. ASME*, **74**, pp. 969–975.
- [19] Wenzel, U., and Müller-Steinhagen, H., 1994, "Heat Transfer to Mixtures of Acetone, Isopropanol and Water Under Subcooled Flow Boiling Conditions—II. Predictions of Heat Transfer Coefficients," *Int. J. Heat Mass Transfer*, **33**, pp. 185–194.
- [20] Steiner, H., Kobor, A., and Gebhard, L., 2005, "A Wall Heat Transfer Model for Subcooled Boiling Flow," *Int. J. Heat Mass Transfer*, **48**, pp. 4161–4173.
- [21] Liu, Z., and Winterton, R. H. S., 1991, "A General Correlation for Saturated and Subcooled Flow Boiling in Tubes and Annuli Based on a Nucleate Boiling Equation," *Int. J. Heat Mass Transfer*, **34**, pp. 2759–2766.
- [22] Steiner, D., and Taborek, J., 1992, "Flow Boiling Heat Transfer in Vertical Tubes Correlated by an Asymptotic Model," *Heat Transfer Eng.*, **13**, pp. 43–69.
- [23] Kutateladze, S. S., 1963, *Fundamentals of Heat Transfer*, Arnold, London.
- [24] Churchill, S. W., 1972, "Comprehensive Correlating Equations for Heat, Mass and Momentum Transfer in Fully Developed Flow in Smooth Tube," *Ind. Eng. Chem. Fundam.*, **15**, pp. 789–900.
- [25] Churchill, S. W., and Chu, H. H. S., 1972, "Correlating Equations for Laminar and Turbulent Free Convection From a Vertical Plate," *Int. J. Heat Mass Transfer*, **18**, pp. 1823–1829.
- [26] Pioro, I. L., Rohsenow, W., and Doerffer, S. S., 2004, "Nucleate Pool-Boiling Heat Transfer. II: Assessment of Prediction Methods," *Int. J. Heat Mass Transfer*, **47**, pp. 5045–5057.

Manish Mishra¹

Department of Mechanical Engineering,
National Institute of Technology,
Raipur (formerly Government Engineering
College, Raipur), India 492001
e-mail: mishra_md@yahoo.com

P. K. Das

Department of Mechanical Engineering,
Indian Institute of Technology,
Kharagpur, India 721302
e-mail: pkd@mech.iitkgp.ernet.in

Sunil Sarangi

Cryogenic Engineering Centre,
Indian Institute of Technology,
Kharagpur, India 721302
e-mail: ssarangi@hijli.iitkgp.ernet.in

Dynamic Behavior of Three-Fluid Crossflow Heat Exchangers

A transient temperature response of three-fluid heat exchangers with finite and large capacitance of the separating sheets is investigated numerically for step, ramp, exponential, and sinusoidal perturbations provided in the central (hot) fluid inlet temperature. The effect of two-dimensional longitudinal conduction in the separating sheet and of axial dispersion in the fluids on the transient response has been investigated. A comparison of the dynamic behavior of four possible arrangements of three-fluid crossflow heat exchangers has also been presented. [DOI: 10.1115/1.2401616]

Keywords: axial dispersion, finite difference, longitudinal conduction, three-fluid heat exchanger, transient behavior

Introduction

The thermo-hydraulic theory of two-fluid exchangers is well developed and available in the standard literature [1]. The well-established algorithm for the thermal design of a two-fluid heat exchanger, however, has no equivalent when the physical situation implies more than one thermal communication, such as heat losses to the ambient and the introduction of a third fluid.

Most heat exchanger applications in the process, power, transportation, thermal energy recovery, electronics, and aerospace industries involve transfer of thermal energy between two fluids through one thermal communication. However, in recent years some processes with heat transfer between three fluids have become important. Three-fluid and multi-fluid heat exchangers are widely used in cryogenics and different chemical processes, such as air separation, helium separation from natural gas, purification and liquefaction of hydrogen, and ammonia gas synthesis. Three-fluid heat exchangers allow a more compact and economical design also in various other applications.

A wide literature is available on the steady state behavior of three-fluid heat exchangers. A pioneering effort [2] in analyzing crossflow problem considering it to be a case of heat transfer with three heat agents or streams has been given. There was another work by Sorlie [3] among the first few, developing a general theory for two-temperature effectiveness of three-fluid heat exchangers of parallel and counter flow type. Extending the work of Sorlie [3], an analytical relationship was developed by Aulds and Barron [4] between the design variables for a general three-fluid heat exchanger with three thermal communications. Due to the complexity involved with the addition of other operating conditions, a numerical method was used by Barron and Yeh [5] for obtaining the temperature distribution and heat exchanger effectiveness of counter-current three-fluid heat exchangers that included the effect of longitudinal conduction of both the separating walls. Sekulic and Kmecko [6] analyzed the performance of three-fluid parallel stream heat exchangers on the basis of effectiveness and compared four possible arrangements of combining the streams with two thermal communications. Willis and Chapman [7] made an effort to present the performance of a three-fluid crossflow heat exchanger graphically in terms of the temperature

effectiveness. An exact analytical solution of three-fluid crossflow heat exchangers was first tried by Baclic et al. [8] for unmixed flow arrangements using Laplace transforms. Sekulic and Shah [9] gave a very comprehensive review of methodologies for analyzing the steady state performance of three-fluid heat exchangers. The effect of longitudinal conduction in wall on the thermal performance of three-fluid crossflow heat exchanger was numerically calculated by Yuan and Kou [10]. Later, three arrangements of different repetitive patterns were analyzed [11] in terms of overall heat recovery and uniformity of preheating on three fluid streams. The effect of wall longitudinal conduction on thermal performance of three-fluid crossflow heat exchangers under steady state was again investigated by Yuan and Kou [12], and the three arrangements of the fluid streams were compared. Yuan and Kou [13] further investigated the entropy generation in a three-fluid crossflow heat exchanger in the presence of wall longitudinal conduction using a numerical technique.

Although heat exchangers mostly operate under steady state conditions, steady state analysis is not adequate for situations like start-up, shutdown, failure, and accidents. The transient response of heat exchangers needs to be known for designing control strategies and for taking care of thermal stresses in mechanical design. This has been motivation for the determination of transient temperature fields and a few analytical and semi-analytical works [14,15] have also been performed on dynamic behavior of three-fluid heat exchangers.

In the present work, the transient temperature response of the three-fluid crossflow heat exchanger having large and finite core capacity with all the fluids unmixed is investigated numerically for step, ramp, exponential, and sinusoidal perturbations provided in the central fluid inlet temperature. The four possible arrangements [9] for three-fluid crossflow heat exchangers (Fig. 1) have also been compared.

Mathematical Modeling

A direct-transfer, three-fluid, crossflow plate-fin heat exchanger is shown schematically in Fig. 2(a). For the mathematical analysis the two separating sheets having one fluid on either side are taken separately. The following assumptions are made for the analysis.

1. All the fluids are single phase, unmixed, and do not contain any volumetric source of heat generation.
2. The thermo-physical properties of the fluid streams and the walls are constant and uniform.
3. The central fluid is either the hottest or the coldest fluid.

¹Corresponding author.

Contributed by the Heat Transfer Division of ASME for publication in the JOURNAL OF HEAT TRANSFER. Manuscript received April 5, 2005; final manuscript received August 26, 2006; published online January 30, 2008. Review conducted by Anthony M. Jacobi.

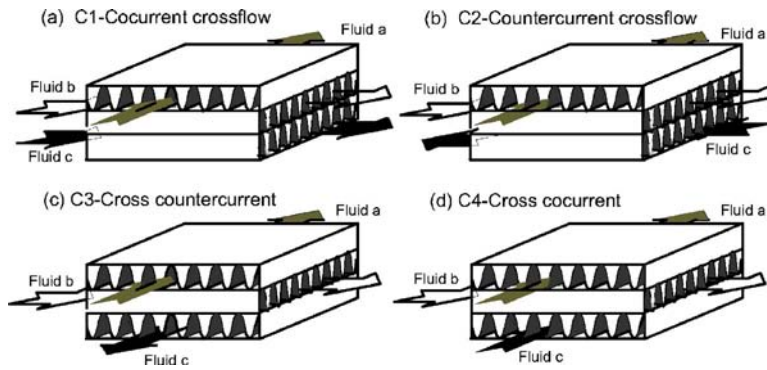


Fig. 1 Four possible arrangements for three-fluid single-pass crossflow heat exchanger [9]

4. The exchanger shell or shroud is adiabatic and the effects of the asymmetry in the top and bottom layers are neglected.
5. Flow is well mixed in any of the passages, so that variation of temperature and velocity in the fluid streams in a direction normal to the separating plate (z direction) are negligible.
6. The primary and secondary areas of the separating plates have been lumped together, so that the variation of wall temperature is also two-dimensional.
7. Transverse conduction through fins between adjacent separating sheets is neglected. This implies there will be a temperature extremum in the fin temperature profile [16].
8. The thermal resistances on both sides, comprising film heat transfer coefficients of primary and secondary surface and fouling resistance, are constant and uniform.
9. Heat transfer area per unit base area and surface configurations are constant.

10. Transverse thermal resistance of the separating sheets in a direction normal to it (z direction) is negligible.

Due to the introduction of a third fluid, the process of energy exchange in a three-fluid heat exchanger is more complex compared to that in a conventional heat exchanger. The central fluid stream exchanges heat simultaneously with two adjacent streams. The exact distribution of this thermal energy plays an important role in steady state as well as in the dynamic behavior of the heat exchanger. This distribution depends upon the conditions of all three fluids and the total area associated with them. As the thermophysical properties of the top and the bottom fluid streams may be different in a general situation, it is likely that the two separating sheets will have different temperatures, and the fins in the central passage will have an asymmetric temperature profile. This indicates that the central stream may transfer heat to the top and the bottom separating sheets at different rates. To take care of this phenomenon it is assumed that part of the secondary surface is associated with the top separating sheet (w_1), and the rest is associated with the bottom separating sheet (w_2). This idealization is depicted in Figs. 2(a) and 2(b).

Assuming $(\eta hA)_{b-w_1}$ and $(\eta hA)_{b-w_2}$ are the convective conductances associated with the top and the bottom separating sheet, respectively, the following relationship can be obtained

$$\frac{1}{(\eta hA)_{b-w_1}} + \frac{1}{(\eta hA)_{b-w_2}} = \frac{1}{(\eta hA)_b} \quad (1)$$

A nondimensional parameter ϕ as defined in Eq. (2) may be introduced.

$$\frac{(\eta hA)_{b-w_1}}{(\eta hA)_b} = \frac{1}{\phi} \quad \text{and} \quad \frac{(\eta hA)_{b-w_2}}{(\eta hA)_b} = \frac{1}{(1-\phi)} \quad (2)$$

Proceeding with the same logic, it may be assumed that the total thermal capacity of the separating sheets is also distributed among the upper and lower sheets in the ratio ψ and $(1-\psi)$, respectively.

$$(Mc)_{w_1} + (Mc)_{w_2} = (Mc)_w \quad (3)$$

Then,

$$\frac{(Mc)_{w_1}}{(Mc)_w} = \psi \quad \text{and} \quad \frac{(Mc)_{w_2}}{(Mc)_w} = (1-\psi) \quad (4)$$

Based on the above assumptions and idealizations, the conservation of energy for the three fluid streams and the two separating sheets can be expressed in nondimensional form for an infinitesimal small control volume as follows.

For fluid streams a , b , and c one gets Eqs. (5)–(7), respectively.

$$\frac{V_a}{R_{ab}} \frac{\partial T_a}{\partial \theta} = T_{w_1} - T_a - \frac{E_{ab}}{R_{ab}} \frac{\partial T_a}{\partial Y} + \frac{N_a E_{ab}}{Pe_a R_{ab}} \frac{\partial^2 T_a}{\partial Y^2} \quad (5)$$

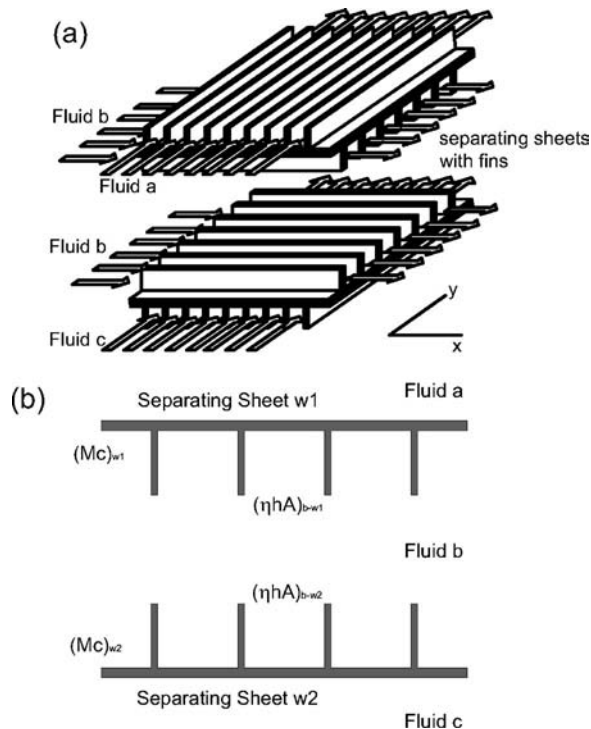


Fig. 2 Schematic representation of (a) flow and separating sheet with fins and (b) distribution of convective resistance of fluid b and the heat capacity of the separating sheet with fins

$$V_b \frac{\partial T_b}{\partial \theta} = \frac{1}{\phi} (T_{w1} - T_b) + \frac{1}{(1-\phi)} (T_{w2} - T_b) - \frac{\partial T_b}{\partial X} + \frac{N_a}{Pe_b} \frac{\partial^2 T_b}{\partial X^2} \quad (6)$$

When fluid c is moving in the x direction

$$\frac{V_c}{R_{cb}} \frac{\partial T_c}{\partial \theta} = T_{w2} - T_c - \frac{E_{cb}}{R_{cb}} \frac{\partial T_c}{\partial X} + \frac{N_a E_{cb}}{Pe_c R_{cb}} \frac{\partial^2 T_c}{\partial X^2} \quad (7a)$$

When fluid c is moving in the y direction

$$\frac{V_c}{R_{cb}} \frac{\partial T_c}{\partial \theta} = T_{w2} - T_c - \frac{E_{cb}}{R_{cb}} \frac{\partial T_c}{\partial Y} + \frac{N_a E_{cb}}{Pe_c R_{cb}} \frac{\partial^2 T_c}{\partial Y^2} \quad (7b)$$

Similarly for the two separating sheets $w1$ and $w2$, heat conduction equations are given in Eqs. (8) and (9), respectively.

$$\psi \frac{\partial T_{w1}}{\partial \theta} = R_{ab} (T_a - T_{w1}) + \frac{1}{\phi} (T_b - T_{w1}) + \lambda_x N_a \frac{\partial^2 T_{w1}}{\partial X^2} + \lambda_y N_a \frac{\partial^2 T_{w1}}{\partial Y^2} \quad (8)$$

$$(1-\psi) \frac{\partial T_{w2}}{\partial \theta} = \frac{1}{(1-\phi)} (T_b - T_{w2}) + R_{cb} (T_c - T_{w2}) + \lambda_x N_a \frac{\partial^2 T_{w2}}{\partial X^2} + \lambda_y N_a \frac{\partial^2 T_{w2}}{\partial Y^2} \quad (9)$$

Here Pe is the axial dispersive Peclet number given by $(mc)L/A_c D$, where D is the diffusion coefficient of the fluid representative of the effect of axial dispersion.

It may be noted that five nondimensional parameters for the steady state performance of a three-fluid heat exchanger were specified in an earlier work [9]. On the other hand, one needs nine nondimensional parameters, namely NTU , E_{a-b} , E_{c-b} , R_{a-b} , R_{c-b} , $V_{a,b,c}$, and $T_{c,in}$. The extra parameters are necessary in the present case to take care of the thermal capacity of the fluid streams and the separating sheets.

Further, one can introduce the number of transfer units (NTU) for the three-fluid heat exchanger and replace Na in terms of NTU . Conventionally NTU for the three-fluid heat exchanger is defined considering the thermal interaction of the central fluid stream with any one of the streams [9]. According to this convention NTU can be defined as follows

$$NTU = \left[(mc)_a \left(\frac{1}{(\eta h A)_{b-w1}} + \frac{1}{(\eta h A)_a} \right) \right]^{-1} \quad (10)$$

$$\text{or } \frac{1}{NTU} = C_a \left(\frac{\phi}{(\eta h A)_b} + \frac{1}{(\eta h A)_a} \right)$$

From the definition of R_{a-b} and E_{a-b} it can be shown that

$$Na = E_{a-b} NTU \left(\phi + \frac{1}{R_{a-b}} \right) \quad (11)$$

Equations (5)–(9) are subjected to the following initial and boundary conditions

$$T_a(X, Y, 0) = T_b(X, Y, 0) = T_c(X, Y, 0) = T_{w1}(X, Y, 0) = T_{w2}(X, Y, 0) = 0 \quad (12)$$

$$\left. \frac{\partial T_{w1}(X, Y, \theta)}{\partial X} \right|_{X=0} = \left. \frac{\partial T_{w1}(X, Y, \theta)}{\partial X} \right|_{X=N_a} = \left. \frac{\partial T_{w1}(X, Y, \theta)}{\partial Y} \right|_{Y=0} = \left. \frac{\partial T_{w1}(X, Y, \theta)}{\partial Y} \right|_{Y=N_a} = 0 \quad (13)$$

$$\left. \frac{\partial T_{w2}(X, Y, \theta)}{\partial X} \right|_{X=0} = \left. \frac{\partial T_{w2}(X, Y, \theta)}{\partial X} \right|_{X=N_a} = \left. \frac{\partial T_{w2}(X, Y, \theta)}{\partial Y} \right|_{Y=0} = \left. \frac{\partial T_{w2}(X, Y, \theta)}{\partial Y} \right|_{Y=N_a} = 0 \quad (14)$$

$$T_a(X, 0, \theta) = T_{a,in} = 0 \quad (15)$$

$$\left. \frac{\partial T_a(X, Y, \theta)}{\partial Y} \right|_{Y=N_a} = 0 \quad (16)$$

$$T_b(0, Y, \theta) = T_{b,in} = \bar{\phi}(\theta) \quad (17)$$

$$\left. \frac{\partial T_b(X, Y, \theta)}{\partial X} \right|_{X=N_a} = 0 \quad (18)$$

$$T_{c,in}(X, Y, \theta) = T_{c,in} \quad (19)$$

where $T_{c,in}$ is $T_c(0, Y, \theta)$, $T_c(N_a, Y, \theta)$, $T_c(X, N_a, \theta)$, and $T_c(X, 0, \theta)$ for the arrangements $C1$, $C2$, $C3$, and $C4$, respectively.

When fluid c flows in the x direction

$$\left. \frac{\partial T_c(X, Y, \theta)}{\partial X} \right|_{X=Z} = 0, \quad (20a)$$

where $Z=Na$ and 0 for the arrangements $C1$ and $C2$, respectively.

When fluid c flows in the y direction

$$\left. \frac{\partial T_c(X, Y, \theta)}{\partial Y} \right|_{Y=Z} = 0, \quad (20b)$$

where $Z=0$ and Na for the arrangements $C3$ and $C4$, respectively.

Equations (5)–(9) along with the boundary conditions (12)–(20) give the complete formulation of a three-fluid crossflow heat exchanger. Solution of this set of equations will give the dynamic performance of heat exchanger once the nine basic input parameters NTU , E_{a-b} , E_{c-b} , R_{a-b} , R_{c-b} , $V_{a,b,c}$, and $T_{c,in}$ along with the two additional parameters $Pe_{a,b}$ and $\lambda_{x,y}$ are specified. Here $\bar{\phi}(\theta)$ is the perturbation given to the inlet temperature of the central fluid, $T_{b,in}$. In the present investigation, the following perturbations have been considered.

$$\bar{\phi}(\theta) = \begin{cases} 1, & \text{for step input} \\ \begin{bmatrix} \alpha \theta, & \theta \leq 1, \\ 1, & \theta > 1, \end{bmatrix} & \text{for ramp input} \\ 1 - e^{-\alpha \theta}, & \text{for exponential input} \\ \sin(\alpha \theta), & \text{for sinusoidal input} \end{cases} \quad (21)$$

where α is assumed to be unity.

Method of Solution

The conservation equations are discretized using the finite difference technique. The forward difference scheme is used for time derivatives, while the upwind scheme and central difference scheme are used for the first and second order space derivatives, respectively [17]. The difference equations along with the boundary conditions are solved using the Gauss-Seidel iterative technique. The convergence of the solution has been checked by varying the number of space grids and size of the time steps. The solution gives the two-dimensional temperature distribution for all three fluids as well as for the separator plate. Additionally one may calculate the mean exit temperatures as follows

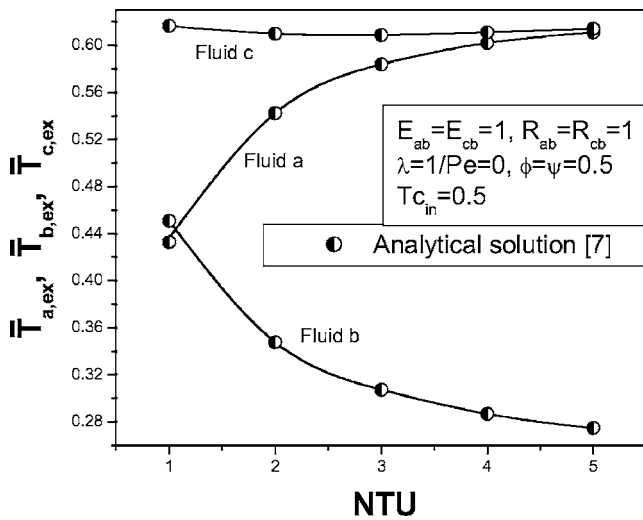


Fig. 3 Validation of the numerical results with the analytical steady state solutions [8]

$$\bar{T}_{a,ex} = \frac{\int_0^{Na} T_{a,ex} u \, dy}{\int_0^{Na} u \, dy}, \quad \bar{T}_{b,ex} = \frac{\int_0^{Na} T_{b,ex} v \, dx}{\int_0^{Na} v \, dx}$$

$$\text{and } \bar{T}_{c,ex} = \frac{\int_0^{Na} T_{c,ex} w \, dy'}{\int_0^{Na} w \, dy'} \quad (22)$$

where $y' = x$ or y at $E_{ab} - E_{cb} = 1$, depending upon the direction of flow of fluid c .

Results and Discussions

To check the validity of the numerical scheme, the solution for the steady state condition for the arrangement C4 $R_{ab} = R_{cb} = 1$, $V = \lambda = 0$, $Pe = \infty$, $T_{a,in} = 0$, $T_{b,in} = 1$, and $T_{c,in} = 0.5$ was compared with the analytical solutions [8]. Excellent agreement was observed as shown in Fig. 3.

The transient behavior of the three-fluid crossflow heat exchanger has been studied for different excitations given to the central (hot) fluid inlet temperature. Performance of the heat exchanger was studied over a wide range of parameters as well as for sufficient time duration so that steady state conditions are obtained for each individual excitation. Some of the salient results are discussed in the next sections.

Case I: Heat Exchanger With Large Core Capacity in the Absence of Core Longitudinal Conduction and Axial Dispersion. Though the formulation has been done for a generalized case, an example has been taken where the core capacity is large. This makes $V_a = V_b = V_c \approx 0$, and the results are applicable to gas-to-gas heat exchangers.

Figures 4(a)–4(c) exhibit the performance of the heat exchanger at $NTU = 1, 5$, and 10 for step, ramp, and exponential inputs, respectively. In all the cases, the steady state exit temperature is reached by the three streams within a small time interval at $NTU = 1$. However, the difference of mean exit temperatures (at steady state) is the maximum in this case with the bottom and the upper layers having the maximum and the minimum values of temperature, respectively. This is a common trend for step, ramp,

and exponential excitations as depicted in Figs. 4(a)–4(c), respectively.

The time required to reach the steady state increases with the increase of NTU . Nevertheless, with the increase of NTU , equalization of temperature between different streams takes place as more area for heat transfer is available. The temperature difference between the coldest stream and the hottest stream decreases at any time interval. Further, the exit temperatures of the two extreme fluid layers become identical from the very beginning even at $NTU = 5$. It may be noted that, although the inlet temperature of fluid a is lower than that of fluid b , its exit temperature is higher than that of fluid b at higher $NTUs$.

For a sinusoidal variation of the inlet temperature of the central fluid, two different $NTUs$, 1 and 5 , have been considered, and the results are depicted in Fig. 4(d). At lower NTU , steady state is reached early even in the case of sinusoidal excitation as the previous cases. The time lag of oscillations increases with the increase in NTU . All the temperature responses have a periodic nature whose amplitude and frequency vary with time and attain a constant value once steady state is reached. At steady state the mean exit temperatures of all three fluid streams have a steady periodic nature, which can be described by a suitable sine function. This fact may be appreciated from Fig. 5. Here all the mean exit temperatures of the three fluids have been plotted as functions of the inlet temperature of the central fluid. Near the steady state, three Lissajous figures of elliptic shapes are obtained for the three exit temperatures. This indicates that the mean temperatures at outlet are also experiencing a sinusoidal variation with the same frequency as $T_{b,in}$ but with different amplitudes. Therefore, for a sinusoidal excitation of the central fluid, Fig. 5 provides a very convenient and concise way of determining the response of all three fluid streams under steady state conditions.

The effect of the conductance ratio on the mean exit temperature of the three fluids is depicted in Fig. 6. Although the conductance ratio does not have any effect on the steady state performance of the heat exchanger, its effect should not be neglected during the transients. From Fig. 6, it may be noted that a lower value of the conductance ratio increases the time to reach the steady state and the effect is more pronounced in the central fluid stream.

Case II: Heat Exchanger With Finite Core Capacitance, Core Longitudinal Conduction, and Axial Dispersion. In the second case the transient behavior has been investigated with the introduction of the heat capacity ratio (V), two-dimensional longitudinal conduction in the separating sheets, and axial dispersion in the fluids.

Because the step, ramp, and exponential responses give similar behavior as observed earlier, only a step excitation has been considered for further analysis. Similar to the previous case, arrangement C4 only has been considered for the effect of various parameters.

The effect of longitudinal conduction in a heat exchanger core has been studied next. The exit temperature responses of the three fluids are depicted in Fig. 7. Initially, the temperature of the hotter fluids b and c decreases with an increase in longitudinal conduction, showing a reduction in the mean exit temperatures. The effect is not comparably significant on the lower temperature fluid (fluid a). However, in the latter part of the transient period, performance of the fluids in the upper and lower layers deteriorates. The change in the performance of the middle layer fluid is insignificant near steady state.

The effect of axial dispersion on the step response of the three fluids for arrangement C4 has been depicted in Fig. 8. It shows that the increase of axial dispersion (decrease in Pe) adversely affects the performance of the heat exchanger. The mean exit temperature of the hotter fluids (fluids b and c) increases, and there is reduction in that of the cold fluid (fluid a). The difference is larger at smaller Pe , and it decreases with an increase in Pe . Practically,

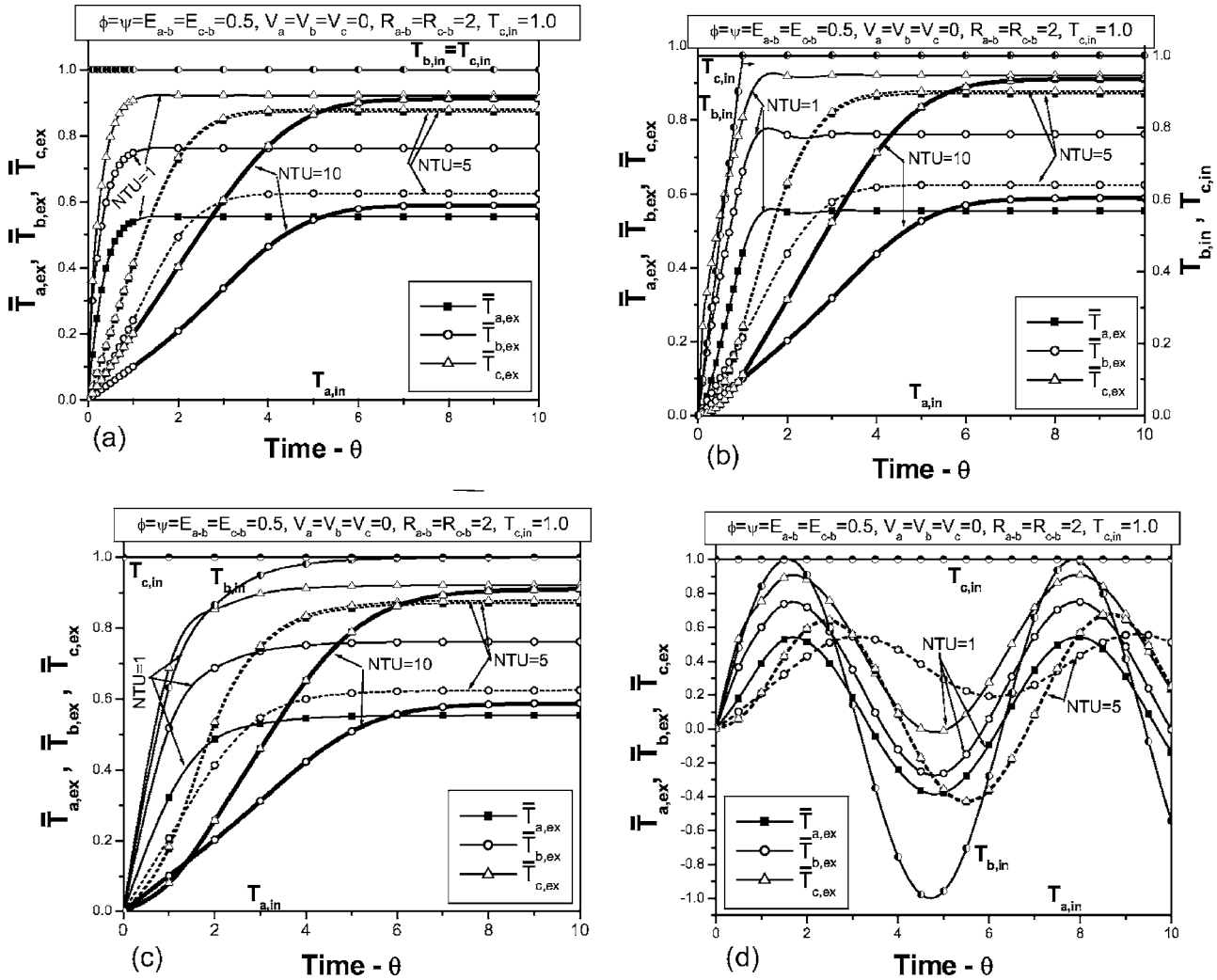


Fig. 4 Effect of NTU on (a) step, (b) ramp, (c) exponential, and (d) sinusoidal response for three-fluid crossflow heat exchanger with large core capacity in the absence of longitudinal conduction and axial dispersion

above $Pe=20$, the effect of axial dispersion is not very significant, and the difference in the performance is very small.

Comparison of Different Arrangements. A dynamic analysis of different arrangements of a three-fluid single-pass crossflow heat exchanger for step disturbances in the central fluid stream has been conducted and is depicted in Fig. 9. It shows that for the central (hot) fluid, the mean exit temperature can be given in decreasing order as $C2 > C3 > C4 > C1$ (Fig. 9(b)). For the upper and lower fluids, the mean exit temperature decreases as $C4 < C1 < C2 < C3$ (Figs. 9(a) and 9(c)). However, the differences in the mean exit temperature between arrangements C2 and C3, and between C1 and C4, are very small for all three fluids. The selection of the arrangements can be done on the basis of the relative importance of the fluids. For the central (hot) fluid, arrangements C2 and C3 are better where all the fluid combinations are either cross or counter. However, arrangements C1 and C4 are better for the cold fluids (fluid *a* and fluid *c*). Between the cross-co-current (C4) and the cross-counter-current (C3) heat exchangers, C4 performs better if the cold fluids are the desired fluids. This has also been proved earlier by the steady state analysis [6,18]. The behaviors for ramp and exponential inputs are similar to that for a step input because of the specific nature of the input functions.

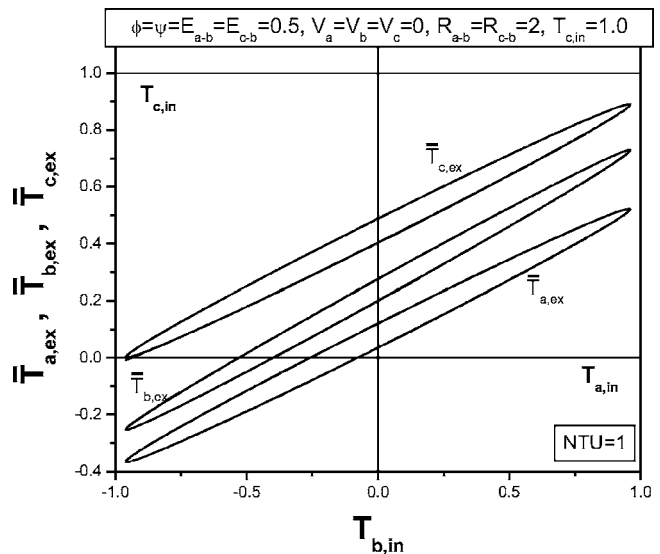


Fig. 5 Steady state variation of mean exit temperature of the three fluids with respect to the hot fluid inlet temperature for sinusoidal excitation

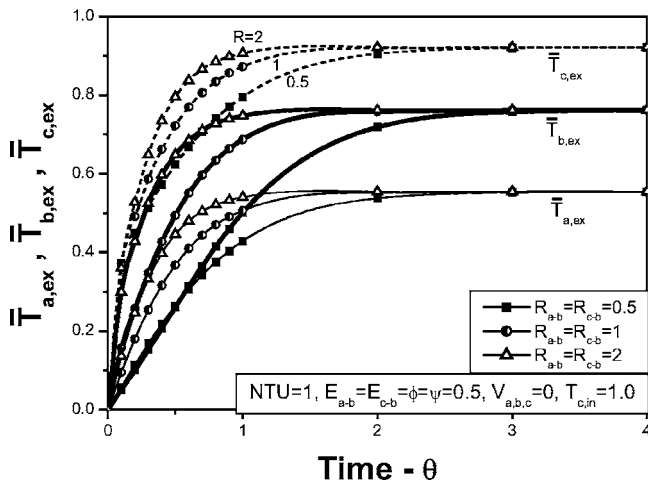


Fig. 6 Variation of mean exit temperature of the three fluids with conductance ratio R

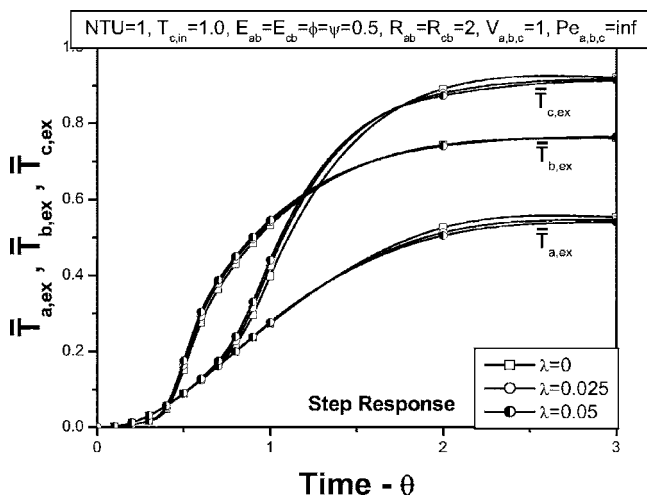
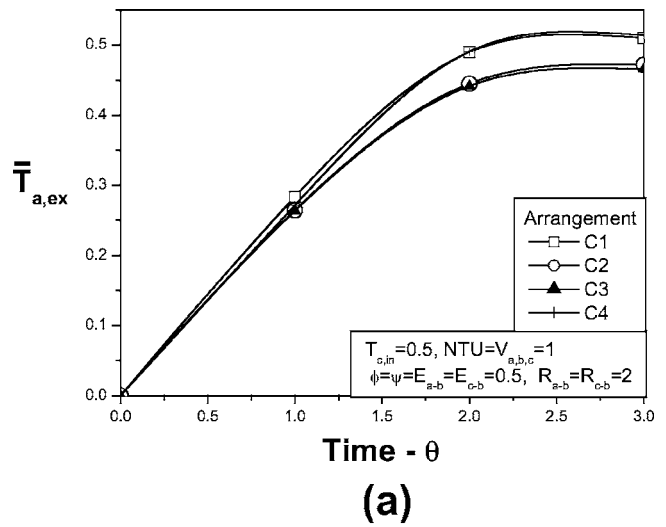


Fig. 7 Effect of longitudinal conduction on step response of mean exit temperature of the three fluids for arrangement C4

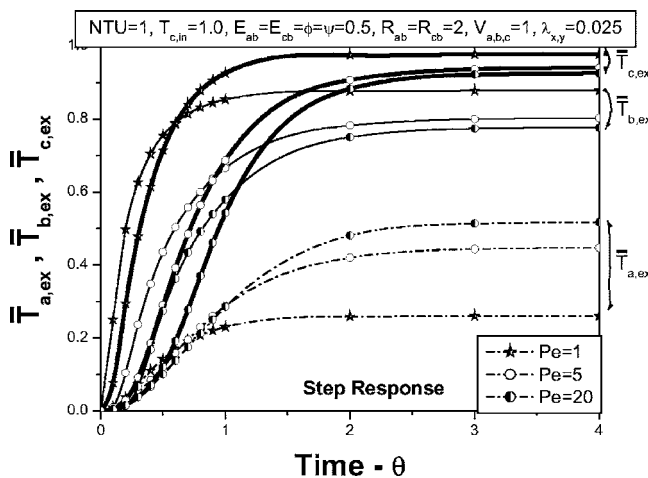


Fig. 8 Effect of axial dispersion on step response of mean exit temperature of the three fluids for arrangement C4

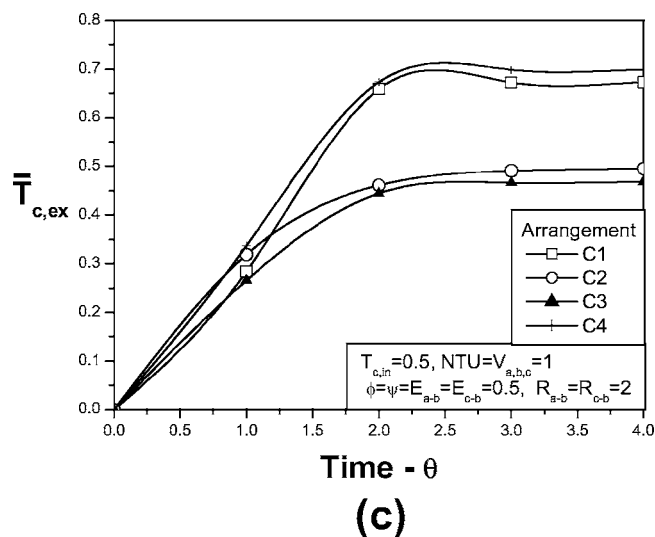
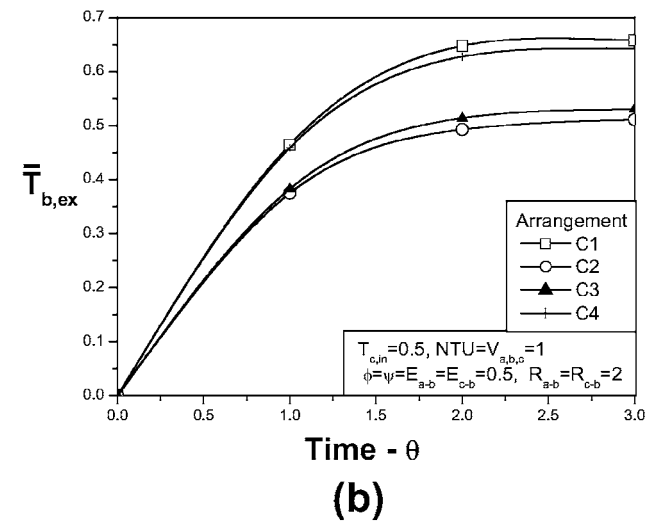


Fig. 9 Comparison of the four possible arrangements of three-fluid crossflow heat exchanger for step response. (a) fluid a , (b) fluid b , and (c) fluid c .

Conclusion

In the analysis, a typical case of three-fluid crossflow heat exchanger with large core capacity is analyzed based on a finite

difference technique. The analysis has been extended to finite core capacity in the presence of core longitudinal conduction and axial dispersion. In general, it has been seen that at low NTU the heat exchanger reaches the steady state within a small interval of time, whereas at high NTU the temperature difference between the streams decreases. In the case of a sinusoidal excitation, the exit temperatures initially show unsteady periodic behavior. Gradually this becomes steady while the frequency ultimately reaches the frequency of the input excitation. It has been shown that the functional dependence of exit temperatures on the inlet excitation can be depicted with the help of Lissajous plots under steady state. Different arrangements for single pass crossflow heat exchangers have also been compared.

Although the numerical solution considered above has been applied to a few typical examples, other cases of transient heat transfer in three-fluid heat exchangers can also be analyzed. Moreover, from the given analysis one can determine the transient behavior of the core temperature at different time instants, which may be needed for mechanical design and calculation of thermal stresses.

Nomenclature

- A, A_{HT} = heat transfer area, m^2
 A_c = flow area, m^2
 C = heat capacity rate (mc), W/K
 c, Cp = specific heat, J/kg-K
 $C1, C2, C3,$
 $C4$ = crossflow arrangements
 D = diffusion coefficient, W/m-K
 $E_{a,c-b}$ = capacity rate ratio = $(mc)_{a,c}/(mc)_b$
 h = heat transfer coefficient, W/m²-K
 k = thermal conductivity of the separating sheet, W/m
 L = heat exchanger length, m
 M = mass of the separating sheet, kg
 m = mass flow rate of fluid, kg/s
 $Na = (\eta hA/mc)_b$
 NTU = number of transfer units, $(UA)_{a-b}/(mc)_a$
 Pe = axial dispersive Peclet number = $(mc)L/A_c D$
 Q, q = rate of heat transfer, W
 $R_{a,c-b}$ = conductance ratio = $(\eta hA)_{a,c}/(\eta hA)_b$
 $Ru = (UA)_{a-b}/(UA)_{c-b}$
 T = dimensionless temperature = $(t - t_{a,in})/(t_{b,in} - t_{a,in})$
 t = temperature
 \bar{T} = dimensionless mean temperature
 \bar{t} = mean temperature
 U = overall heat transfer coefficient, W/m²-K
 u, v, w = velocity of flow, m/s
 V = heat capacity ratio = $LA_c pc/Mc_w$
 $X = (\eta hA/mc)_b x/L_x = Na(x/L_x)$
 $Y = (\eta hA/mc)_b y/L_y = Na(y/L_y)$

Greek Letters

- δ = equivalent thickness of the separating sheet, m
 η = overall surface efficiency
 $\theta = (\eta hA)_b \tau / (Mc)_w$, dimensionless time
 λ = longitudinal heat conduction parameter, $\lambda_x = k\delta L_x / L_x (mc)_b$, $\lambda_y = k\delta L_y / L_y (mc)_b$

μ = dynamic viscosity, N-s/m²

ρ = density, kg/m³

τ = time, s

$\bar{\phi}(\cdot)$ = perturbation in hot fluid inlet temperature

$\phi = (\eta hA)_{b-w1}/(\eta hA)_b$

$\psi = (Mc)_{w1}/(Mc)_w$

Subscripts

- a, b, c = fluid streams a, b and c
 c, h = cold and hot side
 ex = exit
 i, in = inlet
 max = maximum
 $mean$ = mean value
 min = minimum
 o, out = exit/outlet
 w = separating wall
 $1, 2$ = state 1 and 2

References

- [1] Shah, R. K., and Sekulic, D. P., 1998, "Heat Exchangers," in *Handbook of Heat Transfer*, W. M. Rosenhow, J. P. Hartnett, and Y. J. Cho, eds., McGraw Hill, New York, pp. 17.63–17.76.
- [2] Rabinovich, G. D., 1962, "On a Particular Case of Stationary Heat Transfer With Cross Flow of Heat Agents," *Int. J. Heat Mass Transfer*, **5**, pp. 409–412.
- [3] Sorlie, T., 1962, "Three-Fluid Heat Exchanger Design Theory—Counter and Parallel Flow," Technical Report No. 54, Dept. of Mech. Eng., Stanford University, Stanford, CA.
- [4] Aulds, D. D., and Barron, R. F., 1967, "Three-Fluid Heat Exchanger Effectiveness," *Int. J. Heat Mass Transfer*, **10**, pp. 1457–1462.
- [5] Barron, R. L., and Yeh, S. L., 1976, "Longitudinal Conduction in a Three-Fluid Heat Exchanger," ASME Paper No. 76-WA, HT-9, pp. 2–7.
- [6] Sekulic, D. P., and Kmecko, I., 1995, "Three-Fluid Crossflow Heat Exchanger Effectiveness—Revisited," *ASME J. Heat Transfer*, **117**, pp. 226–229.
- [7] Willis, N. C., Jr., and Chapman, A. J., 1968, "Analysis of Three-Fluid Crossflow Heat Exchanger," *ASME J. Heat Transfer*, **90**, pp. 333–339.
- [8] Baclic, B. S., Sekulic, D. P., and Gvozdenac, D. D., 1982, "Performance of Three-Fluid Single Pass Crossflow Heat Exchanger," in *Heat Transfer*, U. Grigull, E. Hahne, K. Stephan, and J. Straub, eds., Hemisphere, Washington, pp. 167–172.
- [9] Sekulic, D. P., and Shah, R. K., 1995, "Thermal Design Theory of Three-Fluid Heat Exchangers," *Adv. Heat Transfer*, **26**, pp. 219–328.
- [10] Yuan, P., and Kou, H. S., 1998, "The Effect of Longitudinal Conduction in a Three-Fluid Crossflow Heat Exchanger," *Numer. Heat Transfer, Part A*, **34**, pp. 135–150.
- [11] Kou, H. S., and Yuan, P., 2001, "Thermal Analysis of Plate-Fin Crossflow Heat Exchanger Including Three Fluids With Different Arrangements," *Int. J. Transp. Phenom.*, **3**, pp. 29–41.
- [12] Yuan, P., and Kou, H. S., 2001, "The Comparison of Longitudinal Wall Conduction Effect on the Crossflow Heat Exchangers Including Three Fluid Streams With Different Arrangements," *Appl. Therm. Eng.*, **21**, pp. 1891–1907.
- [13] Yuan, P., and Kou, H. S., 2001, "Entropy Generation on a Three-Gas Crossflow Heat Exchangers With Longitudinal Wall Conduction," *Int. Commun. Heat Mass Transfer* **28**(6), pp. 803–813.
- [14] Sekulic, D. P., and Herman, C., 1987, "Transient Temperature Fields in a Three-Fluid Heat Exchanger," *Proc. XVII Int. Congr. Refrig.*, Vienna, IFF, Paris, Vol. B, pp. 833–837.
- [15] Bielski, S., and Malinowski, L., 2003, "A Semi-Analytical Method for Determining Unsteady Temperature Fields in a Parallel-Flow Three-Fluid Heat Exchanger," *Int. Commun. Heat Mass Transfer*, **30**(8), pp. 1071–1080.
- [16] Prasad, B. S. V., 1997, "Fin Efficiency and Mechanisms of Heat Exchange Through Fins in Multi-Stream Plate-Fin Heat Exchangers: Development and Application of a Rating Algorithm Passages," *Int. J. Heat Mass Transfer*, **40**(18), pp. 4279–4288.
- [17] Ozisic, M. N., 1994, *Computational Methods in Heat Transfer*, CRC, London.
- [18] Ellis, W. E., 1968, "Comparative Evaluations of Alternative Flow Configurations of Three-Fluid, Cross Flow, Heat Exchangers," M.S. Thesis, Dept. of Mech. Eng., Rice University, Houston, TX.

Film Cooling and Heat Transfer on Two Cutback Trailing Edge Models With Internal Perforated Blockages

Jung-ho Choi

Shantanu Mhetras

Je-Chin Han

e-mail: jc-han@tamu.edu

Sai C. Lau

Department of Mechanical Engineering,
Texas A&M University,
College Station, TX 77843-3123

Ron Rudolph

Siemens Power Generation, Inc.,
1680 South Central Boulevard,
Jupiter, FL 33458

Experiments to study heat transfer and film cooling on the cutback trailing edge of a turbine blade with slot ejection were performed. Heat transfer from two rows of perforated blockage inserts for lateral impingement on the coolant channel walls prior to coolant ejection into the freestream was also investigated. The internal test geometry is similar to the crossover impingement hole design used in modern gas turbine blades for trailing edge cooling. A liquid crystal technique based on hue value detection was used to measure the heat transfer coefficient on a trailing edge film-cooling model with slot ejection and an internal model with perforated blockage inserts. It was also used to determine the film effectiveness on the cutback trailing edge. For the internal model with the perforated blockage inserts, Reynolds numbers based on the hydraulic diameter of the slot and exit velocity were 5000, 10,000, 20,000, and 30,000 and corresponding coolant-to-freestream velocity ratios ranged from 0.26 to 1.83 for the external model with slot ejection, respectively. The experiments were performed for two different designs, 1 and 2, with Design 1 incorporating two different configurations with a staggered/inline slot exit arrangement and Design 2 with a staggered slot exit arrangement. Both designs utilized a 90 deg flow turn into the blockage inserts as an entrance to the test section to simulate a realistic blade passage design. Results show that the internal design geometry of the trailing edge and Reynolds numbers can affect heat transfer in an internal model with perforated blockage inserts. Design 2 with a wider entrance channel and a sloped land near the ejection slots provided low heat transfer coefficients in the internal as well as external model but gave higher film-cooling effectiveness from slot ejection.

[DOI: 10.1115/1.2780174]

Introduction

Thermodynamic analysis of gas turbines shows that the thermal efficiency and power output can be increased with higher turbine inlet temperatures. Modern gas turbines try to approach these high temperatures ($\sim 1500^\circ\text{C}$) to improve performance but are limited by the maximum allowable thermal stresses for the blade material. Usually, several cooling techniques, such as internal convective cooling and film cooling on the blade exterior, are used to cool the hot blade to increase its low cycle fatigue life. One of the hardest regions to cool is the trailing edge as it must be thin to reduce aerodynamic losses. This conflicts with blade cooling design requirements as enough coolant cannot be channeled into a thin trailing edge. Additional constraints due to structural integrity and manufacturing difficulty for internal cooling passage geometry in this thin section also arise. One of the cooling techniques frequently used by turbine designers for the trailing edge is using spanwise slots to provide film cooling, which are obtained by removing material from the pressure side surface. Pin fins or blockage inserts similar to those used in the present study have also been used to enhance heat transfer in the internal coolant channels for the trailing edge.

Several studies have been performed for aerodynamics and film-cooling effectiveness by slot injection on the trailing edge. Uzol et al. [1] studied discharge coefficients from a cutback trailing edge with several cutback lengths, spanwise rib spacing,

freestream Reynolds number, and chordwise rib length. Aerodynamic loss characteristics using particle image velocimetry (PIV) flow measurement technique was studied by Uzol and Camci [2] for different ejection rates and cutback lengths. In a study by Telisinghe et al. [3], total pressure losses from a conventional trailing edge and a cutback trailing edge were found to be similar. An experimental and numerical investigation for trailing edge slot injection was performed by Holloway et al. [4,5] under realistic engine flow conditions. Periodic vortex shedding from the pressure side lip was found to cause a relatively fast decay in film-cooling effectiveness on the cutback portion of the trailing edge for larger lip thicknesses. The effect of complex three-dimensional slots obtained by using closely spaced spanwise rib partitions on adiabatic film-cooling effectiveness was studied by Martini and Schulz [6] on a cutback trailing edge. Experiments were performed for a large scale trailing edge model with low-speed, hot mainstream air. This resulted in a coolant-to-mainstream density ratio of 1.5. Grouping of coolant jets was observed resulting in local hot spots. Martini et al. [7,8] in two papers did experimental and numerical investigations on film cooling and heat transfer for the same experimental setup described earlier. Effect of cooling geometry (spanwise ribs and pins) prior to coolant injection into the mainstream was investigated. The observed fast decay in film-cooling effectiveness was attributed to vortex shedding from the pressure side lip similar to that observed by Holloway et al. [4,5]. Rib arrays though found give lower heat transfer coefficients close to the exit of the slot. Cunha et al. [9] studied the impact of trailing edge ejection on heat transfer using a closed form, analytical solution for temperature profiles for four different configurations. Impact of several geometrical design features on the trailing edge design and durability was investigated. Heat transfer on

Contributed by the Heat Transfer Division of ASME for publication in the JOURNAL OF HEAT TRANSFER. Manuscript received January 11, 2006; final manuscript received March 21, 2007; published online January 25, 2008. Review conducted by Minking Chyu.

the crossover impingement surfaces for a trailing edge internal cooling design was studied by Chyu et al. [10]. Very high heat transfer was observed on the side surfaces normal to the impinging jets. However, large variations in heat transfer were observed on all surfaces. Cakan and Taslim [11] studied mass transfer on the cutback and land region for three different geometries and several blowing ratios. Similar heat transfer levels were observed for all three geometries. Higher heat transfer was noticed on the land sides as compared to the cutback slot.

Internal heat transfer measurements to simulate trailing edge ejection were performed by Lau et al. [12]. They tested several geometries with varying ejection flow exit configurations and used pin fins as turbulators to enhance heat transfer. Local measurements using the naphthalene sublimation technique were performed by McMillin and Lau [13]. The Sherwood numbers were found to decrease downstream due to mass extraction from the ejection holes. Heat transfer in ribbed trapezoidal channels simulating a trailing edge was performed by Taslim and Li [14] with and without bleed holes. Large spanwise variations in heat transfer were observed in the trapezoidal channel, which reduced when bleed holes were added. Effect of crossover jets and ribs was studied by Taslim et al. [15] in a trapezoidal channel to simulate the trailing edge of a blade. Effect of normal and inclined jets was studied on heat transfer using a liquid crystal technique. They concluded that proper arrangement of ribs and jets can give high and uniform heat transfer on the walls. In another study similar to the present investigation, Lau et al. [16] performed internal mass transfer measurements using the naphthalene sublimation technique. They performed tests using the same trailing edge design geometry used in the present study. The perforated blockages were found to enhance heat (mass) transfer from 20% to 70% on the test walls as compared to a smooth channel with the same hydraulic diameter. The first test section with larger hole-to-channel cross-sectional area ratio (Design 1) gave higher heat (mass) transfer enhancement in the first and second chambers. Effect of pin fins on internal heat transfer in a trailing edge geometry prior to ejection through cutback slots has been investigated by Chen et al. [17]. They found that the heat transfer behavior on the pin endwalls was typical of pin fins with heat transfer increasing over the first four pin rows and then decreasing gradually.

Slot film cooling has been investigated by several researchers and a brief synopsis of prior studies is presented. While most of the studies are for slots with a two-dimensional flow structure, some published researches for three-dimensional slots are also discussed. A comprehensive survey of film-cooling investigations prior to 1971 was done by Goldstein [18] and included data for discrete holes as well as slots. It was noted that the slot coolant-to-mainstream blowing ratio and normalized distance downstream of slot breakout are key parameters to which film effectiveness can be correlated. Wieghardt [19] conducted an experimental study injecting heated flow through slots angled 30 deg to the mainstream. Kacker and Whitelaw [20,21] investigated the influence of slot height, slot-lip thickness, and slot turbulence intensity on the film effectiveness for a uniform density, two-dimensional wall jet. Papell [22] investigated the effects of slot angle of injection (α) relative to mainstream flow on film effectiveness and made measurements for $\alpha=45$ deg, 80 deg, and 90 deg. The investigation revealed a significant decrease in slot film effectiveness as the angle was increased. Rostogi and Whitelaw [23] and Patankar et al. [24] reported experimental results for the adiabatic wall effectiveness downstream of three-dimensional slots made up of discrete holes discharging parallel to the mainstream. Rastogi and Whitelaw [23] concluded that an increase in lip thickness and pitch to diameter ratio leads to a decrease in film effectiveness. Paxson and Mayle [25] performed theoretical and experimental investigations on the influence of the mainstream thermal boundary on film effectiveness. Nina and Whitelaw [26] and Taslim [27] investigated adiabatic film-cooling effectiveness of different slot geometries. Taslim [27] showed that the film effectiveness is

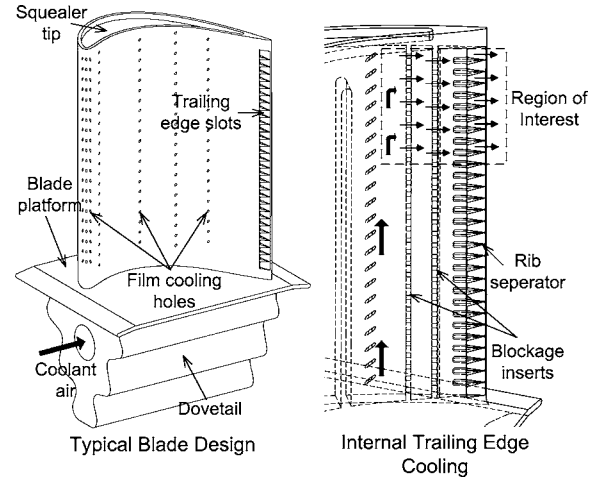


Fig. 1 Schematic drawing of a typical turbine blade with a cutback TE and impingement blockage inserts

strongly sensitive to the slot-lip thickness to height ratio in the range from 0.5 to 1.25. Sturgess [28,29] focused on combustor slots with a circular inlet followed by a lip overhang acting as a mixing chamber.

In addition to film cooling and heat transfer on the cutback region, this paper also presents results for perforated blockage inserts placed upstream in the coolant flow before it exits from the slot. Studies with similar blockage inserts have been performed by Moon and Lau [30] and Lau et al. [31]. Moon and Lau [30] investigated heat transfer between two perforated blockages and pressure drop across the blockages for turbulent flow in a rectangular channel using thermochromic liquid crystals. They found that the lateral impingement from jets through these perforated blockages enhanced heat transfer but with a significant rise in the pressure penalty resulting in a thermal performance of less than 1 for large Reynolds numbers. They also discerned that the local heat transfer was the lowest immediately downstream of the upstream blockage insert, the highest upstream of the downstream blockage insert, and relatively high in the region of reattachment of the jets. Lau et al. [31] studied round and square hole geometries in the perforated blockage inserts. Perforated blockages with round holes resulted in a higher heat (mass) transfer on the walls but also caused a larger pressure drop as compared to perforated blockages with square holes. Additional information pertaining to published studies on internal cooling with turbulators as well as external film cooling of gas turbine components has been compiled by Han et al. [32].

The primary motivation for this paper is to investigate the effect of film cooling and heat transfer by slot ejection on the trailing edge as well as to investigate the presence of perforated blockages on pressure drop and heat transfer prior to coolant ejection from the slots. Some trailing edge blade designs use a combination of turbulators and slot ejection to cool the trailing edge and the present paper tries to model this design philosophy. Figure 1 shows a typical trailing edge cooling configuration employed in modern gas turbine blades. Perforated blockage inserts used result in lateral impingement on the pressure and suction sidewalls of the blade, which helps in extracting heat from the blade surface. By modeling a section of this blade design, it is hoped that this study will provide a complete representation of the pressure drop and heat transfer characteristics for a typical, nonrotating trailing edge model using these inserts. Additionally, a 90 deg bend at the entrance to the blockage inserts simulates the spanwise internal flow of coolant.

Thermochromic liquid crystals have been used to obtain local distributions of heat transfer coefficients and film-cooling effectiveness for all cases. Three different configurations with two de-

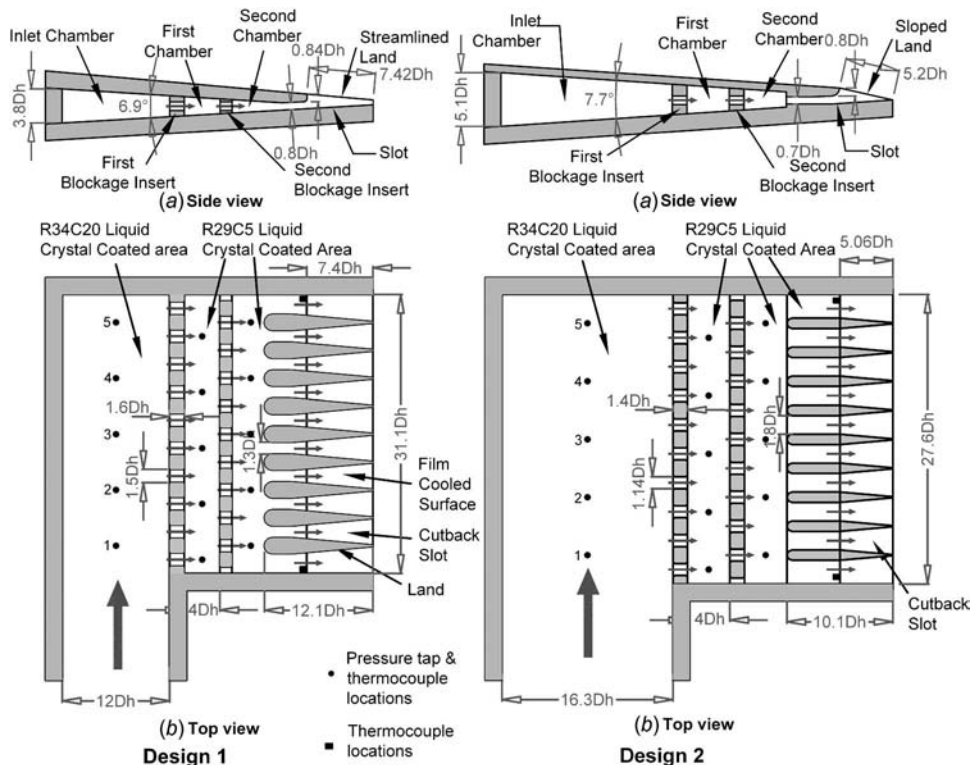


Fig. 2 Schematic of the two TE models

sign models have been tested. The two design models are used to investigate the effect of entrance channel size as well as the effect of a streamlined land or a sloped land for the chordwise rib separators, which form the cutback slots on the trailing edge. In addition, the effects of a staggered or inline arrangement of the rib separators with respect to the holes in the perforated blockage inserts have also been investigated. Four different Reynolds numbers based on slot exit dimensions have been tested ranging from 5000 to 30,000, which correspond to slot exit velocity ratios ranging from 0.3 to 1.83 for Design 1 and from 0.26 to 1.56 for Design 2, respectively.

Experimental Setup

Figure 2 shows a schematic view of the trailing edge design models 1 and 2 for internal as well as external cooling. The dimensions shown in Fig. 2 are expressed in terms of the hydraulic diameter of a channel formed between adjacent chordwise rib separators before the coolant ejects on the cutback slot region. The trailing edge (TE) model is designed to simulate only a portion of the blade TE, as shown in Fig. 1. The external model, scaled up by five times, was mounted in a low-speed suction-type wind tunnel with a maximum velocity of up to 34 m/s (inlet Mach number = 0.1). Detailed information on the wind tunnel can be found in Ref. [33]. The 2.3:1 contraction nozzle at the wind tunnel inlet produced uniform flow at the entrance of the test section. The wind tunnel had an inlet cross section of $60.96 \times 30.48 \text{ cm}^2$. A $5 \mu\text{m}$ cotton filter and packed plastic straw flow straightener box were installed in front of the nozzle inlet. The channel cross section of the wind tunnel was 30.48 cm (width) \times 15.24 cm (height). A 5.6 kW axial blower downstream of the wind tunnel generated the suction necessary for the desired air flow. A central air-conditioning system maintained the mainstream temperature at 22°C . A turbulence grid was set upstream of the test surface, which created a turbulence intensity of 6% near the TE test model. It was composed of a square mesh of aluminum tubes, 13 tubes in the vertical direction and 7 tubes in the horizontal direction. The

diameter of each tube was 0.635 cm, so the turbulent length scale near the cutback region was approximately 1 cm. Figure 3 shows a 2D schematic of the experimental setup. The coolant air, supplied from a compressor, passes through a flow control valve and orifice flow meter. The coolant then passes through a 5 kW pipe heater and a bypass valve before it enters the inlet channel for the TE model. Figure 4 shows a schematic of the wind tunnel and TE test section assembly.

A three-dimensional, isometric view of Design 1 is shown in Fig. 5. Two test sections were fabricated to test the two design models and were fitted in the wind tunnel such that the cover plate (pressure surface with cutback TE) was parallel to the mainstream flow direction. Both test models have a taper causing the coolant flow to accelerate as it takes a turn to enter the turbulated portion. This design is similar to thin, converging TE region in a turbine vane or blade. This taper results in a trapezoidal inlet channel for the coolant, as depicted in Fig. 2. The inlet channel for Design 2 is wider than that for Design 1. The inlet channel forces the coolant to enter the turbulated region through a 90 deg bend provided to simulate realistic internal passage geometry in a blade. As the coolant flow turns, it enters two rows of perforated blockage in-

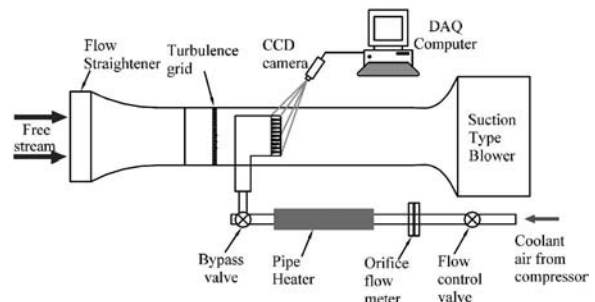


Fig. 3 Schematic of wind tunnel and coolant flow loop

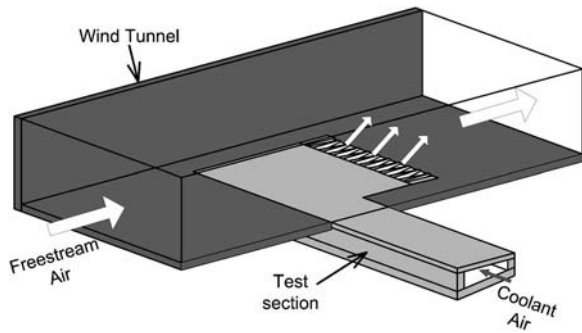


Fig. 4 Trailing edge test section placed in wind tunnel

serts. The holes in these inserts are staggered with respect to each other to enhance internal heat transfer. The holes are rectangular in cross section with rounded corners and with aspect ratios of 1.54 for Design 1 and 1.38 for Design 2. Heat transfer from coolant flow through these inserts is measured by using liquid crystal thermography on one wall. The flow then exits through slots onto the cutback TE region and provides film cooling. The slots are formed by periodic spanwise placement of chordwise rib separators, which taper on the cutback region. The slot aspect ratio for Design 2 (2.55) is larger than that for Design 1 (1.67). The slot-lip thickness to height ratio is around 1.1 for both designs. Design 1 has a longer cutback region as compared to Design 2. The land, defined as the surface on the rib separators which is uncooled and is directly exposed to the mainstream, is streamlined or parallel to the freestream in the wind tunnel for Design 1. For Design 2 though, the land is inclined by 8.8 deg to freestream to account for the shorter cutback region and also to minimize the adverse effect of vortex shedding from the slot lip. A total of three different TE configurations was tested, as shown in Fig. 6: (1) staggered ar-

angement, (2) inline arrangement of the chordwise rib separators with respect to the jet holes on the second blockage insert, and (3) staggered arrangement for Design 2.

Measurement Theory and Data Analysis

Seventeen T-type thermocouples were also instrumented to measure the coolant temperature in the test section. The thermocouple locations in Design 1 and Design 2 test models are shown as dark dots in Fig. 2. Five thermocouples were instrumented in each chamber downstream of each hole in the blockage insert for the internal cooling case and two thermocouples were instrumented at the slot exit for the film-cooling case. The thermocouple readings were measured by a Fluke 2285B Data Logger. Pressure taps located on the TE model at the same locations as internal thermocouples were used to record the static pressure distribution using a micromanometer. Pressure measurements were expressed as the pressure coefficient calculated as

$$C_p = \frac{P_s - P_\infty}{0.5\rho V_c^2} \quad (1)$$

The pressure coefficient C_p was obtained from the static pressure difference from each tap, P_s and atmosphere, P_∞ and the average slot exit velocity, V_c . Average pressure coefficients for each chamber were obtained by averaging five static pressure readings per chamber. At a given Reynolds number, a higher pressure coefficient indicates a higher static pressure.

Internal Heat Transfer Measurement. The liquid crystal thermography technique was utilized to obtain detailed local heat transfer coefficients for internal heat transfer enhancement from the blockage inserts and film-cooling effectiveness and heat transfer coefficients on the cutback TE. Internal heat transfer tests were performed for Reynolds numbers of 5000, 10,000, 20,000, and 30,000 based on slot exit dimensions for both test models. The test surfaces were prepared by first coating them with a layer of non-

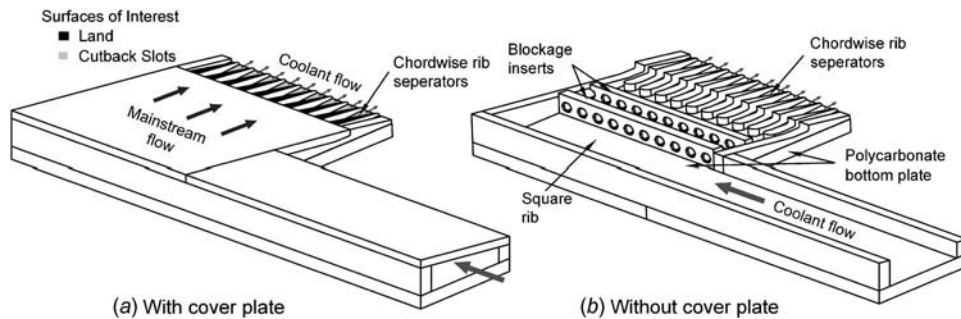


Fig. 5 Three-dimensional, isometric view of Design 1 with a straight inlet and staggered rib separator configuration

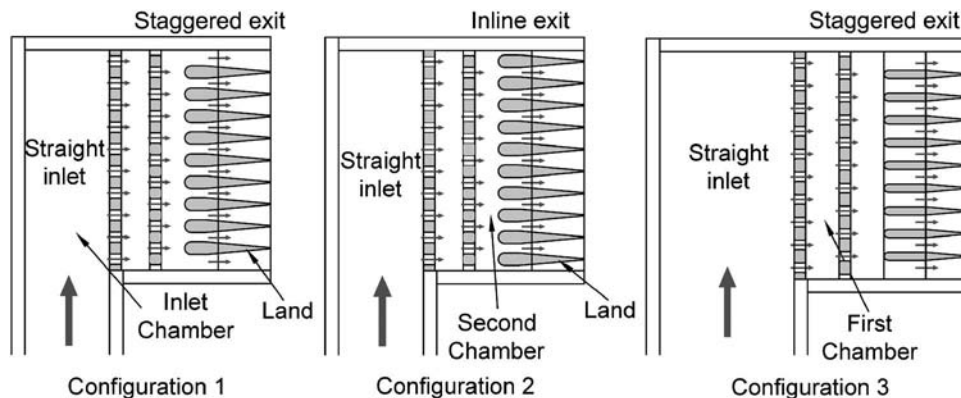


Fig. 6 Test configuration matrix

reflective black paint. Liquid crystal paint was then sprayed on the test surface using an airbrush. Two different liquid crystals were used to determine the internal heat transfer coefficients since the heat transfer coefficients in the inlet chamber were much lower than those in the other chambers. R34C20W was used in the inlet chamber while R29C4W was used in the first and second chambers. Both liquid crystal paints were calibrated for hue on a test piece fitted with a heater on its underside for several incremental temperatures under the same optical conditions used during the experiments. Internal heat transfer measurements were performed on one wall of the test section. A transient hue detection technique was used, based on the principle of a semi-infinite solid. The coolant air was passed through a pipe heater as shown in Fig. 3 and was heated until about 38°C. Before testing was begun, the coolant air was made to bypass the test section through a bypass valve. Freestream flow in the wind tunnel was turned off for internal heat transfer experiments. The test surface was made from polycarbonate (1.27 cm thick), which has a thermal conductivity and diffusivity of 0.1812 W/mK and $1.073 \times 10^{-7} \text{ m}^2/\text{s}$, respectively. These low property magnitudes and the relatively large thickness of the polycarbonate sheet enabled the use of the semi-infinite solid assumption over the short duration of the experiment. For a one-dimensional semi-infinite solid, the 1D transient conduction, equation, the initial condition, and the boundary condition are

$$k \frac{\partial^2 T}{\partial x^2} = \rho c_p \frac{\partial T}{\partial t} \quad (2)$$

at

$$t = 0 \quad T = T_i$$

at

$$x = 0 \quad -k \frac{\partial T}{\partial X} = h(T_w - T_c) \quad \text{as } x \rightarrow \infty \quad T = T_i$$

The solution to Eq. (2) at the convective boundary surface ($x = 0$) is the following:

$$\frac{T_w - T_i}{T_c - T_i} = 1 - \exp\left(\frac{h^2 \alpha t}{k^2}\right) \operatorname{erfc}\left(\frac{h\sqrt{\alpha t}}{k}\right) \quad (3)$$

By measuring the initial temperature (T_i) of the surface, the coolant temperature (T_c), the color change wall temperature (T_w), and the color change time (t), the local internal heat transfer coefficient (h) can be calculated from Eq. (3). The initial temperature of the test surface was around ambient temperature and was recorded before each experiment began. During the experiment, the hot coolant was made to flow through the test section causing the liquid crystal coated test surface to heat up and change color with time. Images of this color change on the test surface were recorded using a charge coupled device (CCD) camera for the entire duration of the experiment, which was about 200 s. Image acquisition was stopped when the upper band limit of the liquid crystal paint was crossed. A computer program analyzed the captured images and recorded the time required for the hue value to reach 50 at each pixel location. The coolant temperature was found to decrease continuously during the experiment as the coolant air convected heat to the test section. Thermocouples located in each chamber tracked the coolant temperature change with time. The temperature difference in the spanwise direction was less than 2.2°C in the inlet chamber and was 1.7°C in the first and second chambers. The average coolant temperature from the five thermocouples in each chamber was calculated and was used as the reference temperature to calculate the heat transfer coefficient in each chamber. Equation (3) was corrected for this changing average coolant temperature by applying Duhamel's superposition theorem (Kwak and Han [34]), which can be written as

$$T_w - T_i = (T_{c,0} - T_1) F\left(\frac{h\sqrt{\alpha t}}{k}\right) + \sum_{i=1}^n \left\{ F\left[\frac{h\sqrt{\alpha(t - \tau_i)}}{k}\right] \Delta T_{c,i} \right\} \quad (4)$$

where $F(x) = 1 - \exp(x^2) \operatorname{erfc}(x)$ and ΔT_c is the step change in the coolant temperature with τ_i . A computer program converted the acquired data into the heat transfer coefficient for each pixel using the above equation.

Film Cooling and Heat Transfer Measurement on Cutback Trailing Edge. A steady state hue detection technique was used for measuring film-cooling effectiveness while a transient technique similar to that used for measuring internal heat transfer was used to measure heat transfer on the cutback TE. R34C20W and R29C4W were used as the liquid crystal paint for the steady state and transient tests, respectively. Reynolds numbers of 5000, 10,000, 20,000, and 30,000 were tested by changing coolant air velocity. Corresponding velocity ratios ($M = V_c/V_m$) were 0.3, 0.61, 1.22, and 1.83 for Design 1 and 0.26, 0.52, 1.04, and 1.56 for Design 2, respectively. Two different experiments were run to obtain the film effectiveness (η) and the heat transfer coefficient (h). In the first experiment, to measure film effectiveness, the surface of the test model was not heated while the coolant air was heated (up to 38°C) by a pipe heater. This resulted in a coolant-to-mainstream density ratio of ~ 0.95 . Coolant temperature was monitored using two thermocouples placed at the location when the coolant exits on the cutback TE, as indicated in Fig. 2. After starting the wind tunnel and the hot coolant flow, when the test surface reached a steady state (unchanging color), the camera captured images of the test surface. The film temperature (T_f) in Eq. (5) was replaced by the adiabatic wall temperature (T_{aw}), which was determined by the hue (color) of the liquid crystal and from the calibration curve and the adiabatic film effectiveness (η) was calculated.

$$\eta = \frac{T_f - T_m}{T_c - T_m} = \frac{T_{aw} - T_m}{T_c - T_m} \quad (5)$$

In the second experiment, for measuring heat transfer on the cutback TE, a transient test was performed. The test surface was heated using a detachable heater while the coolant was not heated. Before initializing the experiment, the test surface was heated uniformly using a removable heater. The initial temperature distribution was recorded using a wide band liquid crystal, R34C20W. Upon recording the initial temperature distribution, this wide band liquid crystal paint was removed from the test surface, which was then resprayed with R29C4W before the experiment. The test surface was then heated until the reference temperatures became the same as those of the initial temperature measurement test (43°C) and then the heater was removed. Reference temperatures were measured by two thermocouples located close to the slot exit (Fig. 2) to ensure the same initial temperature conditions for each test. The wind tunnel and unheated coolant flow through the test section were started and an image acquisition system involving a camera was triggered simultaneously. Images of the test surface were captured until the test surface temperature fell below the lower band limit of the liquid crystal paint. The total duration of the experiment was about 200 s. Data analysis was performed by replacing the coolant temperature T_c in Eqs. (3) and (4) by the freestream temperature (T_m) on the lands and coolant temperature (T_c) on the cutback slots. The temperature difference between freestream and coolant was less than 2°C. Using the images captured from the camera, Eq. (4), modified with the appropriate regional air temperature (T_m or T_c), was solved at each pixel to obtain the detailed external heat transfer coefficient distributions.

Uncertainty calculations were performed based on a confidence level of 95% and are based on the uncertainty analysis method of

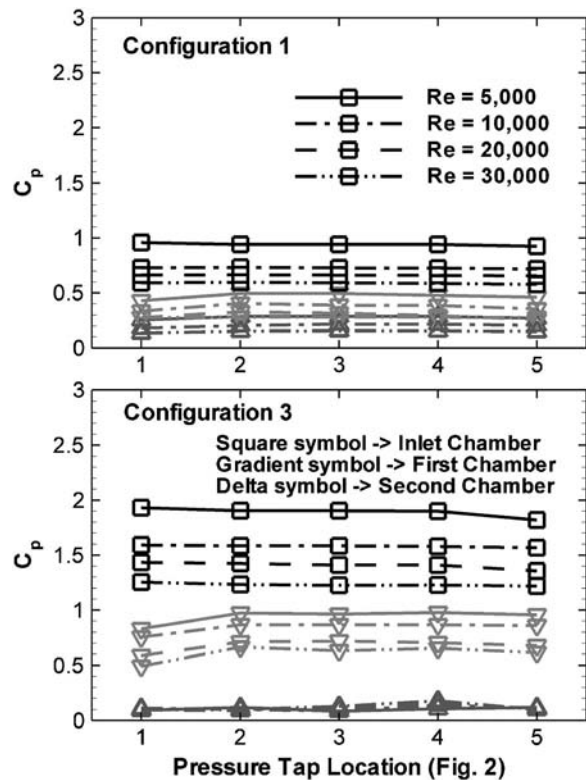


Fig. 7 Spanwise pressure coefficient distribution for Configurations 1 and 3

Coleman and Steele [35]. Highest relative uncertainties were observed for the lowest Reynolds numbers. Errors in velocity measurement were as high as $\pm 10.2\%$ for $Re=5000$ going down to $\pm 1.8\%$ for $Re=30,000$. Similarly, relative uncertainties for pressure coefficients were as high as $\pm 13.8\%$ for $Re=5000$ going down to $\pm 2\%$ for $Re=30,000$. For the four Reynolds numbers tested in this study, the maximum relative uncertainty for the averaged internal as well as external heat transfer coefficients occurring at $Re=5000$ was $\pm 8.23\%$. The individual uncertainties in the measurement of the time of color change ($\Delta t = \pm 0.5$ s), the mainstream temperature ($\Delta T_m = \pm 1^\circ C$), the color change temperature ($\Delta T_w = \pm 0.2^\circ C$), and the wall material properties ($\Delta \alpha/k^2 = \pm 5\%$) were included in the calculation of relative uncertainty for the average heat transfer coefficient. Due to the transient nature of the experiment, uncertainty due to heat loss from the underside of the Plexiglas test wall is small as the thickness of the Plexiglas substrate (1.27 cm) is sufficient for the assumption of a semi-infinite solid. Heat losses are estimated to be less than 2% in the duration of the experiment. It should be noted that lateral heat conduction may occur in the Plexiglas wall within the short duration of the experiment. This is especially true near sharp edges formed by the interfaces between the blockage inserts and test wall for internal flow and slot and lands for external flow. At these locations, the semi-infinite solid assumption may no longer be valid resulting in large uncertainties in the data close to these edges. However, the data presented in these regions provide an idea of the data range even though the quantitative results might be off by a larger percentage. Hence, caution should be exercised before directly applying the data on the land surfaces.

Highest uncertainty for the film-cooling effectiveness results was $\pm 9.8\%$ occurring for the lowest blowing ratio/Reynolds number. Fiber-glass insulation was used on the underside of the slot wall to prevent heat loss. However, due to the steady state nature of the experiment, significant lateral heat conduction may also occur within the three-dimensional surface geometries on the slot

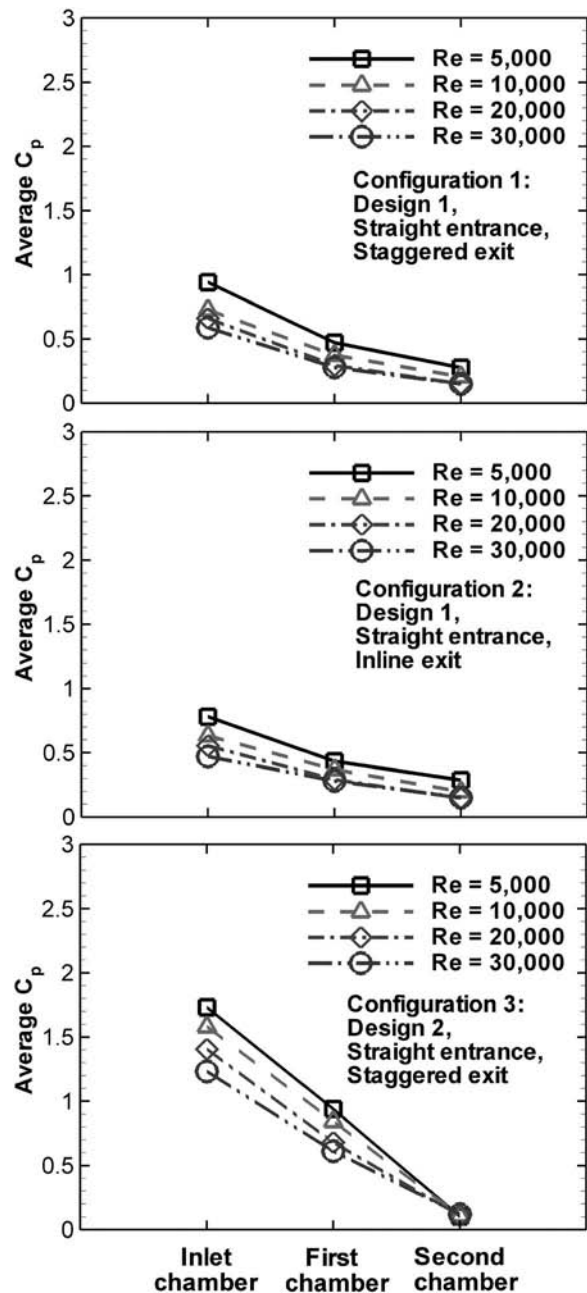


Fig. 8 Effect of Reynolds number chamberwise averaged pressure coefficient distribution for all configurations

surface as noted earlier, resulting in a biased adiabatic temperature near these sharp edges. This is especially true for data presented on the land surfaces where errors due to heat conduction are large.

Internal Cooling Trailing Edge Model

Pressure Coefficients. The static pressure was measured using a micromanometer at five locations in each chamber. The resulting plots of the spanwise variation in pressure coefficient for each chamber are plotted in Fig. 7 for configurations 1 and 3. The pressure coefficient increases with decreasing Reynolds number at given chamber due to lower slot exit velocity at lower Reynolds number. The nearly constant spanwise pressure distribution indicates that the static pressure variation in the chamber is very small as compared to the static pressure drop through the blockage inserts. Pressure coefficient though is higher near the entrance of the test section in the inlet chamber (at Point 1) and decreases along

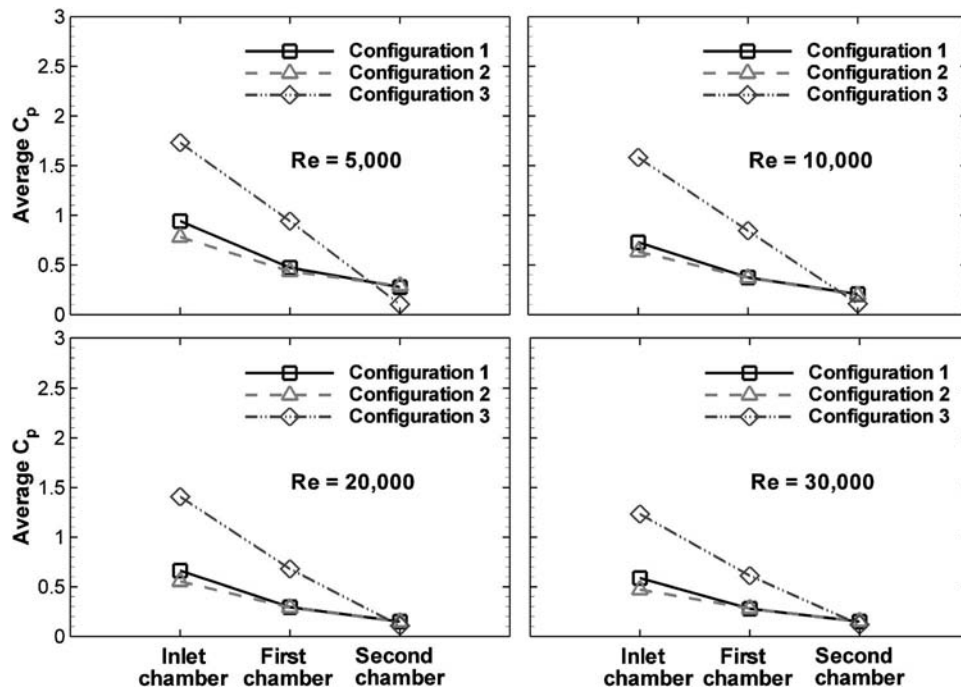


Fig. 9 Effect of configuration on chamberwise averaged pressure coefficients

the span. On the other hand, the pressure coefficient in the first chamber shows a slightly increasing trend from Point 1 to Point 5. This causes higher mass flow through the first blockage insert holes close to the 90 deg bend entrance due to a larger pressure drop across them. The mass flow in the inlet chamber gets depleted due to coolant ejection as it flows along the inlet chamber's span. This causes the static pressure to reduce, resulting in lower mass flow through holes near the end of the inlet chamber.

The effect of Reynolds number on the chamberwise averaged pressure coefficient distribution for all configurations is shown in Fig. 8. The average pressure coefficient is higher for the inlet chamber than the other chambers. The streamwise reduction in the average pressure coefficient magnitudes is mainly due to the static pressure loss as the coolant flows through the perforated blockage inserts. The second chamber shows the lowest pressure coefficient due to lowest static pressure. Chamberwise averaged pressure coefficients for all configurations have been compared in Fig. 9. For Design 1, a staggered exit gives a 20% higher pressure coefficient in the inlet chamber as compared to an inline exit with the static pressures in the second chamber remaining the same and the first chamber falling almost linearly in-between them. Design 2, which has a larger coolant blockage area ratio due to a much larger flow cross-sectional area, shows much higher average pressure coefficient magnitudes. The average pressure coefficient for the inlet and first chamber is about two times higher than Design 1 for the straight inlet and staggered exit configurations. The exit average pressure coefficients for Design 2 (second chamber) though are lower than Design 1 due to wider slots in Design 2, which provide a smaller flow resistance for coolant flow.

Local Heat Transfer Distribution. The internal local heat transfer coefficient distributions for Configurations 1 and 3 are shown in Figs. 10 and 11, respectively, for four different Reynolds numbers. Contour plots for Configuration 2 are not presented due to space limitations. Arrows indicate coolant flow direction and ejection hole location in the blockage insert. Higher heat transfer coefficients are desirable in the internal model to counter heat flux entering the blade from the hot mainstream in a gas turbine. The local heat transfer coefficient increases with increasing Reynolds number. For a given Re, heat transfer coefficients decrease along

the spanwise flow direction in the inlet chamber. As flow ejects through the blockage inserts, the mass flow and hence the local Re reduce in the spanwise flow direction in the inlet chamber, causing this observed reduction in heat transfer coefficients. This also results in a nonuniform flow distribution through the holes in first blockage insert as the flow distribution depends on the spanwise static pressure distribution in the inlet and the first chamber shown in Fig. 7. The mass flow through the blockage insert holes is higher closer to the 90 deg bend entrance of the inlet chamber.

High local heat transfer coefficients can be observed in the first and second chambers when the coolant jet ejected through the insert holes reattaches on the side surface. The peak heat transfer coefficient from this lateral impingement depends on the local hole mass flow and is higher close to the inlet chamber 90 deg bend entrance. The holes in the second blockage insert are staggered with respect to the first insert. A second high heat transfer coefficient spot in the first chamber can be discerned just downstream of the reattachment region near the second blockage insert. This may occur due to stagnation from jet impingement on the second blockage insert wall. Local heat transfer from stagnation near the second blockage is about 10% higher than at flow attachment points. Higher Reynolds numbers show more noticeable reattachment and stagnation points. Also, the peak heat transfer coefficients are higher in the first chamber as compared to the second. The second chamber has a smaller chamber height than the first chamber due to the tapered bounding walls of the model. Thus, the reattachment height for the jets through the second insert is smaller, which may explain the reduction in the peak heat transfer coefficients in the second chamber.

Contour plots for Configuration 3, as shown in Fig. 11, also show local heat transfer coefficient distributions in the slot passages formed by the chordwise rib separators before they exit on the cutback trailing edge. Reattachment in the first chamber occurs further downstream in Design 2 as compared to Design 1 due to a larger step between the hole center and test surface in Design 2. Thus, the ejecting jet from the first insert travels a longer distance before reattachment as compared to Design 1. The stagnation and reattachment region overlap causing very high heat transfer just upstream of the second blockage insert. The larger step

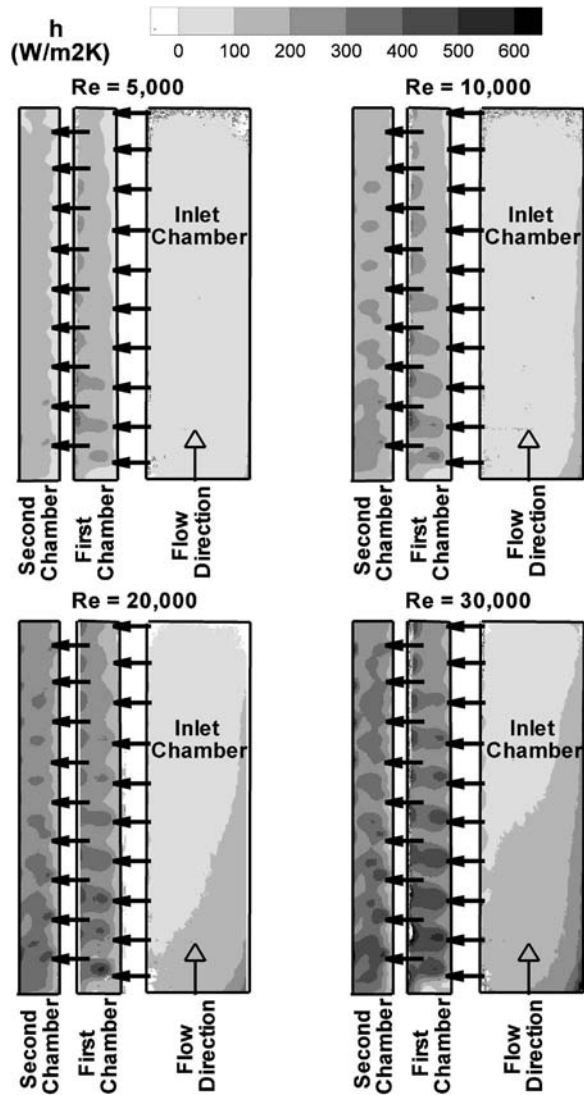


Fig. 10 Internal heat transfer coefficients for Design 1 with a straight inlet and staggered slot arrangement (Configuration 1)

also results in a larger recirculation zone, which might explain the lower heat transfer coefficients observed immediately downstream of the first insert in the first chamber as compared to Design 1. The second chamber shows lower but more uniform heat transfer coefficients similar to that observed for Configuration 1. Similar trends were also observed by Lau et al. [16] using the naphthalene sublimation technique for both Design 1 and Design 2. However, the local heat transfer coefficients observed by them are about 10% higher than the present study.

Spanwise Average Heat Transfer. The streamwise Nusselt number distributions, based on spanwise average, are shown in Fig. 12 for all three different configurations. The averaged Nusselt numbers are presented as a function of the normalized distance (x/Dh) from inlet chamber. For Design 1, the spanwise average heat transfer decreases with an increase in the normalized distance (x/Dh) in the inlet chamber. In the first chamber, the heat transfer coefficient is low immediately downstream of the first blockage, which may be due to the presence of a slow moving recirculation zone and then shows a sharp increase at the reattachment point of the ejecting jet. Stagnation due to jet impingement on the second blockage further enhances heat transfer. The jet reattachment point can also be clearly observed in the second chamber. The heat transfer distribution in the inlet chamber for the inline exit slot

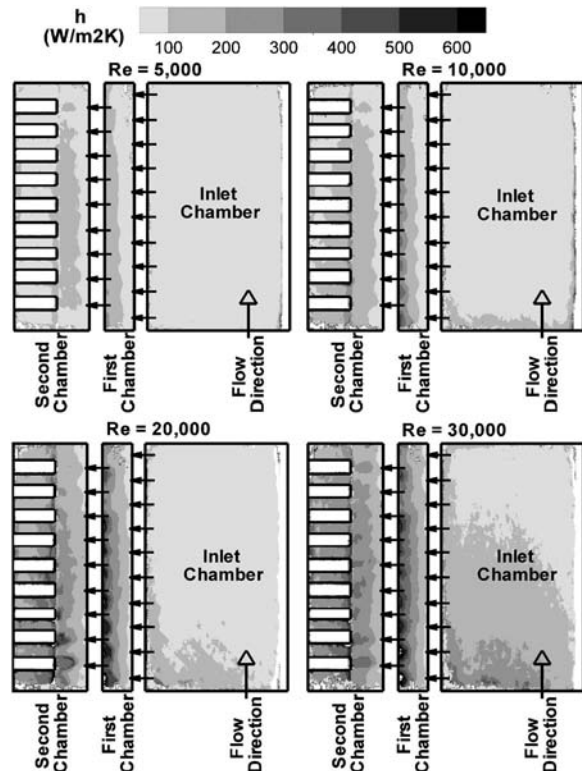


Fig. 11 Internal heat transfer coefficients for Design 2 with a straight inlet and staggered slot arrangement (Configuration 3)

(Configuration 2) is similar to that for the staggered exit slot arrangement (Configuration 1) for Design 1. Thus, the slot alignment near the exit of the model does not affect the upstream inlet chamber heat transfer distribution. On the other hand, high Nusselt numbers can be observed in the first chamber for Configuration 2 at higher Reynolds numbers. The Nusselt number distribution in the second chamber for Configuration 1 is also very similar to that for the staggered slot arrangement in Configuration 1.

Design 2 shows a different distribution as compared to Design 1. Heat transfer coefficients show a slightly increasing trend in the inlet chamber. In the first chamber, the heat transfer coefficients increase sharply until the second insert wall where stagnation occurs. In the second chamber, heat transfer coefficients increase until the reattachment point, then decrease and further downstream. Figure 13 shows the chamberwise averaged Nusselt number plotted versus Reynolds number. The Nusselt numbers are found to steadily increase with Reynolds number as expected. Design 1 with inline slot arrangement, in general, gives slightly higher average heat transfer than the other configurations. The inlet chamber shows the lowest heat transfer for both designs with the first chamber showing the best. Best heat transfer characteristics for the first chamber can be observed for Design 1 with an inline exit (Configuration 2) while for the second chamber, Configurations 1 and 2 show highest heat transfer.

External Cutback Trailing Edge Model

Local Heat Transfer Distribution. Figure 14 shows the Stanton number ($St = h / \rho C V_m$) distributions for Configurations 1 and 3 for four different blowing ratios as well as for no coolant flow. Stanton number distributions are presented on the land formed by the rib separators, which was calculated from the freestream temperature (T_m), and on the cutback slots, which was calculated from the coolant temperature (T_c). It should be noted that a high Stanton number resulting from coolant flow on the cutback slot region is desirable, whereas on the lands, a higher Stanton number

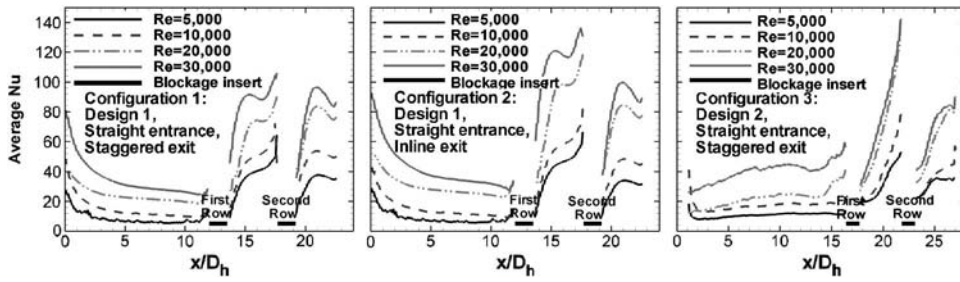


Fig. 12 Spanwise averaged internal Nusselt numbers for all configurations

is detrimental to the TE design as it represents heat flux entering the blade through the hot freestream in a gas turbine. In the contour plots, a white region, near the slot exit for $M=0$, indicates no data due to time limits for validity of 1D assumption on the transient liquid crystal technique. A relatively symmetric distribution in Stanton numbers can be observed in the spanwise direction for all cases. Generally, Stanton number increases with increasing Reynolds number on the cutback slot except for $M=0$. Stanton numbers for the highest blowing ratio are about two to three times higher than those for the lowest blowing ratio depending on the test configuration. Under no coolant flow conditions ($M=0$), the Stanton number is very low, close to the slot exit on the cutback region due to flow recirculation and then increases sharply as the freestream reattaches on the cutback slot. This flow reattachment region, however, gets disturbed by coolant ejection through the slot resulting in lower Stanton numbers for low blowing ratios ($M < 1$). Stanton numbers on the cutback slot with coolant flow are highest close to the slot exit and decrease slightly further downstream due to boundary layer growth on the slot surface. For low blowing ratios ($M < 1$), the coolant flow is dominant on the slot while the freestream flow is dominant on the land. However, for higher blowing ratios ($M > 1$), the coolant also effects the land. Higher Stanton numbers can be observed near the tip of the land for Design 1, which may be due to coolant mixing with the freestream. On the other hand, a shorter and sloped land in Design 2 shows smaller enhancement in Stanton numbers on the land.

Spanwise Average Heat Transfer. Similar observations can be made from spanwise averaged Stanton numbers plotted as a function of x/Ms , where s is the slot height, as shown in Fig. 15 for all configurations. Spanwise averaged data for the center five lands and five slots are presented for the cutback slot as well as the lands for all three configurations. A steady increase in heat transfer on the cutback slots can also be observed with increasing blowing ratio for all configurations shown. It can also be noted that the rate of increase in Stanton number on the cutback slot region with increasing blowing ratio is higher than that for the lands. For the lowest blowing ratio, lands show higher heat transfer but for the largest blowing ratio, the cutback slots show higher heat transfer. Heat transfer magnitudes on the lands for Configurations 1 and 2, close to the slot exit (at low x/Ms) for all coolant blowing ratios, are similar. As the streamwise distance increases, the trends diverge, indicating that coolant mixing with the freestream provides higher heat transfer on the lands with increasing blowing ratio similar to the phenomenon observed from the contour plots in Fig. 14. On the other hand, for Configuration 3, the land region is uniformly affected by blowing ratio almost over its entire length.

$$St = 0.0287 Re_x^{-0.2} Pr^{-0.4} M \quad (6)$$

The spanwise averaged data for the cutback slots have been compared to a correlation for turbulent flow over a flat plate given by Eq. (6) (Martini et al. [7]). The Reynolds number for the cool-

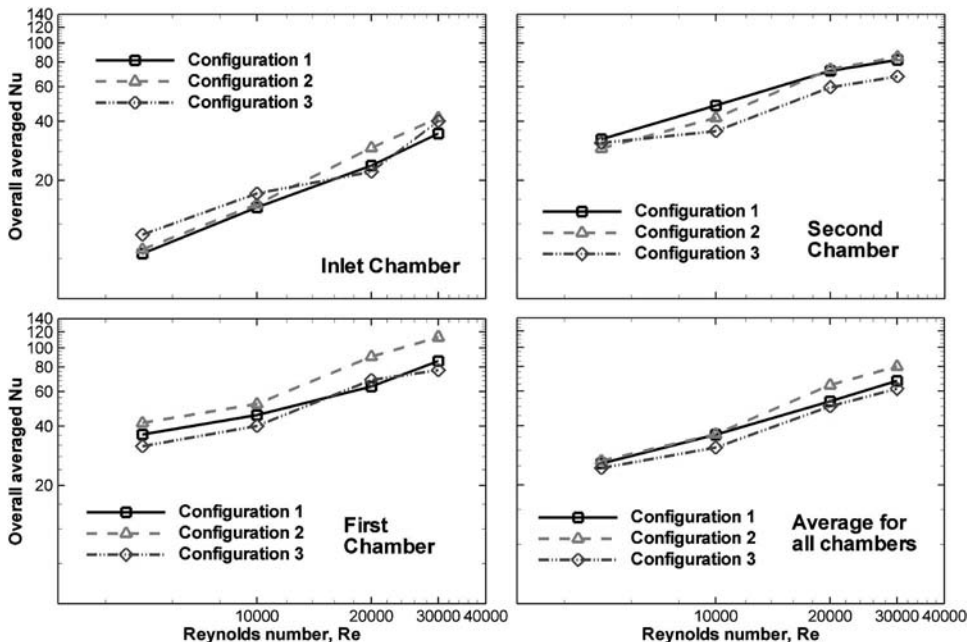


Fig. 13 Effect of configuration on chamberwise averaged internal Nusselt numbers

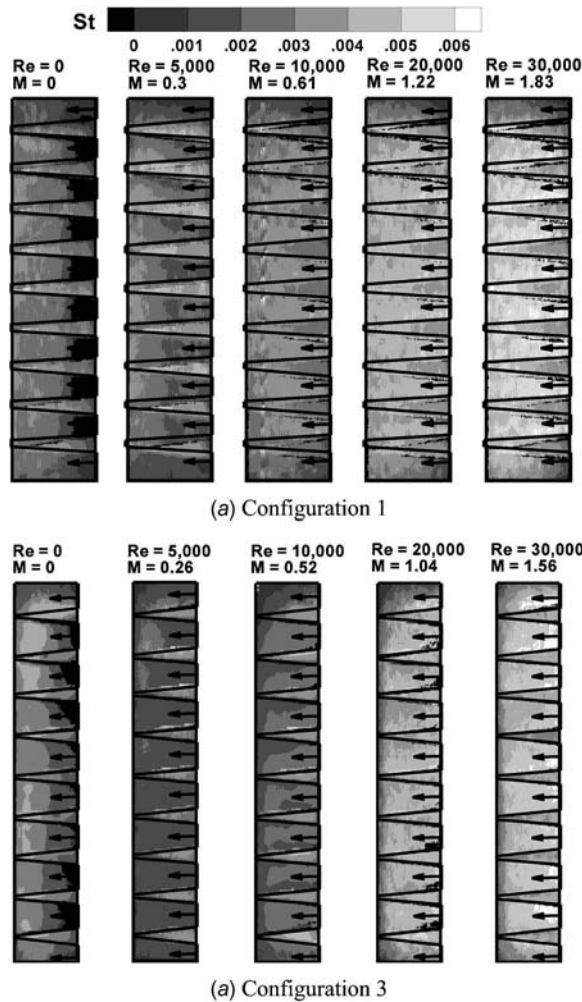


Fig. 14 Local Stanton number distribution on cutback slots and lands for Designs 1 and 2

ant air is based on the streamwise distance measured starting from the leading edge of the chordwise rib separators. This location was chosen to account for the finite thickness of the boundary layer when the coolant exits onto the cutback surface. Excellent comparison is obtained between the Stanton number distributions and Eq. (6) for Design 2 for the cutback slot. However, the correlation fails to accurately estimate the heat transfer for Design 1. Larger mainstream flow interaction with the coolant flow for Design 1 as well as larger boundary layer thickness due to loss in coolant momentum from the expanding slot channel may contribute to this effect.

Figure 16 compares the overall averaged Stanton number distributions for all configurations for the lands, cutback slots, and for both lands and slots. Heat transfer on the lands for Configurations 1 and 2 is similar. This indicates that internal geometry changes for the design Model 1 do not affect heat transfer on the lands but can significantly increase or decrease heat transfer on the slots. For Design 1, a staggered exit gives higher Stanton numbers on the cutback slot as compared to an inline exit. As the coolant wraps around rib separators after impinging on them, additional unsteady effects due to formation of corner vortices along the edges of the rib separators may disturb the coolant flow, thereby promoting higher heat transfer as it exits the slot. Overall, heat transfer on the lands and cutback slot regions is slightly lower for Design 2, which may be attributed to the small incline

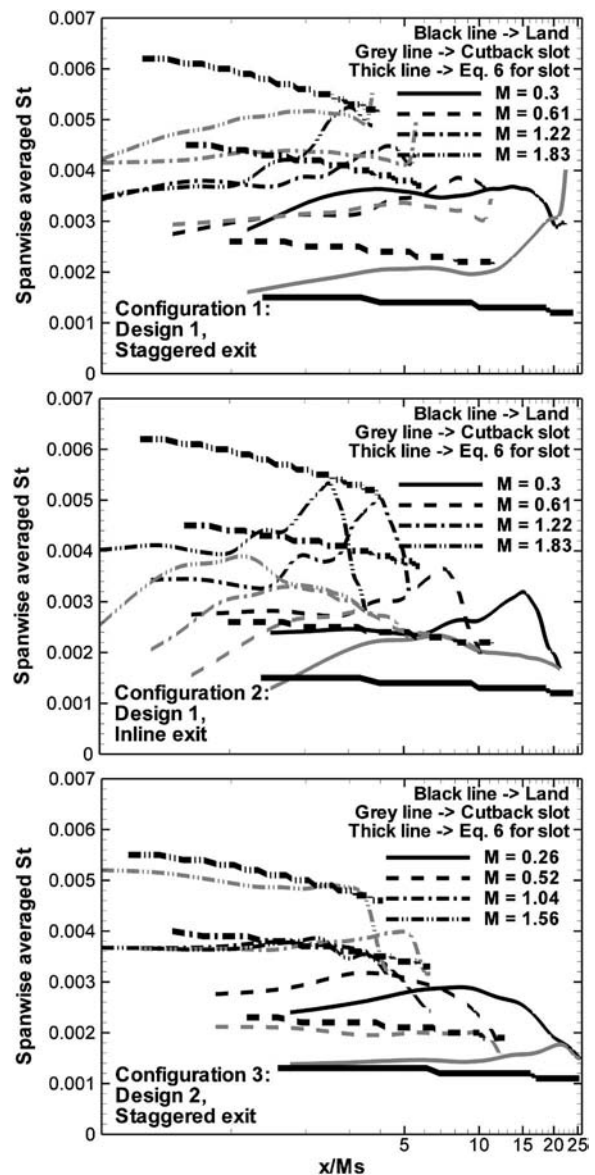


Fig. 15 Spanwise averaged distributions of Stanton number on the cutback slots and lands for all configurations

provided for the land surface and the shorter cutback length while Configuration 1 shows highest heat transfer for lands and slots combined.

Local Film-Cooling Effectiveness Distribution. Figure 17 shows the film-cooling effectiveness distributions on the cutback slots and lands for all four blowing ratios and for Configurations 1 and 3. The film-cooling effectiveness distribution is spanwise symmetric, similar to that observed for the Stanton number distributions. A higher effectiveness on the lands and cutback slots prevents contact between the hot freestream and the blade in a gas turbine and hence is advantageous. Effectiveness on the cutback region is very high as the coolant exits the slot. The effectiveness magnitudes close to the slot exit are equal to 1, suggesting that the freestream is not able to mix with the coolant in this region. The high effectiveness magnitudes observed for both designs in the near slot region are comparable to those observed by Martini et al. [7]. Effectiveness levels in their research paper were found to decrease by only $\sim 10\%$ to about 0.9 at $x/s \sim 6$ similar to that observed in the present study. It should be noted that both designs

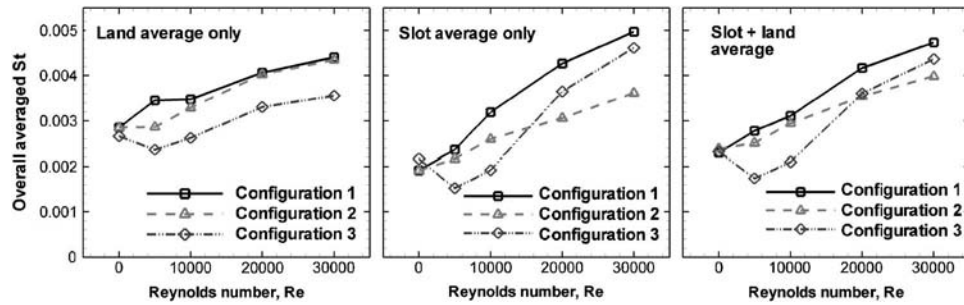


Fig. 16 Effect of configuration on overall averaged Stanton number distributions

in the present study have a smaller streamwise cutback length to slot height ratio ($L/s=9.2$ for Design 1 and $L/s=7.2$ for Design 2) than Martini et al. [6]. Computational fluid dynamics (CFD) studies by Chen et al. [17] also showed very high effectiveness in the

cutback slots with almost no heat flux across the slots for $M > 1.3$.

For lower blowing ratios ($M < 1$), the effectiveness diminishes rapidly close to the end of the cutback model. Vortex shedding from the lip formed due to the cover plate thickness may interact with the coolant resulting in strong mixing near the edge of the cutback region causing this dramatic reduction in effectiveness. Similar phenomenon has been observed by Telisinghe et al. [3] and Martini and Schulz [6]. Another reason for this drop could be due to lower coolant momentum as a result of slot expansion on the cutback surface, which makes the coolant flow more susceptible to this vortex shedding. The present study though shows that overall effectiveness decreases with increasing blowing ratio as compared to Martini and Schulz [6] who show higher effectiveness with increasing blowing ratio. This may be attributed to a higher coolant-to-mainstream density ratio used by them as well as due to differences in the geometries between the two tests. The density ratio arises due to the difference in temperatures of the coolant and mainstream and is ~ 0.95 in the present study compared to 1.6 on Martini and Schulz [6]. Film-cooling effectiveness decreases in the streamwise direction on the cutback slot with increasing blowing ratio as a higher momentum jet will tend to lift off and mix with the freestream directly. Design 2 shows a lower degradation in effectiveness with increasing blowing ratio, which may be due to the shorter cutback length as compared to Design 1. The shorter cutback length helps to minimize film degradation from vortex shedding from the lip. The sloped land used in Design 2 also results in more mixing of the coolant and freestream resulting in higher effectiveness on the lands in Design 2, particularly near the end of the cutback region. It should be noted that the effectiveness magnitudes on the land surfaces may be influenced by heat conduction related errors due to the three-dimensional nature of the test geometry resulting in larger than expected values on the lands.

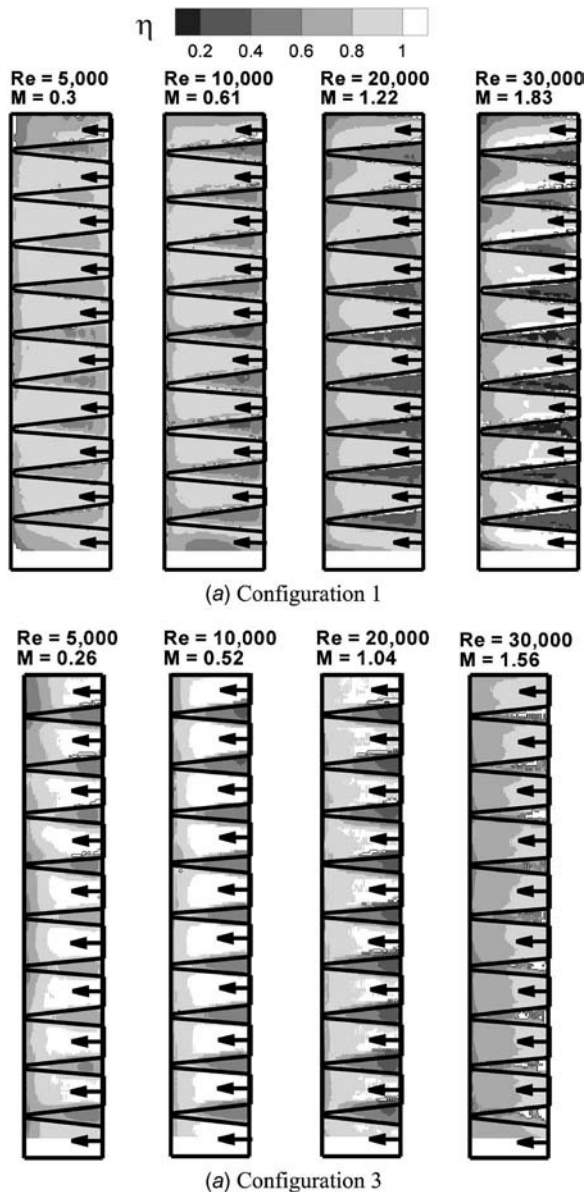


Fig. 17 Local film-cooling effectiveness distribution on cutback slots and lands for Designs 1 and 2

Spanwise Average Film-Cooling Effectiveness. These trends can be clearly confirmed from the spanwise averaged effectiveness plots shown in Fig. 18. The effectiveness is spanwise averaged for five center cutback slots and lands. Data are shown on the lands and slots. The present data have been compared with a correlation for tangential slot film cooling given by Mukherjee [36] on a flat plate with no pressure gradient. Relatively good comparison is obtained for low blowing ratios. However, at higher blowing ratios, the effectiveness magnitudes are much lower than those predicted by the correlation. As the coolant exits the slot, high effectiveness on the cutback region and low effectiveness on the lands can be observed. The trends for effectiveness on the lands and slots appear to converge near the end of the cutback region. Film-cooling effectiveness on the land shows an increasing trend with streamwise distance as more coolant gets entrained onto its surface and then starts decreasing sharply after reaching a peak. The drop in effectiveness on the cutback slot region begins at almost the same location as the drop occurring on the land. The vortex shedding from the lip may contribute to this concurrent

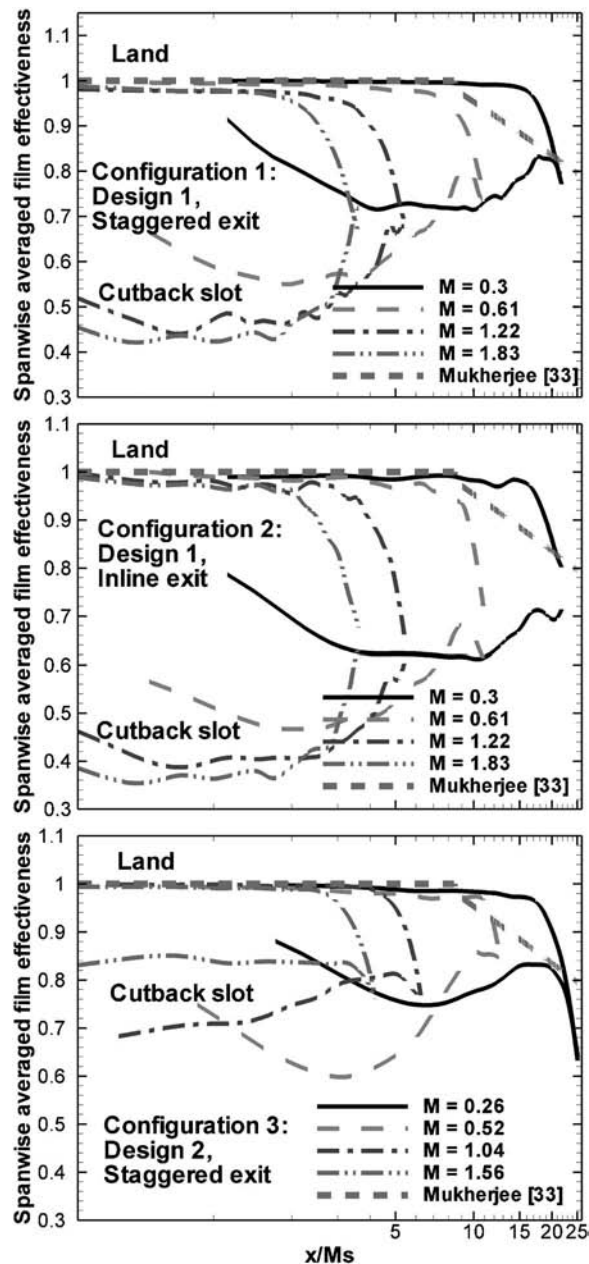


Fig. 18 Spanwise averaged film-cooling effectiveness distributions for the cutback slots, lands, and land and slot combined for all configurations

drop in effectiveness. Figure 19 shows a comparison between overall averaged film cooling effectiveness on the cutback TE including the slots and lands for all configurations. Design 2, in general, shows higher effectiveness magnitudes as compared to Design 1 for the cutback slots as well as lands. The inline slot arrangement used in Configuration 2 gives the lowest average film cooling effectiveness.

Conclusions

The influence of Reynolds number, blowing ratio, and three different configurations on two typical cutback TE models on static pressure, heat transfer, and film cooling effectiveness was investigated experimentally in a low-speed wind tunnel. The three different configurations used were (1) staggered or (2) inline exit

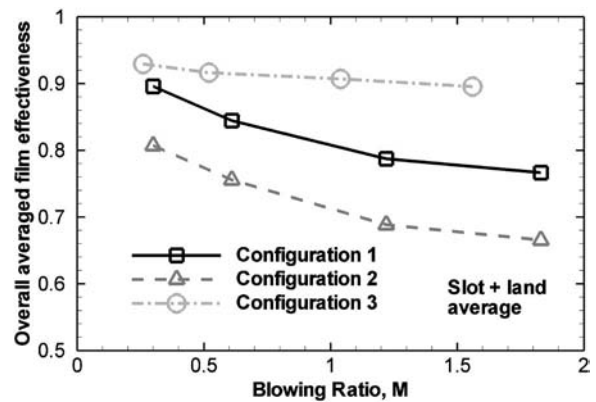


Fig. 19 Effect of configuration on overall averaged film-cooling effectiveness distributions on the cutback TE

alignment slot in Design 1 and (3) staggered slot arrangement in Design 2. The main conclusions inferred from this study are presented below.

1. Increasing Reynolds number decreases pressure coefficient for internal cooling. The effect of a staggered or inline slot exit arrangement on the pressure coefficient is relatively small as compared to the pressure loss through the blockage inserts. Higher pressure loss occurs in design Model 2 as compared to design Model 1. Configuration 1 with an inline exit shows the lowest overall pressure drop.
2. Increasing Reynolds number increases heat transfer in the internal cooling model. Lateral impingement from perforated blockage inserts substantially increases internal heat transfer on the model walls but also increases pressure loss significantly.
3. Design 1 shows higher averaged internal heat transfer coefficients as compared to Design 2.
4. Increasing blowing ratio enhances heat transfer and decreases film effectiveness for external cooling on the cutback slots and lands.
5. A sloped land results in lower heat transfer on the land surface as compared to a streamlined land used in Design 1. Also, on the cutback slot region, a staggered slot exit arrangement (Configuration 1) gives best heat transfer results.
6. Overall, Design 2 with a sloped land with a shorter cutback slot gives higher film effectiveness on the cutback slot and land as compared to a zero slope land and a longer cutback slot used in Design 1.

Acknowledgment

This work was prepared with the support of Siemens-Westinghouse Power Corporation.

Nomenclature

- C = specific heat of air (J/kg K)
- C_p = pressure coefficient ($= (P_s - P_{amb}) / 0.5 \rho V_c^2$)
- D_h = hydraulic diameter of slot (m)
- h = heat transfer coefficient ($W/m^2 K$)
- k = thermal conductivity (W/mK)
- L = cutback slot length in streamwise direction (m)
- M = average coolant-to-freestream blowing ratio ($= V_c / V_m$)
- P_∞ = atmospheric pressure during testing (Pa)
- P_s = static pressure in internal test model (Pa)
- Re = Reynolds number ($= \rho V_c D_h / \mu$)
- s = slot height (m)
- St = Stanton number ($= h / \rho C V_m$)
- t = color change time during experiment (s)

T_{aw} = adiabatic wall temperature ($^{\circ}\text{C}$)
 T_c = temperature of coolant at test section inlet ($^{\circ}\text{C}$)
 T_f = film temperature on film cooled surface ($^{\circ}\text{C}$)
 T_i = initial liquid crystal coated surface temperature ($^{\circ}\text{C}$)
 T_m = freestream temperature in the wind tunnel ($^{\circ}\text{C}$)
 T_w = test surface temperature during testing ($^{\circ}\text{C}$)
 TE = trailing edge of a blade
 x = streamwise distance (m)
 V_c = slot exit velocity (m/s)
 V_m = mainstream or freestream air velocity in wind tunnel (34 m/s)
 α = thermal diffusivity
 η = local film-cooling effectiveness
 ρ = density of coolant air at slot exit (kg/m^3)

References

- [1] Uzol, O., Camci, C., and Glezer, B., 2001, "Aerodynamic Loss Characteristics of a Turbine Blade With Trailing Edge Coolant Ejection: Part 1—Effect of Cut-Back Length, Spanwise Rib Spacing, Free-Stream Reynolds Number, and Chordwise Rib Length on Discharge Coefficients," *ASME J. Turbomach.*, **123**, pp. 238–248.
- [2] Uzol, O., and Camci, C., 2001, "Aerodynamic Loss Characteristics of a Turbine Blade With Trailing Edge Coolant Ejection: Part 2—External Aerodynamics, Total Pressure Losses, and Predictions," *ASME J. Turbomach.*, **123**, pp. 249–257.
- [3] Telisinghe, J. C., Ireland, P. T., Jones, T. V., Barrett, D., and Son, C., 2006, "Comparative Study Between a Cut-Back and Conventional Trailing Edge Film Cooling System," ASME Paper No. GT2006-91207.
- [4] Holloway, D. S., Leylek, J. H., and Buck, F. A., 2002, "Pressure Side Bleed Film Cooling: Part 1—Steady Framework for Experimental and Computational Results," ASME Paper No. GT-2002-30471.
- [5] Holloway, D. S., Leylek, J. H., and Buck, F. A., 2002, "Pressure Side Bleed Film Cooling: Part 2—Unsteady Framework for Experimental and Computational Results," ASME Paper No. GT-2002-30472.
- [6] Martini, P., and Schulz, A., 2004, "Experimental and Numerical Investigation of Trailing Edge Film Cooling by Circular Wall Jets Ejected From a Slot With Internal Rib Arrays," *ASME J. Turbomach.*, **126**, pp. 229–236.
- [7] Martini, P., Schulz, A., and Bauer, H.-J., 2006, "Film Cooling Effectiveness and Heat Transfer on the Trailing Edge Cut-back of Gas Turbine Airfoils With Various Internal Cooling Designs," *ASME J. Turbomach.*, **128**(1), pp. 196–205.
- [8] Martini, P., Schulz, A., Bauer, H.-J., and Whitney, C. F., 2006, "Detached Eddy Simulation of Film Cooling Performance on the Trailing Edge Cut-Back of Gas Turbine Airfoils," *ASME J. Turbomach.*, **128**(2), pp. 292–299.
- [9] Cunha, F. J., Dahmer, F. T., and Chyu, M. K., 2006, "Analysis of Airfoil Trailing Edge Heat Transfer and Its Significance in Thermal-Mechanical Design and Durability," *ASME J. Turbomach.*, **128**(4), pp. 738–746.
- [10] Chyu, M. K., Uysal, U., and Li, P.-W., 2002, "Convective Heat Transfer in a Triple-Cavity Structure Near Turbine Blade Trailing Edge," *Proceedings of IMECE'02*, International Mechanical Engineers Congress, New Orleans, Nov. 17–22.
- [11] Cakan, M., and Taslim, M. E., 2007, "Experimental and Numerical Study of Mass/Heat Transfer on an Airfoil Trailing-Edge Slots and Lands," *ASME J. Turbomach.*, **129**(2), pp. 281–293.
- [12] Lau, S. C., Han, J. C., and Batten, T., 1989, "Heat Transfer, Pressure Drop and Mass Flow Rate in Pin Fin Channels With Long and Short Trailing Edge Ejection Holes," *ASME J. Turbomach.*, **111**, pp. 116–122.
- [13] McMillin, R. D., and Lau, S. C., 1994, "Effect of Trailing Edge Ejection on Local Heat (Mass) Transfer in Pin Fin Cooling Channels in Turbine Blades," *ASME J. Turbomach.*, **116**, pp. 159–164.
- [14] Taslim, M. E., and Li, T., 1995, "Experimental Study of the Effects of Bleed Holes on Heat Transfer and Pressure Drop in Trapezoidal Passages With Tapered Turbulators," *ASME J. Turbomach.*, **117**(2), pp. 281–289.
- [15] Taslim, M. E., Li, T., and Spring, S. D., 1998, "Measurements of Heat Transfer Coefficients in Rib-Roughened Trailing-Edge Cavities With Crossover Jets," ASME Paper No. 98-GT-435.
- [16] Lau, S. C., Cervantes, J., Han, J. C., and Rudolph, R. J., "Internal Cooling near Trailing Edge of a Gas Turbine Airfoil With Cooling Airflow Through Blockages With Holes," ASME Paper No. GT2006-91230.
- [17] Chen, S. P., Li, P. W., Chyu, M. K., Cunha, F. J., and Abdel-Messeh, W., 2006, "Heat Transfer in an Airfoil Trailing Edge Configuration With Shaped Pedestals Mounted Internal Cooling Channel and Pressure Side Cutback," ASME Paper No. GT2006-91019.
- [18] Goldstein, R. J., 1971, "Film Cooling," *Advances in Heat Transfer*, Vol. 7, Academic, New York, pp. 321–379.
- [19] Wiegardt, K., 1946, "Hot-Air Discharge for De-Icing," A. A. F. Translation F-TS-919-RE.
- [20] Kacker, S. C., and Whitelaw, J. H., 1968, "The Effect of Slot Height and Slot Turbulence Intensity on the Effectiveness of the Uniform Density, Two Dimensional Wall Jet," *ASME J. Heat Transfer*, pp. 469–475.
- [21] Kacker, S. C., and Whitelaw, J. H., 1969, "An Experimental Investigation of the Influence of Slot-Lip-Thickness on the Impervious-Wall Effectiveness of the Uniform-Density, Two-Dimensional Wall Jet," *Int. J. Heat Mass Transfer*, **12**, pp. 1201–1206.
- [22] Papell, S. S., 1960, "Effect on Gaseous Film Cooling Injection Through Angled Slots and Normal Holes," NASA Report No. TN-D-299.
- [23] Rostogi, A. K., and Whitelaw, J. H., 1973, "The Effectiveness of Three-Dimensional Film Cooling Slots-I. Measurement," *Int. J. Heat Mass Transfer*, **16**, pp. 1665–1672.
- [24] Patankar, S. V., Rostogi, A. K., and Whitelaw, J. H., 1973, "The Effectiveness of Three-Dimensional Film Cooling Slots-II. Predictions," *Int. J. Heat Mass Transfer*, **16**, pp. 1679–1681.
- [25] Paxson, D. E., and Mayle, R. E., 1988, "The Influence of Main Stream Thermal Boundary Layer on Film Cooling Effectiveness," ASME Paper No. 88-GT-17.
- [26] Nina, M. N. R., and Whitelaw, J. H., 1971, "The Effectiveness of Film Cooling With Three Dimensional Slot Geometries," ASME Paper No. 71-GT-11.
- [27] Taslim, M. E., 1992, "Experimental Investigation of Film Cooling Effectiveness for Slots of Various Exit Geometries," *J. Thermophys. Heat Transfer*, **6**(2), pp. 302–307.
- [28] Sturgess, G. J., 1985, "Design of Combustor Cooling Slots for High Film Effectiveness: Part 1—Film General Development," ASME Paper No. 85-GT-35.
- [29] Sturgess, G. J., 1985, "Design of Combustor Cooling Slots for High Film Effectiveness: Part 2—Film Initial Development," ASME Paper No. 85-GT-36.
- [30] Moon, S. W., and Lau, S. C., 2002, "An Experimental Study of Local Heat Transfer Distribution Between Blockage With Holes in a Rectangular Channel," ASME Paper No. IMECE 2002-33673.
- [31] Lau, S. C., Cervantes, J., Han, J. C., Rudolph, R. J., and Flannery, K., 2003, "Measurement of Wall Heat (Mass) Transfer for Flow Through Blockage With Round and Square Holes in a Wide Rectangular Channel," *Int. J. Heat Mass Transfer*, **46**(21), pp. 3991–4001.
- [32] Han, J. C., Dutta, S., and Ekkad, S. V., 2000, *Gas Turbine Heat Transfer and Cooling Technology*, Taylor & Francis, New York.
- [33] Young, C. D., Han, J. C., Huang, Y., and Rivir, R. B., 1992, "Influence of Jet-Grid Turbulence on Flat Plate Turbulent Boundary Layer Flow and Heat Transfer," *ASME J. Heat Transfer*, **114**, pp. 65–72.
- [34] Kwak, J. S., and Han, J. C., 2003, "Heat Transfer Coefficients and Film Cooling Effectiveness on the Squealer Tip of a Gas Turbine Blade," *ASME J. Turbomach.*, **125**, pp. 648–657.
- [35] Coleman, H. W., and Steele, W. G., 1989, *Experimentation and Uncertainty Analysis for Engineers*, Wiley, New York.
- [36] Mukherjee, D. K., 1976, "Film Cooling With Injection Through Slots," *ASME J. Eng. Power*, **98**, pp. 556–559.

Heat Transfer in the Flow of a Cold, Axisymmetric Vertical Liquid Jet Against a Hot, Horizontal Plate

Jian-Jun Shu¹
Graham Wilks

School of Mechanical and Aerospace
Engineering,
Nanyang Technological University,
50 Nanyang Avenue,
Singapore 639798, Singapore

The paper considers heat transfer characteristics of thin film flow over a hot horizontal flat plate resulting from a cold vertical jet of liquid falling onto the surface. A numerical solution of high accuracy is obtained for large Reynolds numbers using the modified Keller box method. For the flat plate, solutions for axisymmetric jets are obtained. In a parallel approximation theory, an advanced polynomial approximation for the velocity and temperature distribution is employed and results are in good agreement with those obtained using a simple Pohlhausen polynomial and the numerical solutions.

[DOI: 10.1115/1.2780180]

Keywords: thin film flow, large Reynolds numbers, modified Keller box method

1 Introduction

As has been noted earlier, the draining flow of liquid under gravity through banks of horizontal tubes occurs frequently in technological processes involving heat or mass transfer. The mode of drainage may be in the form of droplets, columns, or continuous sheets. After having examined the sheet mode of drainage, it is natural to move on to a closer inspection of the columnar mode of drainage. Again, if the film thickness is small relative to a typical tube dimension, the impact surface may be regarded as locally plane [1]. Accordingly, an initial prototype model for columnar impingement is simply that of a vertical round jet striking a plane horizontal surface. The flow model is thus axisymmetric, and considerable simplification of the governing equations can be made. Some detailed understanding of the flow and heat transfer characteristics at the point of impingement may be obtained and possible methodologies identified for examining the nonaxisymmetric flow in due course.

Analytically, Watson [2] found a similarity solution of the boundary-layer equations governing such a flow and also considered by approximate methods the initial growth of the boundary layer from the stagnation point where the similarity solution does not hold. Chaudhury [3] obtained a supplementary thermal solution using an orthogonal polynomial. Some recent progress [1,4–9] has been made in investigating various problems of a liquid jet impinging on a solid surface. In this paper, the theoretical results are improved and an accurate numerical solution is obtained for the heat transfer in the flow of a cold, axisymmetric vertical liquid jet against a hot horizontal plate.

2 Modeling

The problem to be examined concerns film cooling, which occurs when a cold vertically draining column strikes a hot horizontal plate. Although a column of fluid draining under gravity is accelerated and thin at impact [10,11], it is reasonable to model the associated volume flow as a jet of uniform velocity U_0 and radius H_0 , as illustrated in Fig. 1(a). The notation $Q = \pi H_0^2 U_0$ is

introduced for the flow rate and a film Reynolds number may be defined as $Re = U_0 H_0 / \nu$, where ν is the kinematic viscosity of the fluid. The underlying hydrodynamics of the fluid flow have been delineated by Watson [2]. Exactly the same physical assessment of the flow field applies, as was outlined in Ref. [4]. Subregions (i)–(v) are once again appropriate and the solution, to follow, similarly uses this understanding of the basic hydrodynamics.

In practice, the flow against a plane wall is terminated by a hydraulic jump. The objective here is in due course to develop a methodology for the flow around a tube where no such phenomenon is observed. Accordingly, the associated complications of a possible hydraulic jump will not be considered.

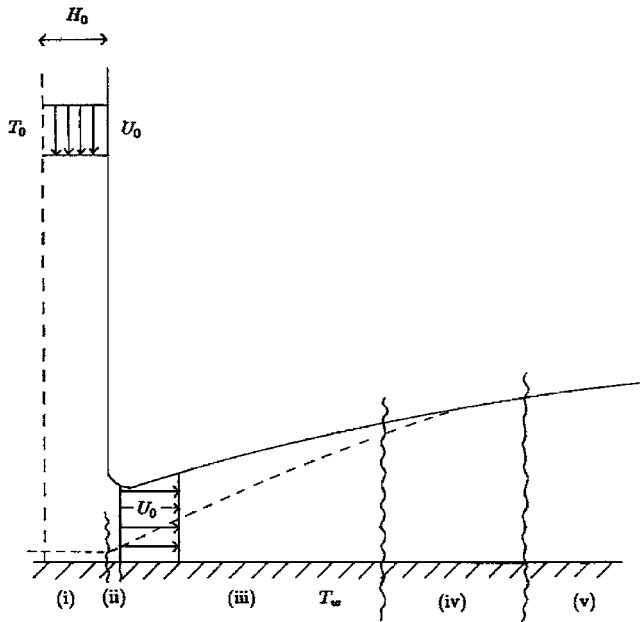
Heat transfer estimates can be obtained under the assumptions of a constant temperature T_w at the plane and zero heat flux on the free surface. When water is the coolant medium, then it has to be noted that the rates of viscous and thermal diffusion are appreciably different, and the point at which viscous effects penetrate the free surface occurs before the point at which the free surface first experiences the presence of the hot plane. To develop an approximation, the flow field is thus divided into regions, as illustrated in Fig. 1(b).

2.1 Region 1. When an impinging circular jet strikes a plane surface, it experiences an eventually inviscid radially symmetric division and deflection through 90 deg. In the immediate vicinity of the point of impact, viscous effects begin to influence the flow field. At that point, an imbedded axisymmetric stagnation boundary layer of thickness $O(\nu H_0 / U_0)^{1/2}$ or $O(H_0 Re^{-1/2})$ occurs. For high flow rates $Re \gg 1$ and to a first approximation, the stagnation boundary-layer thickness is negligibly small. The presence of the solid boundary more significantly influences the flow within the deflected jet away from the point of impact. Here, a viscous boundary layer develops against the horizontal plate. The effects of viscosity are eventually present throughout the film and the form of a solution identifies a point of viscous penetration of the free surface, marking the end of Region 1. For Prandtl numbers greater than 1, a parallel thermal diffusion occurs, but thermal effects do not penetrate the free surface at the end of Region 1.

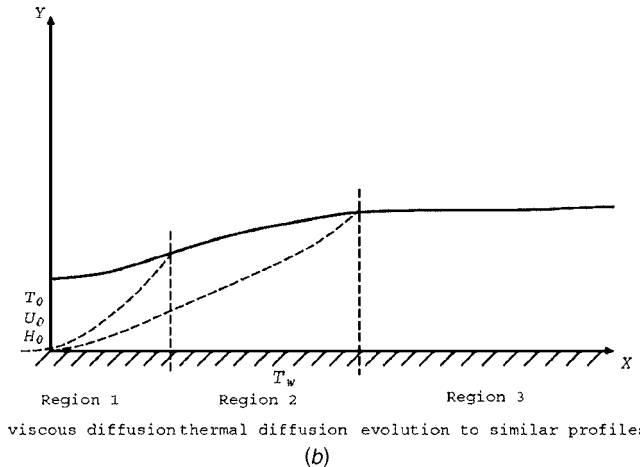
2.2 Region 2. Over Region 2, thermal diffusion continues until the presence of the hot plate eventually influences the free surface. This point of penetration marks the end of Region 2. Accordingly, Region 2 describes the developing temperature distribution within an established hydrodynamic flow field since the

¹Corresponding author.

Contributed by the Heat Transfer Division of ASME for publication in the JOURNAL OF HEAT TRANSFER. Manuscript received December 15, 2006; final manuscript received May 3, 2007; published online January 25, 2008. Review conducted by Giulio Lorenzini.



(i) Imbedded stagnation boundary layer
(ii) Outer inviscid deflection region
(iii) Quasi Blasius viscous diffusion
(iv) Transition around viscous penetration
(v) Similarity film flow
The dashed line represents the hydrodynamic boundary layer.



viscous diffusion thermal diffusion evolution to similar profiles
(b) Basis of approximate solution.

form of the solution in Region 1 is designed to coalesce directly with the Watson similarity solution for velocity and film thickness at the boundary between Regions 1 and 2.

2.3 Region 3. Once the influence of the hot plate penetrates the free surface, the surrounding air acts as an insulator, and here, there is zero heat flux from the free surface. As a consequence, the film gradually approaches a uniform temperature distribution, coinciding with the temperature of the plate. Region 3 monitors the approach to this asymptotic state.

To assess the validity of the approximate method, a full numerical solution of the model equations is then obtained. Results and comparisons are presented at the conclusion of the paper.

3 Governing Equations

The flow under investigation has been modeled as a steady, axisymmetric flow of incompressible fluid. In the absence of body forces and viscous dissipation, the equations expressing conservation of mass, momentum, and energy are, consequently,

$$\nabla \cdot \mathbf{V} = 0 \quad (1)$$

$$\rho(\mathbf{V} \cdot \nabla)\mathbf{V} = -\nabla P + \mu \nabla^2 \mathbf{V} \quad (2)$$

$$\rho C_p (\mathbf{V} \cdot \nabla)T = k \nabla^2 T \quad (3)$$

where $\mathbf{V}=(v_r, v_z)$ are velocity components associated with cylindrical coordinates (r, z) measured along the plate from the axis of deflection and normal to the plate, respectively. ρ , μ , C_p , and k are the density, dynamic viscosity, specific heat at constant pressure, and thermal conductivity of the cooling fluid in the jet, respectively. T and P are, respectively, the temperature and pressure within the fluid.

The specific boundary conditions under which the equations are to be solved closely parallel those of Ref. [4]. In particular, at the wall, the no slip condition and the constant temperature T_w require

$$v_r = v_z = 0, T = T_w \quad \text{at } z = 0, r \geq 0 \quad (4)$$

On the free surface, assuming negligible shear stress and heat flux requires

$$\frac{\partial v_r}{\partial z} = 0, \quad \frac{\partial T}{\partial z} = 0 \quad \text{at } z = H(r), r \geq 0 \quad (5)$$

The conservation of volume constraint applies at any given r station and, hence,

$$2\pi \int_0^{H(r)} r v_r(r, z) dz = \text{const} = \pi H_0^2 U_0 \quad \text{for } r \geq 0 \quad (6)$$

Under the assumption that the film thickness remains thin relative to a characteristic horizontal dimension, a boundary-layer treatment of the equations allows a significant simplification.

The following nondimensional variables are introduced:

$$x = \frac{r}{\text{Re}^{1/3} H_0}, \quad \bar{Y} = \frac{\text{Re}^{1/3} z}{H_0} \quad (7)$$

$$\bar{H}(x) = \frac{\text{Re}^{1/3} H(r)}{H_0} \quad (8)$$

$$\bar{U} = \frac{v_r}{U_0}, \quad \bar{V} = \frac{\text{Re}^{2/3} v_z}{U_0}, \quad \bar{\phi} = \frac{T - T_w}{T_0 - T_w}, \quad p = \frac{P}{\rho U_0^2} \quad (9)$$

In the limit $\text{Re} \rightarrow +\infty$ with x remaining $O(1)$, the following equations are obtained:

$$\frac{\partial}{\partial x}(x\bar{U}) + \frac{\partial}{\partial \bar{Y}}(x\bar{V}) = 0 \quad (10)$$

$$\bar{U} \frac{\partial \bar{U}}{\partial x} + \bar{V} \frac{\partial \bar{U}}{\partial \bar{Y}} = -\frac{\partial p}{\partial x} + \frac{\partial^2 \bar{U}}{\partial \bar{Y}^2} \quad (11)$$

$$0 = \frac{\partial p}{\partial \bar{Y}} \quad (12)$$

$$\text{Pr} \left(\bar{U} \frac{\partial \bar{\phi}}{\partial x} + \bar{V} \frac{\partial \bar{\phi}}{\partial \bar{Y}} \right) = \frac{\partial^2 \bar{\phi}}{\partial \bar{Y}^2} \quad (13)$$

where $\text{Pr} = \nu / \kappa$ is the Prandtl number with ν as the kinematic viscosity, μ / ρ , and κ as the thermometric conductivity, $k / \rho C_p$ and $\Delta T = T_w - T_0$. In common with standard boundary-layer theory, Eq.

(12) implies that the pressure across the film remains constant. In the absence of external pressure gradients and with zero shear assumed on the free surface, the pressure term in Eq. (11) is identically zero.

In nondimensional variables, the boundary conditions now read

$$\bar{U} = \bar{V} = \bar{\phi} = 0 \quad \text{at } \bar{Y} = 0, x \geq 0 \quad (14)$$

$$\frac{\partial \bar{U}}{\partial \bar{Y}} = \frac{\partial \bar{\phi}}{\partial \bar{Y}} = 0 \quad \text{at } \bar{Y} = \bar{H}(x), x \geq 0 \quad (15)$$

$$\int_0^{\bar{H}(x)} x \bar{U} d\bar{Y} = \frac{1}{2} \quad \text{for } x \geq 0 \quad (16)$$

These have been quoted in the context of the fully developed film flow field, which is approached in Region 3. The hydrodynamic equations of this system have been shown by Watson [2] to possess similarity solutions. A simple supplementary thermal solution of uniform temperature is also present. These solutions provide the basis for developing comprehensive approximations for the complete flow field downstream of the radial symmetry point of impingement incorporating Regions 1–3.

4 Downstream Similarity Solutions

The equations to be solved are

$$\frac{\partial}{\partial x}(x\bar{U}) + \frac{\partial}{\partial \bar{Y}}(x\bar{V}) = 0 \quad (17)$$

$$\bar{U} \frac{\partial \bar{U}}{\partial x} + \bar{V} \frac{\partial \bar{U}}{\partial \bar{Y}} = \frac{\partial^2 \bar{U}}{\partial \bar{Y}^2} \quad (18)$$

$$\text{Pr} \left(\bar{U} \frac{\partial \bar{\phi}}{\partial x} + \bar{V} \frac{\partial \bar{\phi}}{\partial \bar{Y}} \right) = \frac{\partial^2 \bar{\phi}}{\partial \bar{Y}^2} \quad (19)$$

subject to boundary conditions (14)–(16).

Note that the equations governing the hydrodynamics (Eqs. (17) and (18)) are independent of the energy equation (Eq. (19)). These are examined as follows. It is well known that, using Mangler's transformations [12], the calculation of axially symmetrical boundary layers on bodies of revolution, in an unlimited expanse of fluid, can be reduced to the calculation of complementary two-dimensional flows. The flow currently under consideration represents the axially symmetric equivalent of the two-dimensional flow examined in Ref. [4]. Here, we examine the possibility that the Mangler's transformations applied to the set of Eqs. (17) and (18) under the specified hydrodynamic boundary conditions have a two-dimensional equivalent differential system.

Let

$$x' = \int_0^x t^2 dt = \frac{x^3}{3} \quad (20)$$

and

$$\bar{Y}' = x\bar{Y} \quad (21)$$

then

$$\bar{U}' = \bar{U} \quad (22)$$

$$\bar{V}' = \frac{1}{x} \left(\bar{V} + \frac{\bar{Y}\bar{U}}{x} \right) \quad (23)$$

With these new' variables, Eqs. (17) and (18) become

$$\frac{\partial \bar{U}'}{\partial x'} + \frac{\partial \bar{V}'}{\partial \bar{Y}'} = 0 \quad (24)$$

$$\bar{U}' \frac{\partial \bar{U}'}{\partial x'} + \bar{V}' \frac{\partial \bar{U}'}{\partial \bar{Y}'} = \frac{\partial^2 \bar{U}'}{\partial \bar{Y}'^2} \quad (25)$$

The boundary conditions are

$$\bar{U}' = \bar{V}' = 0 \quad \text{at } \bar{Y}' = 0 \quad (26)$$

$$\frac{\partial \bar{U}'}{\partial \bar{Y}'} = 0 \quad \text{at } \bar{Y}' = x\bar{H}(x) = \bar{H}'(x') \quad (27)$$

and

$$\int_0^{\bar{H}'(x')} \bar{U}' d\bar{Y}' = \frac{1}{2} \quad (28)$$

With the minor modification of the conservation of volume flow constraint, the differential system formally reproduces the hydrodynamic system examined in Ref. [4]. Introducing a similarity variable $\eta = \bar{Y}' / \bar{H}'(x')$, a stream function form of solution $\psi(x, \bar{Y}') = \bar{U}_s(x) \bar{h}(x) f(\eta)$ leads to the Watson similarity solution as the solution of

$$2f''' + 3c^2 f'^2 = 0 \quad f'(0) = 0 \quad f'(1) = 1 \quad f''(1) = 0$$

Here, $\bar{U}_s(x)$ represents the nondimensional unknown velocity at the free surface and c can be obtained analytically as

$$\frac{\Gamma(1/3)\Gamma(1/2)}{3\Gamma(5/6)} \approx 1.402$$

As a result, the axisymmetric solution can be directly inferred from the solution of Ref. [4] as

$$\bar{U}_s(x) = \frac{27c^2}{8\pi^2(x^3 + l^3)} \quad (29)$$

$$\bar{h}(x) = \frac{2\pi}{3\sqrt{3}}(x^3 + l^3) \quad (30)$$

Here, l is a nondimensional leading edge shift constant. The solutions hold at large distances from the jet incidence and l may be associated with an indeterminate origin of such a flow solution. An estimate of l may be obtained by further consideration of the growth of the boundary layer from the point of impact of the jet. The effects of viscous retardation are seen to result in a simultaneous thickening of the film and a reduction in the free surface velocity.

In the original dimensional variables,

$$U_s(r) = \frac{27c^2}{8\pi^4} \frac{Q^2}{\nu(r^3 + L^3)} \quad (31)$$

$$H(r) = \frac{2\pi^2}{3\sqrt{3}} \frac{\nu}{Q} \frac{(r^3 + L^3)}{r} \quad (32)$$

The velocity distribution within the film is given by

$$v_r(r, z) = U_s(r) f'(\eta) \quad (33)$$

where $f(\eta)$ is the Watson similarity solution whose properties have been presented in Ref. [4].

The associated asymptotic downstream similarity solution for the temperature distribution is obtained by examining Eq. (19) with $\bar{\phi}(x, \bar{Y}') = \bar{\phi}(\eta)$, together with the associated similarity transformations. The resultant equation is

$$\bar{\phi}'' = 0 \quad (34)$$

subject to the boundary conditions

$$\bar{\phi}(0) = 0 \quad \bar{\phi}'(1) = 0 \quad (35)$$

The solution must therefore be $\bar{\phi} \equiv 0$, confirming a uniform temperature distribution in the film equal to the temperature of the plate, T_w .

5 Approximate Solutions

The solutions obtained in the previous section are asymptotic solutions, which are valid well downstream of the location of jet impingement and deflection along the plane. An approximation scheme is now presented, which looks more closely at the flow at impingement. The solution is built up from this vicinity, stage by stage, to provide comprehensive details of the velocity and temperature distribution at radial stations away from the origin.

5.1 Region 1. The discussion of Region 1 follows closely that of the sheet drainage flow of Ref. [4]. At impact, an inviscid deflection of the draining sheet occurs over a negligibly small length scale. Only after deflection is the flow aware of the presence of the solid boundary, and only then do viscous effects begin to influence the flow field. The development of a viscous boundary layer within a uniform velocity film accounts for the close parallel in this region with Blasius boundary-layer flow. Similarly, the temperature differential between the plane and the fluid only begins to influence the temperature distribution after deflection. Thus, a developing thermal boundary layer may also be anticipated from $r=0$.

The equations governing the viscous and thermal boundary layers are exactly the same as Eqs. (17)–(19), but the boundary conditions, as in Ref. [4], now read

$$\bar{U} = 0, \quad \bar{V} = 0, \quad \bar{\phi} = 0 \quad \text{at } \bar{Y} = 0, \quad x \geq 0$$

($\bar{U} \rightarrow 1$, $\bar{\phi} \rightarrow 1$ as \bar{Y} approaches the outer limits of the viscous and thermal boundary layers, respectively)

$$\bar{U} = 1, \quad \bar{\phi} = 1 \quad \text{at } x = 0, \quad \bar{Y} > 0$$

The transformations

$$\psi(x, \bar{Y}) = \sqrt{\frac{2}{3}} x^{3/2} \bar{f}(\bar{\eta}), \quad \bar{\phi}(x, \bar{Y}) = \bar{\phi}(\bar{\eta}), \quad \bar{\eta} = \sqrt{\frac{3}{2}} \frac{\bar{Y}}{x^{1/2}}$$

$$\bar{U} = \frac{1}{x} \frac{\partial \psi}{\partial \bar{Y}}, \quad \bar{V} = -\frac{1}{x} \frac{\partial \psi}{\partial x} \quad (36)$$

lead once again to

$$\bar{f}''' + \bar{f}\bar{f}'' = 0$$

$$\frac{1}{\text{Pr}} \bar{\phi}'' + \bar{f}\bar{\phi}' = 0$$

subject to boundary conditions

$$\bar{f}(0) = 0, \quad \bar{f}'(0) = 0, \quad \bar{\phi}(0) = 0$$

$$\bar{f}'(\bar{\eta}) \rightarrow 1, \quad \bar{\phi}(\bar{\eta}) \rightarrow 1 \quad \text{as } \bar{\eta} \rightarrow +\infty$$

Full details of these solutions may be referred to in Ref. [4]. Following the arguments of Ref. [4], a device which essentially suppresses the transition region may be introduced. An approximate velocity profile,

$$\bar{U}(x, \bar{Y}) = \bar{U}_s(x) f' \left(\frac{\bar{Y}}{\delta(x)} \right), \quad \eta = \frac{\bar{Y}}{\delta(x)} \quad (37)$$

is assumed, where $f'(\eta)$ is the original Watson similarity profile and $\delta(x)$ is the nondimensional boundary-layer thickness. The profile is then used in a Kármán–Pohlhausen method of solution. Over Region 1, unretarded fluid is present when $x < x_0$, say, where x_0 marks the point of penetration of viscous effects on the free

surface, so that $\bar{U}_s(x) = 1$ and $\delta(x) < \bar{h}(x)$ over $0 < x < x_0$. For $x > x_0$ into Region 2, $\delta(x) \equiv \bar{h}(x)$ and $\bar{U}_s(x) < 1$ in a manner that, using the conservation of flow constraint, can be matched directly onto the asymptotic similarity solutions.

The use of $f'(\eta)$ is feasible only because its integral properties are readily available for use in the momentum integral equation, which reads

$$\left(\frac{1}{x^2} \right) \frac{d}{dx} \int_0^{\delta(x)} \bar{U}(1 - \bar{U}) d\bar{Y} = \left(\frac{\partial \bar{U}}{\partial \bar{Y}} \right)_{\bar{Y}=0} \quad (38)$$

Using Eq. (37) gives

$$\left(\frac{1}{x^2} \right) \frac{d}{dx} \left\{ \delta(x) \int_0^1 f'(1 - f') d\eta \right\} = \frac{f''(0)}{\delta(x)} = \frac{c}{\delta(x)}$$

The integral

$$\int_0^1 (f' - f'^2) d\eta = \frac{2(\pi - c\sqrt{3})}{3\sqrt{3}c^2} \quad (39)$$

and the equation for the boundary-layer thickness is

$$\frac{d}{dx} (\delta^2) = \frac{3\sqrt{3}c^3 x^2}{\pi - c\sqrt{3}}$$

and, hence,

$$\delta^2(x) = \frac{\sqrt{3}c^3 x^3}{\pi - c\sqrt{3}} \quad (40)$$

where $\delta(x)=0$ has been assumed at $x=0$, which is valid in the limit of the underlying assumption.

Invoking the conservation of volume flow at x_0 , the end point of Region 1 effectively suppresses the transition region and leads to

$$\int_0^{\delta(x)} \bar{U} d\bar{Y} + (\bar{h} - \delta) = \frac{1}{2} \quad (41)$$

or

$$\delta \int_0^1 f'(\eta) d\eta + (\bar{h} - \delta) = \frac{1}{2} \quad (42)$$

giving

$$\bar{h}(x) = \frac{1}{2} + \left(1 - \frac{2\pi}{3\sqrt{3}c^2} \right) \delta \quad (43)$$

Since $\delta(x_0) = \bar{h}$,

$$x_0 = \sqrt[3]{\frac{9\sqrt{3}c(\pi - c\sqrt{3})}{16\pi^2}} \approx 0.46216 \quad (44)$$

and matching the free surface velocity at $x=x_0$ leads to

$$l = \sqrt[3]{\frac{9\sqrt{3}c}{16\pi^2} (3\sqrt{3}c - \pi)} \approx 0.8308 \quad (45)$$

5.2 Alternative Profiles. The fact that the integral properties of the Watson similarity profile are readily calculated has been used to advantage in Sec. 5.1. Its use, however, in the energy integral equation is not as convenient as a polynomial representation or approximation for the velocity profile. For instance, the Pohlhausen profile

$$f'_p(\eta) = 2\eta - 2\eta^3 + \eta^4 \quad (46)$$

may again be used in assessing aggregate properties of the flow.

The result is an estimate of the boundary-layer thickness given by

$$\delta_p^2 = \frac{420x^3}{37} \quad (47)$$

which leads to

$$x_{0p} = \frac{\sqrt[3]{3330}}{42} \approx 0.3555 \quad (48)$$

$$l_p = \sqrt[3]{\frac{27783c^2 - 370\pi^2}{8232\pi^2}} \approx 0.8560 \quad (49)$$

as compared to Eqs. (44) and (45).

Alternatively, the fourth order polynomial approximation to $f'(\eta)$

$$f'_w(\eta) = c\eta + (4 - 3c)\eta^3 + (2c - 3)\eta^4 \quad (50)$$

may be used. The viscous boundary-layer thickness for this profile is given by

$$\delta_w^2 = \frac{420cx^3}{72 + 39c - 19c^2} \quad (51)$$

and

$$x_{0w} = \sqrt[3]{\frac{5(72 + 39c - 19c^2)}{21c(8 + 3c)^2}} \approx 0.46697 \quad (52)$$

$$l_w = \sqrt[3]{\frac{567c^3(8 + 3c)^2 - 40\pi^2(72 + 39c - 19c^2)}{168\pi^2c(8 + 3c)^2}} \approx 0.8293 \quad (53)$$

which very closely approximate Eqs. (44) and (45). Consequently, the polynomial $f'_w(\eta)$ is used in subsequent developments of velocity and temperature distributions.

The temperature characteristics of Region 1 are now considered. The energy integral equation of Eq. (19) becomes

$$\left(\frac{1}{x^2}\right) \frac{d}{dx} \int_0^{\delta_T(x)} \bar{U}(1 - \bar{\phi}) d\bar{Y} = \frac{1}{Pr} \left(\frac{\partial \bar{\phi}}{\partial \bar{Y}}\right)_{\bar{Y}=0} \quad (54)$$

where $\delta_T(x)$ denotes the outer limits of the region of thermal diffusion. When $Pr > 1$, it may be anticipated that $\delta_T(x) < \delta(x)$ over $0 < x < x_0$. With $\eta_T = \bar{Y} / \delta_T(x)$ and the ratio δ_T / δ denoted by Δ so that $\eta = \Delta \eta_T$, the solution for $\delta_T(x)$ may be developed by assuming profiles for \bar{U} and $\bar{\phi}$.

The two profile pairs of Ref. [4] have been used

$$\bar{U}(\eta) = f'_p(\eta), \quad \bar{\phi}(\eta_T) = f'_p(\eta_T)$$

$$\bar{U}(\eta) = f'_w(\eta), \quad \bar{\phi}(\eta_T) = f'_w(\eta_T) \quad (55)$$

as each pairing ensures identical velocity and temperature distributions for $Pr=1$ when also $\Delta=1$. It is expected that the second pairing has advantages in effecting the transition at the end of Region 1.

The resultant equations for Δ are

$$\Delta^3(168 - 27\Delta^2 + 7\Delta^3) = \frac{148}{Pr} \quad (56)$$

$$\Delta^2 D(\Delta) = \frac{4(72 + 39c - 19c^2)}{Pr} \quad (57)$$

where $D(\Delta) = 168c(3-c)\Delta + 27(4-3c)(5-2c)\Delta^3 - 7(3-2c)(12-5c)\Delta^4$, as obtained previously.

5.3 Region 2. The continuing diffusion of hot wall effects within a hydrodynamic setting prescribed by the Watson similarity solution is monitored in Region 2. The velocity on the free surface is no longer uniform but is prescribed in nondimensional terms by Eq. (29). The viscous boundary-layer thickness $\delta(x)$ is now one and the same as $\bar{h}(x)$, namely,

$$\delta(x) = \bar{h}(x) = \frac{2\pi}{3\sqrt{3}}(x^3 + l_w^3)$$

The energy integral equation (Eq. (54)) remains appropriate, and the progressive thermal diffusion implies that $\delta_T(x) \rightarrow \delta(x) = \bar{h}(x)$.

In prescribing profiles, $\eta_T = \bar{Y} / \delta_T(x)$ may again be utilized, but now $\Delta(x) = \delta_T(x) / \delta(x)$ is no longer constant and tends to 1 at the end of Region 2.

An equation for $\delta_T(x)$ may be obtained by introducing the following profiles into the energy equation

$$\bar{U}(x, \eta) = \bar{U}_s(x) f'_w(\eta)$$

$$\bar{\phi}(x, \eta_T) = f'_w(\eta_T) \quad (58)$$

to give

$$\frac{\delta_T(x)}{x^2} \frac{d}{dx} [\bar{U}_s(x) D(\Delta) \delta_T(x)] = \frac{2520c}{Pr} \quad (59)$$

which in turn leads to

$$\frac{d}{dx} (\Delta^2) = \frac{10080x^2}{cPr(x^3 + l_w^3)\Delta[336c(3-c) + 108(4-3c)(5-2c)\Delta^2 - 35(3-2c)(12-5c)\Delta^3]} \quad (60)$$

This first order equation may now be integrated with initial data $\Delta(x_{0w}; Pr)$ as far as $\Delta(x_{1w}(Pr); Pr) = 1$.

$$\begin{aligned} & \Delta^3 [3360c(3-c) + 648(4-3c)(5-2c)\Delta^2 - 175(3-2c)(12-5c)\Delta^3] \\ & = \frac{50400}{cPr} \ln \frac{x^3 + l_w^3}{x_{1w}^3 + l_w^3} + 6660 + 2001c - 1222c^2 \end{aligned} \quad (61)$$

where x_{1w} is used to denote the end of Region 2, as predicted using the Watson polynomial profile. Beyond x_{1w} , viscous and thermal effects are present throughout the film. For comparison, the Pohlhausen equivalent has also been computed and included

in the subsequent illustration of results.

The values of $x_{1w}(Pr)$ are listed in Table 1. The numerical details for various Pr are presented in Table 2.

5.4 Region 3. In both Regions 1 and 2, it has been assumed that at the edge of the developing thermal boundary layer the temperature smoothly assimilates into that of the impinging jet. As a consequence, zero heat flux has been invoked. In Region 3, the same boundary condition, in fact, remains valid. Here, however, it is justified by the assumption of negligible heat transfer between the liquid free surface and the surrounding air. Consequently, the temperature of the film rises as a result of continuing heat input at

Table 1 The values of x_{1w} (Pr) for various Prandtl numbers

Pr	x_{1w} (Pr)
1.0	0.4670
2.0	0.6274
3.0	0.7513
4.0	0.8616
5.0	0.9663
6.0	1.0691
7.0	1.1722
8.0	1.2773
9.0	1.3856
10.0	1.4980

the plate. The temperature is thus asymptotic to T_w .

Using the following profiles:

$$\begin{aligned} \bar{U}(x, \eta) &= \bar{U}_s(x) f'_w(\eta) \\ \bar{\phi}(x, \eta) &= \beta(x) f'_w(\eta) \end{aligned} \quad (62)$$

where now $\eta = \bar{Y}/\bar{h}(x)$, the energy integral equation now reads

$$\left(\frac{1}{x^2}\right) \left[\frac{d}{dx} \int_0^{\bar{h}(x)} \bar{U}(\beta - \bar{\phi}) d\bar{Y} - \int_0^{\bar{h}(x)} \bar{U} \frac{d\beta}{dx} d\bar{Y} \right] = \frac{1}{\text{Pr}} \left(\frac{\partial \bar{\phi}}{\partial \bar{Y}} \right)_{\bar{Y}=0} \quad (63)$$

Here, $\beta(x)$ monitors the adjustment of the film temperature to T_w . The result is an equation for $\beta(x)$ within the framework of the prescribed film thickness, namely,

$$\frac{72 + 39c - 19c^2}{630} \frac{d}{dx} [\bar{U}_s \bar{h} \bar{\beta}] - \frac{8 + 3c}{20} \bar{U}_s \bar{h} \frac{d\bar{\beta}}{dx} = \frac{c}{\text{Pr}} \frac{\beta x^2}{\bar{h}} \quad (64)$$

Remembering that $\bar{U}_s(x)\bar{h}(x) = 3\sqrt{3}c^2/4\pi$, Eq. (64) becomes

$$\frac{d\beta}{dx} = - \frac{2520\beta x^2}{c(360 + 111c + 38c^2)\text{Pr}(x^3 + l_w^3)} \quad (65)$$

and, hence,

$$\beta(x) = \left(\frac{x_{1w}^3 + l_w^3}{x^3 + l_w^3} \right)^{840/c(360+11c+38c^2)\text{Pr}} \approx \left(\frac{x_{1w}^3 + l_w^3}{x^3 + l_w^3} \right)^{1.015\text{Pr}} \quad (66)$$

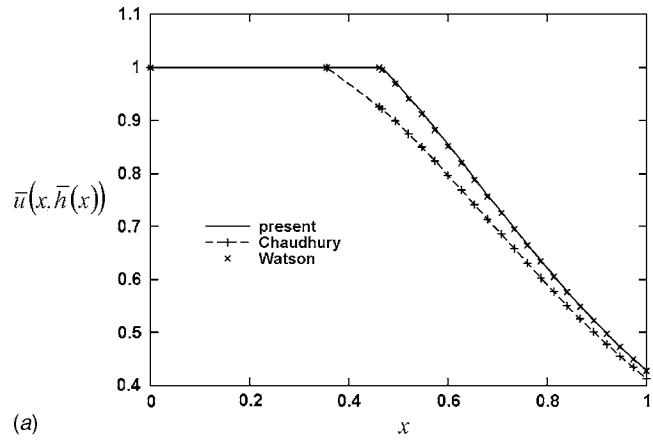
which satisfies the requirements $\beta[x_{1w}(\text{Pr})]=1$ and has $\beta \rightarrow 0$ at rates dependent on Pr.

6 Approximation Results

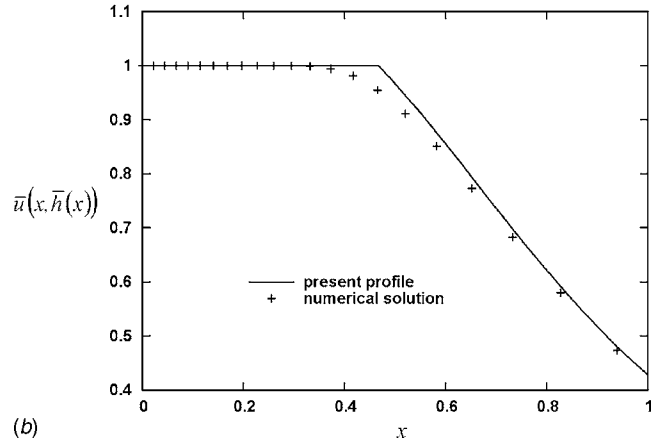
The approximation scheme outlined provides comprehensive details of the flow and heat transfer characteristics for the model flow. Estimates of film thickness, velocity and temperature distributions, skin friction, and heat transfer coefficients over the entire region downstream of the point of impingement can be obtained.

Table 2 Numerical results for $\Delta(x)$ in Region 2 for various Prandtl numbers

$\frac{x-x_{0w}}{x_{1w}-x_{0w}}$	$\Delta(x)$ Pr=2	Pr=5	Pr=10
0.0	0.7878	0.5775	0.4575
0.1	0.8092	0.6253	0.5347
0.2	0.8306	0.6728	0.6085
0.3	0.8520	0.7193	0.6769
0.4	0.8734	0.7644	0.7389
0.5	0.8947	0.8081	0.7948
0.6	0.9160	0.8500	0.8450
0.7	0.9372	0.8902	0.8899
0.8	0.9583	0.9286	0.9304
0.9	0.9792	0.9652	0.9669
1.0	1.0000	1.0000	1.0000



(a)



(b)

Fig. 2 (a) Comparison of free surface velocity for the respective profiles; (b) free surface velocity for the numerical solution and the present profile

ditions, skin friction, and heat transfer coefficients over the entire region downstream of the point of impingement can be obtained.

6.1 Film Thickness and Velocity and Temperature Distributions. To indicate the underlying implications of the hydrodynamic modeling, the free surface velocity has been illustrated for the respective profiles in Fig. 2(a). The associated velocity profile development within the deflected film is illustrated schematically in Fig. 3. Overall predictions of film thicknesses appear in Fig. 4(a). A more detailed indication of the region by region form of solution appears in Fig. 5. For the range of Prandtl numbers Pr=2, 5, and 10, film thickness profiles incorporating the viscous and thermal diffusion processes to penetration are presented. A typical set of temperature distributions within the film covering the evolution between initial thermal diffusion and the asymptotic linear profile is illustrated in Fig. 6.

6.2 Skin Friction and Heat Transfer Coefficients. The elements of interest in engineering practice are the shear stress at the solid boundary, i.e., the skin friction and the rate of heat transfer at the boundary. The skin friction is defined as

$$\tau = \mu \left(\frac{\partial v_r}{\partial z} \right)_{z=0} \quad (67)$$

leading to the nondimensional skin friction coefficient

$$\bar{\tau} = \left(\frac{H_0^2 \mu^2}{\rho U_0^4} \right)^{1/3} \frac{\tau}{x} = \frac{\tau \text{Re}^{2/3}}{\rho U_0^2 x} = \left(\frac{\partial \bar{U}}{\partial \bar{Y}} \right)_{\bar{Y}=0} \quad (68)$$

From the approximations, it gives

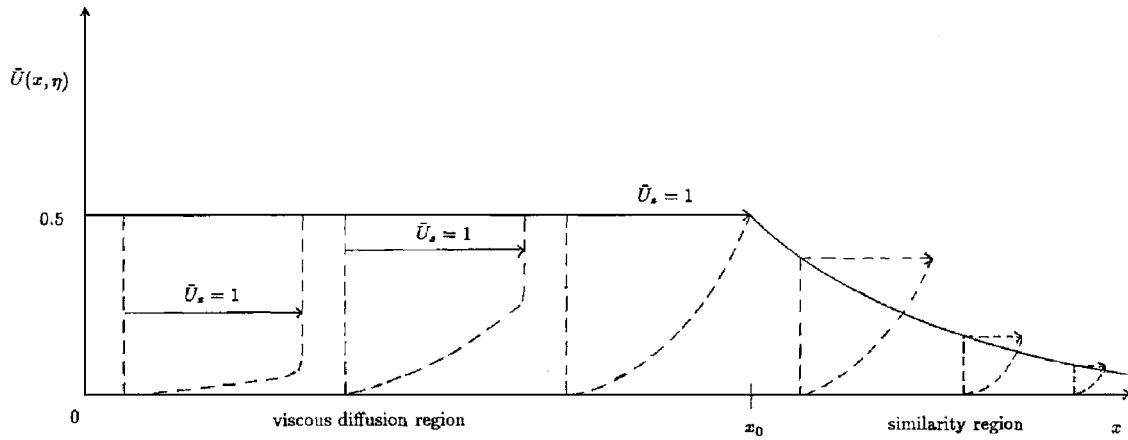


Fig. 3 Velocity profile development within the deflected film

$$\bar{\tau}_p = \sqrt{\frac{37}{105x^3}} \quad (\text{in Region 1})$$

$$= \frac{81\sqrt{3}c^2}{8\pi^3(x^3 + l_p^3)^2} \quad (\text{in Regions 2 and 3}) \quad (69)$$

$$\bar{\tau}_w = \sqrt{\frac{(72 + 39c - 19c^2)c}{420x^3}} \quad (\text{in Region 1})$$

$$= \frac{81\sqrt{3}c^3}{16\pi^3(x^3 + l_w^3)^2} \quad (\text{in Regions 2 and 3}) \quad (70)$$

Graphs of $\bar{\tau}(x)$ are plotted in Fig. 7(a). The integrable square root singularity is consistent with the Blasius boundary-layer equivalent.

The most significant film cooling design factor is the heat transfer across the film. The heat transfer at the solid boundary is given by

$$q = -\kappa \left(\frac{\partial T}{\partial z} \right)_{z=0} = \frac{\kappa \Delta T \text{Re}^{1/3} x}{H_0} \left(\frac{\partial \bar{\phi}}{\partial \bar{Y}} \right)_{\bar{Y}=0} \quad (71)$$

where $\Delta T = T_w - T_0$. The nondimensional version of this is known as the Nusselt number defined as

$$\text{Nu} = \frac{q H_0}{\kappa \Delta T \text{Re}^{1/3} x} = \left(\frac{\partial \bar{\phi}}{\partial \bar{Y}} \right)_{\bar{Y}=0} \quad (72)$$

The results are

$$\text{Nu}_p = \frac{1}{\Delta_p(\text{Pr})} \sqrt{\frac{37}{105x^3}} \quad (\text{in Region 1})$$

$$= \frac{1}{\Delta_p(x; \text{Pr})} \frac{3\sqrt{3}}{\pi(x^3 + l_p^3)} \quad (\text{in Region 2})$$

$$= \frac{3\sqrt{3}}{\pi(x^3 + l_p^3)} \left(\frac{x_p^3 + l_p^3}{x^3 + l_p^3} \right)^{840/367c^2 \text{Pr}} \quad (\text{in Region 3}) \quad (73)$$

and

$$\text{Nu}_w = \frac{1}{\Delta_w(\text{Pr})} \sqrt{\frac{(72 + 39c - 19c^2)c}{420x^3}} \quad (\text{in Region 1})$$

$$= \frac{1}{\Delta_w(x; \text{Pr})} \frac{3\sqrt{3}c}{2\pi(x^3 + l_w^3)} \quad (\text{in Region 2})$$

$$= \frac{3\sqrt{3}c}{2\pi(x^3 + l_w^3)} \left(\frac{x_w^3 + l_w^3}{x^3 + l_w^3} \right)^{840/c(360+111c+38c^2)\text{Pr}} \quad (\text{in Region 3}) \quad (74)$$

The predictions of Nu_w for a range of Prandtl numbers are presented in Fig. 8(a). The values of $\Delta_p(\text{Pr})$ and $\Delta_w(\text{Pr})$ have been obtained from Eqs. (56) and (57), respectively. $\Delta_w(x; \text{Pr})$ satisfies

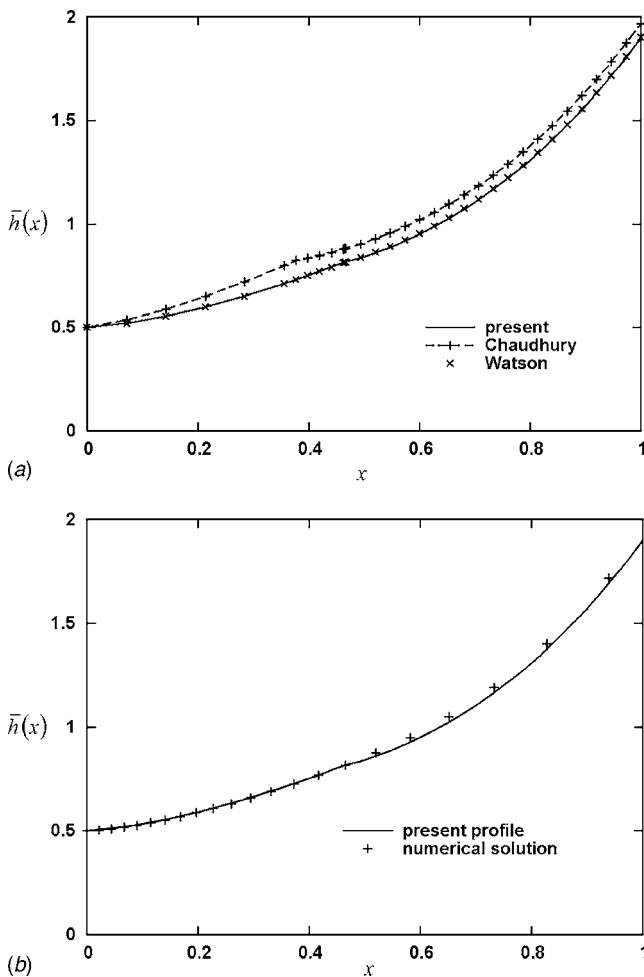


Fig. 4 (a) Comparison of film thickness for the respective profiles; (b) film thickness for the numerical solution and the present profile

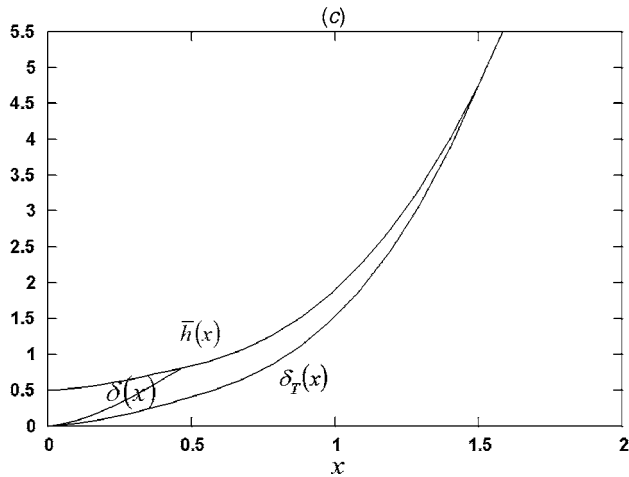
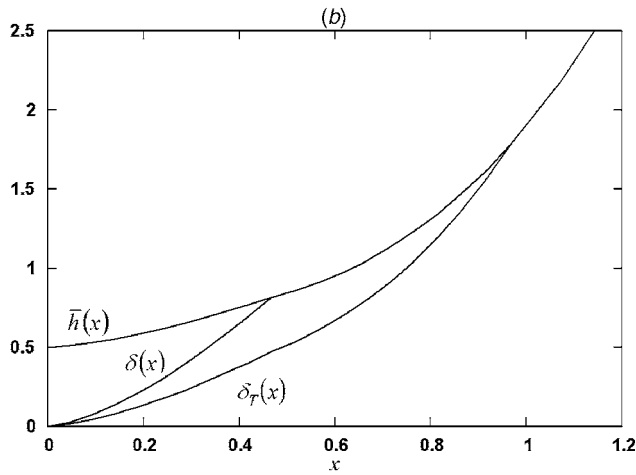
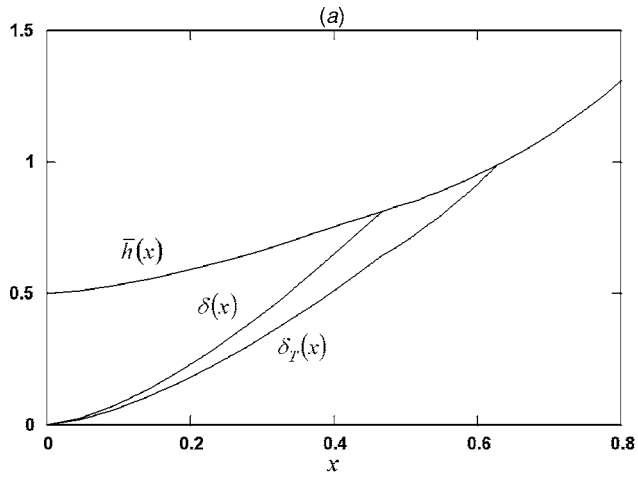


Fig. 5 Film, viscous, and thermal boundary-layer thicknesses for Pr=(a) 2, (b) 5, and (c) 10 using the present profile

Eq. (61). Accordingly, $\Delta_p(x; \text{Pr})$ satisfies the following equation:

$$\Delta^3(3360 - 648\Delta^2 + 175\Delta^3) = \frac{50,400}{c^2 \text{Pr}} \ln \frac{x^3 + l_p^3}{x_{1p}^3 + l_p^3} + 2887 \quad (75)$$

7 Numerical Solutions

The continuity (Eq. (10)) is eliminated by introducing a stream function ψ defined by

$$\bar{U} = \frac{1}{x} \frac{\partial \psi}{\partial \bar{Y}}, \quad \bar{V} = -\frac{1}{x} \frac{\partial \psi}{\partial x} \quad (76)$$

Owing to the geometry, $\bar{H}(x)$ is singular at $x=0$. To remove this singularity, y and $\bar{h}(x)$ are introduced and given by

$$y = x\bar{Y}, \quad \bar{h}(x) = x\bar{H}(x) \quad (77)$$

Substituting Eqs. (76) and (77) into Eqs. (10)–(16) gives

$$\frac{\partial^3 \psi}{\partial y^3} = \left(\frac{1}{x^2}\right) \left(\frac{\partial \psi}{\partial y} \frac{\partial^2 \psi}{\partial x \partial y} - \frac{\partial \psi}{\partial x} \frac{\partial^2 \psi}{\partial y^2} \right) \quad (78)$$

$$\frac{\partial^2 \bar{\phi}}{\partial y^2} = \left(\frac{\text{Pr}}{x^2}\right) \left(\frac{\partial \psi}{\partial y} \frac{\partial \bar{\phi}}{\partial x} - \frac{\partial \psi}{\partial x} \frac{\partial \bar{\phi}}{\partial y} \right) \quad (79)$$

subject to boundary conditions

$$\psi = 0, \quad \frac{\partial \psi}{\partial y} = 0, \quad \bar{\phi} = 0 \quad \text{at } y = 0, \quad x \geq 0 \quad (80)$$

$$\psi = \frac{1}{2}, \quad \frac{\partial^2 \psi}{\partial y^2} = 0, \quad \frac{\partial \bar{\phi}}{\partial y} = 0 \quad \text{at } y = \bar{h}(x), \quad x \geq 0 \quad (81)$$

$$\bar{h} = \frac{1}{2}, \quad \psi = y, \quad \bar{\phi} = 1 \quad \text{at } x = 0, \quad 0 < y \leq \frac{1}{2} \quad (82)$$

where the initial condition (Eq. (82)) appears due to the original initial condition

$$H = \frac{H_0^2}{2r}, \quad v_r = U_0, \quad T = T_0 \quad \text{at } r = 0, \quad 0 < z \leq \frac{H_0^2}{2r} \quad (83)$$

In anticipation of the use of a Keller box method and its attractive extrapolation features, the differential system (Eqs. (78)–(82)) is recast as the following first order system:

$$\frac{\partial \psi}{\partial y} = \bar{u}$$

$$\frac{\partial \bar{u}}{\partial y} = \bar{v}$$

$$\frac{\partial \bar{v}}{\partial y} = \left(\frac{1}{x^2}\right) \left(\bar{u} \frac{\partial \bar{u}}{\partial x} - \bar{v} \frac{\partial \psi}{\partial x} \right)$$

$$\frac{\partial \bar{\phi}}{\partial y} = \bar{w}$$

$$\frac{\partial \bar{w}}{\partial y} = \left(\frac{\text{Pr}}{x^2}\right) \left(\bar{u} \frac{\partial \bar{\phi}}{\partial x} - \bar{w} \frac{\partial \psi}{\partial x} \right) \quad (84)$$

whose boundary conditions are

$$\psi = 0, \quad \bar{u} = 0, \quad \bar{\phi} = 0 \quad \text{at } y = 0, \quad x \geq 0$$

$$\psi = \frac{1}{2}, \quad \bar{v} = 0, \quad \bar{w} = 0 \quad \text{at } y = \bar{h}(x), \quad x \geq 0$$

$$\bar{h} = \frac{1}{2}, \quad \psi = y, \quad \bar{\phi} = 1 \quad \text{at } x = 0, \quad 0 < y \leq \frac{1}{2} \quad (85)$$

The following coordinate transformation, what simultaneously maps the film thickness onto the unit interval and removes the Blasius singularity at the origin, is introduced

$$x = \xi^{2/3}, \quad y = \frac{\xi \eta \bar{h}}{\xi + 1 - \eta}$$

The dependent variables are transformed as

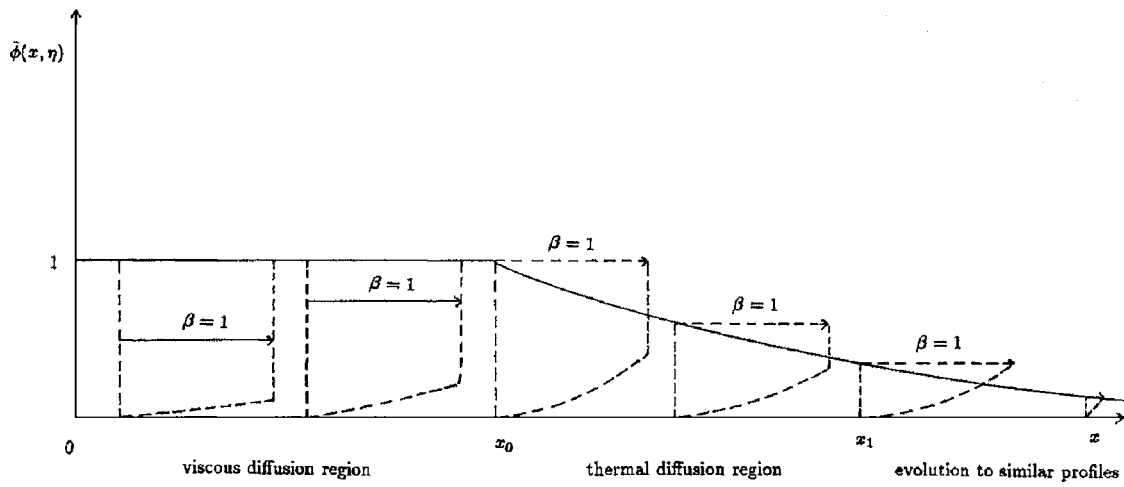


Fig. 6 Temperature profile development within the deflected film

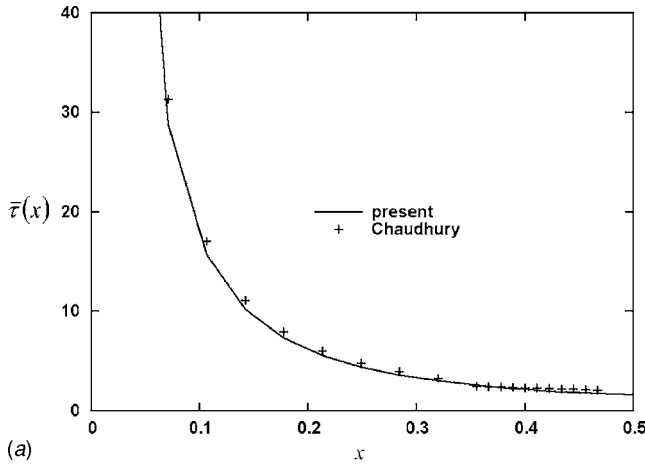
$$\psi = \frac{\xi}{\xi + 1 - \eta} f, \quad \bar{u} = \frac{u}{(1 + \xi)^2}, \quad \bar{v} = \frac{\xi + 1 - \eta}{\xi(1 + \xi)^4} v$$

$$f_\eta = \frac{(1 + \xi)hu}{\xi + 1 - \eta} - \frac{f}{\xi + 1 - \eta}$$

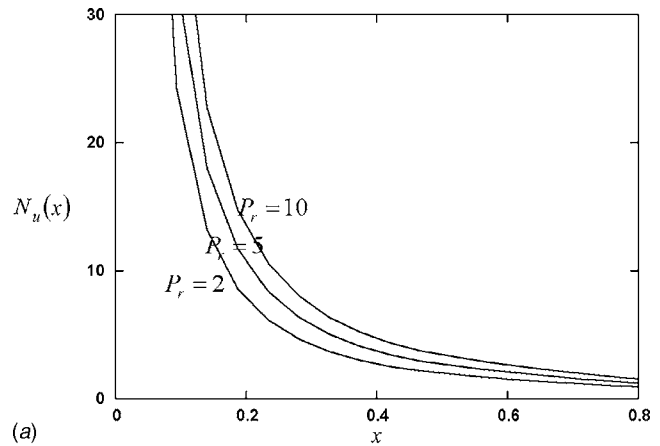
$$\bar{\phi} = \phi, \quad \bar{w} = \frac{\xi + 1 - \eta}{\xi(1 + \xi)^2} w, \quad \bar{h} = (1 + \xi)^2 h$$

$$u_\eta = \frac{(1 + \xi)hv}{\xi + 1 - \eta}$$

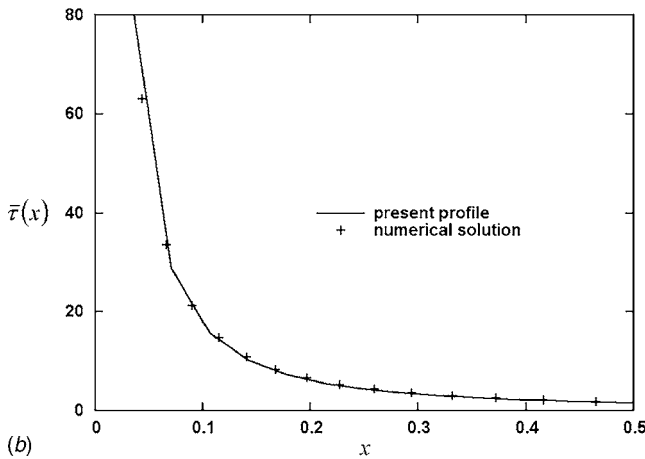
The equations to be solved now read



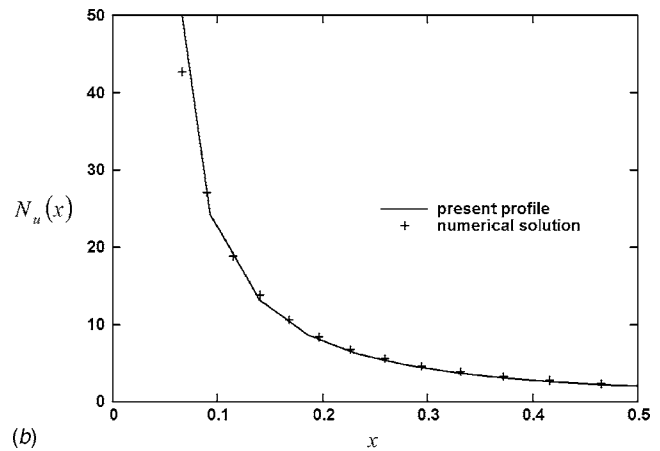
(a)



(a)



(b)



(b)

Fig. 7 (a) Skin friction for the present and the Chaudhury profiles; (b) skin friction for the numerical solution and the present profile

Fig. 8 (a) Heat transfer coefficient for various Prandtl numbers; (b) heat transfer coefficient for the numerical solution and the present profile at \$Pr=2\$

$$v_\eta = \frac{v}{\xi+1-\eta} - \frac{3\xi(1+\xi)^2 hu^2}{(\xi+1-\eta)^3} - \frac{3(1-\eta)(1+\xi)^3 hfv}{2(\xi+1-\eta)^4} + \frac{3\xi(1+\xi)^3 h}{2(\xi+1-\eta)^3} (uu_\xi - vf_\xi)$$

$$\phi_\eta = \frac{(1+\xi)hw}{\xi+1-\eta}$$

$$w_\eta = \frac{w}{\xi+1-\eta} - \frac{3Pr(1-\eta)(1+\xi)^3 hfw}{2(\xi+1-\eta)^4} + \frac{3Pr\xi(1+\xi)^3 h}{2(\xi+1-\eta)^3} (u\phi_\xi - wf_\xi) \quad (86)$$

subject to

$$f=0, \quad u=0, \quad \phi=0 \quad \text{at } \eta=0, \quad \xi \geq 0$$

$$f=\frac{1}{2}, \quad v=0, \quad w=0 \quad \text{at } \eta=1, \quad \xi \geq 0$$

$$h=\frac{1}{2}, \quad f=f_0(\eta), \quad \phi=\phi_0(\eta) \quad \text{at } \xi=0, \quad 0 < \eta \leq 1 \quad (87)$$

where the initial profiles $f_0(\eta)$ and $\phi_0(\eta)$ are found by putting $\xi=0$ and $h=1/2$ into Eq. (86) and solving, subject to conditions $f=u=\phi=0$ at $\eta=0$ and $u=1, \phi=1$ at $\eta=1$.

The parabolic system of equations and boundary conditions (Eqs. (86) and (87)) has been solved by marching in the ξ direction using a modification of the Keller box method. A nonuniform grid is placed on the domain $\xi \geq 0, 0 \leq \eta \leq 1$, and the resulting difference equations are solved by Newton iteration. Solutions are obtained on different sized grids and Richardson's extrapolation used to produce results of high accuracy. A full account of the numerical method and the details of implementation are beyond the scope of this paper and will be reported separately [13]. The detailed numerical method procedure for this case is fully discussed in Ref. [1]. For the axisymmetric flat plate in this paper, the relevant physical parameters should be chosen as

$$F(x)=0 \quad G(x)=\frac{1}{x} \quad x_s = +\infty \quad \gamma = \frac{1}{2} \quad \alpha = \frac{2}{3} \quad \beta = 2$$

The solution scheme was successfully tested against previously reported results [14–19].

8 Results

A typical run has a coarse grid of dimension 60×48 in the (ξ, η) domain with each cell being divided into one to four sub-cells. Because of the coordinate singularity at $\xi=0, \eta=1$, a non-uniform grid is employed and given by $\xi=(1/3)\sinh[\bar{\xi}^{1.5}(1+\bar{\xi}^{1.5})]$, $\eta=1-(1-\bar{\eta})^{1.5}$, where $\bar{\xi}$ and $\bar{\eta}$ are uniform. When $\Delta\bar{\xi} \equiv 0.044618955$ and $\Delta\bar{\eta} \equiv 1/47$, this gives $\Delta\xi \sim 0.004$ and $\Delta\eta \sim 0.003$ near the singularity, which is sufficiently small to give good accuracy, and this enabled us to integrate as far as $\xi \sim 10^9$, which is necessary for the profile at infinity to be determined with sufficient accuracy. From the convergence of the extrapolation process, the absolute error is 9×10^{-7} . A typical set of numerical data is presented in Table 3.

Figures 2(b), 4(b), 7(b), 8(b), and 9(a) show excellent agreement between the full numerical solutions and the theoretical results obtained using an assumed present quartic velocity profile (Eq. (50)). Figure 9(b) shows free surface temperature for various Prandtl numbers. As Pr increases, the temperature decrease becomes more gradual.

Table 3 Film thickness, free surface velocity, and temperature for the axisymmetric flat plate with Pr=2

x	Film thickness $\bar{h}(x)$	Free surface velocity $\bar{u}[x, \bar{h}(x)]$	Free surface temperature $\bar{\phi}[x, \bar{h}(x)]$
0.000	0.500	1.000	1.000
0.115	0.539	1.000	1.000
0.197	0.587	1.000	1.000
0.294	0.659	1.000	1.000
0.416	0.767	0.981	0.999
0.520	0.875	0.911	0.989
0.733	1.191	0.682	0.891
1.072	2.206	0.368	0.660
1.669	6.338	0.128	0.389
1.968	9.930	8.188×10^{-2}	0.310
2.817	27.742	2.931×10^{-2}	0.185
5.228	1.735×10^2	4.685×10^{-3}	7.372×10^{-2}
10.791	1.520×10^3	5.348×10^{-4}	2.484×10^{-2}
25.010	1.892×10^4	4.297×10^{-5}	7.031×10^{-3}
46.931	1.250×10^5	6.504×10^{-6}	2.734×10^{-3}
1.347×10^2	2.957×10^6	2.749×10^{-7}	5.620×10^{-4}
1.073×10^3	1.495×10^9	5.438×10^{-10}	2.500×10^{-5}
1.321×10^4	2.784×10^{12}	2.920×10^{-13}	6.00×10^{-7}
1.385×10^5	3.212×10^{15}	2.531×10^{-16}	0.000
1.000×10^6	1.209×10^{18}	6.723×10^{-19}	0.000

9 Concluding Remarks

Both numerical and approximate solutions for the flow of a cold axisymmetric vertical jet against a horizontal flat plate have been obtained. The level of agreement in estimating film thickness and velocity and temperature distributions is remarkably good insofar

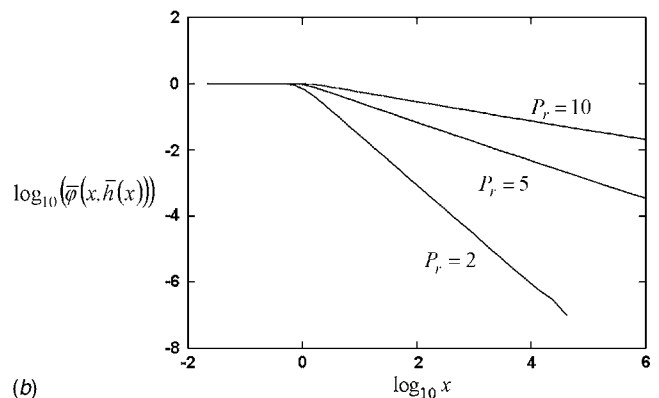
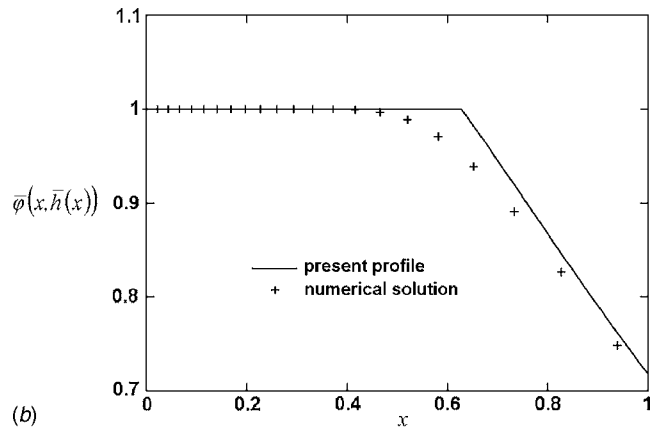


Fig. 9 (a) Free surface temperature for the numerical solution and the present profile at Pr=2 (b) free surface temperature for various Prandtl numbers

as predictions of skin friction and heat transfer characteristics are concerned. Although it is valuable to have demonstrated a successful, robust Keller-box algorithm, it is also noteworthy that the approximation may provide a satisfactory methodology for the assessment of practical configurations, sufficient for the purposes of engineering practice.

Nomenclature

C_p	= specific heat
(f, u, v, ϕ, w)	= dependent variables
f_0, ϕ_0	= initial profiles
H, h	= film thicknesses
H_0	= jet semithickness
k	= thermal conductivity
l	= leading edge shift constant
Nu	= Nusselt number
P, p	= pressure
Pr	= Prandtl number
Q	= $U_0 H_0$
q	= heat flux
$(r, z), (x, Y)$	= Cartesian coordinates measured along and normal to the plate
Re	= Reynolds number
T	= temperature
T_0	= jet temperature
T_w	= plate temperature
U_0	= jet velocity
\bar{U}_s	= free surface velocity
$\mathbf{V}=(U, V)$	= velocity and its components
x_0, x_1	= ends of Regions 1 and 2

Greek Symbols

β	= dimensionless free surface temperature
Γ	= gamma function
Δ	= δ_T / δ
δ, δ_T	= dimensionless boundary-layer thicknesses of velocity and temperature variations
η_T	= η / Δ
κ	= thermometric conductivity
μ, ν	= dynamic and kinematic viscosities
(ξ, η)	= dimensionless coordinates
ρ	= density
τ	= skin friction
ψ	= stream function

Subscript

w = Watson

Superscript

$-$ = dimensional analysis

References

- [1] Shu, J.-J., and Wilks, G., 2007, "Heat Transfer in the Flow of a Cold, Two-Dimensional Draining Sheet Over a Hot, Horizontal Cylinder," *Eur. J. Mech. B/Fluids*, **26**(6), pp. 1–5.
- [2] Watson, E. J., 1964, "The Radial Spread of a Liquid Jet Over a Horizontal Plane," *J. Fluid Mech.*, **20**(3), pp. 481–499.
- [3] Chaudhury, Z. H., 1964, "Heat Transfer in a Radial Liquid Jet," *J. Fluid Mech.*, **20**(3), pp. 501–511.
- [4] Shu, J.-J., and Wilks, G., 1996, "Heat Transfer in the Flow of a Cold, Two-Dimensional Vertical Liquid Jet Against a Hot, Horizontal Plate," *Int. J. Heat Mass Transfer*, **39**(16), pp. 3367–3379.
- [5] Zhao, Y. H., Masuoka, T., Tsuruta, T., and Ma, C. F., 2002, "Conjugated Heat Transfer on a Horizontal Surface Impinged by Circular Free-Surface Liquid Jet," *JSME Int. J., Ser. B*, **45**(2), pp. 307–314.
- [6] Shu, J.-J., 2004, "Microscale Heat Transfer in a Free Jet Against a Plane Surface," *Superlattices Microstruct.*, **35**(3–6), pp. 645–656.
- [7] Guerra, D. R. S., Su, J., and Freire, A. P. S., 2005, "The Near Wall Behavior of an Impinging Jet," *Int. J. Heat Mass Transfer*, **48**(14), pp. 2829–2840.
- [8] Rice, J., Faghri, A., and Cetegen, B., 2005, "Analysis of a Free Surface Film From a Controlled Liquid Impinging Jet Over a Rotating Disk Including Conjugate Effects, With and Without Evaporation," *Int. J. Heat Mass Transfer*, **48**(25–26), pp. 5192–5204.
- [9] Shu, J.-J., and Wilks, G., 2007, "Heat Transfer in the Flow of a Cold, Axisymmetric Jet Over a Hot Sphere," *Int. J. Therm. Sci.*, **46**(12), pp. 1–5.
- [10] Shu, J.-J., 2004, "Impact of an Oblique Breaking Wave on a Wall," *Phys. Fluids*, **16**(3), pp. 610–614.
- [11] Shu, J.-J., 2004, "Slamming of a Breaking Wave on a Wall," *Phys. Rev. E*, **70**(6), p. 066306.
- [12] Rosenhead, L., 1963, *Laminar Boundary Layers*, Oxford University Press, New York.
- [13] Shu, J.-J., and Wilks, G., 1995, "An Accurate Numerical Method for Systems of Differentio-Integral Equations Associated With Multiphase Flow," *Comput. Fluids*, **24**(6), pp. 625–652.
- [14] Shu, J.-J., and Wilks, G., 1995, "Mixed-Convection Laminar Film Condensation on a Semi-Infinite Vertical Plate," *J. Fluid Mech.*, **300**, pp. 207–229.
- [15] Shu, J.-J., and Pop, I., 1997, "Inclined Wall Plumes in Porous Media," *Fluid Dyn. Res.*, **21**(4), pp. 303–317.
- [16] Shu, J.-J., and Pop, I., 1998, "Transient Conjugate Free Convection from a Vertical Flat Plate in a Porous Medium Subjected to a Sudden Change in Surface Heat Flux," *Int. J. Eng. Sci.*, **36**(2), pp. 207–214.
- [17] Shu, J.-J., and Pop, I., 1998, "On Thermal Boundary Layers on a Flat Plate Subjected to a Variable Heat Flux," *Int. J. Heat Fluid Flow*, **19**(1), pp. 79–84.
- [18] Shu, J.-J., and Pop, I., 1999, "Thermal Interaction Between Free Convection and Forced Convection Along a Conducting Plate Embedded in a Porous Medium," *Hybrid Methods in Engineering: ---Modeling, Programming, Analysis, Animation*, **1**(1), pp. 55–66.
- [19] Shu, J.-J., and Pop, I., 1999, "Thermal Interaction Between Free Convection and Forced Convection Along a Vertical Conducting Wall," *Heat Mass Transfer*, **35**(1), pp. 33–38.

Heatline Visualization of Natural Convection in a Porous Cavity Occupied by a Fluid With Temperature-Dependent Viscosity

K. Hooman¹

e-mail: k.hooman@uq.edu.au

H. Gurgenci

School of Engineering,
The University of Queensland,
Brisbane, Queensland 4072, Australia

Temperature-dependent viscosity effect in buoyancy driven flow of a gas or a liquid in an enclosure filled with a porous medium is studied numerically based on the general model of momentum transfer in a porous medium. The exponential form of viscosity-temperature relation is applied to examine three cases of viscosity-temperature relation: constant, decreasing, and increasing. Application of arithmetic and harmonic mean values of the viscosity is also investigated for their ability to represent the Nusselt number versus the effective Rayleigh number. Heat lines are illustrated for a more comprehensive investigation of the problem. [DOI: 10.1115/1.2780179]

Keywords: natural convection, heatline visualization, porous media, variable property, numerical, non-Darcy

1 Introduction

Most previous studies on free convection in porous media assumed the viscosity of the fluid to be constant. However, there are special cases where the viscosity changes with temperature while other fluid properties remain relatively constant, see, for example, Ref. [1]. On the other hand, variable-property free convection in a porous cavity has been analyzed by some authors, as surveyed by Nield and Bejan [2].

Nield [3,4] argued that property variation should not affect convection if one uses an effective Rayleigh number based on mean values. Chu and Hickox [5] reported that even extreme viscosity variations did not have a significant effect on the overall free convection heat transfer coefficient provided the properties were evaluated at the arithmetic mean temperature and a correction factor was used. Siebers et al. [6] have come up with a similar conclusion for free convection of air along a vertical plate.

On the other hand, applying the general model of Vafai and Tien [7] and Hsu and Cheng [8], Guo and Zhao [9] numerically studied the natural convection of poly-alpha-olefin (PAO) with a temperature-dependent viscosity and predicted a higher Nusselt number when the viscosity decreased with the temperature. With properties evaluated at the arithmetic mean temperature (of hot and cold walls), their results still showed significant differences between constant- and variable-property flows. For example, for $Da=10^{-4}$ and $Ra=10$, their Nu was about 75% higher than Nu_{cp} .

Apparently, more investigation is needed to study the effect of temperature-dependent viscosity on natural convection. This work addresses the issue by considering a square porous cavity, depicted in Fig. 1, similar to that of Refs. [10–12]. Following recommendations by Ref. [13], the exponential model for viscosity-temperature relation is applied here for flow of an incompressible fluid. The viscosity of a gas usually increases with temperature and the viscosity of a liquid does the reverse. We consider both cases.

Previous work on the effects of property variation on convection heat transfer in fluids clear of solid material has been sur-

veyed by Kakaç [14]. Recently, Narasimhan and Lage [1] have reviewed the issue for forced convection in a porous duct.

2 Model Equations

Incompressible natural convection of a fluid with temperature-dependent viscosity in a square enclosure filled with homogeneous, saturated, isotropic porous medium with the Oberbeck–Boussinesq approximation for the density variation in the buoyancy term is considered, as shown in Fig. 1(a). The solid matrix and the fluid are in local thermal equilibrium. The governing equations can be written as

$$\frac{\partial(u^* \varphi)}{\partial x^*} + \frac{\partial(v^* \varphi)}{\partial y^*} = \frac{\partial}{\partial x^*} \left(\Gamma_{\varphi} \frac{\partial \varphi}{\partial x^*} \right) + \frac{\partial}{\partial y^*} \left(\Gamma_{\varphi} \frac{\partial \varphi}{\partial y^*} \right) + S_{\varphi} \quad (1)$$

where φ stands for the dependent variables u^* , v^* , and T^* , and Γ_{φ} and S_{φ} are the corresponding diffusion and source terms, respectively, for the general variable φ , as summarized in Table 1.

The exponential model assumes

$$\eta = \nu/\nu_c = \exp(b\theta) \quad (2)$$

where b is positive/negative in the case of a gas/liquid whose viscosity increases/decreases with an increase in temperature. Our dimensionless temperature is $\theta = k(T^* - T_c)/(q''L)$ following Bejan's [15] recommendation to select the lowest temperature as the reference temperature for heatline visualization purposes. One also notes that the Taylor series expansion for very small values of b leads to linear or inverse linear ν - θ relation as

$$\nu = \nu_c(1 + b\theta) \quad (3a)$$

$$\nu^{-1} = \nu_c^{-1}(1 - b\theta) \quad (3b)$$

similar to Refs. [16–19].

The dimensionless stream function is defined as

$$u = \partial\psi/\partial y \quad (4a)$$

$$v = -\partial\psi/\partial x \quad (4b)$$

Taking the curl of x^* - and y^* -momentum equations and eliminating the pressure terms, one has

$$u \cdot \nabla \omega = Pr_c [(\nabla^2 \omega - s^2 \omega) e^{b\theta} - \Lambda |U| \omega + S_w] \quad (5)$$

where

¹Corresponding author.

Contributed by the Heat Transfer Division of ASME for publication in the JOURNAL OF HEAT TRANSFER. Manuscript received November 2, 2006; final manuscript received May 1, 2007; published online January 28, 2008. Review conducted by Jose L. Lage.

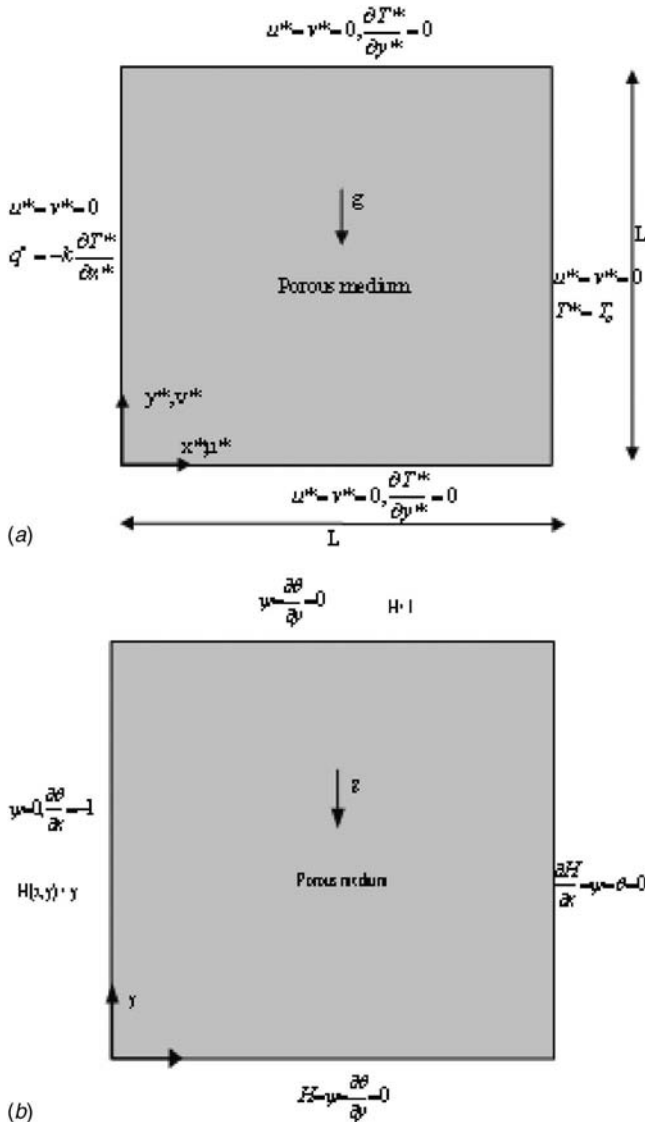


Fig. 1 (a) Definition sketch and (b) dimensionless boundary conditions

Table 1 Summary of the solved governing equations

Equations	φ	Γ_φ	S_φ
Continuity	1	0	0
x^* momentum	u^*/ϕ	ν	$-\frac{1}{\rho} \frac{\partial p^*}{\partial x^*} - \frac{\nu u^*}{K} - \frac{C_F \phi u^* U^* }{K^{1/2}}$
y^* momentum	v^*/ϕ	ν	$g\beta(T^* - T_c) - \frac{1}{\rho} \frac{\partial p^*}{\partial y^*} - \frac{\nu v^*}{K} - \frac{C_F \phi v^* U^* }{K^{1/2}}$
Energy	T^*	α	0

Table 2 Present Nu versus those in the literature for $s=1000$ ($Da=10^{-6}$)

Ra	Present	Ref. [10]	Ref. [11]	Ref. [20]
50	1.57	1.57	—	—
100	2.09	2.09	2.11	1.93
200	2.75	2.78	2.78	2.71
500	3.98	4.06	4.05	3.91
10^3	5.29	5.41	5.35	5.07

$$S_w = s^2 \left(\frac{\partial \eta}{\partial x} \frac{\partial \psi}{\partial x} + \frac{\partial \eta}{\partial y} \frac{\partial \psi}{\partial y} \right) + \Lambda \left(\frac{\partial |U|}{\partial x} \frac{\partial \psi}{\partial x} + \frac{\partial |U|}{\partial y} \frac{\partial \psi}{\partial y} \right) + Ra_f \frac{\partial \theta}{\partial x} - \left[\frac{\partial}{\partial y} \left(\frac{\partial \eta}{\partial x} \frac{\partial^2 \psi}{\partial x \partial y} + \frac{\partial \eta}{\partial y} \frac{\partial^2 \psi}{\partial y^2} \right) + \frac{\partial}{\partial x} \left(\frac{\partial \eta}{\partial x} \frac{\partial^2 \psi}{\partial x^2} + \frac{\partial \eta}{\partial y} \frac{\partial^2 \psi}{\partial x \partial y} \right) - \frac{\partial \eta}{\partial x} \frac{\partial \omega}{\partial x} - \frac{\partial \eta}{\partial y} \frac{\partial \omega}{\partial y} \right] \quad (6)$$

The vorticity directed in the z direction is defined as

$$\omega = -\nabla^2 \psi \quad (7)$$

The thermal energy equation now takes the following form:

$$u \cdot \nabla \theta = \nabla^2 \theta \quad (8)$$

The Nusselt number, following Merrikh and Mohamad [11], is defined as actual heat transfer divided by pure conduction as

$$Nu = 1/\theta_{wall,av} \quad (9a)$$

$$\theta_{wall,av} = \int_0^1 \theta(0,y) dy \quad (9b)$$

where $\theta_{wall,av}$ is the average dimensionless temperature measured over the left (heated) wall. Following Bejan [15], the *heatfunction* concept is applied, which is an invention similar to the stream function but more suitable to visualize heat transfer. The heatfunction, $H^*(x^*, y^*)$, intrinsically satisfies the thermal energy equation while the stream function does the same for the mass continuity equation. Patterns of $H^* = \text{const}$ *heatlines* are lines across which the net flow of energy is zero. Nondimensional heatfunction is defined as

$$\frac{\partial H}{\partial y} = u\theta - \frac{\partial \theta}{\partial x} \quad (10a)$$

$$-\frac{\partial H}{\partial x} = v\theta - \frac{\partial \theta}{\partial y} \quad (10b)$$

The problem is now to solve Eqs. (5)–(10) subject to the boundary conditions shown in Fig. 1(b).

3 Numerical Details

All runs were performed on a 90×90 grid. Our Rayleigh–Darcy number, or simply Ra hereafter, is limited to 10^3 while our Da ranges from 10^{-6} to 1; the modified Prandtl number and the inertia parameter are both fixed at unity, similar to Ref. [11]. Grid independence was verified by running different combinations of s , Ra_f , and b on 90×90 and 120×120 grids to observe less than 1% difference between results obtained on different grids. The convergence criterion (maximum relative error in the values of the dependent variables between two successive iterations) was set at 10^{-5} .

According to Table 2, our results are close to those of Refs. [10,11,20] for $Da=10^{-6}$, while Table 3 checks our Nu at higher Da ($Da=0.01$ or $s=10$) against Ref. [20]. Their results were for an isothermally heated cavity but, following Bejan [15], one can modify their Nu–Ra correlation to compare against a problem with

Table 3 Present Nu versus those of Ref. [20] for $s=10$ and $C_F=0$

Ra	Present Nu	Ref. [20]
100	1.48	1.48
200	1.84	1.84
500	2.41	2.42
1000	2.93	2.92

isoflux heating. The Rayleigh number based on temperature difference in an isothermally heated cavity can be related to a heat flux based Ra, here Ra_f , as

$$Ra_{\Delta T} = Ra_f / Nu \quad (11)$$

In this way $Nu = C Ra_{\Delta T}^m$ reads $Nu = (C Ra_f^m)^{1/(1+m)}$, as noted by Bejan [15] for free convection in a cavity without a porous medium.

4 Results and Discussion

Figure 2 shows line diagrams of $v(x, 0.5)$ and $\theta(x, 0.5)$ for Ra

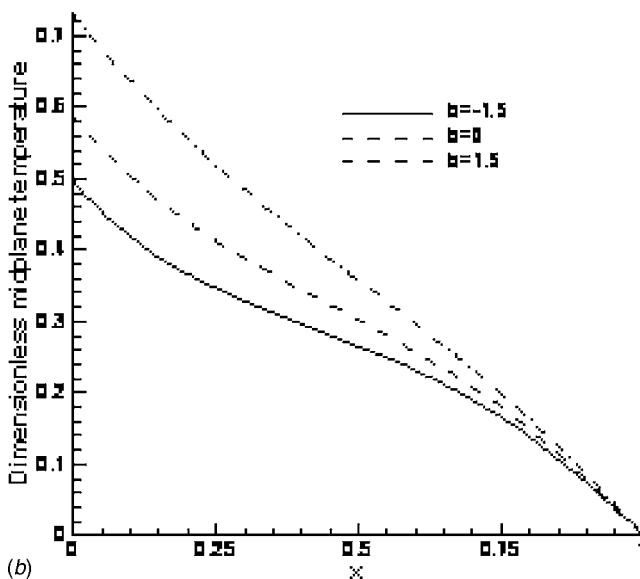
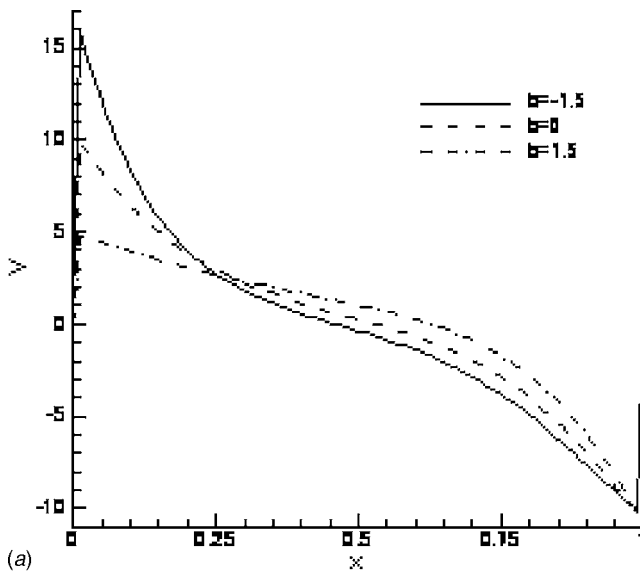


Fig. 2 Horizontal midplane velocity (top) and temperature (bottom) for different values of b with $Ra=50$ and $s=1000$

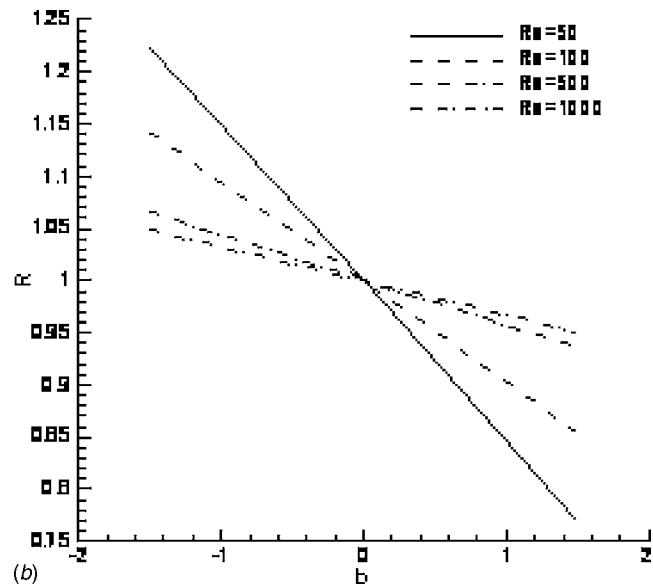
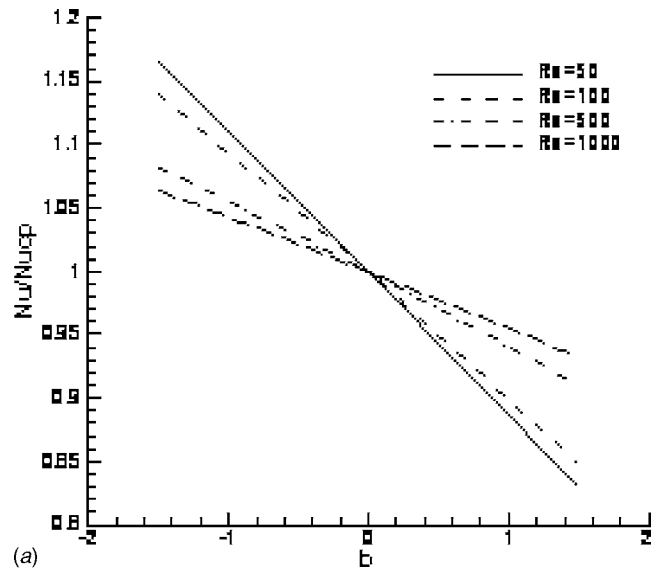


Fig. 3 The variation of Nu/Nu_{cp} (top) and R (bottom) versus b with some values of Ra ($s=100$)

$=50$ with various b values. For a constant-property fluid ($b=0$), the velocity peaks near the opposing walls more or less mirror each other. If the viscosity has a decreasing relation with temperature ($b < 0$), the absolute value of the peak vertical velocity near the heated wall is higher than its counterpart near the opposing wall (cold wall). With $b > 0$, the situation is reversed and the vertical velocity is higher nearer the cold wall. Lower levels of θ are predicted with a decrease in b , which may be a manifestation of increased convection equalizing the temperatures as b is reduced. Moreover, with $b=1.5$ and $Ra=50$, the dimensionless midplane temperature varies almost linearly with x , which implies a conduction-dominated heat transfer.

Figure 3 shows the dependence of the Nu/Nu_{cp} and R on b . The dependence is higher at smaller Ra . For the range of variables considered, Nu and the stream function vary from their constant-property values by up to 20% and 25%, respectively.

According to Fig. 4, the net energy path consists of two vertical boundary layers connected through an energy tube located along the upper wall. The two walls maintain different boundary conditions and their boundary layers are therefore different. At the iso-

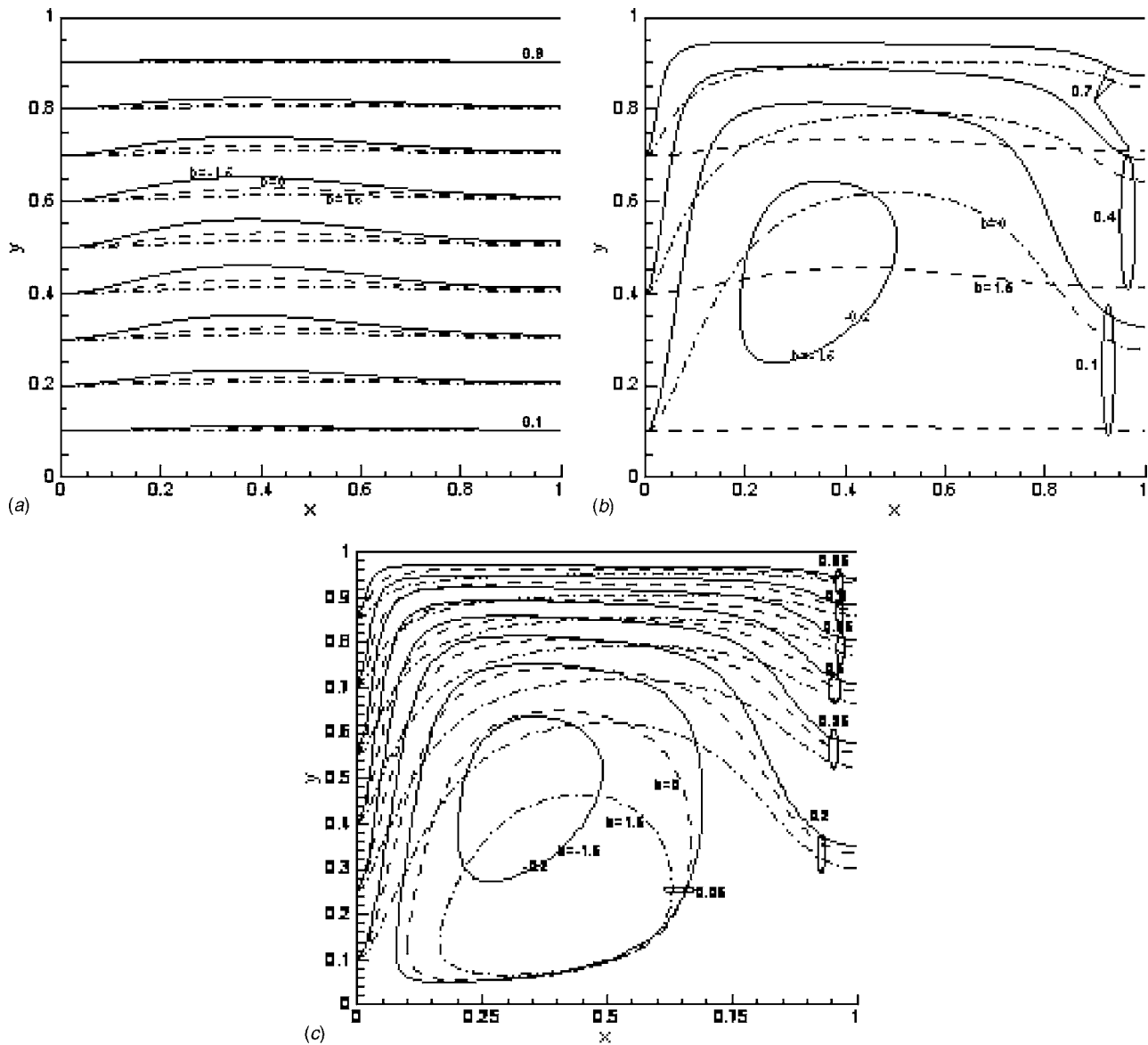


Fig. 4 Heat lines for various b values with $Ra=50$ and (A) $s=1$, (B) $s=100$, and (C) $s=1000$

thermal wall, the heatlines are normal to the wall. At the isoflux wall, the heatline slope shows the amount of energy transferred from the wall and vertical increments in heatfunctions are constant. As seen, horizontal heatlines imply conduction-dominated heat transfer and this dominance becomes clearer with $b > 0$. For example, almost perfectly horizontal heatlines at $b=1.5$ indicates the heat transfer occurring almost entirely by conduction, a situation already observed at this value of b by the linear temperature distribution in Fig. 2. The degree of upward deflection of the heatlines represents the strength of convective heat flow, interpreted as “heat rises” by Bejan [15]. It seems that heatlines can be used to show the onset of convection instead of isotherms. However, investigation of this possibility is left for a future report. As b decreases or s increases at a fixed value of Ra , the heatlines become denser near the top wall, which implies higher heat transfer rate. Nevertheless, this is probably more due to the fact that Ra_f had to be increased to maintain a constant Ra with an increase in s .

The above results demonstrate the apparently destabilizing effect of viscosity decreasing with increased temperature when Ra is calculated at T_c . Let us now see what happens when using average Rayleigh numbers.

Nield [3] recommends using harmonic average for the fluid viscosity in effective Rayleigh number, i.e.,

$$Ra_{\text{eff}} = (Ra_C + Ra_H)/2 \quad (12)$$

Applying the average wall temperature for the hot wall, one has

$$Ra_H = Ra \exp(-b/Nu) \quad (13)$$

With $Ra_C = Ra$, it leads to

$$Ra_{\text{eff}} = Ra[1 + \exp(-b/Nu)]/2 \quad (14)$$

Equation (14) can be used to find Ra_{eff} only when one knows Nu . This makes its application somehow difficult. However, as a first approximation, one can apply the Nu_{cp} value instead of Nu . It will be shown, by Tables 4 and 5, that this approximation will lead to a maximum error of 6% in Nu .

Table 4 shows a sample of Ra_{eff} for limiting values of b , s , and Ra considered in this study. Also available in this table is Nu/Nu_{cp} calculated in two ways. The first method is application of Ra_{eff} as recommended by Nield [3] with $b=0$. The Nusselt number then is divided by Nu_{cp} evaluated at $Ra=Ra_C$. This column is labeled as “Estimated” in Tables 4 and 5. The second approach (which was taken so far) is calculating Nu numerically (for a case with non-

Table 4 Calculation of Ra_{eff} and Nu

s	b	Ra	Ra_{eff}	Nu/ Nu_{cp}	
				Estimated	Numerical
10	-1.5	50	86.02	1.149	1.145
	1.5	50	34.08	0.934	0.91
10^3	-1.5	50	72.25	1.164	1.168
	1.5	50	37.08	0.883	0.833
10	-1.5	10^3	1312.7	1.067	1.07
	1.5	10^3	797.33	0.927	0.923
10^3	-1.5	10^3	1153.05	1.061	1.064
	1.5	10^3	876.35	0.947	0.932

Table 5 Calculation of Ra_{eff} and Nu for $s=10$

Ra	b	Ra_{eff}	Nu/ Nu_{cp}	
			Estimated	Numerical
100	-1.5	187.76	1.178	1.152
	1.5	68.15	0.905	0.887
200	-1.5	325.97	1.135	1.113
	1.5	144.25	0.919	0.894
500	-1.5	714.65	1.097	1.08
	1.5	384.51	0.934	0.904
10^3	-1.5	1335.73	1.078	1.076
	1.5	799.14	0.943	0.932

zero value of b) and then dividing it by its value also numerically calculated at constant property—both calculations done at the same Ra. This column is labeled as “Numerical” in Tables 4 and 5.

As another check on Nield’s theory and based on Eq. (11), we recover the correlations reported by Lauriat and Prasad [20] as

$$\frac{Nu}{Nu_{cp}} = \left(\frac{Ra_{eff}}{Ra} \right)^{m/(1+m)} \quad (15)$$

Making use of Eq. (14), Eq. (15) reads

$$\frac{Nu}{Nu_{cp}} = \left[\frac{1 + \exp(-b/Nu)}{2} \right]^{m/(1+m)} \quad (16)$$

where to the first approximation,

$$\frac{Nu}{Nu_{cp}} = \left[\frac{1 + \exp(-b/Nu_{cp})}{2} \right]^{m/(1+m)} \quad (17)$$

Results of Eq. (17) are shown in Table 5 with a procedure similar to that described above concerning the data in Table 4. Seemingly, the Ra_{eff} approach works well even when the viscosity ratio can reach as high/low values as 4.5/0.22 while the arithmetic mean value for the viscosity may not be a proper option. For example, applying Eq. (2), Ra_{eff}/Ra_{am} reads

$$\frac{Ra_{eff}}{Ra_{am}} = \left\{ \frac{1 + \exp(-b/Nu)}{2 \exp[-b/(2Nu)]} \right\} \quad (18)$$

where Ra_{am} is the Rayleigh number with the viscosity being evaluated at the arithmetic mean temperature. As $b \rightarrow 0$, the Ra

ratio tends to 1. However, increasing b , the ratio differs substantially from unity. For example, with $s=10$ and $Ra=100$, $Nu_{cp} = 1.48$ based on Table 3. With $b=3$, the Rayleigh ratio becomes 1.56, which leads to a 12% change in the associate Nu when the correlation by Ref. [20] is applied.

5 Conclusion

Temperature-dependent viscosity effect on free convection in a porous cavity is studied numerically based on the general model of momentum transfer in a porous medium. It is found that the effective Rayleigh number works well within the range of the parameters considered here. Applying Ra_{eff} , one can still use the constant-property results and this, in turn, will reduce the computational time and expense required for solving a variable-viscosity problem. Moreover, it was observed that application of heatlines gives us a higher resolution as they show lines along which energy is transferred. Dissimilar heatline patterns were observed for different vertical wall boundary conditions. An important parameter is the degree of upward deflection in heatlines as it indicates the heat transfer enhancement. It was also shown that for variable-property free convection in a porous cavity, the Nu-Ra correlation for isothermal walls can still be modified for isoflux cases. In this way, one can use Nu_{cp} in our Eq. (14) instead of Nu (which is unknown and hence can hamper further progress) within a reasonable range of error.

Acknowledgment

The first author, the scholarship holder, acknowledges the support provided by The University of Queensland in terms of UQILAS, Endeavor IPRS, and School Scholarship.

Nomenclature

b = viscosity variation number
 C_F = inertia coefficient
 Da = the Darcy number, $Da = K/L^2$
 g = gravitational acceleration
 H^* = heatfunction
 H = dimensionless heatfunction
 k = porous medium thermal conductivity
 K = permeability
 L = cavity height
 Nu = the Nusselt number
 P^* = pressure
 Pr_c = modified Prandtl number, $Pr_c = \phi \nu_c / \alpha$
 q'' = heat flux
 R = maximum stream function ratio,
 $R = \psi_{\max} / \psi_{\max, cp}$
 Ra_f = the Rayleigh number, $Ra_f = g \beta L^4 q'' / (\nu_c \alpha k)$
 Ra = Rayleigh–Darcy number, $Ra = Ra_f / s^2$
 $Ra_{\Delta T}$ = the Rayleigh number based on ΔT , $Ra_{\Delta T} = g \beta \Delta T L^3 / (\nu_c \alpha)$
 s = porous media shape parameter, $s = Da^{-1/2}$
 S_φ = source term for φ equation
 S_ω = source term for vorticity transport equation
 T^* = temperature
 T_c = cold wall temperature
 u^* = x^* velocity
 $(u, v) = (u^*, v^*)L / \alpha$
 $|U^*|$ = mean velocity $(u^{*2} + v^{*2})^{1/2}$
 $|U|$ = dimensionless mean velocity $(u^2 + v^2)^{1/2}$
 v^* = y^* velocity
 x^*, y^* = horizontal and vertical coordinates
 $(x, y) = (x^*, y^*) / L$

Greek Symbols

α = thermal diffusivity of the porous medium
 β = thermal expansion coefficient
 Γ_φ = diffusion parameter
 Λ = inertial parameter $\Lambda = C_F L \phi^2 / (Pr_c \sqrt{K})$
 θ = dimensionless temperature
 η = kinematic viscosity ratio
 μ = fluid viscosity
 ν = kinematic viscosity
 ρ = fluid density
 Ψ = stream function
 φ = generic variable
 ϕ = porosity
 ω = vorticity

Subscripts

am = arithmetic mean
 av = average
 C = cold wall

cp = constant property
 eff = effective
 H = hot wall

References

- [1] Narasimhan, A., and Lage, J. L., 2005, "Variable Viscosity Forced Convection in Porous Medium Channels," *Handbook of Porous Media*, K. Vafai, ed., Taylor & Francis, New York, pp. 195–233.
- [2] Nield, D. A., and Bejan, A., 2006, *Convection in Porous Media*, Springer-Verlag, New York.
- [3] Nield, D. A., 1994, "Estimation of an Effective Rayleigh Number for Convection in a Vertically Inhomogeneous Porous-Medium or Clear Fluid," *Int. J. Heat Fluid Flow*, **15**, pp. 337–340.
- [4] Nield, D. A., 1996, "The Effect of Temperature-Dependent Viscosity on the Onset of Convection in a Saturated Porous Medium," *ASME Trans. J. Heat Transfer*, **118**, pp. 803–805.
- [5] Chu, T. Y., and Hickox, C. E., 1990, "Thermal-Convection With Large Viscosity Variation in an Enclosure With Localized Heating," *ASME Trans. J. Heat Transfer*, **112**, pp. 388–395.
- [6] Siebers, D. L., Moffatt, R. F., and Schwind, R. G., 1985, "Experimental, Variable Properties Natural-Convection From a Large, Vertical, Flat Surface," *ASME Trans. J. Heat Transfer*, **107**, pp. 124–132.
- [7] Vafai, K., and Tien, C. L., 1981, "Boundary and Inertia Effects on Flow and Heat-Transfer in Porous-Media," *Int. J. Heat Mass Transfer*, **24**, pp. 195–203.
- [8] Hsu, C. T., and Cheng, P., 1990, "Thermal Dispersion in a Porous-Medium," *Int. J. Heat Mass Transfer*, **33**, pp. 1587–1597.
- [9] Guo, Z. L., and Zhao, T. S., 2005, "Lattice Boltzmann Simulation of Natural Convection With Temperature-Dependent Viscosity in a Porous Cavity," *Prog. Comput. Fluid Dyn.*, **5**, pp. 110–117.
- [10] Prasad, V., and Kulacki, F. A., 1984, "Natural-Convection in a Rectangular Porous Cavity With Constant Heat-Flux on One Vertical Wall," *ASME Trans. J. Heat Transfer*, **106**, pp. 152–157.
- [11] Merrikh, A. A., and Mohamad, A. A., 2002, "Non-Darcy Effects in Buoyancy Driven Flows in an Enclosure Filled With Vertically Layered Porous Media," *Int. J. Heat Mass Transfer*, **45**, pp. 4305–4313.
- [12] Antohe, B. V., and Lage, J. L., 1997, "The Prandtl Number Effect on the Optimum Heating Frequency of an Enclosure Filled With Fluid or With a Saturated Porous Medium," *Int. J. Heat Mass Transfer*, **40**, pp. 1313–1323.
- [13] Harms, T. M., Jog, M. A., and Manglik, R. M., 1998, "Effects of Temperature-Dependent Viscosity Variations and Boundary Conditions on Fully Developed Laminar Forced Convection in a Semicircular Duct," *ASME Trans. J. Heat Transfer*, **120**, pp. 600–605.
- [14] Kakaç, S., 1987, "The Effect of Temperature-Dependent Fluid Properties on Convective Heat Transfer," *Handbook of Single-Phase Convective Heat Transfer*, S. Kakaç, R. K. Shah, and W. Aung, eds., Wiley, New York.
- [15] Bejan, A., 2004, *Convection Heat Transfer*, Wiley, Hoboken, NJ.
- [16] Nield, D. A., Porneala, D. C., and Lage, J. L., 1999, "A Theoretical Study, With Experimental Verification, of the Temperature-Dependent Viscosity Effect on the Forced Convection Through a Porous Medium Channel," *ASME Trans. J. Heat Transfer*, **121**, pp. 500–503.
- [17] Nield, D. A., and Kuznetsov, A. V., 2003, "Effects of Temperature-Dependent Viscosity in Forced Convection in a Porous Medium: Layered-Medium Analysis," *J. Porous Media*, **6**, pp. 213–222.
- [18] Hooman, K., 2006 "Entropy-Energy Analysis of Forced Convection in a Porous-Saturated Circular Tube Considering Temperature-Dependent Viscosity Effects," *Int. J. Exergy*, **3**, pp. 436–451.
- [19] Hooman, K., and Gurgenci, H., 2007, "Effects of Temperature-Dependent Viscosity Variation on Entropy Generation, Heat, and Fluid Flow Through a Porous-Saturated Duct of Rectangular Cross-Section," *Appl. Math. Mech.*, **28**, pp. 69–78.
- [20] Lauriat, G., and Prasad, V., 1987, "Natural-Convection in a Vertical Porous Cavity—A Numerical Study for Brinkman-Extended Darcy Formulation," *ASME Trans. J. Heat Transfer*, **109**, pp. 688–696.

Moving Boundary-Moving Mesh Analysis of Freezing Process in Water-Saturated Porous Media Using a Combined Transfinite Interpolation and PDE Mapping Methods

P. Rattanadecho¹

Faculty of Engineering,
Thammasat University (Rangsit Campus),
Pathumthani 12121, Thailand
e-mail: ratphadu@engr.tu.ac.th

S. Wongwises

Department of Mechanical Engineering,
King Mongkut's University of Technology
Thonburi,
91 Suksawas 48,
Rasburana, Bangkok 10140, Thailand

This paper couples the grid generation algorithm with the heat transport equations and applies them to simulate the thermal behavior of freezing process in water-saturated porous media. Focus is placed on establishing a computationally efficient approach for solving moving boundary heat transfer problem, in two-dimensional structured grids, with specific application to an unidirectional solidification problem. Preliminary grids are first generated by an algebraic method, based on a transfinite interpolation method, with subsequent refinement using a partial differential equation (PDE) mapping (parabolic grid generation) method. A preliminary case study indicates successful implementation of the numerical procedure. A two-dimensional solidification model is then validated against available analytical solution and experimental results and subsequently used as a tool for efficient computational prototyping. The results of the problem are in good agreement with available analytical solution and experimental results.

[DOI: 10.1115/1.2780177]

Keywords: solidification, transfinite interpolation, PDE mapping, moving boundary

Introduction

Transient heat transfer problems involving solidification or melting processes generally refer to as “moving boundary” or “phase change.” Solidification and melting are important parts of manufacturing processes such as crystal growth, casting, welding, coating process, thermal energy storage, aerodynamic ablation, pipeline transport in permafrost regions, and cryosurgery and in the transportation of coal in coal weather, thermal energy storage, ice accretion on vehicles and static structures, solidification of alloys, food processing, freeze drying, chemical processes, and cryopreservation of engineering tissues. In all these processes, phase changes of material are caused by the heat transfer to and from both of the phases on either side of the interface. This yields melting if the net heat is added to the solid part of the interface and solidification when the net heat is subtracted.

Up to the present time, the related problems of solidification process in 1D have been investigated both experimentally and numerically by many researchers and up to date reviews are available; Landua [1], Murray and Landis [2], Frivik and Comini [3], Sparrow and Broadbent [4], Voller and Cross [5], Weaver and Viskanta [6], Chellaiah and Viskanta [7], Hasan et al. [8], Charn-Jung and Kaviani [9], Rattanadecho [10,11], Pak and Plumb [12], Hao and Tao [13], Attinger and Poulikakos [14], Jiang et al. [15], Hao and Tao [16], Elgafy et al. [17], and Ayasoufi et al. [18]. Regarding specific analysis to moving boundary problems, in a 2D or 3D, there have been significant research studies executed in

the recent past including Lynch [19], Cao et al. [20], Chatterjee and Prasad [21], Duda et al. [22], Saitoh [23], Gong and Mujumdar [24], and Beckett et al. [25].

When solving a moving boundary problem, complication arises because the interface between the solid and liquid phases is moving as the latent heat is absorbed or released at the interface. As such, the position of the interface is not known a priori and the domains over which the energy equations are solved vary. Also, physical quantities such as enthalpy and transport properties vary discontinuously across these interfaces. Therefore, solutions to moving boundary problems, especially for multidimensional domains, should cope with difficulties associated with the nonlinearity in the interfacial conditions and unknown positions of arbitrary interfaces. Moreover, in numerical approximations of this problem with discontinuous coefficients, often the largest numerical errors are introduced in a neighborhood of the discontinuities. These errors are often greatly reduced if the grid generation and solution procedure are separated with the discontinuities and special formulas are used to incorporate the jump conditions directly into the numerical model.

It is well known that the construction itself of a coordinate grid in a specified domain is not a trivial matter and the numerical solution of the governing partial differential equations upon it is indeed a formidable computational task, which in turn puts a high premium on grid generator that can provide an optimum resolution with an economy of nodal points. It is found that these two items, grid generation and solution procedure, are separate and distinct operations, and as such should be treated in an independent and modular way. The means for grid generation should not be dictated by the limitations of a given specific flow solution procedure and conversely the method that determines the flow should accept as input an arbitrary set of coordinate points, which constitutes the grid. In general, of course, these two operations

¹Corresponding author.

Contributed by the Heat Transfer Division of ASME for publication in the JOURNAL OF HEAT TRANSFER. Manuscript received June 14, 2006; final manuscript received April 20, 2007; published online January 25, 2008. Review conducted by Jose L. Lage.

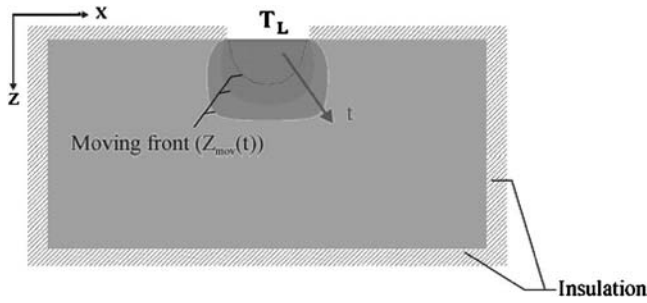


Fig. 1 Physical model

can never be totally independent because the logistic structure of the information, the location of outer boundaries, the nature of coordinate, and the types of grid singularities are items that have to be closely coordinated between the flow solver and the grid generator (Eriksson [26]). Grid generation for multidimensional geometries using transfinite interpolation functions was studied by Coons [27], Cook [28], and Gordon and Hall [29]. Ettouney and Brown [30] successfully modeled slightly nonplanar interfaces by using an algebraic grid generation system where the interface was described in terms of univariate function.

Although grid generation is the heart of most numerical algorithms for flow problems or nonphase change problem, little effort has been reported on phase change problems, particularly the problem that is to couple the grid generation algorithm with the heat transport equations.

This paper deals with thermodynamically consistent numerical predictions of freezing process of water in a rectangular cavity filled with a porous medium subjected to a constant temperature heat sink using moving grids. They will also permit a continuous determination of the unidirectional freezing front move and indicate the internal temperature distribution with a greater degree of boundary complexity and offer the highest overall accuracies and smooth grid point distribution. Numerically, for generating a boundary/interface fitted coordinate system, structured grids are initialized using transfinite interpolation algebraic methods and the quality of structured grids can be significantly improved by applying parabolic-partial differential equation (PDE) methods. These methods iteratively solve unsteady conduction's equation together with moving boundary condition considering conduction as the only mode of heat transfer.

Analysis of Heat Transport and Freezing Front

The two-dimensional system illustrated schematically in Fig. 1 is considered. Initially, the walls are all insulated and the rectangular cavity is filled with a porous medium (PM) consisting of the glass beads and phase change material (PCM) in the liquid state (water), both at the fusion temperature T_f . At time, $t > 0$, a strip of isothermal surface, T_L , less than the fusion temperature is imposed on the partial top wall. Freezing is initiated at this partial wall and the freezing interface moves from top to bottom.

Assumptions. In order to analyze the process of heat transport due to freezing of water in a rectangular cavity filled with a PM subjected to a constant temperature heat sink, we introduce the following assumptions:

- (1) The temperature field can be assumed to be two dimensional.
- (2) The thermal equilibrium exists between PCM and PM; this is possible when the porous matrix has a little larger thermal conductivity than the PCM, and the interphase heat transfer can be properly neglected.
- (3) Properties of PM are isotropic.
- (4) The volumetric change due to solidification is negligible.
- (5) The effect of the natural convection in liquid is negligible.

Table 1 Thermal properties of the unfrozen layer and frozen layer

Properties	Unfrozen layer	Frozen layer
ρ (kg/m ³)	1942.0	1910.0
a (m ² /s)	0.210×10^{-6}	0.605×10^{-6}
λ (W/m K)	0.855	1.480
c_p (J/kg K)	2.099×10^3	1.281×10^3

Basic Equations. The applicable differential equation for two-dimensional heat flow with averaged thermal properties in both the unfrozen and frozen layers, are, respectively,

$$\frac{\partial T_l}{\partial t} = a_l \left(\frac{\partial^2 T_l}{\partial x^2} + \frac{\partial^2 T_l}{\partial z^2} \right) \quad (1)$$

$$\frac{\partial T_s}{\partial t} = a_s \left(\frac{\partial^2 T_s}{\partial x^2} + \frac{\partial^2 T_s}{\partial z^2} \right) \quad (2)$$

After some mathematical manipulations, a transformation model of the original governing differential equations becomes [2]

$$\frac{\partial T_l}{\partial t} = a_l \left(\frac{\partial^2 T_l}{\partial x^2} + \frac{\partial^2 T_l}{\partial z^2} \right) + \left(\frac{\partial T_l}{\partial z} \right) \frac{dz}{dt} \quad (3)$$

$$\frac{\partial T_s}{\partial t} = a_s \left(\frac{\partial^2 T_s}{\partial x^2} + \frac{\partial^2 T_s}{\partial z^2} \right) + \left(\frac{\partial T_s}{\partial z} \right) \frac{dz}{dt} \quad (4)$$

where the last terms of Eqs. (3) and (4) result from a coordinate transformation attached to the moving boundary. In the unfrozen layer, if internal natural convection can be neglected because the presence of glass beads minimizes the effect of natural convection current.

Treatment of the Moving Boundary. A consideration of the energy balance at the interface between the unfrozen layer and frozen layer provides the following equation (moving boundary or Stefan condition):

$$\left(\lambda_s \frac{\partial T_s}{\partial z} - \lambda_l \frac{\partial T_l}{\partial z} \right) \left[1 + \left(\frac{\partial z_{\text{mov}}}{\partial x} \right)^2 \right] = \rho_s L_s \frac{\partial z_{\text{mov}}}{\partial t} \quad (5)$$

where $\partial z_{\text{mov}} / \partial t$ is the velocity of fusion front or freezing front, and L_s the latent heat of fusion. To avoid changes in the physical dimensions as the freezing front progresses, $\rho_s = \rho_l$ will be specified. In this study, the thermal conductivity, λ_l and λ_s , are bulk-average values for the glass beads and the water or ice, respectively (refer to Table 1).

Boundary Conditions. Subject to appropriate initial condition and the boundary conditions are as follows:

- (a) *The localized freezing condition.* The constant temperature heat sink is imposed on the partial top wall:

$$T = T_L \quad (6)$$

- (b) *Adiabatic condition.* The walls except the position of localized heating condition are all insulated:

$$\frac{\partial T}{\partial x} = \frac{\partial T}{\partial z} = 0 \quad (7)$$

Grid Generation by Transfinite Interpolation and PDE Mapping

Generally, two types of structured grid generation are in use: algebraic method, i.e., transfinite interpolation and PDE methods. Transfinite interpolation method provides a relatively easy way of obtaining an initial grid that can be refined and smoothed by other techniques, whether algebraic, PDE method. For more complex

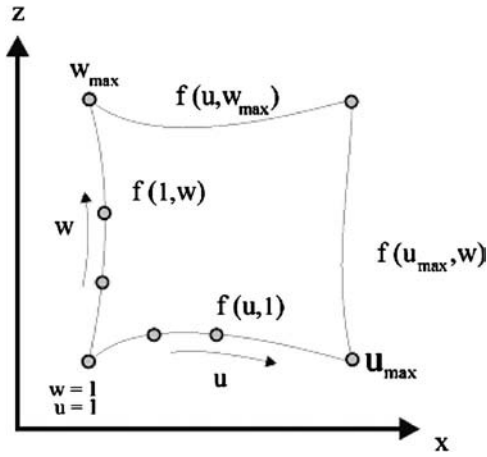


Fig. 2 The parametric domain with $f_{(u,w)}$ specified on planes of constant u, w

geometries, such as this work, it is preferable to construct grid initially by transfinite interpolation and to refine the grid filled in Cartesian coordinates in the interior of a domain by parabolic-PDE method subsequently.

Transfinite Interpolation. The present method of constructing a two-dimensional boundary-conforming grid for a freezing sample is a direct algebraic approach based on the concept of transfinite interpolation. In this method, no partial differential equations are solved to obtain the curvilinear coordinates, and the same system is used for the entire domain. The algebraic method can be easier to construct than PDE mapping methods and give easier control over grid characteristics, such as orthogonality and grid point spacing. However, this method is sometime criticized for allowing discontinuities on the boundary to propagate into the interior and for not generating grids as smooth as those generated by the PDE mapping method. The main idea behind this work, prior to generation of grids by PDE mapping methods, it is preferable to obtain first preliminary grids using the algebraic method, i.e., transfinite interpolation method. The combined transfinite interpolation and PDE mapping methods are used to achieve a very smoother grid point distribution and boundary point discontinuities are smoothed out in the interior domain.

For the concept of transfinite interpolation method, a significant extension of the original formulation by Gordon and Hall [29] have made it possible to initially generate global grid system with geometry specifications only on the outer boundaries of the computation domain and yet obtain a high degree of local control. Moreover, to successfully track the moving boundary front, the grid generation mapping must adapt to large deformations of the interface shape while maintaining as much orthogonality and smoothness as possible. Due to the generality of the method, it has been possible to use more advanced mappings than conventional types and thereby improve the overall efficiency of the grid in terms of computational work for a given resolution.

In Fig. 2, the present method of constructing a two-dimensional boundary-conforming grid for a sample is a direct algebraic approach based on the concept of transfinite or multivariate interpolation. It is possible to initially generate global single plane transformations with geometry specifications only on outer boundaries of the computational domain.

Let $f(u, w) = [x(u, w), z(u, w)]$ denote a vector-valued function of two parameters u, w defined on the region $u_1 \leq u \leq u_{\max}, w_1 \leq w \leq w_{\max}$. This function is not known throughout the region, only on certain planes (Fig. 2).

The transfinite interpolation procedure then gives the interpolation function $f_{(u,w)}$ by the recursive algorithm:

$$f_{(u,w)}^{(1)} = A_{1(u)}f_{(1,w)} + A_{2(u)}f_{(u_{\max},w)}$$

$$f_{(u,w)} = f_{(u,w)}^{(1)} + B_{1(w)}[f_{(u,1)} - f_{(u,1)}^{(1)}] + B_{2(w)}[f_{(u,w_{\max})} - f_{(u,w_{\max})}^{(1)}] \quad (8)$$

where $A_{1(u)}, A_{2(u)}, B_{1(w)}$, and $B_{2(w)}$ defined the set of univariate blending functions, which only have to satisfy the following conditions:

$$A_{1(1)} = 1 \quad A_{1(u_{\max})} = 0$$

$$A_{2(1)} = 0 \quad A_{2(u_{\max})} = 1$$

$$B_{1(1)} = 1 \quad B_{1(w_{\max})} = 0$$

$$B_{2(1)} = 0 \quad B_{2(w_{\max})} = 1$$

Further, the general form in algebraic equations can be defined as

$$A_{1(u)} = \frac{u_{\max} - u}{u_{\max} - 1} \quad A_{2(u)} = 1 - A_{1(u)}$$

$$B_{1(w)} = \frac{w_{\max} - w}{w_{\max} - 1} \quad B_{2(w)} = 1 - B_{1(w)} \quad (9)$$

The grid motion defined from a moving boundary motion is modeled using a Stefan equation (Eq. (13)) with a transfinite mapping method.

PDE Mapping. In the proposed grid generation mapping, all grids discussed and displayed have been couched in terms of finite difference algorithm applications, with the understanding that whatever nonuniform grid exists in the physical space, there exists a transformation which will recast it as a uniform rectangular grid in the computational space. The implicit-finite difference calculations are then made over this uniform grid in the computational space, after which the field results are transferred directly back to the corresponding points in the physical space. The purpose of generating a smooth grid that conforms to physical boundaries of problem is, of course, to solve the partial differential equations specified in the problem by finite difference scheme, capable of handling general nonorthogonal curvilinear coordinates.

Corresponding to Fig. 1, as freezing proceeds, a freezing front denoted here z_{mov} is formed. Due to the existence of this freezing front, the frozen (ice) and unfrozen (water) domains are irregular and time dependent. To avoid this difficulty, a curvilinear system of coordinates is used to transform the physical domain into rectangular region for the computational domain.

It is convenient to introduce a general curvilinear coordinate system as follows (Anderson [31]):

$$x = x(\xi, \eta) \quad z = z(\xi, \eta) \quad \text{or} \quad \xi = \xi(x, z) \quad \eta = \eta(x, z) \quad (10)$$

The moving boundaries are immobilized in the dimensionless (ξ, η) coordinate for all times. With the details omitted, then the transformation of Eqs. (3) and (5) can be written, respectively, as:

$$\begin{aligned} \frac{\partial T_l}{\partial t} = & \frac{a_l}{J^2} \left(\alpha \frac{\partial^2 T_l}{\partial \xi^2} - 2\beta \frac{\partial^2 T_l}{\partial \xi \partial \eta} + \gamma \frac{\partial^2 T_l}{\partial \eta^2} \right) + \frac{a_l}{J^3} \left[\left(\alpha \frac{\partial^2 x}{\partial \xi^2} \right) \left(z_{\xi} \frac{\partial T_l}{\partial \eta} \right. \right. \\ & \left. \left. - z_{\eta} \frac{\partial T_l}{\partial \xi} \right) + \alpha \frac{\partial^2 z}{\partial \xi^2} - 2\beta \frac{\partial^2 z}{\partial \xi \partial \eta} + \gamma \frac{\partial^2 z}{\partial \eta^2} \left(-x_{\xi} \frac{\partial T_l}{\partial \eta} \right) \right] \\ & + \frac{1}{J} \left(x_{\xi} \frac{\partial T_l}{\partial \eta} \right) \frac{dz}{dt} \end{aligned} \quad (11)$$

$$\frac{\partial T_s}{\partial t} = \frac{a_s}{J^2} \left(\alpha \frac{\partial^2 T_s}{\partial \xi^2} - 2\beta \frac{\partial^2 T_s}{\partial \xi \partial \eta} + \gamma \frac{\partial^2 T_s}{\partial \eta^2} \right) + \frac{a_s}{J^3} \left[\left(\alpha \frac{\partial^2 x}{\partial \xi^2} \right) \left(z_\xi \frac{\partial T_s}{\partial \eta} - z_\eta \frac{\partial T_s}{\partial \xi} \right) + \alpha \frac{\partial^2 z}{\partial \xi^2} - 2\beta \frac{\partial^2 z}{\partial \xi \partial \eta} + \gamma \frac{\partial^2 z}{\partial \eta^2} \left(-x_\xi \frac{\partial T_s}{\partial \eta} \right) \right] + \frac{1}{J} \left(x_\xi \frac{\partial T_s}{\partial \eta} \right) \frac{dz}{dt} \quad (12)$$

$$\left[\lambda_s \frac{1}{J} \left(x_\xi \frac{\partial T_s}{\partial \eta} \right) - \lambda_l \frac{1}{J} \left(x_\xi \frac{\partial T_l}{\partial \eta} \right) \right] \left\{ 1 + \left[\frac{1}{J} \left(z_\eta \frac{\partial z_{\text{mov}}}{\partial \xi} - z_\xi \frac{\partial z_{\text{mov}}}{\partial \eta} \right) \right]^2 \right\} = \rho_s L_s \frac{\partial z_{\text{mov}}}{\partial t} \quad (13)$$

where $J = x_\xi z_\eta - x_\eta z_\xi$, $\alpha = x_\eta^2 + z_\eta^2$, $\beta = x_\xi x_\eta + z_\xi z_\eta$, $\gamma = x_\xi^2 + z_\xi^2$ and x_ξ, x_η, z_ξ , and z_η denote partial derivatives, J is the Jacobian,

β, α, γ are the geometric factors, and η, ξ are the transformed coordinates.

Solution Method

In order to initiate numerical simulation, a very thin layer of freeze with a constant thickness $z_{\text{mov}(0)}$ was assumed to be present. This initial condition is obtained from the Stefan solution in the freeze and a linear temperature distribution in the frozen layer. Tests revealed that the influence of $z_{\text{mov}(0)}$ could be neglected as $z_{\text{mov}(0)}$ was sufficiently small.

The transient heat equations (Eqs. (11) and (12)) and the Stefan equation (Eq. (13)) are solved by using implicit-finite difference method. A system of nonlinear equations results whereby each equation for the internal nodes can be cast into a numerical discretization.

In transient heat equation for unfrozen layer,

$$T_l^{n+1}(k, i) = \left(\frac{1}{1 + \frac{2a_l \Delta t}{J^2(k, i)} \{ [\alpha(k, i) / \Delta \zeta \Delta \xi] + [\gamma(k, i) / \Delta \eta \Delta \eta] \}} \right) \left(T_l^n(k, i) + \frac{a_l \Delta t}{J^2(k, i)} \left[\alpha(k, i) \frac{T_l^{n-1}(k, i+1) + T_l^{n+1}(k, i-1)}{\Delta \zeta \Delta \xi} \right] - 2\beta(k, i) \right) \times \left\{ \left[\frac{T_l^{n-1}(k+1, i+1) - T_l^{n+1}(k-1, i+1)}{2\Delta \eta} - \frac{T_l^{n-1}(k+1, i-1) - T_l^{n+1}(k-1, i-1)}{2\Delta \zeta} \right] \right\} / 2\Delta \zeta + \gamma(k, i) \times \left[\frac{T_l^{n-1}(k+1, i) + T_l^{n+1}(k-1, i)}{\Delta \eta \Delta \eta} \right] + \frac{a_l \Delta t}{J^3(k, i)} \left(\left[\alpha(k, i) \frac{X(k, i+1) - 2X(k, i) + X(k, i-1)}{\Delta \zeta \Delta \zeta} \right] \left\{ \left[\frac{Z(k, i+1) - Z(k, i-1)}{2\Delta \zeta} \right] \right\} \right) \times \left[\frac{T_l^{n-1}(k+1, i) - T_l^{n+1}(k-1, i)}{2\Delta \eta} \right] - \left[\frac{Z(k+1, i) - Z(k-1, i)}{2\Delta \eta} \right] \left[\frac{T_l^{n-1}(k, i+1) - T_l^{n+1}(k, i-1)}{2\Delta \zeta} \right] + \alpha(k, i) \times \left[\frac{Z(k, i+1) - 2Z(k, i) + Z(k, i-1)}{\Delta \zeta \Delta \zeta} \right] - 2\beta(k, i) \left\{ \left[\frac{Z(k+1, i+1) - Z(k-1, i+1)}{2\Delta \eta} \right] - \left[\frac{Z(k+1, i-1) - Z(k-1, i-1)}{2\Delta \eta} \right] \right\} / 2\Delta \zeta + \gamma(k, i) \left[\frac{Z(k+1, i) - 2Z(k, i) + Z(k-1, i)}{\Delta \eta \Delta \eta} \right] * \left\{ - \frac{[X(k, i+1) - X(k, i-1)]}{2\Delta \zeta} \right\} \times \left[\frac{T_l^n(k+1, i) - T_l^n(k-1, i)}{2\Delta \eta} \right] + \frac{1}{J(k, i)} \left[\frac{X(k, i+1) - X(k, i-1)}{2\Delta \zeta} \right] \left[\frac{T_l^n(k+1, i) - T_l^n(k-1, i)}{2\Delta \eta} \right] dz(k, i) \quad (14)$$

In transient heat equation for frozen layer,

$$T_s^{n+1}(k, i) = \left(\frac{1}{1 + [2a_l \Delta t / J^2(k, i)] \{ [\alpha(k, i) / \Delta \zeta \Delta \xi] + [\gamma(k, i) / \Delta \eta \Delta \eta] \}} \right) \left(T_s^n(k, i) + \frac{a_l \Delta t}{J^2(k, i)} \left[\alpha(k, i) \frac{T_s^{n-1}(k, i+1) + T_s^{n+1}(k, i-1)}{\Delta \zeta \Delta \xi} \right] - 2\beta(k, i) \right) \times \left\{ \left[\frac{T_s^{n-1}(k+1, i+1) - T_s^{n+1}(k-1, i+1)}{2\Delta \eta} - \frac{T_s^{n-1}(k+1, i-1) - T_s^{n+1}(k-1, i-1)}{2\Delta \zeta} \right] \right\} / 2\Delta \zeta + \gamma(k, i) \times \left[\frac{T_s^{n-1}(k+1, i) + T_s^{n+1}(k-1, i)}{\Delta \eta \Delta \eta} \right] + \frac{a_l \Delta t}{J^3(k, i)} \left(\left[\alpha(k, i) \frac{X(k, i+1) - 2X(k, i) + X(k, i-1)}{\Delta \zeta \Delta \zeta} \right] \left\{ \left[\frac{Z(k, i+1) - Z(k, i-1)}{2\Delta \zeta} \right] \right\} \right) \times \left[\frac{T_s^{n-1}(k+1, i) - T_s^{n+1}(k-1, i)}{2\Delta \eta} \right] - \left[\frac{Z(k+1, i) - Z(k-1, i)}{2\Delta \eta} \right] \left[\frac{T_s^{n-1}(k, i+1) - T_s^{n+1}(k, i-1)}{2\Delta \zeta} \right] + \alpha(k, i) \times \left[\frac{Z(k, i+1) - 2Z(k, i) + Z(k, i-1)}{\Delta \zeta \Delta \zeta} \right] - 2\beta(k, i) \left\{ \left[\frac{Z(k+1, i+1) - Z(k-1, i+1)}{2\Delta \eta} \right] - \left[\frac{Z(k+1, i-1) - Z(k-1, i-1)}{2\Delta \eta} \right] \right\} / 2\Delta \zeta + \gamma(k, i) \left[\frac{Z(k+1, i) - 2Z(k, i) + Z(k-1, i)}{\Delta \eta \Delta \eta} \right] * \left\{ - \frac{[X(k, i+1) - X(k, i-1)]}{2\Delta \zeta} \right\} \times \left[\frac{T_s^n(k+1, i) - T_s^n(k-1, i)}{2\Delta \eta} \right] + \frac{1}{J(k, i)} \left[\frac{X(k, i+1) - X(k, i-1)}{2\Delta \zeta} \right] \left[\frac{T_s^n(k+1, i) - T_s^n(k-1, i)}{2\Delta \eta} \right] * dz(k, i) \quad (15)$$

In Stefan condition,

$$\begin{aligned}
Z^{n+1}(k,i) = & Z^n(k,i) + \frac{\Delta T}{\rho_s L_s} \left\{ \left[\frac{\lambda_s}{J(k-1,i)} * \left[\frac{X(k-1,i+1) - X(k-1,i-1)}{2\Delta\zeta} \right] \left[\frac{3T(k,i) - 4T(k-1,i) + T(k-2,i)}{2\Delta\eta} \right] \right. \right. \\
& - \left. \frac{\lambda_l}{J(k+1,i)} * \left[\frac{X(k+1,i+1) - X(k+1,i-1)}{2\Delta\zeta} \right] \left[\frac{-3T(k,i) + 4T(k+1,i) - T(k+2,i)}{2\Delta\eta} \right] \right\} \left(1 + \left[\frac{Z^n(k+1,i) - Z^n(k-1,i)}{2\Delta\eta} \right] \right) \\
& \times \left[\frac{Z^n(k+1,i) - Z^n(k-1,i)}{2\Delta\zeta} \right] - \left[\frac{Z^n(k,i+1) - Z^n(k,i-1)}{2\Delta\zeta} \right] \left[\frac{Z^n(k,i+1) - Z^n(k,i-1)}{2\Delta\eta} \right]^2 \quad (16)
\end{aligned}$$

The details of computational schemes and strategy for solving the combined transfinite interpolation functions (Eqs. (8) and (9)) and PDE mapping (Eqs. (14)–(16)) are illustrated in Fig. 3.

The calculation conditions were as follows:

- (1) The time step of $dt=1$ s is used for the computation of

temperature field and location of freezing front.

- (2) Number of grid: $N=100(\text{length}) \times 100(\text{height})$.

- (3) Relative errors in the iteration procedure of 10^{-8} were chosen.

Experiment

The freezing experiments are performed in a rectangular test cell filled with a PM (porosity, $\phi=0.4$) with inside dimensions of 10 cm in length (x), 5 cm in height (z), and 2.5 cm in depth (y). The partial horizontal top wall and bottom wall and the vertical front and back walls are made of acrylic resin with a thickness of 3 mm. The entire test cell is covered with 8 cm thick Styrofoam on all sides to minimize the effect of heat losses and condensation of moisture at the walls. The partial top wall, which serves as a constant temperature heat sink, is multipass heat exchanger. Heat exchanger is connected through a valve system to constant temperature bath where the liquid nitrogen is used as the cooling medium. The distributions of temperature within the sample are measured using the thermocouples with a diameter of 0.15 mm. Thirty thermocouples are placed at the midplane of test cell ($y=1.25$ cm) in both horizontal and vertical directions ($x-z$ plane) with longitudinal and transverse intervals of 10 mm. These thermocouples are connected to data logger and computer through which the temperatures could be measured and store at pre-selected time intervals. The positions of freezing front in the sample are determined by interpolating the fusion temperature from the thermocouple reading.

The uncertainty in the results might come from the variations in humidity, room temperature, and human error. The calculated uncertainty associated with temperature is less than 2.70%. The calculated uncertainties in all tests are less than 2.75%.

Results and Discussions

Validation Test. In order to verify the accuracy of the present numerical study, the present numerical algorithm was validated by performing simulations for a planar freezing front in a phase change slab (water) with a dimension of 10 cm(x) \times 5 cm(z). The initial temperature of 0°C is described throughout each layer. Thereafter, the constant temperature heat sink ($T_L=-80^\circ\text{C}$) is imposed on the partial top wall. The results are compared with the analytical solution appeared in the classical paper [32], which is also commonly referred to in literature, for the freezing of a phase change slab (water) at the same condition. Figure 4 clearly shows a good agreement of the locations of freezing front. All of these favorable comparisons lend confidence in the accuracy of the numerical results of the present work.

Freezing Front Tracking Grid Generation System. To illustrate the efficiency of the grid generation system during the freezing of water in a rectangular cavity with a dimension of 10 cm(x) \times 5 cm(z) filled with a PM (porosity, $\phi=0.4$) subjected to a constant temperature heat sink (single heat sink with strip length of 20 mm), the initial temperature of 0°C is described throughout each layer. Thereafter, the constant temperature heat sink ($T_L=-40^\circ\text{C}$) is imposed on the partial top wall. The calcu-

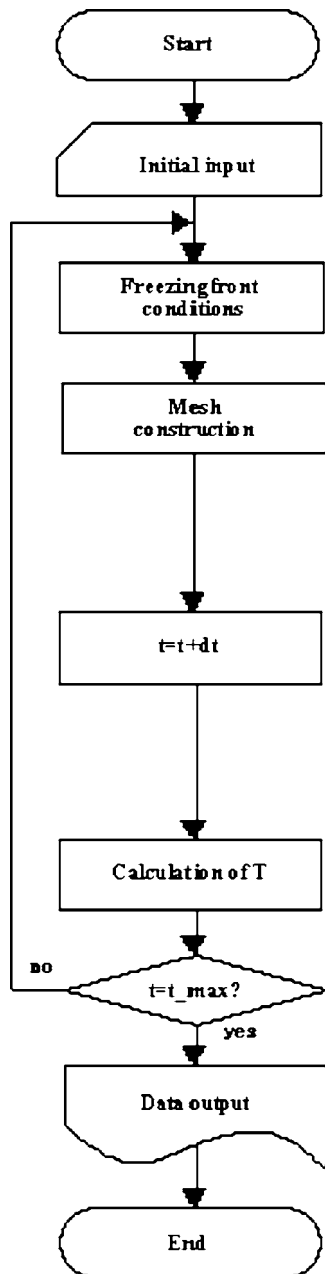


Fig. 3 Strategy for calculation

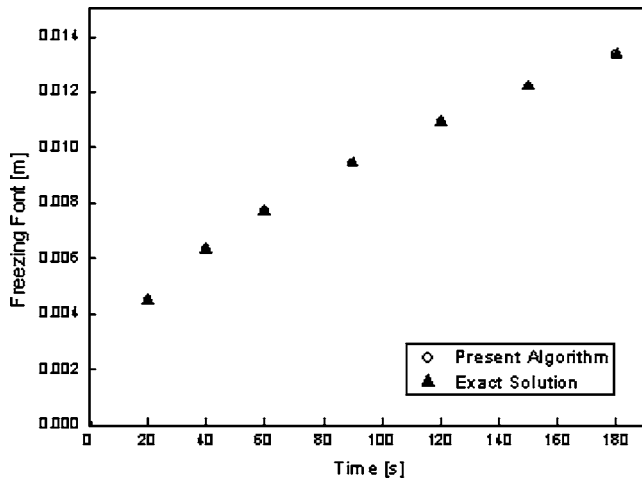


Fig. 4 Validation test for a planar freezing front in a phase-change slab

lated results are based on the thermal properties from Table 1.

In order to check the influence of numerical grid on the solutions, computations were carried out using 100×50 and 100×100 grids on entire computational domain, respectively. The results obtained from this study are presented in Fig. 5 in the form of an interface deformation (freezing front). It is obvious from the figure that with the present method, the overall interface deformation qualitatively remains the same for two different grids; however, the spreading of the melt in both directions in the first case (using 100×50 grids) is higher than the second case (using 100×100 grids). In addition, it is also evident that the solution was yet to reach a grid independent state. At this point, it may be mentioned here that the main objective of the present paper is not to demonstrate the features of phase change freezing problem but

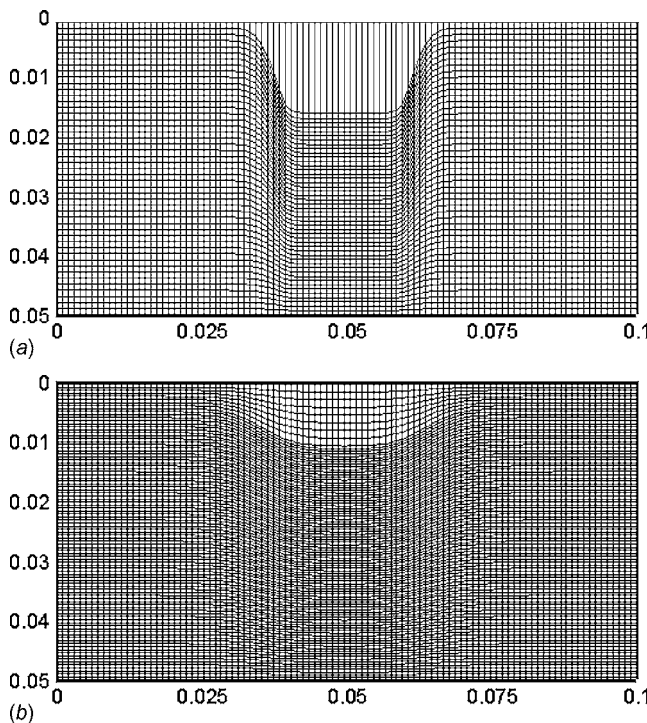


Fig. 5 The interface deformation in computational domain with different numerical grids: (a) 100×50 grids (b) 100×100 grids

to present novel numerical approach to solve phase change problem on a moving grids. Hence, no further study was carried out to obtain a grid independent solution and all the subsequent results are presented for 100×100 grid.

The following results (Figs. 6(a)–6(f)) show grids that fit curves, which are the typical shapes seen during deformation of an interface with respect to elapsed times. Furthermore, the grids show significant variation of density and skewness along the interface. It can be seen that the location of freezing front is progressed with respect to elapsed times. During the initial stages of freezing, the shape of the interface in each region becomes flatter as the freezing front moves further away from the fixed boundary indicating principally 1D heat flow. As time progresses, the curve on the interface gradually beetles indicating the 2D effect.

Figure 7 shows the measured and simulated results of the freezing front during the freezing of water in a rectangular cavity (with a dimension of $10 \text{ cm}(x) \times 5 \text{ cm}(z)$) filled with a PM subjected to a constant temperature heat sink. In this comparison, the single constant temperature heat sink, $T_L = -40^\circ\text{C}$, is applied. The observation of the freezing front depicted from the figure reveals that the simulated results and experimental results are qualitatively consistent. However, the experimental data are significantly lower than the simulated results. Discrepancy may be attributed to heat loss and nonuniform heating effect along the surface of supplied load. Numerically, the discrepancy may be attributed to uncertainties in the thermal and physical property data. In addition, the source of the discrepancy may be attributed to natural convection effect in liquid.

It is found that the grid is able to maintain a significant amount of orthogonality and smoothness both within the interior and along the boundary as the grid points redistributed themselves to follow the interface. These results show the efficiency of the present method for the moving boundary problem.

Freezing Process. The present work is to couple the grid generation algorithm with the transport equations. The thermal analysis during freezing process will be discussed in this section. The simulations of temperature distribution within rectangular cavity filled with porous media in the vertical plane ($x-z$) corresponding to grid simulating the deformation of an interface (Figs. 6(a)–6(f)) are shown in Figs. 8(a)–8(f)). Since the present work is to couple the grid generation algorithm with the transport equations, the thermal analysis during freezing process will be discussed as follows. When a constant temperature heat sink is applied during localized freezing process, heat is conducted from the hotter region in unfrozen layer to the cooler region in frozen layer. At the initial stages of freezing, the freezing fronts seem to be a square in shape indicating principally 1D heat flow, as explained for Figs. 6(a)–6(f)). Later, the freezing fronts gradually exhibit a typical shape for 2D heat conduction dominated freezing. However, as the freezing process persists, the freezing rate progresses slowly. This is because most of heat conduction takes place the leading edge of frozen layer (freeze layer), which is located further from unfrozen layer. Consequently, small amount of heat can conduct to the frozen layer due to the freeze region acting as an insulator and causing freezing fronts to move slowly with respect to elapsed times. Considering the shapes of the freezing front with respect to elapsed times, each freezing region of the rectangular cavity shows signs of freezing, while the outer edge displays no obvious sign of freezing indicating that the temperature does not fall below 0°C . Nevertheless, at the long stages of freezing, the spreading of the freeze in both the $x-z$ directions (semicircular shape) is clearly shown.

This study shows the capability of the present method to correctly handle the phase change problem. With further quantitative validation of the present method, this method can be used as a tool for investigating in detail this particular freezing of phase change slab at a fundamental level.

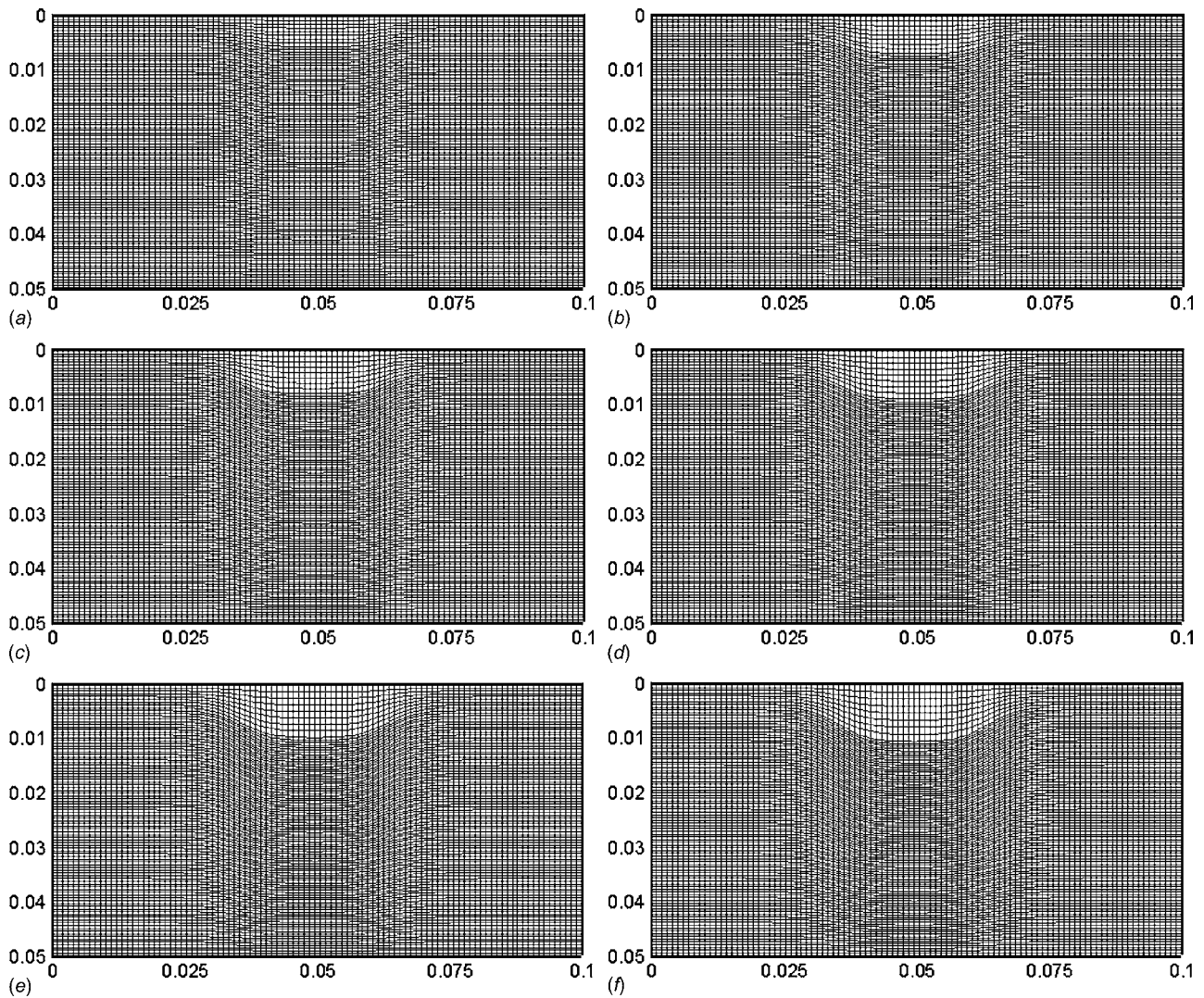


Fig. 6 Grid simulating the deformation of an interface: (a) freezing time of 30 s, (b) freezing time of 60 s, (c) freezing time of 90 s, (d) freezing time of 120 s, (e) freezing time of 150 s, and (f) freezing time of 180 s

Conclusions

Mesh quality has the largest impact on solution quality. A high quality mesh increases the accuracy of the computational flow

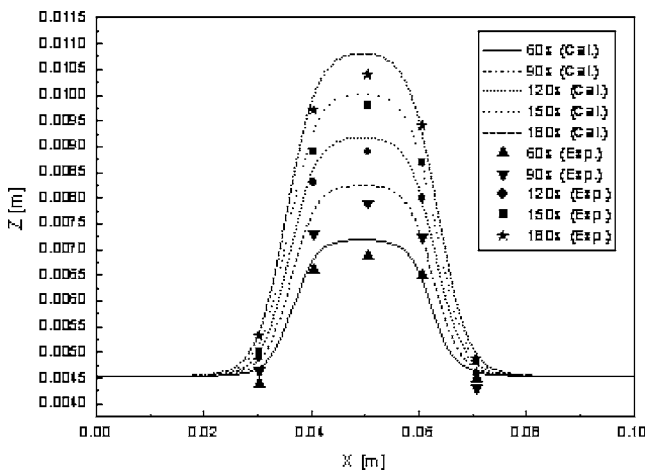


Fig. 7 Comparison of experimental data and simulated freezing front from present numerical study

solution and improves convergence. Therefore, it is important to provide tools for obtaining and improving a mesh.

In this study, the freezing of water in a rectangular cavity filled with a PM subjected to a constant temperature heat sink has been investigated numerically. A generalized mathematical model and an effective calculation procedure is proposed. A preliminary case study indicates the successful implementation of the numerical procedure. A two-dimensional freezing model is then validated against available analytical solutions and experimental results and subsequently used as a tool for efficient computational prototyping. Simulated results are in good agreement with available analytical solution and experimental results. The successful comparison with analytical solution and experiments should give confidence in the proposed mathematical treatment, and encourage the acceptance of this method as useful tool for exploring practical problems.

The next phase, which has already begun, is to couple the grid generation algorithm with the complete transport equations that determine the moving boundary front and buoyancy-driven convection in the unfrozen layer (liquid). Moreover, some experimental studies will be performed to validate numerical results.

Acknowledgments

The authors are pleased to acknowledge Thailand Research Fund for supporting this research work. Professor K. Aoki of the

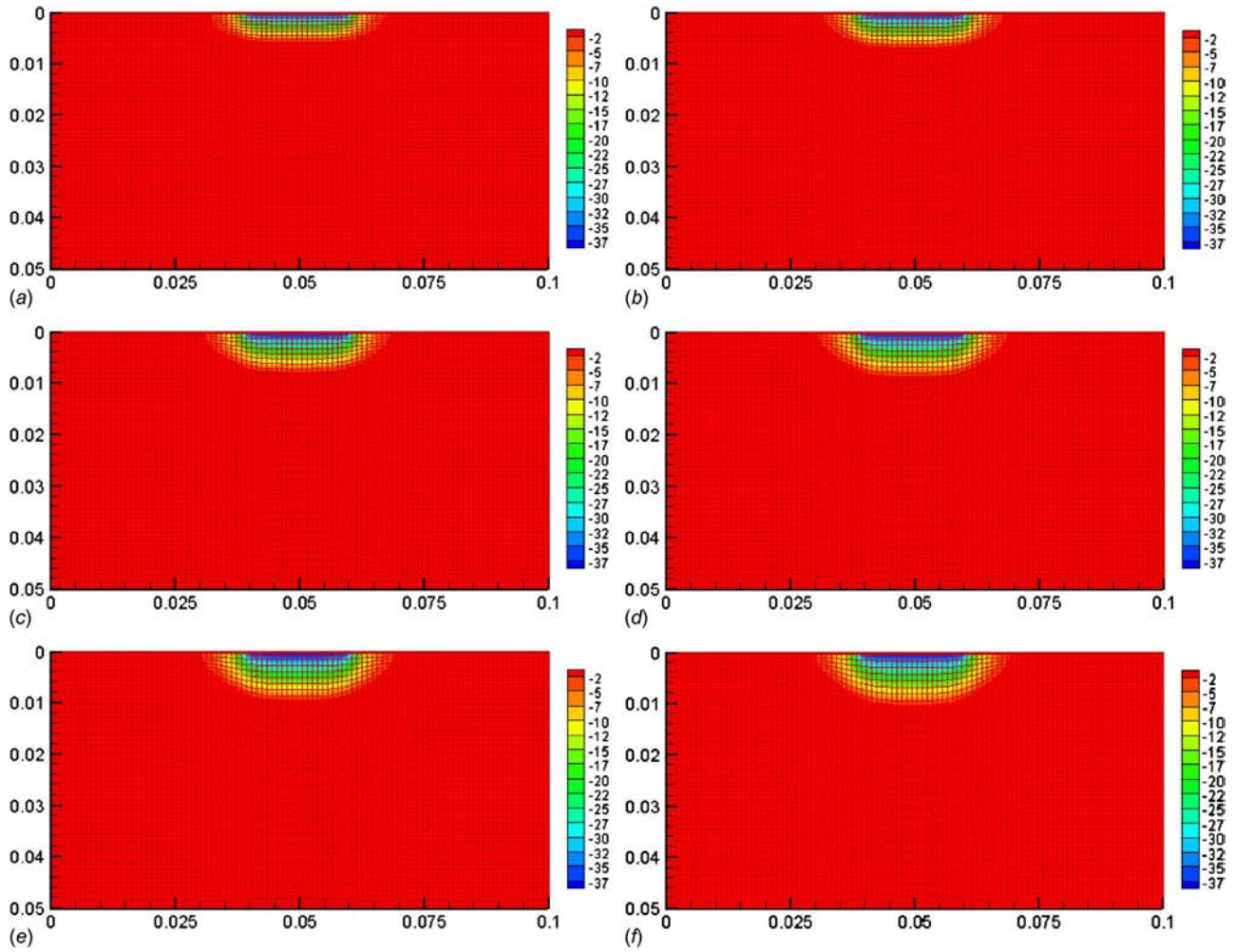


Fig. 8 The simulations of temperature distribution (Unit: °C): (a) freezing time of 30 s, (b) freezing time of 60 s, (c) freezing time of 90 s, (d) freezing time of 120 s, (e) freezing time of 150 s, and (f) freezing time of 180 s

Nagaoka University of Technology are also gratefully acknowledged for his valuable recommendations in this research area.

Nomenclature

- a = thermal diffusivity (m²/s)
- C_p = specific heat capacity (J/kg K)
- L = latent heat (J/kg)
- T = temperature (°C)
- t = time (s)
- x, z = Cartesian coordinates
- λ = effective thermal conductivity (W/mK)
- ϕ = porosity

Subscripts

- i = initial
- f = fusion
- j = layer number
- l = unfrozen
- s = frozen

Appendix

In this section, we will derive a transformation model of the governing differential equations for using in the numerical calculation. The details are shown below.

1 General Transformation of the First and Second Derivatives

Considering the first derivative of any parameters can be written as

$$\frac{\partial}{\partial x} = \frac{1}{J} \left(z_\eta \frac{\partial}{\partial \xi} - z_\xi \frac{\partial}{\partial \eta} \right)$$

$$\frac{\partial}{\partial z} = \frac{1}{J} \left(x_\xi \frac{\partial}{\partial \eta} - x_\eta \frac{\partial}{\partial \xi} \right) \quad (A1)$$

where J is Jacobian. It can be written as

$$J = x_\xi z_\eta - x_\eta z_\xi \quad (A2)$$

$$x_\xi = \frac{\partial x}{\partial \xi} \quad (A3)$$

Considering the second derivative of any parameters, we will establish the second derivative of Laplace equation of parameter A where Eqs. (A1) and (A3) are related:

$$\nabla^2 A = \left(\frac{\partial^2}{\partial x^2} + \frac{\partial^2}{\partial z^2} \right) A = \frac{1}{J^2} \left(\alpha \frac{\partial^2 A}{\partial \xi^2} - 2\beta \frac{\partial^2 A}{\partial \xi \partial \eta} + \gamma \frac{\partial^2 A}{\partial \eta^2} \right) + \frac{1}{J^3} \left[(\alpha x_{\xi\xi} - 2\beta x_{\xi\eta} + \gamma x_{\eta\eta}) \left(z_{\xi} \frac{\partial A}{\partial \eta} - z_{\eta} \frac{\partial A}{\partial \xi} \right) + (\alpha z_{\xi\xi} - 2\beta z_{\xi\eta} + \gamma z_{\eta\eta}) \times \left(x_{\eta} \frac{\partial A}{\partial \xi} - x_{\xi} \frac{\partial A}{\partial \eta} \right) \right] \quad (A4)$$

where

$$\begin{aligned} \alpha &= x_{\eta}^2 + z_{\eta}^2 \\ \beta &= x_{\xi} x_{\eta} + z_{\xi} z_{\eta} \\ \gamma &= x_{\xi}^2 + z_{\xi}^2 \end{aligned} \quad (A5)$$

x_{ξ} , x_{η} , z_{ξ} and z_{η} denote the partial derivatives, β, α, γ are the geometric factors, and η, ξ are the transformed coordinates. The related parameter can be defined as

$$\begin{aligned} x &= x(\xi, \eta) \quad z = z(\xi, \eta) \quad \text{or} \quad \xi = \xi(x, z) \quad \eta = \eta(x, z) \\ &\Downarrow \\ x &= x(\xi) \quad z = z(\xi, \eta) \quad \text{or} \quad \xi = \xi(x) \quad \eta = \eta(x, z) \\ \therefore x_{\eta} &= \frac{\partial x}{\partial \eta} = 0 \quad \text{or} \quad \xi_x = \frac{\partial \xi}{\partial x} = 0 \end{aligned} \quad (A6)$$

Corresponding to Eq. (A6), the first derivative of any parameters (Eq. (A1)) can be rewritten as

$$\begin{aligned} \frac{\partial}{\partial x} &= \frac{1}{J} \left(z_{\eta} \frac{\partial}{\partial \xi} - z_{\xi} \frac{\partial}{\partial \eta} \right) \quad \frac{\partial}{\partial z} = \frac{1}{J} \left(x_{\xi} \frac{\partial}{\partial \eta} - x_{\eta} \frac{\partial}{\partial \xi} \right) \\ &\Downarrow \\ \frac{\partial}{\partial x} &= \frac{1}{J} \left(z_{\eta} \frac{\partial}{\partial \xi} - z_{\xi} \frac{\partial}{\partial \eta} \right) \quad \frac{\partial}{\partial z} = \frac{1}{J} \left(x_{\xi} \frac{\partial}{\partial \eta} \right) \end{aligned} \quad (A7)$$

where

$$\begin{aligned} J &= x_{\xi} z_{\eta} - x_{\eta} z_{\xi} \\ &\Downarrow \\ J &= x_{\xi} z_{\eta} \end{aligned} \quad (A8)$$

The second derivative of any parameters (Eq. (A4)) can be also rewritten as

$$\begin{aligned} \nabla^2 A &= \frac{1}{J^2} \left(\alpha \frac{\partial^2 A}{\partial \xi^2} - 2\beta \frac{\partial^2 A}{\partial \xi \partial \eta} + \gamma \frac{\partial^2 A}{\partial \eta^2} \right) + \frac{1}{J^3} \left[(\alpha x_{\xi\xi} - 2\beta x_{\xi\eta} + \gamma x_{\eta\eta}) \right. \\ &\quad \left. \times \left(z_{\xi} \frac{\partial A}{\partial \eta} - z_{\eta} \frac{\partial A}{\partial \xi} \right) + (\alpha z_{\xi\xi} - 2\beta z_{\xi\eta} + \gamma z_{\eta\eta}) \left(x_{\eta} \frac{\partial A}{\partial \xi} - x_{\xi} \frac{\partial A}{\partial \eta} \right) \right] \\ &\Downarrow \\ \nabla^2 A &= \frac{1}{J^2} \left(\alpha \frac{\partial^2 A}{\partial \xi^2} - 2\beta \frac{\partial^2 A}{\partial \xi \partial \eta} + \gamma \frac{\partial^2 A}{\partial \eta^2} \right) + \frac{1}{J^3} \left[(\alpha x_{\xi\xi}) \left(z_{\xi} \frac{\partial A}{\partial \eta} - z_{\eta} \frac{\partial A}{\partial \xi} \right) \right. \\ &\quad \left. + (\alpha z_{\xi\xi} - 2\beta z_{\xi\eta} + \gamma z_{\eta\eta}) \left(-x_{\xi} \frac{\partial A}{\partial \eta} \right) \right] \end{aligned} \quad (A9)$$

where

$$\begin{aligned} \alpha &= x_{\eta}^2 + z_{\eta}^2 \quad \beta = x_{\xi} x_{\eta} + z_{\xi} z_{\eta} \quad \gamma = x_{\xi}^2 + z_{\xi}^2 \\ &\Downarrow \\ \alpha &= z_{\eta}^2 \quad \beta = z_{\xi} z_{\eta} \quad \gamma = x_{\xi}^2 + z_{\xi}^2 \end{aligned} \quad (A10)$$

2 Transformation of Thermal Model

After some mathematical manipulations (Eqs. (A7), (A9), (3), and (4), and Eq. (5)), a transformation model of the governing differential equations becomes

$$\begin{aligned} \frac{\partial T_l}{\partial t} &= \frac{a_l}{J^2} \left(\alpha \frac{\partial^2 T_l}{\partial \xi^2} - 2\beta \frac{\partial^2 T_l}{\partial \xi \partial \eta} + \gamma \frac{\partial^2 T_l}{\partial \eta^2} \right) + \frac{a_l}{J^3} \left[\left(\alpha \frac{\partial^2 x}{\partial \xi^2} \right) \left(z_{\xi} \frac{\partial T_l}{\partial \eta} \right. \right. \\ &\quad \left. \left. - z_{\eta} \frac{\partial T_l}{\partial \xi} \right) + \alpha \frac{\partial^2 z}{\partial \xi^2} - 2\beta \frac{\partial^2 z}{\partial \xi \partial \eta} + \gamma \frac{\partial^2 z}{\partial \eta^2} \left(-x_{\xi} \frac{\partial T_l}{\partial \eta} \right) \right] \\ &\quad + \frac{1}{J} \left(x_{\xi} \frac{\partial T_l}{\partial \eta} \right) \frac{dz}{dt} \end{aligned} \quad (A11)$$

$$\begin{aligned} \frac{\partial T_s}{\partial t} &= \frac{a_s}{J^2} \left(\alpha \frac{\partial^2 T_s}{\partial \xi^2} - 2\beta \frac{\partial^2 T_s}{\partial \xi \partial \eta} + \gamma \frac{\partial^2 T_s}{\partial \eta^2} \right) + \frac{a_s}{J^3} \left[\left(\alpha \frac{\partial^2 x}{\partial \xi^2} \right) \left(z_{\xi} \frac{\partial T_s}{\partial \eta} \right. \right. \\ &\quad \left. \left. - z_{\eta} \frac{\partial T_s}{\partial \xi} \right) + \alpha \frac{\partial^2 z}{\partial \xi^2} - 2\beta \frac{\partial^2 z}{\partial \xi \partial \eta} + \gamma \frac{\partial^2 z}{\partial \eta^2} \left(-x_{\xi} \frac{\partial T_s}{\partial \eta} \right) \right] \\ &\quad + \frac{1}{J} \left(x_{\xi} \frac{\partial T_s}{\partial \eta} \right) \frac{dz}{dt} \end{aligned} \quad (A12)$$

$$\begin{aligned} &\left[\lambda_s \frac{1}{J} \left(x_{\xi} \frac{\partial T_s}{\partial \eta} \right) - \lambda_l \frac{1}{J} \left(x_{\xi} \frac{\partial T_l}{\partial \eta} \right) \right] \left\{ 1 + \left[\frac{1}{J} \left(z_{\eta} \frac{\partial z_{\text{mov}}}{\partial \xi} - z_{\xi} \frac{\partial z_{\text{mov}}}{\partial \eta} \right) \right]^2 \right\} \\ &= \rho_s L_s \frac{\partial z_{\text{mov}}}{\partial t} \end{aligned} \quad (A13)$$

References

- Landua, H. G., 1950, "Heat Conduction in a Melting Solid," *Q. Appl. Math.*, **8**, pp. 81–94.
- Murray, W. D., and Landis, F., 1959, "Numerical and Machine Solutions of Transient Heat Conduction Problem Involving Melting or Freezing," *ASME J. Heat Transfer*, **81**, pp. 106–112.
- Frivik, P. E., and Comini, G., 1982, "Seepage and Heat Flow in Soil Freezing," *ASME J. Heat Transfer*, **104**, pp. 323–328.
- Sparrow, E. M., and Broadbent, J. A., 1983, "Freezing in a Vertical Tube," *ASME J. Heat Transfer*, **105**, pp. 217–225.
- Voller, V., and Cross, M., 1981, "Accurate Solutions of Moving Boundary Problems Using the Enthalpy Method," *Int. J. Heat Mass Transfer*, **24**, pp. 545–556.
- Weaver, J. A., and Viskanta, R., 1986, "Freezing of Liquid-Saturated Porous Media," *ASME J. Heat Transfer*, **108**, pp. 654–659.
- Chelliah, S., and Viskanta, R., 1988, "Freezing of Saturated and Superheated Liquid in Porous Media," *Int. J. Heat Mass Transfer*, **31**, pp. 321–330.
- Hasan, M., Mujumdar, A. S., and Weber, M. E., 1991, "Cyclic Melting and Freezing," *Chem. Eng. Sci.*, **46**(7), pp. 1573–1587.
- Charn-Jung, K., and Kaviani, M., 1992, "Numerical Method for Phase-Change Problems with Convection and Diffusion," *Int. J. Heat Mass Transfer*, **35**(2), pp. 457–467.
- Rattanadecho, P., 2004, "Experimental and Numerical Study of Solidification Process in Unsaturated Granular Packed Bed," *J. Thermophys. Heat Transfer*, **18**(1), pp. 87–93.
- Rattanadecho, P., 2004, "The Theoretical and Experimental Investigation of Microwave Thawing of Frozen Layer Using Microwave Oven (Effects of Layered Configurations and Layered Thickness)," *Int. J. Heat Mass Transfer*, **47**(5), pp. 937–945.
- Pak, J., and Plumb, O. A., 1997, "Melting in a Two-Component Packed Bed," *ASME J. Heat Transfer*, **119**(3), pp. 553–559.
- Hao, Y. L., and Tao, Y.-X., 2001, "Melting of a Solid Sphere Under Forced and Mixed Convection: Flow Characteristics," *ASME J. Heat Transfer*, **123**(5), pp. 937–950.
- Attinger, D., and Poulidakos, D., 2001, "Melting and Resolidification of a Substrate Caused by Molten Microdroplet Impact," *ASME J. Heat Transfer*, **123**(6), pp. 1110–1122.
- Jiang, J., Hao, Y., and Tao, Y.-X., 2002, "Experimental Investigation of Convective Melting of Granular Packed Bed Under Microgravity," *ASME J. Heat Transfer*, **124**(3), pp. 516–524.
- Hao, Y. L., and Tao, Y.-X., 2002, "Heat Transfer Characteristics of Melting Ice Spheres Under Forced and Mixed Convection," *ASME J. Heat Transfer*, **124**(5), pp. 891–903.
- Elgafy, A., Mesalhy, O., and Lafdi, K., 2004, "Numerical and Experimental Investigations of Melting and Solidification Processes of High Melting Point PCM in a Cylindrical Enclosure," *ASME J. Heat Transfer*, **126**(5), pp. 869–875.
- Ayasoufi, A., Keith, T. G., and Rahmani, R. K., 2004, "Application of the Conservation Element and Solution Element Method in Numerical Modeling

- of Three-Dimensional Heat Conduction With Melting and/or Freezing," *ASME J. Heat Transfer*, **126**(6), pp. 937–945.
- [19] Lynch, D. R., 1982, "Unified Approach to Simulation on Deforming Elements With Application to Phase Change Problem," *J. Comput. Phys.*, **47**, pp. 387–441.
- [20] Cao, W., Huang, W., and Russell, R. D., 1999, "An r-Adaptive Finite Element Method Based Upon Moving Mesh PDEs," *J. Comput. Phys.*, **149**, pp. 221–244.
- [21] Chatterjee, A., and Prasad, V., 2000, "A Full 3-Dimensional Adaptive Finite Volume Scheme for Transport and Phase-Change Processes, Part I: Formulation and Validation," *Numer. Heat Transfer, Part A*, **37**(8), pp. 801–821.
- [22] Duda, J. L., Malone, M. F., Notter, R. H., and Vrentas, J. S., 1975, "Analysis of Two-Dimensional Diffusion Controlled Moving Boundary Problems," *Int. J. Heat Mass Transfer*, **18**, pp. 901–910.
- [23] Saitoh, T., 1978, "Numerical Method for Multi-Dimensional Freezing Problems in Arbitrary Domains," *ASME J. Heat Transfer*, **100**, pp. 294–299.
- [24] Gong, Z.-X., and Mujumdar, A. S., 1998, "Flow and Heat Transfer in Convection-Dominated Melting in a Rectangular Cavity Heated From Below," *Int. J. Heat Mass Transfer*, **41**(17), pp. 2573–2580.
- [25] Beckett, G., MacKenzie, J. A., and Robertson, M. L., 2001, "A Moving Mesh Finite Element Method for the Solution of Two-Dimensional Stefan Problems," *J. Comput. Phys.*, **168**(2), pp. 500–518.
- [26] Eriksson, L. E., 1982, "Generation of Boundary-Conforming Grid Around Wing-Body Configurations Using Transfinite Interpolation," *AIAA J.*, **20**, pp. 1313–1320.
- [27] Coons, S. A., 1967, "Surfaces for Computer-Aided Design of Space Forms," Project MAC, Technical Report MAC-TR 44 MIT.
- [28] Cook, W. A., 1974, "Body Oriented Coordinates for Generating 3-Dimensional Meshes," *Int. J. Numer. Methods Eng.*, **8**, pp. 27–43.
- [29] Gordon, W. J., and Hall, C. A., 1973, "Construction of Curvilinear Coordinate Systems and Applications to Mesh Generation," *Int. J. Numer. Methods Eng.*, **7**, pp. 461–477.
- [30] Ettouney, H. M., and Brown, R. A., 1983, "Finite-Element Methods for Steady Solidification Problems," *J. Comput. Phys.*, **49**, pp. 118–150.
- [31] Anderson, J. D., 1995, *Computational Fluid Dynamics*, Int. Ed., McGraw-Hill, New York, Chap. 5.
- [32] Yao, L. S., and Prusa, J., 1990, "Melting and Freezing," *Adv. Heat Transfer*, **19**, pp. 1–95.

Numerical Investigation of Thermofluid Flow Characteristics With Phase Change Against High Heat Flux in Porous Media

Kazuhiya Yuki

e-mail: kyuki@qse.tohoku.ac.jp

Jun Abei

Hidetoshi Hashizume

Saburo Toda

Department of Quantum Science and Energy
Engineering,
Graduate School of Engineering,
Tohoku University,
Sendai 980-8579, Japan

This study numerically evaluates thermofluid flow characteristics in porous medium by a newly developed "modified two-phase mixture model" applying Ergun's law and a two-energy model instead of a one-energy model. In a single-phase flow case, thermal nonequilibrium between a solid phase and a fluid phase is observed in the area where imposed heat conducts from a heating wall and further convective heat transfer is more active. The degree of thermal nonequilibrium has a positive correlation with the increase in flow velocity and heat flux input. In the case of two-phase flow, the thermal nonequilibrium is remarkable in the two-phase region because the solid-phase temperature in this region is far beyond saturation temperature. A difference between these two models is obvious especially in the two-phase flow case, so that the numerical simulation with the modified two-phase mixture model is indispensable under the high heat flux conditions of over 1 MW/m². [DOI: 10.1115/1.2780175]

Keywords: porous media, phase change, modified two-phase mixture model, non-Darcy's law, two-energy model

Introduction

Design for International Thermonuclear Experimental Reactor (ITER) has been concreting shape on purpose to verify the engineering feasibility of fusion reactor. The next step, after the ITER plan, is to construct a prototype reactor that keeps the fusion reaction constantly to generate electrical energy, and then to develop it toward a demonstration reactor to examine the cost of electricity by the nuclear fusion power generation. Establishment of an efficient cooling technology for a divertor, one of the plasma facing components, which is expected to withstand a steady heat load of 20–30 MW/m², is a major R&D issue that will determine the profitability of nuclear fusion power plant.

From this perspective, the authors proposed evaporated fluid porous thermodevice (EVAPORON), a cooling device that utilizes metal porous media, as an innovative cooling technology that enables both high heat flux removal and acquisition of high power energy density, and have been challenging active control of phase change and mass exchange [1,2]. This thermodevice, as shown in Fig. 1, has a heat removal system making use of latent heat transport, where the metal porous medium with high thermal conductivity is attached onto the backside of the divertor, and the high heat flux from the plasma is removed by evaporating the coolant that flows into the porous medium counter to the heat flow. The basic principle of heat removal is active vapor-liquid exchange by capillary force that works in a two-phase region (a kind of heat pipe effect) as well as the enhancement of fin effect by expansion of heat transfer area. Furthermore, as it can obtain high-temperature steam by the active phase change, it is also possible to build a thermal system using a water-steam Rankine cycle in the fusion power plants. To evaluate the performance of EVAPORON, the authors have conducted heat removal experiments using water as a coolant and particle-sintered compact and

fiber-sintered compact of different materials, structures, porosities, and pore sizes as the porous media, and succeeded in removing surface heat flux of more than 50 MW/m², although it was in a local heat input condition [3]. These experiments proved that EVAPORON has an ideal heat-spread function that leverages the combined effect of the latent heat transport in a stagnation region and the fin effect in an outlet region. Furthermore, unlike conventional cooling technologies, the heat removal limit, i.e., CHF, will not be reached easily even when dryout occurs in the stagnation region, which suggests that extremely high heat removal performance can be maintained even when there are abnormal discharges such as plasma disruption.

By the way, to build a more effective cooling system in the future that can remove even higher heat flux and achieve high power energy density simultaneously, the first task is to grasp the two-phase thermofluid flow characteristics in the porous media and to optimize the fine structure of porous media and cooling conditions. As it takes time to identify such optimum conditions through experiment, it is desirable that the conditions need to be estimated by numerical simulation and then verified experimentally. Therefore, the authors introduced a two-phase mixture model developed by Wang et al. [4], applying Darcy's law and a one-energy model based on local thermal equilibrium for the solid, vapor, and liquid phases, and clarified a part of the thermofluid flow characteristics under low heat flux and low flow velocity conditions [5], such as the flow and temperature fields in the porous media and the distribution of liquid saturation near the heating wall.

However, in the case of high heat flux, inevitably it becomes necessary to formulate the governing equations that are applicable under the conditions of high flow velocity. At the same time, it is critical to take into account influences of thermal nonequilibrium between the solid phase and the fluid phase. To cope with this difficulty, this study applies non-Darcy's law and a two-energy model in order to develop the two-phase mixture model into a "modified two-phase mixture model" applicable under the high flow velocity and high heat flux conditions. Furthermore, by using the newly developed modified two-phase mixture model, the two-

Contributed by the Heat Transfer Division of ASME for publication in the JOURNAL OF HEAT TRANSFER. Manuscript received October 4, 2005; final manuscript received May 3, 2007; published online January 30, 2008. Review conducted by Jose L. Lage. Paper presented at the 2005 ASME Heat Transfer Summer Conference (HT2005), San Francisco, CA, July 15–22, 2005.

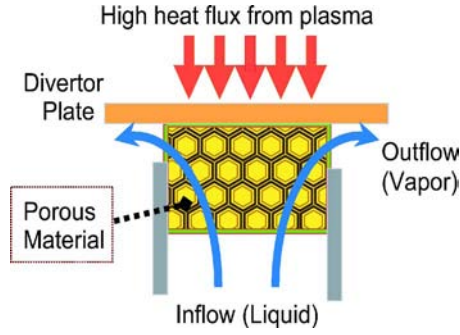


Fig. 1 Heat removal system by EVAPORON

phase thermofluid flow characteristics in the porous medium are evaluated in more details, including quantitative differences between both the models.

Numerical Simulation of Two-Phase Thermofluid Flow in Porous Media Under High Heat Flux

Simulation Domain and Governing Equations. Figure 2 shows the computational domain that almost corresponds to the flow geometry of the authors' proven experiment to remove high heat flux [3]. Water, which works as a coolant, flows in from the bottom of the porous medium counter to the heat flow, and flows out from an exit on the top. The porous medium is a cylindrical bronze-particle-sintered one with the porosity of 42% and the particle size of 160 μm in diameter, and its fine structure is homogeneous and isotropic. The radius l_r and the thickness l_z are 2.5×10^{-2} m and 2.0×10^{-2} m, respectively, and the gap width of the exit, l_{gap} , is 5.0×10^{-3} m. The simulation is performed two dimensionally in the cylindrical coordinate system (r, z) under axial-symmetrical condition. Water with the inlet temperature T_{in} of 20°C flows in at $z=0$ under uniform flow velocity u_{in} , and uniform heat flux q_{in} is imposed at the top surface of $z=l_z$.

In order to construct a modified two-phase mixture model applicable under the high flow velocity, including Forchheimer and post-Forchheimer regimes, Ergun's law mentioned in the next section is first introduced instead of Darcy's law. Taking into account Ergun's correlation is the only difference from the formulation of Wang's two-phase mixture model, and the other derivation processes for the fluid phase are completely the same as Wang's ones [4,6]. Please see his papers for understanding how the following mixture variables and governing equations are derived, including their meanings, and it would easily understand for all the modified equations to become the original equations by Wang et al. if Ergun's constant, C , mentioned later is zero. Furthermore, it was

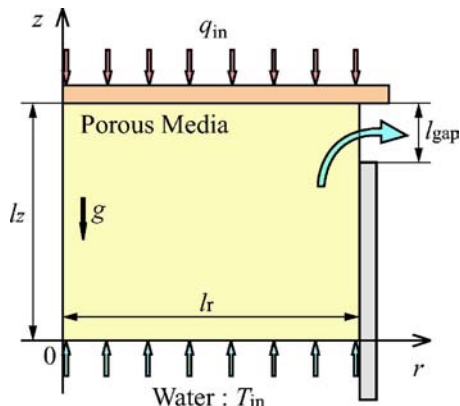


Fig. 2 Computational domain

numerically confirmed that all the data by the modified model completely corresponded with that by Wang's original model, in a laminar regime.

The mixture variables for the fluid phase, such as mixture velocity, mixture enthalpy, etc., are shown below. Mixture density ρ ,

$$\rho = \rho_l s + \rho_v (1 - s) \quad (1)$$

Mixture velocity \mathbf{u} and velocities for liquid and vapor phases, in the form of superficial velocity,

$$\rho \mathbf{u} = \rho_l \mathbf{u}_l + \rho_v \mathbf{u}_v \quad (2)$$

$$\rho_l \mathbf{u}_l = - \frac{K k_{rl}}{\nu_l + C \sqrt{K k_{rl} |\mathbf{u}_l|}} (\nabla p_l - \rho_l \mathbf{g}) \quad (3)$$

$$\rho_v \mathbf{u}_v = - \frac{K k_{rv}}{\nu_v + C \sqrt{K k_{rv} |\mathbf{u}_v|}} (\nabla p_v - \rho_v \mathbf{g}) \quad (4)$$

Mixture enthalpy h and volumetric enthalpy H

$$\rho h = \rho_l s h_l + \rho_v (1 - s) h_v \quad (5)$$

$$H = \rho (h - 2h_{\text{vsat}}) \quad (6)$$

Mixture pressure p ,

$$p = \frac{p_l + p_v}{2} + \frac{1}{2} \int_0^{p_c} [\lambda_v(\xi) - \lambda_l(\xi)] d\xi \quad (7)$$

Mixture kinematic viscosity ν ,

$$\nu = \left(\frac{k_{rl}}{\nu_l} + \frac{k_{rv}}{\nu_v} \right)^{-1} \quad (8)$$

Here, λ_l, λ_v are relative mobilities for the liquid and vapor phases,

$$\lambda_l = \frac{\nu + C \sqrt{K} |\mathbf{u}|}{\nu_l + C \sqrt{K k_{rl} |\mathbf{u}_l|}} k_{rl} \quad (9)$$

$$\lambda_v = \frac{\nu + C \sqrt{K} |\mathbf{u}|}{\nu_v + C \sqrt{K k_{rv} |\mathbf{u}_v|}} k_{rv} \quad (10)$$

The governing equations regarding these mixture variables and important coefficients are given as follows:

- Equation of continuity,

$$\varepsilon \frac{\partial \rho}{\partial t} + \nabla \cdot (\rho \mathbf{u}) = 0 \quad (11)$$

- Momentum equation,

$$\rho \mathbf{u} = - \frac{K}{\nu + C \sqrt{K} |\mathbf{u}|} (\nabla p - \rho \mathbf{g}) \quad (12)$$

$$\rho \kappa = \lambda_l \rho_l + \lambda_v \rho_v \quad (13)$$

- Energy equation for fluid phase,

$$\begin{aligned} \Omega \frac{dH}{dt} + \nabla \cdot (\gamma_h \mathbf{u} H) \\ = \nabla \cdot (\Gamma_h \nabla H) + \nabla \cdot \left[f(s) \frac{K \Delta \rho h_{fg}}{\nu_v + \sqrt{K k_{rv} C} |\mathbf{u}_v|} \mathbf{g} \right] + Q_{sf} \end{aligned} \quad (14)$$

Here, hindrance function $f(s)$,

$$f(s) = k_{rv} \frac{\lambda_l}{\lambda_l + \lambda_v} \quad (15)$$

Effective diffusion coefficient by capillary force,

$$D(s) = \frac{K}{\nu + \sqrt{KC|\mathbf{u}|}} \frac{\lambda_l \lambda_v}{\lambda_l + \lambda_v} [-p'_c] \quad (16)$$

Effective heat capacitance ratio,

$$\Omega = \varepsilon \quad (17)$$

Advection correction coefficient,

$$\gamma_h = \frac{[(\rho_v/\rho_l)(1-s) + s]\{[\lambda_l/(\lambda_l + \lambda_v)] + 1\}h_{vsat} - [\lambda_l/(\lambda_l + \lambda_v)]h_{lsat}}{(2h_{vsat} - h_{lsat})s + [(\rho_v/\rho_l)h_{vsat}](1-s)} \quad (18)$$

Effective diffusion coefficient,

$$\Gamma_h = \frac{h_{fg}}{\rho_l h_{fg} + (\rho_l - \rho_v)h_{vsat}} D(s) + k_{f,eff} \frac{dT}{dH} \quad (19)$$

In order to complete the modified two-phase mixture model, an energy equation for a solid phase should be solved individually by using the following equation:

$$\nabla \cdot (k_{s,eff} \nabla T) - Q_{sf} = 0 \quad (20)$$

Temperatures for each fluid phase, i.e., liquid and vapor, and liquid saturation in the two-phase region, s , are estimated by converting the volumetric enthalpy H as follows because this analysis method is based on an enthalpy method:

$$s = \begin{cases} 1 & H \leq -\rho_l(2h_{vsat} - h_{lsat}) \\ -\frac{H + \rho_v h_{vsat}}{\rho_l h_{fg} + (\rho_l - \rho_v)h_{vsat}} & -\rho_l(2h_{vsat} - h_{lsat}) < H \leq -\rho_v h_{vsat} \\ 0 & H > -\rho_v h_{vsat} \end{cases}$$

$$T = \begin{cases} \frac{H + 2\rho_l h_{vsat}}{\rho_l c_l} & H \leq -\rho_l(2h_{vsat} - h_{lsat}) \\ T_{sat} & -\rho_l(2h_{vsat} - h_{lsat}) < H \leq -\rho_v h_{vsat} \\ T_{sat} + \frac{H + 2\rho_v h_{vsat}}{\rho_v c_v} & H > -\rho_v h_{vsat} \end{cases}$$

In the two-phase region, the vapor phase and the liquid phase are both supposed to be at the same saturation temperature.

Constitutive Equations. The following are constitutive equations that characterize the two-phase thermofluid flow in the porous media. First, as shown by Eqs. (3) and (4), the flow fields of the vapor phase and the liquid phase are derived based on Ergun's law shown below [7]

$$-\nabla p = \frac{\mu}{K} \mathbf{u} + \frac{\rho}{M} |\mathbf{u}| \mathbf{u} = \frac{\mu}{K} \mathbf{u} + \frac{C}{\sqrt{K}} \rho |\mathbf{u}| \mathbf{u} \quad (21)$$

Absolute permeability K is a coefficient with regard to laminar resistance, and inertia permeability M and Ergun constant C are coefficients of the term that represents turbulent resistance. They are given by the following equations:

$$K = \frac{\varepsilon^3 d_p^2}{150(1-\varepsilon)^2} \quad (22)$$

$$M = \frac{\varepsilon^3 d_p^2}{1.75(1-\varepsilon)} \quad C = \sqrt{K}/M \quad (23)$$

Variables that characterize the momentum transport in the two-phase region, such as relative permeabilities k_{rl} and k_{rv} , capillary pressure function $J(s)$, and capillary pressure $p_c(s)$, are strongly dependent on the liquid saturation s . Here, they are given by the following equations with consideration given to the structure of the bronze-particle-sintered porous medium and the cooling condition [8–10].

$$k_{rl} = s^3 \quad (24)$$

$$k_{rv} = (1-s)^2 \quad (25)$$

$$J(s) = 1.417(1-s) - 2.120(1-s)^2 + 1.263(1-s)^3 \quad (26)$$

$$p_c(s) = \frac{\sigma}{\sqrt{K/\varepsilon}} J(s) \quad (26')$$

Effective thermal conductivities of the solid phase and the fluid phase $k_{s,eff}$ and $k_{f,eff}$ are defined as follows.

$$k_{s,eff} = (1-\varepsilon)k_s^* \quad (27)$$

$$\frac{k_{f,eff}}{k_f} = \frac{k_{st}}{k_f} + \Lambda \left(\frac{d_p |\mathbf{u}|}{\nu_f} \right) \left(\frac{c_{pf} \mu_f}{k_f} \right) \quad (28)$$

Here, the effective thermal conductivity when the fluid remains stationary, k_{st} , and the fluid thermal conductivity, k_f , are given by the following equations:

$$k_{st} = k_f \varepsilon \quad (29)$$

$$k_f = k_l s + k_v (1-s) \quad (30)$$

Equation (28) is the one that was derived by Yagi and Kunii [11,12]. Though Λ in the equation is a constant that basically takes a different value depending on a flow direction (in general, 0.1 for the perpendicular direction to the flow and 0.7 for the same direction as the flow), 0.4 is used as the arithmetic mean regardless of the direction in this study because one of our aims is to clarify a difference between the one-energy model and the two-energy model. Moreover, k_s^* in Eq. (27) is thermal conductivity of solid phase, which reflects the fine structure and the degree of particle sintering of porous media. The value is 13.92 W/mK, which represents the thermal conductivity for the bronze porous medium that was used in the authors' experiment [3].

In the two-energy model, it is necessary to take into account the quantity of heat transfer between the solid phase and the fluid phase, Q_{sf} , which is an important factor that has the largest impact on growth of the two-phase region. Especially, in the case that the temperature of the solid phase exceeds the saturation temperature, there is no empirical formula that can exactly evaluate the Q_{sf} in narrow channels of porous media, so that the solid-fluid heat transfer including the latent heat transport was newly modeled by applying existing empirical correlations regarding boiling heat transfer. First, when the solid-phase temperature is lower than the saturation temperature ($T_s < T_{sat}$), the Q_{sf} is given by the following equations:

$$Q_{sf} = h_{sf} a (T_s - T_f) \quad (31)$$

$$\frac{h_{sf} k_f}{d_p} = 2.0 + 1.1 \text{Pr}_f^{1/3} \text{Re}_p^{0.6} \quad (32)$$

Here, T_s and T_f are the solid and fluid temperatures, respectively. $a [=6(1-\varepsilon)/d_p]$ represents a solid-fluid contacting area per unit volume and h_{sf} is heat transfer coefficient between the solid and fluid phases obtained by Wakao et al. [13]. On the other hand, when the solid-phase temperature is the same or higher than the saturation temperature, i.e., the phase change takes place ($T_s \geq T_{sat}$), the heat transfer quantity between the solid phase and the fluid phase, Q_{sf} is newly modeled by the following equation, weighted by the liquid saturation.

$$Q_{sf} = a s q_{all} + a(1-s) h_{sf} (T_s - T_f) \quad (33)$$

$$q_{all} = q_{boil} + q_{conv} \quad (33)$$

Here, q_{all} in the first term of the right side includes influences of pool boiling and forced convection heat transfer of fluid with degree of subcool, and they are calculated by the following equations by Rohsenow et al. [14,15]:

$$q_{boil} = \mu h_{fg} \left[\frac{g(\rho_l - \rho_v)}{\sigma} \right]^{1/2} \left[\frac{c_{pf}(T_s - T_{sat})}{C_{sf} h_{fg}} \right]^{1/0.33} \left(\frac{1}{Pr_f} \right)^{1.7/0.33} \quad (34)$$

$$q_{conv} = \alpha_{conv}(T_s - T_f) \quad (35)$$

$$\left(\frac{\alpha_{conv}}{c_{pf} W} \right) Pr_f^{2/3} = 0.019 \left(\frac{WD_i}{\mu_f} \right) \quad W = \rho |\mathbf{u}| \quad (36)$$

Here, C_{sf} represents a constant determined by the combination of fluid and metal surface, for which 0.006 (water-bronze) is used. W is mass flux, and D_i represents characteristic length that is given as the particle diameter d_p in this calculation.

Boundary Conditions and Analysis Method. In this calculation, the parameters are the heat flux input q_{in} , which is imposed to the porous medium, and the inlet flow velocity u_{in} . The following equations show the boundary conditions.

- Inlet ($z=0$),

$$u = u_{in} \quad (37)$$

$$v = 0 \quad (38)$$

$$H = \rho_l(c_l T_{in} - 2h_{vsat}) = \rho_l(h_{in} - 2h_{vsat}) \quad (39)$$

$$T_s = T_{in} \quad (40)$$

- Heating wall ($z=l_z$),

$$-\Gamma_h \frac{\partial H}{\partial z} = q_f \quad (41)$$

$$-(1 - \varepsilon)k_s^* \frac{\partial T_s}{\partial z} = q_s \quad (42)$$

$$q_s + q_f = q_{in} \quad (43)$$

- Central axis ($r=0$),

$$\frac{\partial u}{\partial r} = v = \frac{\partial p}{\partial r} = \frac{\partial H}{\partial r} = \frac{\partial T_s}{\partial r} = 0 \quad (44)$$

- Wall surface ($r=l_r$),

$$\frac{\partial H}{\partial r} = \frac{\partial T_s}{\partial r} = 0 \quad (0 < z < l_z - l_{gap}) \quad (45)$$

$$p = p_{out} = 1 \text{ atm} \quad (l_z - l_{gap} < z < l_z) \quad (46)$$

In the two-energy model, it is necessary to divide the heat flux input q_{in} into heat flux to the side of the solid phase, q_s , and heat flux to the side of the fluid phase, q_f , as shown in Eqs. (41)–(43). In this calculation, the imposed heat flux is divided by the following equation, referring to conjugate heat-transfer simulation of single-phase flow in the porous media and heat conduction in a solid wall by Oda et al. [16].

$$\frac{q_f}{q_s} = \frac{\varepsilon k_f T_{wf} - T_f}{1 - \varepsilon k_s^* T_{ws} - T_s} \quad (47)$$

In Eq. (47), T_f and T_s are the temperatures of fluid and solid phases in the control volume next to the heating wall, respectively. T_w is the temperature at the surface. It is clear that the heat flux input is divided not only by the porosity but also by the thermal conductivity ratio of the solid to the fluid as well as their tempera-

tures near the surface.

In this simulation, heterogeneous grids, where the grid spacing becomes smaller near the heating wall, are located for the z direction and homogeneous grids for the r direction, with consideration given to the fact that temperature gradient and phase change are conspicuous especially near the heating wall. Naturally, the number of grids strongly depends on the flow conditions, i.e., the single-phase or two-phase flows, and the grid spacing is finer enough to simulate the flow and enthalpy fields. The governing equations mentioned above are discretized by a finite volume method and solved by SIMPLE algorithm [17]. A power-law scheme is employed for discretization of convection and diffusion terms. Temperature dependency of viscosity is also taken into account in order to more exactly simulate the thermofluid flow field near the heating wall.

Quantitative Evaluation of Degree of Thermal Nonequilibrium

Single-Phase Flow Simulation

Influence of Flow Velocity. Figure 3 shows the influence of flow velocity on the thermofluid characteristics ((a) temperature distribution of fluid phase, (b) distribution of thermal nonequilibrium degree ΔT_{non-eq} , and (c) temperature difference from the one-energy model $\Delta T_{one-two}$). The inlet flow velocities u_{in} are 0.001 m/s, 0.005 m/s, and 0.010 m/s and the heat flux input q_{in} is 0.15 MW/m². The vectors in the temperature distribution of the fluid phase are velocity vectors of the liquid phase. The degree of thermal nonequilibrium ΔT_{non-eq} , is the difference between the solid-phase temperature and the fluid-phase temperature estimated by the two-energy model and is normalized by the difference between the maximum temperature of volumetric average temperature T_{av} [$=\varepsilon T_f + (1 - \varepsilon)T_s$] and the inlet temperature T_{in} , as shown below

$$\Delta T_{non-eq} = \frac{T_s - T_f}{T_{avmax} - T_{in}} \quad (48)$$

For quantitative comparison of the difference between the one-energy model and the two-energy model, $\Delta T_{one-two}$, the difference between the temperature by the one-energy model T_{one} and the temperature by the two-energy model, T_{av} , normalized in the same manner, is defined by the following equation:

$$\Delta T_{one-two} = \frac{T_{one} - T_{av}}{T_{avmax} - T_{in}} \quad (49)$$

The temperature distribution of the fluid phase in Fig. 3(a) shows that as the inlet flow velocity increases, heat penetration to the inside of the porous medium is suppressed by enhanced convective heat transfer. This heat transfer enhancement is also confirmed from the radial distribution of heat transfer coefficient at the heating wall in Fig. 4. Here, the heat transfer coefficient h is defined as

$$h = \frac{q_{in}}{T_w(r) - T_{in}} \quad (50)$$

Furthermore, since the outlet area is smaller than the inlet area, the heat transfer coefficient becomes higher in the outlet region due to increase in the flow velocity. From the distribution of degree of thermal nonequilibrium in Fig. 3(b), the influence of thermal nonequilibrium at the lowest inlet flow velocity of 0.001 m/s is the most apparent near the outlet where the flow velocity is higher. However, this area expands toward the central axis parallel to the heating wall with the increase of flow velocity, and then the highest thermal nonequilibrium area can be observed only near the central axis at the inlet flow velocity of 0.010 m/s. In general, it is anticipated that the thermal nonequilibrium takes place in the area where the heat conducts from the heating wall and further the flow velocity is high. This is why the thermal nonequilibrium is

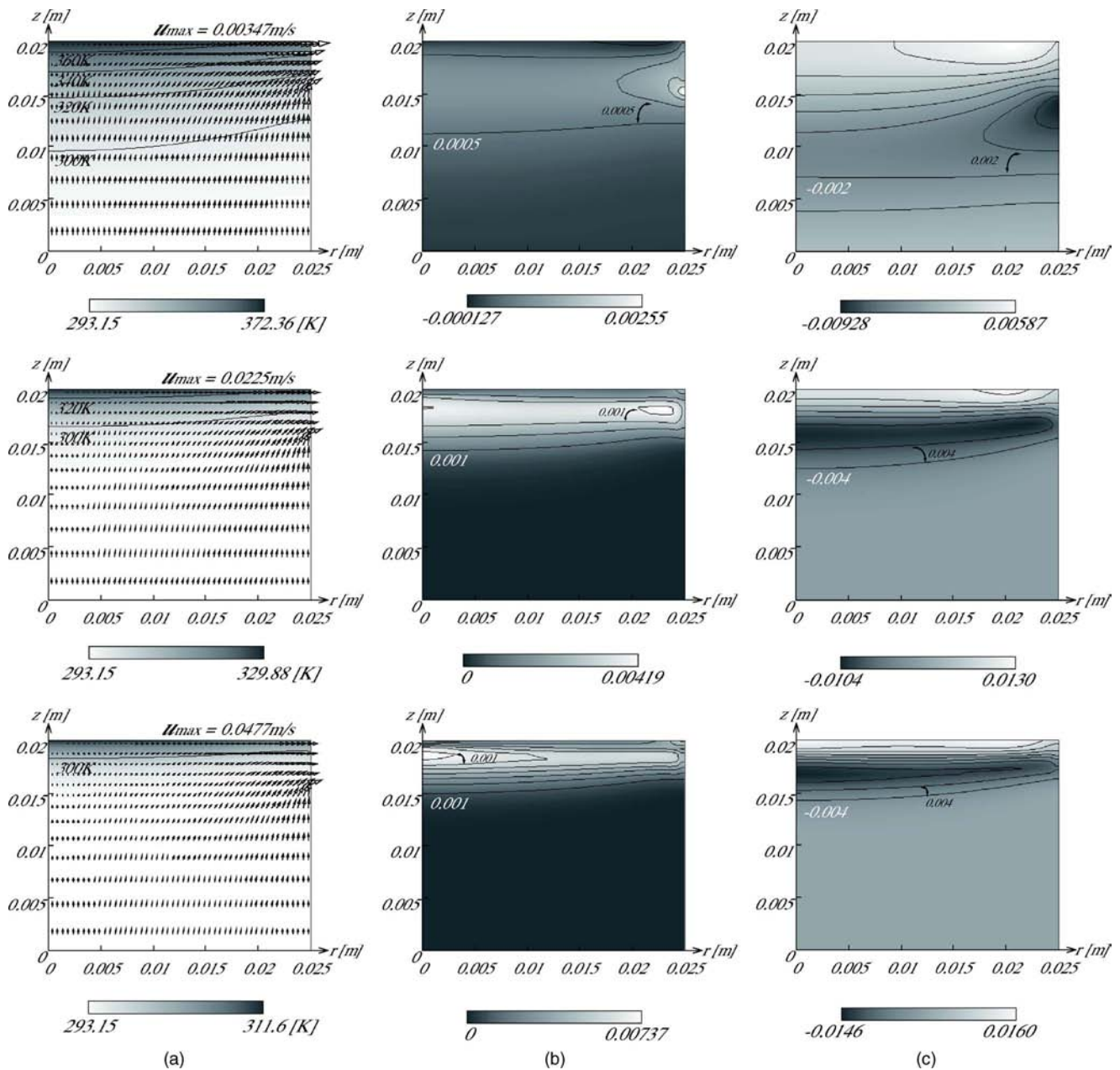


Fig. 3 Influence of flow velocity on thermofluid flow characteristics (single-phase flow)

supposedly low in the vicinity of the heating wall. Under the low velocity conditions, the imposed heat can conduct more inside of the porous medium through the solid phase, so that the influence of thermal nonequilibrium is outstanding especially near the outlet where the flow velocity is much higher. However, as the flow velocity increases, the heat cannot conduct to the inside of the porous medium especially in the outlet area due to the enhancement of convective heat transfer. Therefore, the area with high degree of thermal nonequilibrium moves toward the center where the heat penetrates more inside the porous medium due to the influence of flow stagnation. It means that, in the case of single-phase flow, the balance between the heat conduction in the solid phase from the heating wall and the convective heat transfer surely determines the distribution of degree of thermal nonequilibrium. Also, changes in maximum value of $\Delta T_{\text{non-eq}}$ clearly indicate that the degree of thermal nonequilibrium becomes higher with increasing flow velocity. Comparison between Figs. 3(b) and 3(c) reveals that the temperature estimated by the one-energy

model is higher than that by the two-energy model in the area closer to the heating wall from the high thermal nonequilibrium area, but it is lower in the upstream of the high thermal nonequilibrium area. As mentioned before, in the two-energy model, the heat flux input q_{in} is divided into the heat flux to the solid-phase side q_s and the heat flux to the fluid-phase side q_f . Most of the imposed heat, however, flows into the solid-phase side and is diffused to the inside of the porous medium by its high thermal conductivity, which results in the difference between both the models. Though the heat transfer Q_{sf} between the solid phase and the fluid phase also works, its influence is comparatively limited especially near the heating wall due to lower flow velocity. The fact that the heat transfer coefficient of the two-energy model is somewhat higher than that of the one-energy model in Fig. 4 also results from the energy division effect described above. That is, in the two-energy model, since the heat conducts more inside the porous medium, the temperature rise near the heating wall is sup-

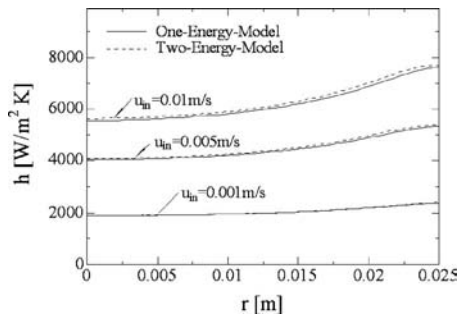


Fig. 4 Radial distribution of heat-transfer coefficient

pressed and the temperature becomes higher than that of the one-energy model in the upstream of the high thermal nonequilibrium area. In addition, the difference between these two models becomes more apparent as the flow velocity increases. However, the degree of thermal nonequilibrium is very low in the range of the present calculation conditions and can be ignored from an engineering perspective. In the case that the thermal conductivity of the solid phase is even higher than that of the fluid phase, the two-energy model is expected to be appropriate.

Influence of Heat Flux. Figure 5 shows the thermofluid flow fields under the conditions of some heat flux inputs. The heat flux input are 0.05 MW/m², 0.10 MW/m², and 0.15 MW/m², and the inlet flow velocity is 0.010 m/s. It is confirmed from Fig. 5(a) that a contour line of 300 K expands with increasing heat flux input toward inside the porous medium and in the radial direction, which means that the heat penetrates more inside the porous medium. In general, in a single-phase flow condition at a constant

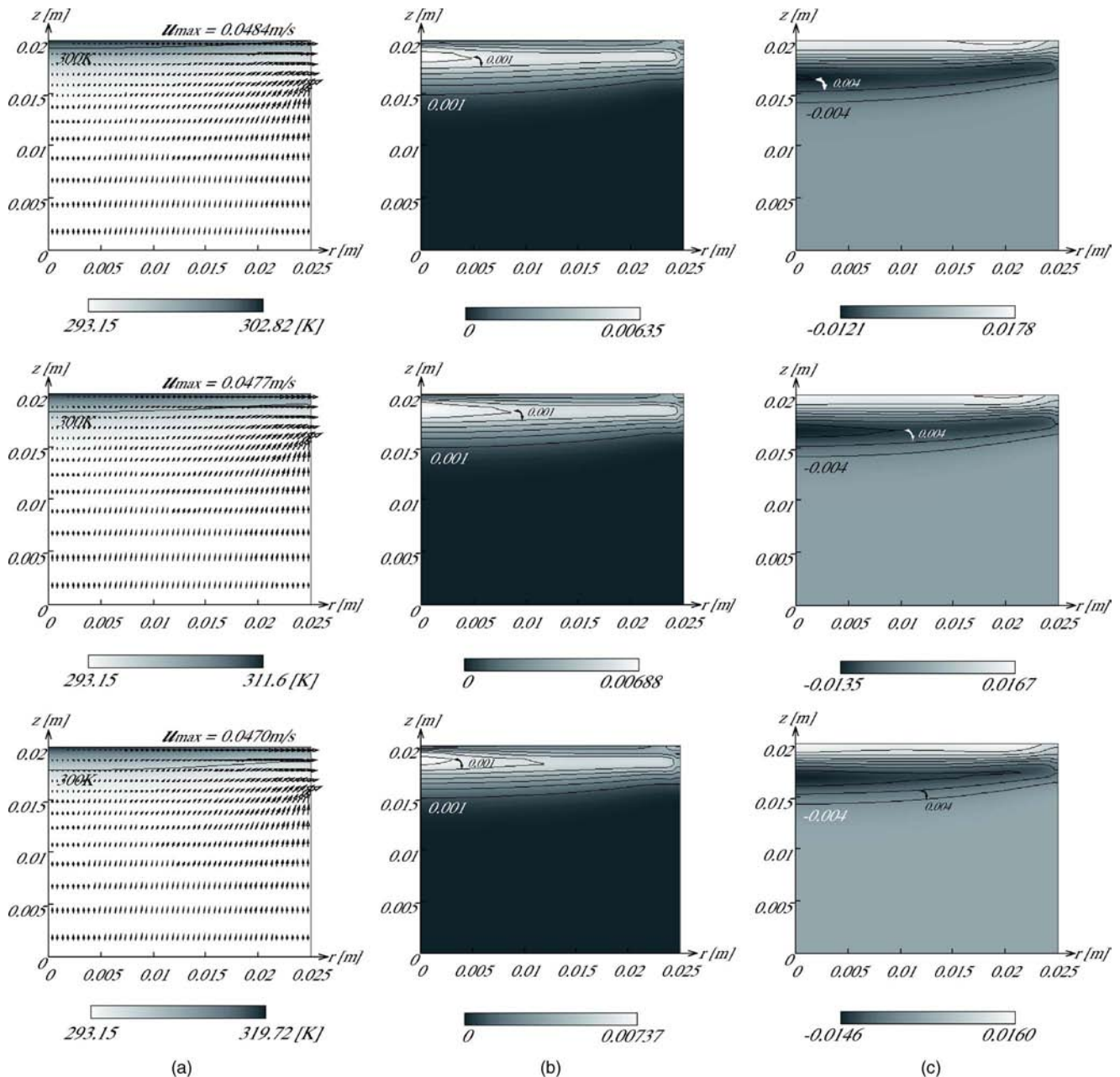


Fig. 5 Influence of heat flux on thermofluid flow characteristics (single-phase flow)

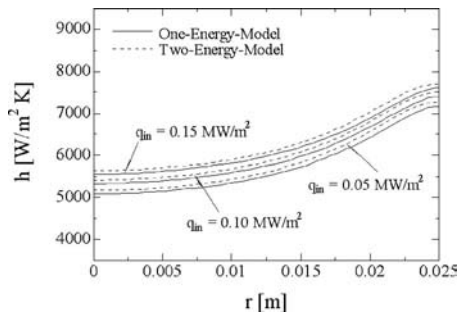


Fig. 6 Radial distribution of heat-transfer coefficient

flow velocity, the distribution of heat transfer coefficient at the heating wall is not basically dependent on the heat flux input. However, Fig. 6 presents that the increase in the heat flux input brings a certain degree of increase in the heat transfer coefficient. This is because the temperature rise near the heating wall, resulted from the increase of the heat flux input, causes decrease in the flow resistance near the wall due to the decrease of viscosity of water. The reason why the heat transfer coefficient of the two-energy model is higher than that of the one-energy model is that the division effect of the heat flux lowers the heating wall temperature in the two-energy model, as mentioned before. Figure 5(b) demonstrates that a high thermal nonequilibrium area expands in the radial direction as the heat flux increases. It is also because the flow velocity especially in the radial direction near the heating wall is accelerated with the increase of the heat flux input.

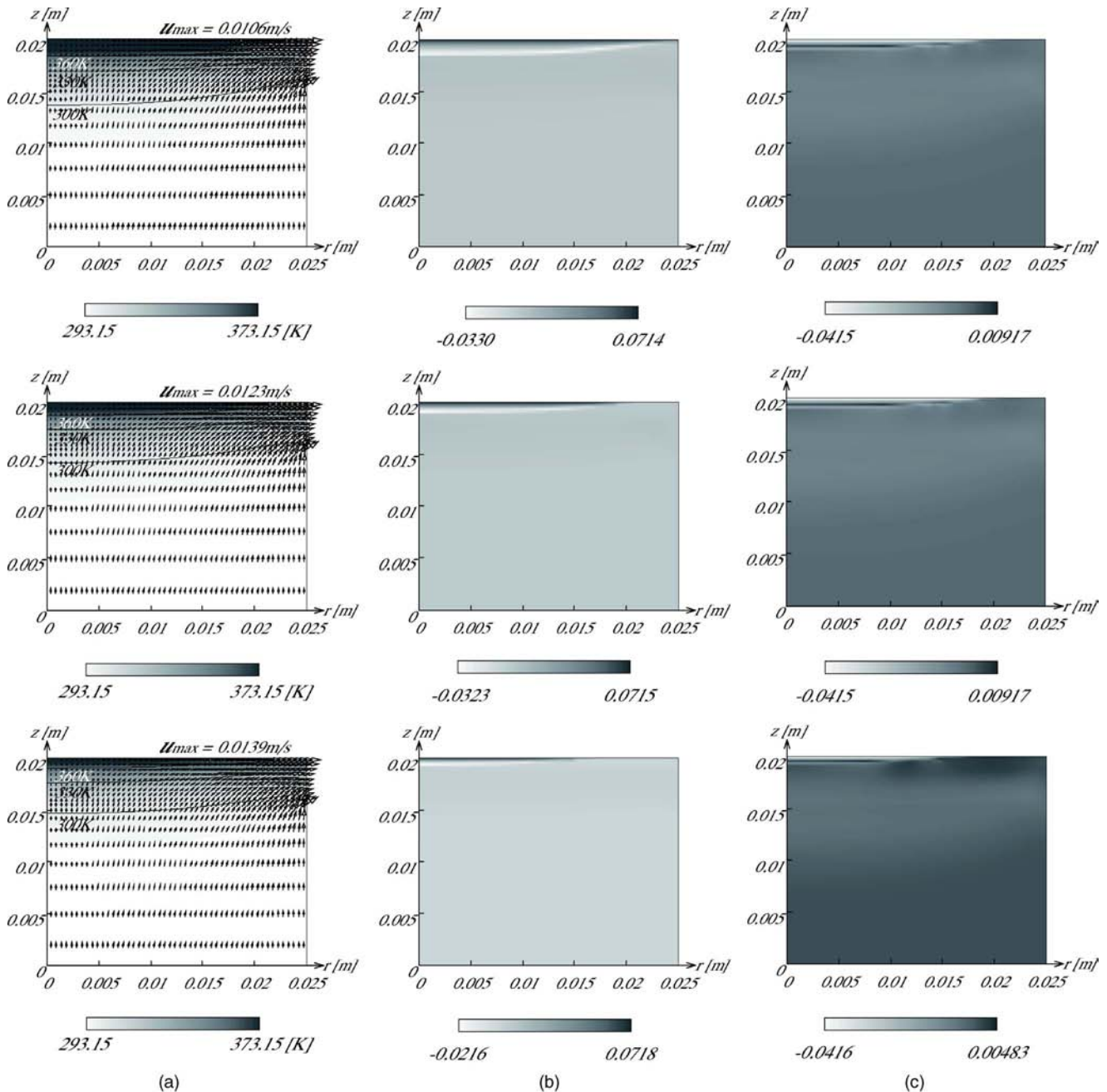


Fig. 7 Influence of flow velocity on thermofluid flow characteristics (two-phase flow)

It is also observed that the distribution of $\Delta T_{\text{one-two}}$, namely, the difference between these two models, is similarly influenced, as shown in Fig. 3(c).

Simulation of Two-Phase Flow

Influence of Flow Velocity. Figure 7 shows the influence of flow velocity on the thermofluid flow characteristics ((a) temperature distribution of fluid phase, (b) distribution of thermal nonequilibrium degree $\Delta T_{\text{non-eq}}$, and (c) distribution of difference from one-energy model $\Delta T_{\text{one-two}}$). The inlet flow velocities are 0.0027 m/s, 0.0030 m/s, and 0.0033 m/s and the heat flux input is 0.34 MW/m². Figure 8 is a distribution of liquid saturation and the vectors in this figure represent the vapor velocity vectors. Figure 7(a) shows that, as in the case of single-phase flow, the increase in the inlet flow velocity enhances the forced convection

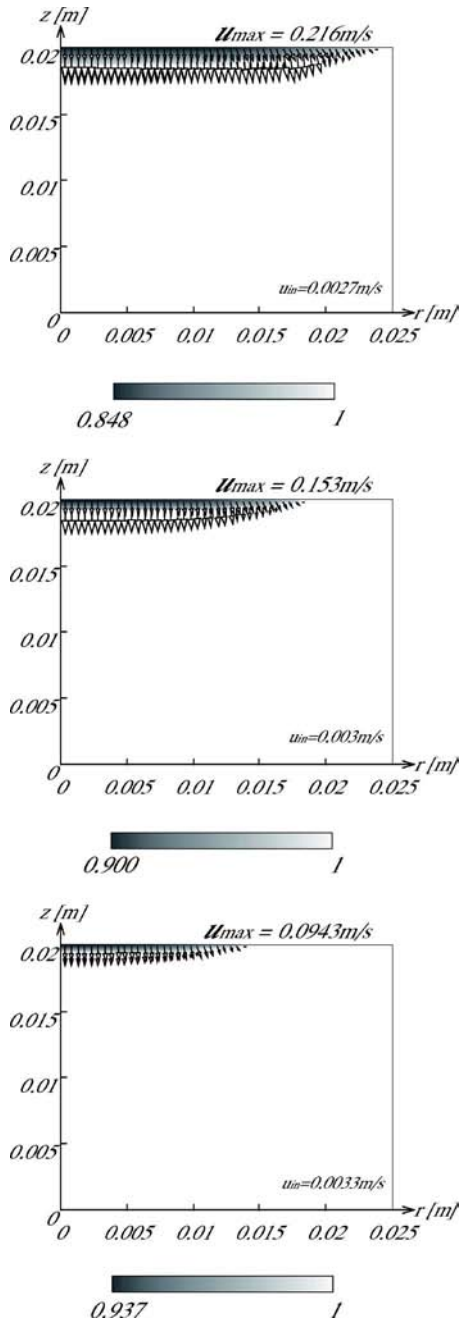


Fig. 8 Influence of flow velocity on liquid saturation distribution

heat transfer especially in the outlet region. Thus, the heat conduction inside the porous medium is suppressed. Also, the liquid saturation distribution in Fig. 8 denotes that a vapor generating region, i.e., the two-phase region, becomes smaller both in the radial and axial directions with increasing inlet flow velocity, which means that the phase change is also suppressed. At this time, the minimum value of liquid saturation also becomes higher. Furthermore, it is confirmed from Fig. 7(b) that the distribution of thermal nonequilibrium is substantially different from that of single-phase flow and that the influence of thermal nonequilibrium is obvious in the two-phase region. That is, it is assumed that the heat transfer between the solid phase and the fluid phase in the two-phase region is dominant in the two-phase flow conditions. Figures 9(a) and 9(b) are the temperature distributions of the solid phase and the fluid phase at the central axis and the heating wall. While the fluid phase in the two-phase region is at the saturation temperature, the solid phase becomes hotter as it comes closer to the heating wall, beyond the saturation temperature. As mentioned before, the two-phase region becomes smaller toward the heating wall with the increase of flow velocity, but it is interesting that the temperatures at the heating wall in the stagnation region are almost the same, regardless of the flow velocity. This agrees with the finding obtained through the authors' experiments that "when the phase change actively occurs near the heating wall, there exists a state where the temperature of heating wall remains the same, regardless of the flow velocity" [18]. As the two-phase region grows up, the liquid saturation in the vicinity of heating wall decreases, which results in the increase of heat flux divided to the solid phase. In this case, the temperature gradient for the solid phase is thought to be sharper, but Fig. 9(a) does not show such a tendency. On the contrary, the temperature gradient of solid phase becomes gentler under the conditions of lower flow velocity. The reason for this is anticipated to be that the heat transfer quantity Q_{sf} from the solid phase to the fluid phase becomes extremely larger. This proves that the heat transfer by the latent heat transport is dominant in the two-phase region. It is also confirmed from Fig. 9(a) that there exists a region where the fluid-phase temperature is higher than the solid-phase temperature. This means that, in the area near the heating wall where the solid-phase temperature is

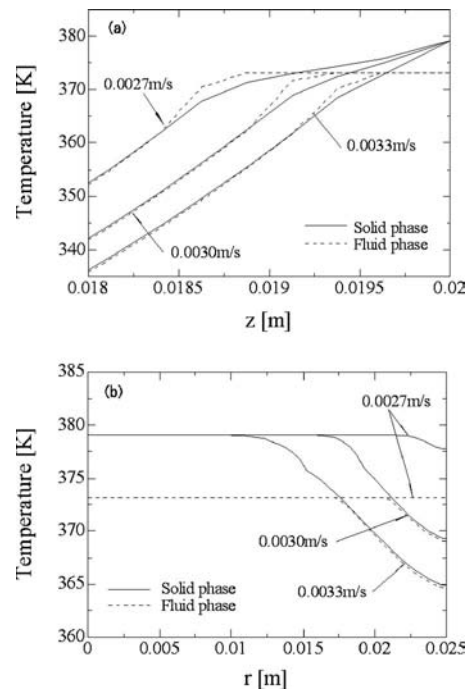


Fig. 9 Temperature distributions of solid phase and fluid phase at central axis and heating wall

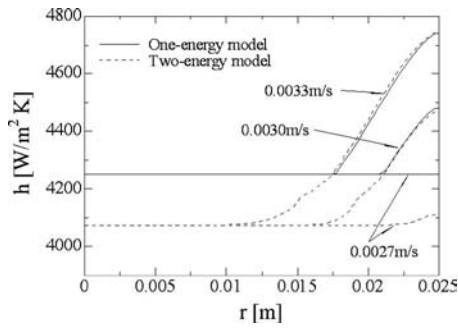


Fig. 10 Radial distribution of heat-transfer coefficient

higher than the saturation temperature, a large quantity of heat Q_{sf} moves from the solid phase to the fluid phase, which results in the enthalpy increase of the fluid phase and the decrease of the solid-phase temperature on the inlet side. As a result, it seems that the temperature inversion between the two phases takes place. This inversion phenomenon needs to be explained in the future by detailed modeling of Q_{sf} , taking into account such factors as condensation and narrowing effect of channel. Naturally, in the two-phase flow case, the difference between the two models is apparent in and near the two-phase region (see Fig. 7(c)). In particular, the average temperature estimated by the two-energy model becomes higher than the T_{one} near the heating wall because the solid-phase temperature exceeds the saturation temperature. This is directly reflected to the distribution of heat transfer coefficient in the radial direction in Fig. 10. Here, the temperature at the heating wall is calculated by interpolating the volumetric average temperature to estimate the heat transfer coefficient. While the temperature in the two-phase region is naturally the saturation temperature in the one-energy model, the average temperature be-

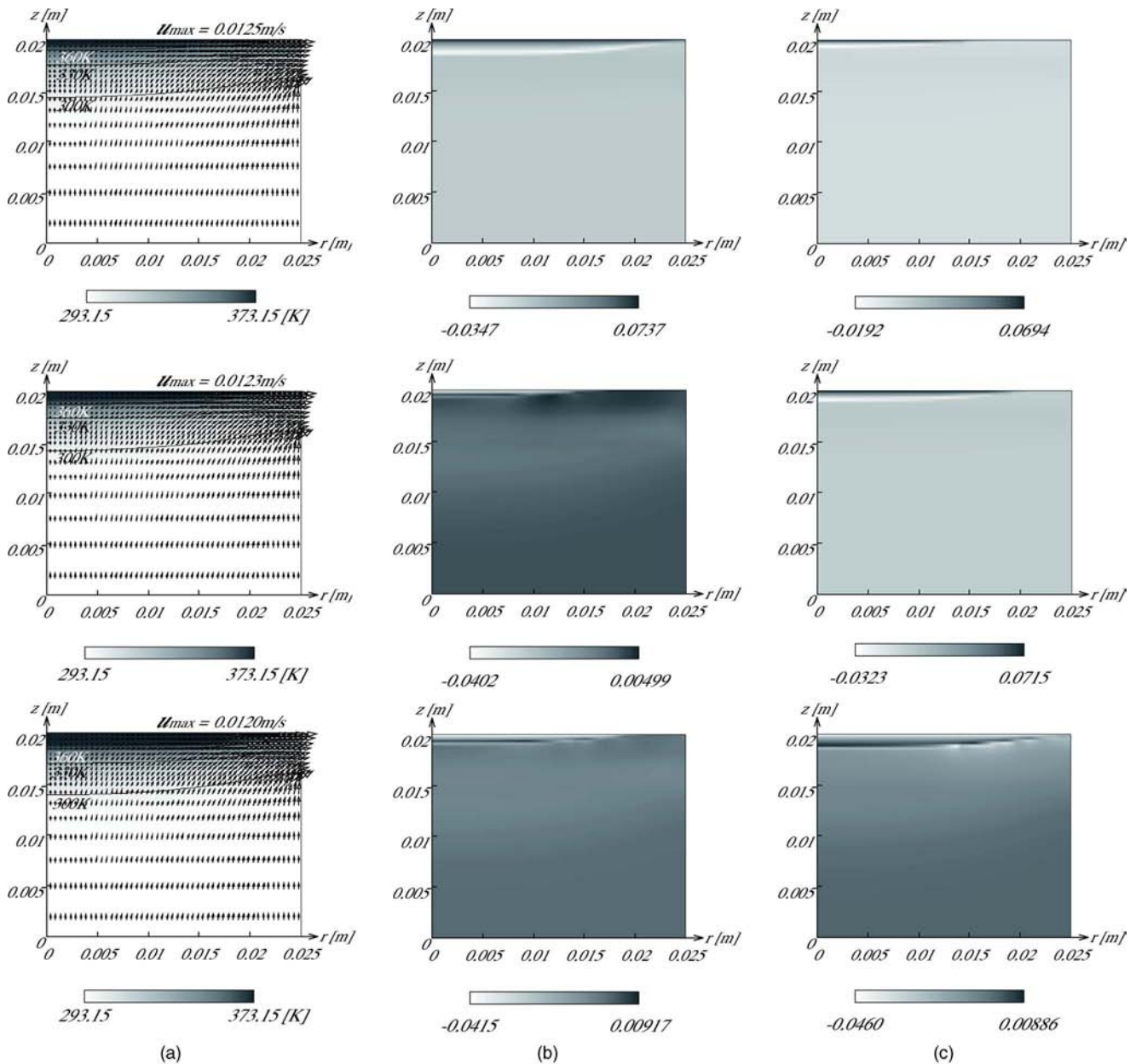


Fig. 11 Influence of heat flux on thermofluid flow characteristics (two-phase flow)

comes higher in the case of the two-energy model because of the influence of the solid-phase temperature. Thus, the heat transfer coefficient obtained from the two-energy model is always lower than that from the one-energy model. In reality, it was observed in the authors' experiments that the temperature at the heating wall, i.e., the interface temperature between the porous medium and the wall, went far beyond the saturation temperature [13,18]. Thus, there is no doubt that the two-energy model produces more realistic and reasonable results for the two-phase thermofluid flow analysis. It should be kept in mind that the heat transfer coefficient by the one-energy model may well be overestimated.

Influence of Heat Flux. Figure 11 presents the changes in the two-phase flow condition for some heat fluxes ((a) temperature distribution of fluid phase, (b) distribution of thermal nonequilibrium degree $\Delta T_{\text{non-eq}}$, and (c) distribution of difference from one-energy model $\Delta T_{\text{one-two}}$). Figure 12 is the liquid saturation distribution

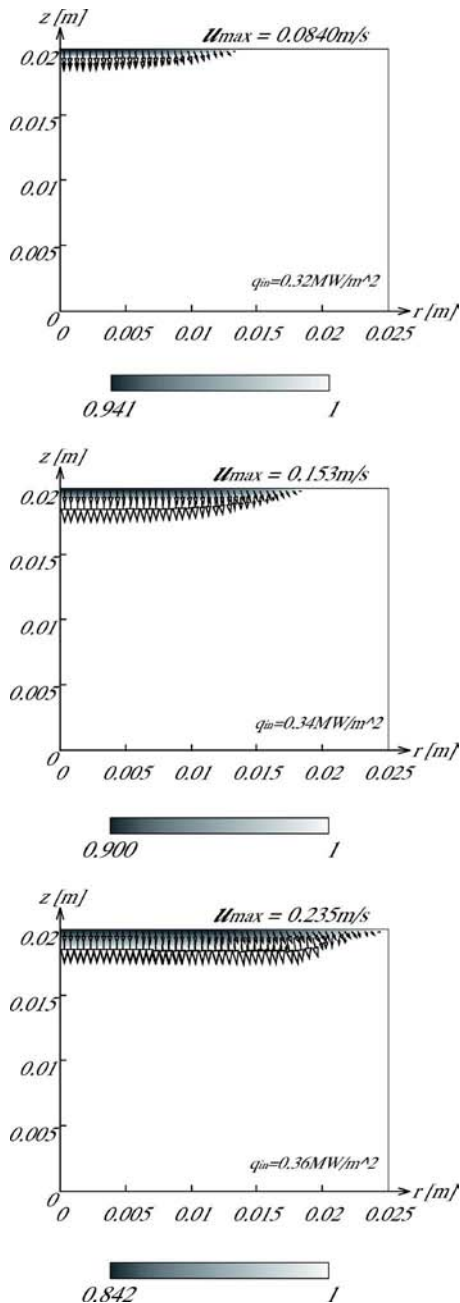


Fig. 12 Influence of heat flux on liquid saturation distribution

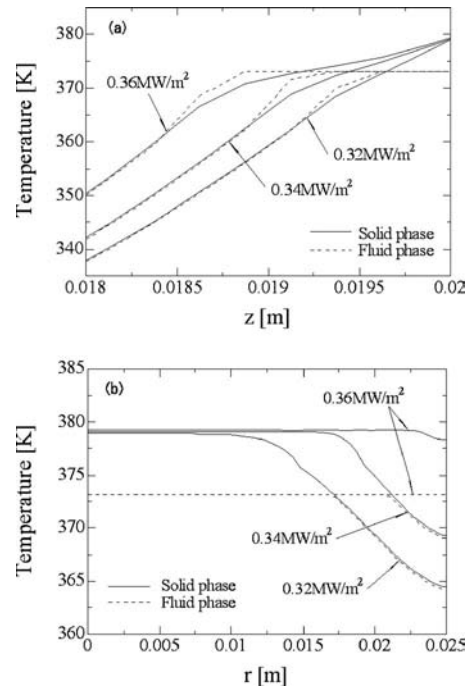


Fig. 13 Temperature distributions of solid phase and fluid phase at central axis and heating wall

bution. The heat flux input are 0.32 MW/m^2 , 0.34 MW/m^2 , and 0.36 MW/m^2 and the inlet flow velocity is 0.003 m/s . Figure 12 suggests that, when the phase change actively takes place, the two-phase region expands in the radial and axial directions with the increase of the heat flux input. In particular, the growth in the radial direction is significant. It is also confirmed that the increase of heat flux leads to lower minimum-liquid saturation and larger vapor velocity. In addition, it is obvious from Figs. 11(a) and 12 that the vapor generated near the heating wall highly contributes to the heat diffusion to the inside of the porous medium. That is, the temperature rise inside the porous medium is accelerated by the heat pipe effect between the generated vapor and the liquid phase. The thermal nonequilibrium, as shown in Fig. 11(c), is also remarkable in the two-phase region, as mentioned before, and the area becomes larger under the conditions of higher heat flux input. Figures 13(a) and 13(b) are the temperature distributions of the solid phase and the fluid phase at the central axis and the heating wall, respectively. They show the same tendency as in Fig. 9, and the solid temperature at the heating wall becomes higher especially in the outlet region according to the growth of two-phase region; that is, the degree of thermal nonequilibrium increases with the increase of the heat flux input. Figure 14 is the radial distribution of the heat transfer coefficient at the heating wall. The distinctive characteristic is that the heat transfer coefficient of the

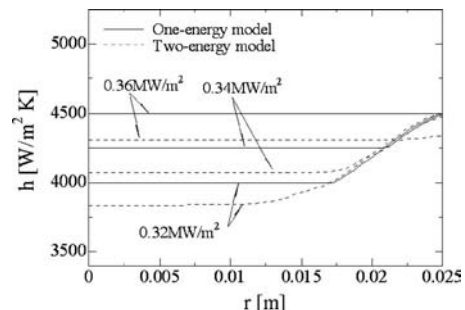


Fig. 14 Radial distribution of heat-transfer coefficient

two-energy model is even lower than that of the one-energy model and becomes higher in the cases of higher heat flux input due to the more active phase change.

Conclusion

This study numerically evaluated the influence of thermal non-equilibrium on thermofluid flow characteristics in porous medium by using a newly formulated “modified two-phase mixture model.” The findings are summarized as follows.

- (1) In a single-phase flow case, the thermal nonequilibrium is observed in the area where imposed heat conducts from a heating wall and further convective heat transfer is more active. The degree of thermal nonequilibrium has a positive correlation with the increase in inlet flow velocity and heat flux input.
- (2) In the case of two-phase flow, the thermal nonequilibrium is remarkable in the two-phase region because solid-phase temperature in the two-phase region is far beyond saturation temperature. The degree of thermal nonequilibrium has a negative correlation with the inlet flow velocity and a positive correlation with the heat flux input. Moreover, it was proven that the inlet flow velocity had little influence on the temperature at the heating wall in the case that the phase change actively takes place.
- (3) A difference between the one-energy model and the two-energy model is obvious especially in the two-phase flow case, so that the numerical simulation with the two-energy model is indispensable especially under the high heat flux condition over 1 MW/m^2 .
- (4) The degree of thermal nonequilibrium is also largely different between the single-phase flow and the two-phase flow, and the degree for the two-phase flow is one digit higher.

It is concluded that it needs to keep in mind that the one-energy model, which underestimates the heating wall temperature in the two-phase flow condition, will definitely overestimate the heat-transfer coefficient. The two-energy model with Ergun’s law surely produces more realistic and reasonable results for the two-phase thermofluid flow analysis under high heat flux and high velocity conditions. As a next step, it is desirable to evaluate the accuracy of the modified two-phase mixture model including the constitutive equations especially for heat transfer between the solid phase and the fluid phase in narrow channels’ network, compared with the experimental data that we will take in the near future.

Nomenclature

- a = specific surface area (m^2/m^3)
 c = specific heat (J/kg K)
 C = Ergun constant
 C_{sf} = constant regarding boiling heat transfer, decided by combination of solid and fluid
 d_p = particle diameter (m)
 D_t = characteristic length (m)
 $D(s)$ = effective diffusion coefficient by capillary force (m^2/s)
 $f(s)$ = hindrance function
 g = gravity (m/s^2)
 h = heat transfer coefficient ($\text{W/m}^2 \text{K}$)
 h_{sf} = heat transfer coefficient between solid and fluid ($\text{W/m}^2 \text{K}$)
 h_{fg} = latent heat of vaporization (J/kg)
 \bar{H} = volumetric enthalpy (J/m^3)
 k = thermal conductivity (W/m K)
 k_r = relative permeability
 K = absolute permeability (m^2)
 l = length of porous medium (m)

- M = inertia permeability (m)
 p = pressure (Pa)
 Pr = Prandtl number
 q = heat flux (W/m^2)
 Q_{sf} = heat transfer quantity between solid and fluid (W/m^3)
 Re = Reynolds number
 s = liquid saturation
 T = temperature (K)
 W = mass flux ($\text{kg/m}^2 \text{s}$)
 u = superficial velocity in z direction (m/s)
 v = superficial velocity in r direction (m/s)
 α_{conv} = convective heat transfer coefficient ($\text{W/m}^2 \text{K}$)
 β = coefficient of cubical expansion
 γ = advection correction coefficient
 Γ = diffusion coefficient (m^2/s)
 ε = porosity
 λ = relative mobility
 Λ = constant in Eq. (28)
 μ = viscosity (Pa s)
 ν = kinematic viscosity (m^2/s)
 ρ = density (kg/m^3)
 σ = surface tension (N/m)
 Ω = effective heat capacitance ratio

Subscripts

- c = capillary
 eff = effective
 f = fluid phase
 h = heating
 gap = gap
 l = liquid phase
 in = inlet
 non-eq = nonequilibrium effect
 one-two = between one-energy and two-energy models
 r = r -direction
 s = solid phase
 sat = saturated state
 st = static state
 v = vapor phase
 w = wall
 z = z -direction
 κ = kinetic

References

- [1] Toda, S., Ebara, S., and Hashizume, H., 1998, “Fundamental Study on High Heat Flux Removal System Using Evaporated Fluid in Metal Porous Media,” *Proceedings of the 11th International Heat Transfer Conference 11th IHTC*, Vol. 4, pp. 503–508.
- [2] Toda, S., and Yuki, K., 2000, “A Challenge to Extremely High Heat Flux Removal Technique Using a Porous Medium,” *Journal of the Heat Transfer Society of Japan*, **39**(159), pp. 23–28, in Japanese.
- [3] Yuki, K., Abei, J., Hashizume, H., and Toda, S., 2005, “Super-High Heat Flux Removal Using Sintered Metal Porous Media,” *J. Therm. Sci.*, **14**(3), pp. 272–280.
- [4] Wang, C. Y., and Beckermann, C., 1993, “A Two-Phase Mixture Model of Liquid-Gas Flow and Heat Transfer in Capillary Porous Media—I. Formulation,” *Int. J. Heat Mass Transfer*, **36**(11), pp. 2747–2758.
- [5] Abei, J., Yuki, K., Hashizume, H., and Toda, S., 2004, “Thermo-Fluid Analysis of Two Phase Flow With Phase Change Against Intense Heat in Porous Media,” *Proceedings of Third International Symposium on Heat Transfer Enhancement and Energy Conservation ISHTEEC’03*, Vol. 1, pp. 319–327.
- [6] Wang, C. Y., 1997, “A Fixed-Grid Numerical Algorithm for Two-Phase Flow and Heat Transfer in Porous Media,” *Numer. Heat Transfer, Part B*, **31**, pp. 85–105.
- [7] Ergun, S., 1952, “Fluid Flow Through Packed Columns,” *Chem. Eng. Prog.*, **48**, pp. 89–94.
- [8] Zhao, T. S., Cheng, P., and Wang, C. Y., 2000, “Buoyancy-Induced Flows and Phase-Change Heat Transfer in a Vertical Capillary Structure With Symmetric Heating,” *Chem. Eng. Sci.*, **55**, pp. 2653–2661.
- [9] Peterson, G. P., and Chang, C. S., 1997, “Heat Transfer Analysis and Evaluation for Two-Phase Flow in Porous-Channel Heat Sinks,” *Numer. Heat Transfer, Part A*, **31**, pp. 113–130.

- [10] Udell, K. S., 1983, "Heat Transfer in Porous Media Heated From Above With Evaporation, Condensation, and Capillary Effects," *ASME J. Heat Transfer*, **105**, pp. 485–492.
- [11] Yagi, S., and Kunii, D., 1957, "Studies on Effective Thermal Conductivities in Packed Beds," *AIChE J.*, **3**, pp. 373–381.
- [12] Yagi, S., and Kunii, D., 1960, "Studies on Heat Transfer Near Wall Surface in Packed Beds," *AIChE J.*, **6**, pp. 97–104.
- [13] Wakao, N., 1979, "Effect of Fluid Dispersion Coefficients on Particle-to-Fluid Heat Transfer Coefficients in Packed Beds," *Chem. Eng. Sci.*, **34**, pp. 325–336.
- [14] Rohsenow, W. M., 1952, "A Method of Correlating Heat Transfer Data for Surface Boiling of Liquids," *Trans. ASME*, **74**, pp. 969–976.
- [15] Clark, J. A., and Rohsenow, W. M., 1954, "Local Boiling Heat Transfer to Water at Low Reynolds Numbers and High Pressures," *Trans. ASME*, **76**, pp. 554–562.
- [16] Oda, Y., Iwai, H., Suzuki, K., and Yoshida, H., 2003, "Numerical Study of Conjugate Heat Transfer for Channel Filled With Porous Insert," *The Sixth ASME-JSME Thermal Engineering Joint Conference*, Paper No. TED-AJ03-418.
- [17] Patankar, S. V., 1980, *Numerical Heat Transfer and Fluid Flow*, McGraw-Hill, New York.
- [18] Togashi, H., Yuki, K., and Hashizume, H., 2005, "Heat Transfer Enhancement Technique With Copper Fiber Porous Media," *Fusion Sci. Technol.*, **47**(3), pp. 740–745.

The Critical Heat Flux Condition With Water in a Uniformly Heated Microtube

A. P. Roday

T. Borca-Tasciuc

M. K. Jensen¹

e-mail: JenseM@rpi.edu

Department of Mechanical, Aerospace and
Nuclear Engineering,
Rensselaer Polytechnic Institute,
Troy, NY 12180-3590

The critical heat flux (CHF) condition needs to be well understood for designing miniature devices involving two-phase flow. Experiments were performed to determine the CHF condition for a single stainless steel tube having an inside diameter of 0.427 mm subjected to uniform heat flux boundary conditions. The effects of mass flux, pressure, and exit quality on the CHF were investigated. The experimental results show that the CHF increases with an increase in mass flux and exit pressure. For all exit pressures, the CHF decreased with an increase in quality in the subcooled region, but with a further increase in quality (near zero quality and above), the CHF was found to have an increasing trend with quality (up to about 25% quality). CHF values in this region were much higher than those in the subcooled region. This suggests that even at very low qualities, the void fraction becomes appreciable, which results in an increase in the average velocity, thereby increasing the CHF limit. [DOI: 10.1115/1.2780181]

Keywords: CHF, boiling, exit quality, subcooled, saturated, microtube

1 Introduction

For more than a decade, one of the important applications of heat transfer engineering has been thermal management of electronic devices, and this is a result of the continuous and rapid development of integrated circuit technology. Moore's law [1] states that the number of transistors in an integrated circuit (IC) doubles every 18 months. Due to the increased packaging density and performance of microelectronic devices, IC chip power has significantly risen in the last two decades. The heat fluxes in these devices are high, from about 50 W/cm² in the current electronic chips to about 2000 W/cm² [2] in semiconductor lasers.

The challenge in cooling such devices is that the chip temperature has to be maintained below 85°C despite the high local heat flux. Such a high heat flux imposes a practical limit on traditional cooling approaches such as natural and forced convection using air. Adoption of liquid cooling in packaging of electronic devices seems to be a viable option as it offers the capability of heat removal rates much higher (more than four times) than that of air cooling. Also, the cooling could be accomplished with or without phase change of the liquid (coolant). The use of two-phase cooling has many attractive features from a thermal perspective, such as reduced flow rate requirements while removing large amounts of heat and operating with lower temperature differences. Hence, two-phase cooling approaches at the small scale have become important; with the current trends in the advancement of microelectromechanical system (MEMS) technology, the fabrication of components for liquid cooling could become more cost effective.

With the development of nanotechnology and fuel-cell technology, more compact and enhanced heat exchangers are being designed with surface area densities as high as 10,000 m²/m³ [3]. Such devices could be useful as fuel reformers in automotive fuel cells, in air separation and cryogenic industries, and in the aerospace industry to reduce weight. The high surface densities associated with these heat exchangers can be achieved by construction techniques that result in a large number of small channels in the

100–1000 μm range [4]. Therefore, mini- and microscale heat transfer is becoming important in such industrial heat exchangers as well. Thus, we see that two-phase heat transfer in such small channels is a potential solution to thermal control (cooling) and thermal processing applications (compact heat exchangers).

Flow boiling in tubes and channels is a complex convective phase change process. In cases where the system is heat flux controlled (electrical heating or nuclear heating), an increase in heat flux ultimately leads to deterioration in heat transfer, often indicated by a sudden sharp rise in the wall temperature or the physical burnout of the wall. This upper limit on the heat flux is defined as the critical heat flux (CHF) condition, and engineers must take this into consideration when designing heat transfer equipment for safe operation. There has been a growing interest to understand the CHF behavior in small micron-sized passages and also to determine if this CHF behavior is similar to that observed in large-sized tubes and channels. Unfortunately, the literature so far has been inconclusive in understanding the parametric effects on the CHF condition. This is partly due to the difficulty in carrying out experiments at the small scale. Some of the existing literature on CHF in mini- and microchannels is reviewed here.

2 Critical Heat Flux Studies in Mini/Microchannels

There are very few investigations of CHF studies in small circular tubes. There have been some studies in tubes with small dimensions (down to about 0.3 mm) involving very high mass velocities intended for extremely high heat flux removal as in fusion reactors [5,6], but studies at lower mass fluxes are very limited. Celata et al. [7] have conducted subcooled CHF studies in tube diameters as small as 0.25 mm, but these were, again, for very high heat fluxes (up to 70 MW/m²) and high mass fluxes (greater than 5000 kg/m² s) in the fusion technology application.

Nariai et al. [8] reported CHF studies with water at ambient exit pressure in stainless steel tubes with inside diameters of 1 mm, 2 mm, and 3 mm; tests were performed from the subcooled to the quality region (very close to zero quality) for mass fluxes ranging from 7000 to 11,000 kg/m² s. The inlet water temperature was between 17°C and 80°C. They indicated that the CHF decreased with an increase in exit quality in the subcooled region (i.e., negative quality indicated subcooled liquid). There was a minimum in the CHF versus quality curve very close to zero quality. As quality

¹Corresponding author.

Contributed by the Heat Transfer Division of ASME for publication in the JOURNAL OF HEAT TRANSFER. Manuscript received January 4, 2007; final manuscript received May 11, 2007; published online January 28, 2008. Review conducted by Anthony M. Jacobi.

was further increased to a positive value, the CHF increased sharply. The maximum exit quality in their data was about 0.05.

A similar trend was observed by Bergles and Rohsenow [9] for CHF with de-ionized water in a stainless steel 2.38 mm tube with $L/D=15$, mass flux of $3000 \text{ kg/m}^2 \text{ s}$, and an exit pressure of 207 kPa. At high subcooling, CHF decreased monotonically with increases in quality; the data then passed through a minimum and then increased in the bulk boiling region. It was argued that at low values of subcooling, the void fraction became appreciable, which caused an increase in average velocity with the result that the burnout limit was raised. They found a strong inverse dependence of CHF on diameter. They referred to earlier work by other researchers who believed that CHF decreased with decrease in diameter when the size was reduced below 2 mm and suggested that this could be due to flow oscillations.

Roach et al. [10] studied the CHF associated with flow boiling of subcooled water in circular tubes with diameters of 1.17 mm and 1.45 mm ($L/D=110$), mass velocities from $250 \text{ kg/m}^2 \text{ s}$ to $1000 \text{ kg/m}^2 \text{ s}$, exit pressures from 345 kPa to 1035 kPa, and inlet temperatures from 49°C to 72°C . They observed the CHF condition at very high exit qualities (around 0.8) indicating dryout. CHF increased with increasing channel diameter, mass flux, and pressure. They found that in both the tube sizes for pressure around 690 kPa and mass flux about $800 \text{ kg/m}^2 \text{ s}$, CHF did not occur at all, and a smooth transition from nucleate to film boiling took place. The deviation for the smaller tube from the Bowring correlation was about 35% for most heat flux values; it should be noted that the Bowring correlation was based on data with diameters from 2 mm to 45 mm.

Oh and Englert [11] conducted subatmospheric CHF experiments with water in a single rectangular aluminum channel heated on one side with electric strip heaters. Their channel cross-section dimensions were $1.98 \times 50.8 \text{ mm}^2$ (hydraulic diameter of 3.8 mm) and heated length of 600 mm ($L/D=160$). The exit pressures ranged from 20 kPa to 85 kPa. The tests were performed with low mass fluxes from $30 \text{ kg/m}^2 \text{ s}$ to $80 \text{ kg/m}^2 \text{ s}$. CHF was found to increase with mass flux, in almost a linear fashion. The relation between subcooling and CHF was also found to be linear although the effect was not significant. Between an inlet subcooling of $44\text{--}66^\circ\text{C}$, CHF increase was just 15%. Experimental CHF data did not match well with the predicted CHF from existing low flow-rate correlations. The closest prediction of the CHF data was with the Lowdermilk correlation [12], which underpredicted the data by about 30%.

CHF experiments were performed by Lazarek and Black [13] with R-113 in a stainless steel tube of inside diameter 3.15 mm ($L/D=40$) in a vertical orientation. The pressure was varied from 124 kPa to 413 kPa. The mass velocities were in the range of $140\text{--}740 \text{ kg/m}^2 \text{ s}$. Inlet subcooling varied between 3°C and 73°C . Following the power increase, the wall temperatures underwent progressively large oscillations due to intermittent rewetting of the passage wall. CHF occurred because of the dryout of the liquid and always at the exit of the heated test-section length. Axial conduction effects on CHF were not assessed in this study even though the test section had a thick wall (0.4 mm).

Bowers and Mudawar [14] conducted studies with R-113 in circular minichannel and microchannel heat sinks machined into large copper blocks. Three parallel channels 2.54 mm diameter each formed the minichannel heat sink. The microchannel heat sink had $510 \mu\text{m}$ diameter channels. They concluded that the CHF was not a function of inlet subcooling in either the mini- or microchannel heat sink.

Yu et al. [15] carried out CHF experiments with water in a stainless steel 2.98 mm inside diameter tube ($L_i/D=305$) and a pressure of about 207 kPa. The outside diameter of the test section was 4.76 mm. CHF was found to decrease with a decrease in mass flux (mass fluxes varied between $50 \text{ kg/m}^2 \text{ s}$ and $200 \text{ kg/m}^2 \text{ s}$). CHF qualities were found to be relatively high, above 0.5. Kami-

dis and Ravigururajan [16] used R-113 to investigate the CHF condition in 1.59 mm, 2.78 mm, 3.97 mm, and 4.62 mm short tubes (L/D ranged from 11 to 24). CHF was found to increase with mass velocity.

Lezzi et al. [17] reported experimental results on CHF in forced convection boiling of water in a horizontal tube of diameter 1 mm and $L/D=250, 500, \text{ and } 1000$. The tube wall thickness was 0.25 mm. The mass flux varied between $800 \text{ kg/m}^2 \text{ s}$ and $2700 \text{ kg/m}^2 \text{ s}$. In all cases the quality at the outlet was high (greater than 0.6), and the CHF was reached through dryout. They concluded that for low mass fluxes and tube diameters down to 1 mm, the effect of the diameter on CHF did not differ from the characteristics of the large diameter tubes. They claimed that no oscillations affected the data, but data on pressure were not reported. Also, conduction along the thick tube wall could significantly affect the CHF. This effect was not assessed in this study.

Jiang et al. [18] conducted CHF studies with water with an array of V-grooved microchannels of either 35 or 58 channels each of $40 \mu\text{m}$ hydraulic diameter and either 10 or 34 channels of $80 \mu\text{m}$ hydraulic diameter. In all the devices tested, the wall temperature increased almost linearly with heat flux until the onset of the CHF condition. The quality at the exit was 1.0 at CHF, indicating a single-phase flow of the vapor. CHF was found to be a function of the flow rate, and CHF increased linearly with an increase in the rate of flow.

Recently, Wojtan et al. [19] investigated saturated CHF in a single uniformly heated microchannel of 0.5 mm and 0.8 mm internal diameters using R-134a and R-245fa. They did not find any influence of inlet subcooling on CHF; at the same mass flux, CHF increased with increasing diameter, which is the opposite effect found by Bergles and Rohsenow [9] whose study covered the subcooled to the saturated region (up to qualities of about 0.12). Wojtan et al. studied the effect of exit quality on CHF only for qualities above 40%. They presented a new correlation to predict CHF in circular uniformly heated microchannel.

Kuan and Kandlikar [20] studied the effect of flow boiling stability on CHF with R-123 in six parallel microchannels (cross-sectional area of each microchannel is $1054 \times 157 \mu\text{m}^2$) machined on a copper block of dimensions $88.9 \times 29.6 \text{ mm}^2$. They developed a theoretical model to represent the CHF mechanism and correlated it with their experimental data.

Koşar et al. [21] obtained a few CHF data with de-ionized water flowing through five parallel microchannels ($227 \mu\text{m}$ hydraulic diameter) micromachined on a silicon wafer. They concluded that the exit pressure did not have any effect on the dependence of CHF, but the CHF was found to increase with an increase in mass velocity. The CHF seemed to decrease with an increase in exit quality (for qualities above 0.5), although there was an upward jump at about $x=0.7$.

Zhang et al. [22] evaluated existing correlations for flow boiling of water with available databases from small diameter tubes and developed a new correlation based on the inlet conditions by doing parametric trend analyses of the collected database.

Thus, there is no general agreement on the mini/microchannel CHF studies conducted so far. For example, in minichannels, Roach et al. [10] found the CHF to increase with increasing channel diameter but Bergles and Rohsenow [9] found an inverse dependence of diameter on CHF. Oh and Englert [11] found a weak linear relationship between inlet subcooling and CHF, but Bowers and Mudawar [14] found that the CHF was not at all affected by the inlet subcooling during their studies in parallel microchannels. Wojtan et al. [19] found, in their studies with single tubes, that the CHF was not dependent on inlet subcooling. The data by Yu et al. [15] indicated that the CHF increased with an increase in exit quality, but the data by Wojtan et al. [19] depicted the opposite effect. The CHF studies by Roach et al. [10] show that the CHF increases with increasing pressure, but the data in some studies [19] do not show a strong dependence of pressure on CHF. Studies such as Refs. [8,9] show that the CHF increases from the

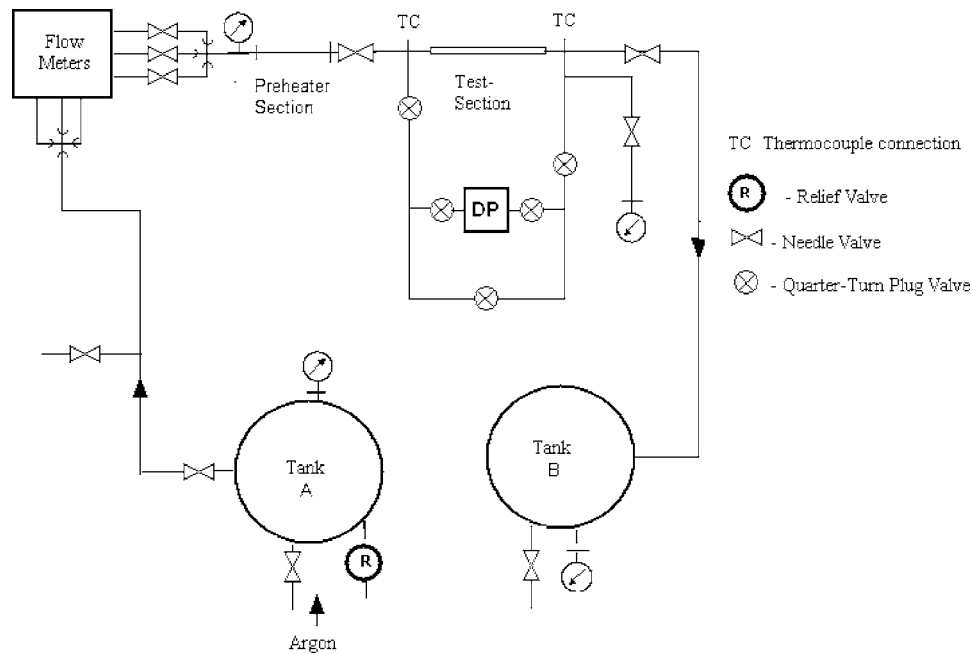


Fig. 1 Description of test facility

subcooled to the saturated region near zero qualities, but other studies have not reported this behavior. Many researchers have attempted to correlate their data with the existing correlations, but the different data vary in the degree of disagreement. Many different correlations have been developed, but they are mostly applicable to the limited data range over which the experiments were conducted.

Overall, there are very limited studies on CHF in the micron-sized dimensions. There are very few studies for CHF at subatmospheric pressures, close to ambient pressure with low mass fluxes, or with tube diameters below $1000 \mu\text{m}$. Most of the studies in the microscale range use parallel rectangular microchannels. Such channels are subject to instabilities and conduction through the block on which the channels are machined, and these conditions affect the CHF condition. Hence, the objective of this paper is to experimentally investigate the effects of mass flux, inlet subcooling, exit quality, and pressure on the CHF condition for a single stainless steel microtube. The tube internal diameter used in this study is 0.427 mm with an outside diameter of 0.55 mm and a heated length of 59 mm . A range of mass fluxes ($315\text{--}1570 \text{ kg/ms}^2$), inlet subcoolings ($2\text{--}50^\circ\text{C}$), and exit pressures ($25.3\text{--}179 \text{ kPa}$) was examined during this study.

3 Experimental Facility and Test Section

3.1 Experimental Facility. The experimental investigations were carried out using the test facility as shown in Fig. 1, which facilitated the flow of water between Tank A and Tank B. The major components of the loop are the two tanks, flowmeters, preheater, test-section assembly, and the pressure transducer arrangement. Water was stored in Tank A, which was equipped with a vacuuming, pressurizing, and a degassing arrangement. As a safety measure, a pressure relief valve was also provided on the tank. Water was circulated in the loop by imposing a pressure difference between the two tanks. Water passed through one of the three rotameters depending on the flow range, and the flow was set by an in-line needle valve. A pressure gauge measured the pressure at the inlet of the preheater section. The water was heated to a desired temperature by passing it through a 200 mm long preheater section. This preheater was constructed by coiling resistance wire around 6.4 mm stainless steel tube. Voltage was ap-

plied to the wire through a variable transformer. The preheated fluid was throttled before it entered the test section. The test section was mounted on an assembly, which facilitated quick replacement of the test section. Detailed discussion of the test section and its mounting is provided later. A differential pressure transducer measured the pressure drop across the test-section length. A Bourdon-type pressure gauge recorded the pressure at the exit of the test section. Following the test section, the fluid entered Tank B from where it was later pumped back to the main storage Tank A.

3.2 Test Section and Guard Heater. The test sections were individual hypodermic tubes made of 304 stainless steel cut from a longer piece of tubing. The test-section ends were sanded and polished on a sander using 400 and 600 grit sand paper, and the final polishing was carried out using a $1 \mu\text{m}$ diamond solution. Microscopic examination of the test section so prepared ensured that no burrs were present. The test section was heated by passing dc through it. For this purpose, $2 \times 2 \text{ cm}^2$ brass strips were soldered at two different locations on the hypodermic tubing and are shown in Fig. 2; electric power wires were soldered on these strips. The voltage to the test section was provided through a dc power supply with variable output between 0 V and 10 V and a current rating of $0\text{--}100 \text{ A}$. The test section was held at its two ends using compression fittings. These fittings housed a Teflon bushing through which the test-section tubing was inserted. Once the test section was inserted, the fitting was tightened to create a leak-tight joint.

The test section was housed inside a guard heater to minimize heat losses during diabatic experiments. A 2.0 cm thick layer of insulation was wrapped around this test section. A 5 cm diameter copper tube, with resistance wire and a thermocouple bonded to it, was secured over this insulation. Then, another 3 cm layer of insulation was wrapped around the copper tube. The guard heater covered the area from compression fitting to compression fitting. The power to this guard heater was controlled through a variable transformer.

T-type thermocouples were mounted at six different locations on the test section for wall temperature measurements. Thermocouples nearer to the exit of the heated section were spaced 1.8 mm apart to better track the CHF condition. Also, one ther-

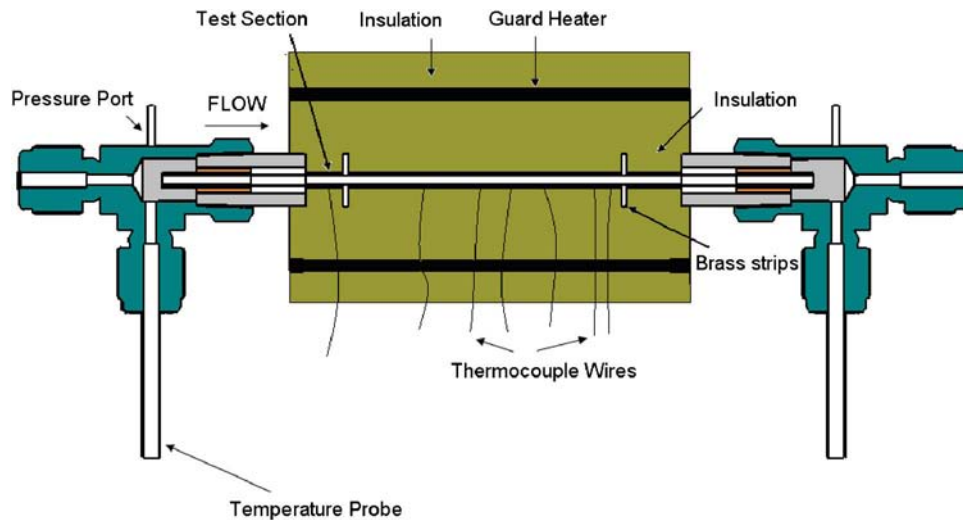


Fig. 2 Test Section Assembly

mocouple was mounted on the test section ahead of the heated length to check for any backflow of vapor and axial conduction away from the heated section. Pressure taps were provided at the two ends of the test section (about 35 mm away from the heated section). Temperature probes measured the temperature of water at the inlet and exit of the test section at the same location as the pressure taps. The inlet and exit portions of the test section were heavily insulated to avoid heat loss.

4 Instrumentation

Five types of measurements were made: temperature, flow rate, pressure, voltage, and geometry of test section (diameter and length).

Temperature measurements. Two different temperature measurements were needed, that of the test-section wall and the working fluid. The wall temperatures were measured using thermocouples made of fine wire (36 AWG, 0.127 mm wire diameter) with beads welded in an inert environment. The inlet and outlet fluid temperatures were measured using probes made from thermocouples to avoid heat conduction through the probe. The accuracy of the temperature measurement using these thermocouples was $\pm 0.3^\circ\text{C}$.

Flow-rate measurement. The flow rate was measured using rotameters. The flowmeter was mounted between the tank and the preheater. To cover the entire range of flow rates needed for the experimentation, a bank of three flowmeters was used. This increased the accuracy of measurement. The accuracy of flow measurement was $\pm 2.0\%$ of the reading.

Pressure measurement. There are two different types of pressure measurements performed during the experiments: pressure level and pressure drop across the test-section length. The pressure level was measured with Bourdon-type pressure gauges at the outlet of the flowmeter and at the exit of the test section. As seen in Fig. 2, the pressure taps were provided outside the test section and were connected to the differential pressure transducer. This transducer measured the total pressure drop across the test-section overall length. The pressure taps were mounted very close to the test-section exit, about 5 mm from the test-section end (35 mm from the heated section). The differential pressure transducer had an accuracy of $\pm 0.25\%$ of full scale. The diaphragm used during these tests had a full scale pressure reading of 86 kPa.

Test-section geometry (diameter and length) measurements. The diameter of the test section used in the experiment was carefully measured using a Unitron optical microscope with a $40\times$ magnification and having a Mitutoyo measuring probe attachment. The length of the test section was measured using vernier calipers. The

accuracy in measuring the diameter was ± 0.00254 mm and on the length was ± 0.03 mm.

Voltage measurement. Power supplied to the test section was measured by taking voltage measurements across the test section and a current shunt sized to ensure high accuracy depending on the current range. The accuracy of the shunts was $\pm 0.25\%$.

Data acquisition system. The outputs from all the instruments were recorded for every experimental run. Manual readings were taken from the flowmeters and the pressure gauges. All other data were directly read through a computerized data acquisition system using LABVIEW[®] software and National Instruments data acquisition and conditioning hardware. A solid-state relay was used to shut off the test-section power when the CHF condition was reached. Two thermocouples nearest to the outlet of the test section were monitored, and once the wall temperature reached a predetermined value, power was cut to the test section. This shut-off ensured that the test section was saved for further experiments. The data acquisition system had the capability of gathering data up to 1000 Hz. The accuracy of voltage measurement was $\pm 0.07\%$. Computer programs for data acquisition and reduction were developed to control the acquisition, reduction, and storage of data.

5 Experimental Procedures

Calibration of the flowmeters was done using the weigh tank technique of measuring the volume of fluid collected in a given amount of time. Calibration of the Bourdon-type pressure gauges was done using a deadweight tester. The differential pressure transducers were calibrated for each diaphragm using a water column over the full pressure range of the transducers.

Water was degassed before circulating in the loop. This was done by passing high pressure argon (an inert gas) through the water stored in Tank A. This gas stripped the dissolved oxygen from water. The process was carried out in vacuum so that the dissolved gases along with the inert gas are pulled out leaving the tank with degassed water. The measured oxygen content was 2.2 ppm.

For an experimental run, the flow was set to the desired value by adjusting the in-line valves. The exit pressure was set by controlling the pressure in Tank B. The preheater and guard heater were turned on and set to the desired values. A criterion of a maximum $\pm 0.5^\circ\text{C}$ variation in wall temperatures in about 15 min was set to detect the quasisteady state as the wall temperatures remained fairly constant after about 15 min, indicating that a steady state was attained. It took up to about 2 h to reach the initial quasisteady state depending on the operating conditions and

about 30 min for each new setting of the flow rate. For every new setting of the inlet temperature, it took another 1 h for the flow to reach steady state. Once the steady state was reached, data were recorded for the set operating conditions.

A single-phase experiment was first performed and the heat loss was estimated by comparing the sensible heat gained by the water (inlet and outlet water temperatures were measured during the experiment) with the power input to the test section. This experiment was done by setting the power to the test section at a particular value and adjusting the guard heater power so that the guard heater temperature was only slightly above the wall temperature on the test section. This ensured minimum heat loss from the test-section wall. The measurements of flow, temperature, and voltages were then recorded.

Next, the guard heater temperature was set close to the saturation temperature (corresponding to the outlet pressure). The inlet fluid temperature was again set to the desired value, steady state was reached, and then the power to the test section was increased in progressively smaller increments until the CHF condition was reached. This condition was marked by a nearly instantaneous rise (the switching time of the relay is about 7 ms) in the wall temperature of about 80–100°C over the saturation temperature.

6 Data Reduction

The measured quantities are the total pressure drop ($\Delta p_{t, \text{expl}}$) from the differential pressure transducer, the volumetric flow rate (Q) from the flowmeter, the test section inside diameter (D), the test-section length (L), the voltage across the shunt (V_{sh}), the voltage across the test section (V_{TS}), the heated length of the test section (L_h), the fluid inlet temperature ($T_{f,i}$), the fluid exit temperature ($T_{f,o}$), and the exit pressure (P_{exit}).

Power to the test section is calculated by the following equation:

$$PW_{\text{TS}} = V_{\text{TS}}I \quad (1)$$

where V_{TS} is the voltage across the test section and I is the current through the test section. The current to the test section was obtained from the current shunt voltage measurement.

Heat loss was estimated by comparing the sensible heat gained by the water in single-phase experiments, which is given by

$$H = \rho Q c_p (T_{f,o} - T_{f,i}) \quad (2)$$

with the electric power input over a wide range of flow rates (Re ranging from 250 to 1200). The guard heater ensured that the heat loss was within $\pm 5\%$. During the two-phase experiments, the guard heater temperature was set slightly higher than the fluid saturation temperature, and it is assumed that the heat loss was similar to that observed during the single-phase tests.

The heat flux was obtained by

$$q'' = 1000PW_{\text{TS}} / \pi DL_h \quad (3)$$

The wall superheat is obtained as

$$\Delta T_{\text{sat}} = T_{w,\text{in}} - T_{\text{sat}} \quad (4)$$

The fluid saturation temperature (T_{sat}) is that corresponding to the measured exit pressure. This was compared with the measured fluid temperature at the outlet of the test section and excellent agreement with the measured and calculated temperatures was obtained. The local inner wall temperature is obtained from the outer wall temperature using a 1D heat conduction model assuming steady-state radial conduction through the wall with uniform heat generation and no heat losses.

The mass flow rate is given by

$$\dot{m} = \rho Q \quad (5)$$

and the mass flux is defined as

$$G = 10^6 \dot{m} / (\pi D^2 / 4) \quad (6)$$

Table 1 Experimental conditions for the CHF study

Parameter	Range
Fluid	De-ionized, degassed water (~2.2 ppm O ₂)
D/D_{out}	0.427 mm/0.550 mm
L_h (mm)	59
P_{exit} (kPa)	179, 102, 25.3
G (kg/m ² s)	315, 560, 870, 1570
ΔT_{sub} (°C)	2–50

Exit quality was obtained from an energy balance between the heat supplied to the test section and the heat gained by the fluid. In the case of subcooled exit flow, enthalpy of the fluid [$h(T)$] is the liquid enthalpy corresponding to that temperature. Thus, the exit quality for a subcooled liquid is defined as

$$x = \frac{h(T) - h_f(P)}{h_{fg}(P)} \quad (7)$$

where h_{fg} is the enthalpy of vaporization corresponding to the exit pressure and h_f is the saturated liquid enthalpy corresponding to the exit pressure.

In the case of an exit flow in the saturation region, the quality is calculated by

$$x = \frac{1}{h_{fg}} \left[\frac{10004L_h q''}{GD} - c_p (T_{\text{sat}} - T_{f,i}) \right] \quad (8)$$

7 Uncertainty Analysis

The uncertainties in the measured quantities propagate through all calculations of the derived quantities. Hence, an uncertainty analysis was performed to estimate these uncertainties. This analysis is based on the method suggested by Kline and McClintock [23]. The results are \dot{m} , $\pm 2.0\%$; G , $\pm 2.3\%$; Re, $\pm 2.4\%$; q'' , $\pm 5.1\%$; and x , $\pm 5.8\%$.

8 Results and Discussion

Experiments were conducted to determine the CHF condition over a range of exit pressures, mass fluxes, and inlet subcoolings in a single stainless steel tube of inside diameter 0.427 mm. The experimental conditions are given in Table 1.

Single-phase experiments were first performed to check for the energy balances. The guard heater power was controlled during both the single- and two-phase experiments. The single-phase pressure drop was found to be in very good agreement with well established theory. The ratio of the total pressure drop (sum of the pressure drops at the entrance, in the developing flow region, fully developed region, and the exit) from the experiment to that calculated using correlations from the literature was within $\pm 6\%$, as can be seen in Fig. 3.

During the single-phase heat transfer experiments, the flow was hydrodynamically fully developed but was thermally developing through the length of the heated section. The heat transfer results were compared with the modified Hausen correlation (for constant heat flux) given below.

$$\text{Nu} = 4.36 + \frac{0.19(\text{Re Pr } D/L)^{0.8}}{1 + 0.117(\text{Re Pr } D/L)^{0.467}} \quad (9)$$

This correlation overpredicted the data by about 34% at lower Reynolds number (Re ~ 200) but underpredicted it by about 50% at Re ~ 1200. These laminar single-phase heat transfer results are consistent with other results from the literature [24,25]. In the two-phase study, there were 50 CHF data points obtained. These include some data points where the characteristic wall temperature rise associated with the CHF condition was not observed. This will be discussed later in this section.

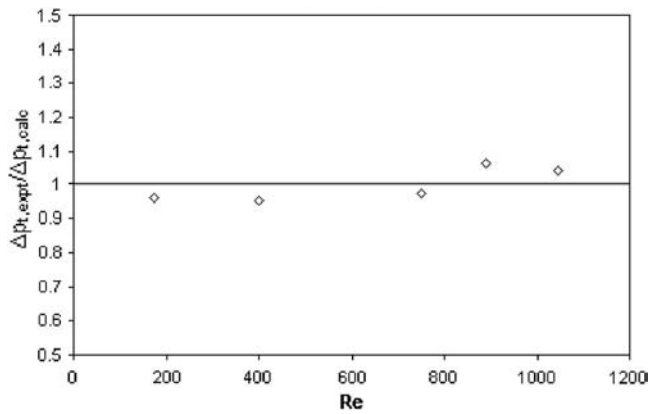


Fig. 3 $\Delta p_{t,expt}/\Delta p_{t,calc}$ versus Re during single-phase flow experiment

8.1 Flow Condition During the Critical Heat Flux Experiments. Flow was stabilized during the CHF experiments by maintaining a very high pressure drop (130–200 kPa) upstream of the test section through use of an inlet throttle valve; the rotameter float position was constant. A thermocouple mounted on the test-section wall just before the heated section did not show any variations in temperature (the temperature was very close to the inlet water temperature), which indicated that there was no backflow of vapor or axial conduction outward from the heated section. The pressure drop showed only small fluctuations with time (single- and two-phase flow regimes) except for very close to the CHF condition. One such plot of pressure drop versus time, at subatmospheric pressure and a mass flow rate of $560 \text{ kg/m}^2 \text{ s}$, is shown in Fig. 4. The magnitude of the fluctuations in Fig. 4 was typical of all tests.

8.2 Wall Temperature Variations With Heat Flux. For the flow boiling tests, there was a characteristic sharp rise in wall temperature at the point of CHF, as can be seen in the plot of wall superheat versus heat flux depicted in Fig. 5. Note, also, that prior to the initiation of the CHF condition, often the wall temperature initially jumped up by about 35°C , then dropped back; with further increases in heat flux, the CHF condition was reached (wall temperature was approximately 165°C). At this point, test-section power was automatically shut off to prevent test-section damage.

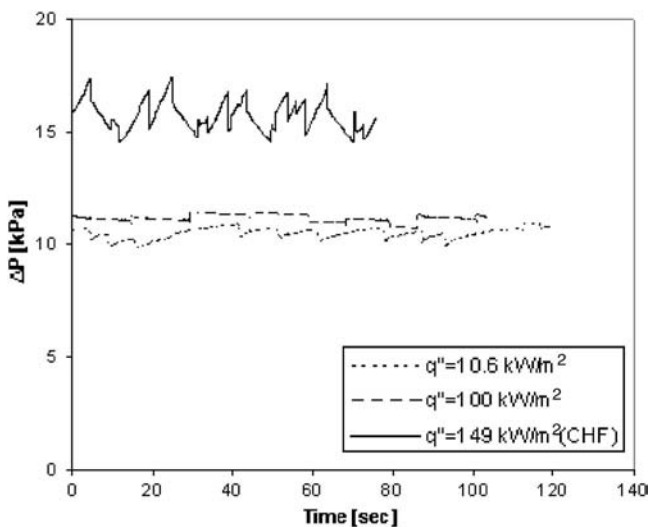


Fig. 4 Pressure drop versus time for $G=560 \text{ kg/m}^2 \text{ s}$, $\Delta T_{sub}=38^\circ\text{C}$, $P_{exit}=25 \text{ kPa}$

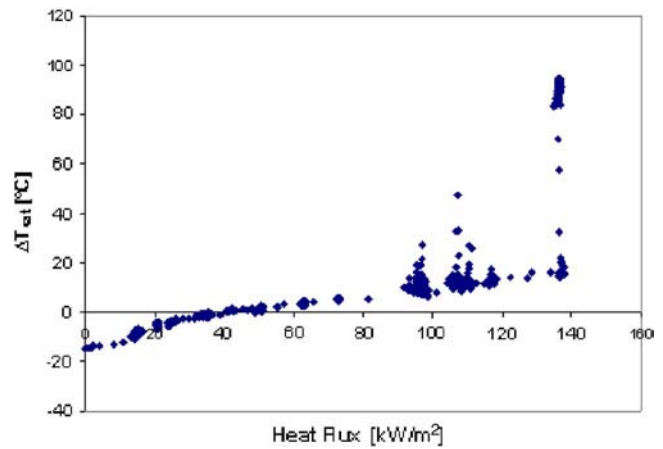


Fig. 5 Wall superheat versus heat flux ($P_{exit}=25 \text{ kPa}$; $G=315 \text{ kg/m}^2 \text{ s}$; $\Delta T_{sub}=15^\circ\text{C}$)

A similar observation was made in other tests with lower mass fluxes where the steady increase in heat flux caused the wall temperatures to increase by about $40\text{--}50^\circ\text{C}$ and then fall back before finally attaining the CHF condition. The jumps in the wall temperature just prior to CHF could be due to the occurrence of dry patches on the tube wall and when the liquid occasionally rewetted the wall, the temperatures would fall back. CHF would occur near the exit when the tube wall became completely dry. Lazarek and Black [13] observed a similar wall temperature response during CHF tests in a 3.1 mm diameter tube at a mass flux of about $270 \text{ kg/m}^2 \text{ s}$. In experiments with higher mass fluxes, the wall temperatures did not exhibit such a sharp intermediate jump, but steadily increased until the CHF condition, with its characteristic temperature rise was reached, similar to that observed with lower mass fluxes.

Figure 6 shows the wall temperatures at six locations along the length of the heated section for two different conditions. For the lower pressure data, it is clear that the CHF occurred toward the exit of the heated section at which point the wall temperatures are considerably higher compared to those closer to the inlet of the test section.

The characteristic CHF did not occur for some of the experiments up to high heat fluxes, at which point power was shut down

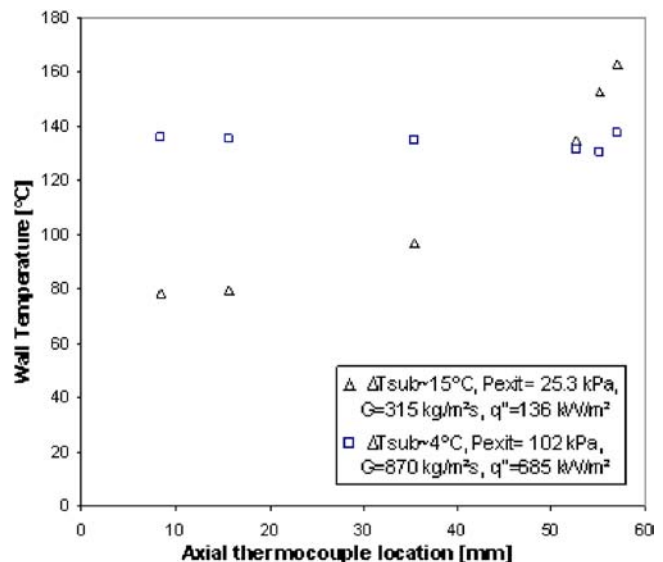


Fig. 6 Axial wall temperature variation ($P_{exit}=25 \text{ kPa}$, 102 kPa)

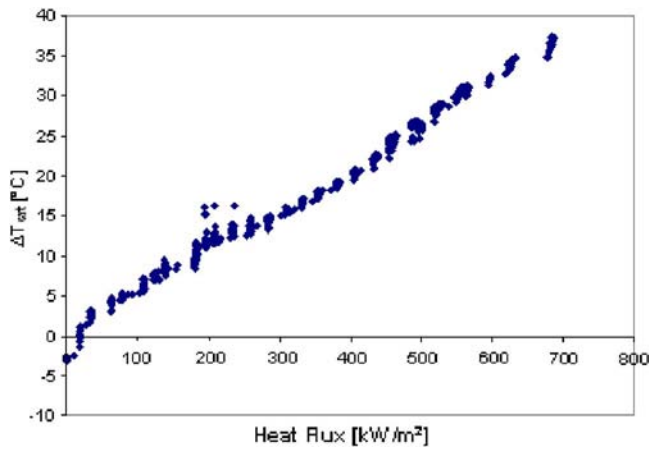


Fig. 7 Wall superheat versus heat flux ($P_{\text{exit}}=102$ kPa; $G=870$ kg/m²s; $\Delta T_{\text{sub}}\sim 4^\circ\text{C}$)

so that the test sections were not destroyed. This happened for some of the tests carried out at low values of inlet subcooling ($\Delta T_{\text{sub}}=2\text{--}7^\circ\text{C}$). Figure 7 shows the exit wall temperature variation with heat flux at an exit pressure of 102 kPa, and one axial temperature data set is also shown in Fig. 6. The wall temperature linearly increased with heat flux but there was no sudden wall temperature spike as is normally associated with the CHF condition. Other tests conducted for slightly lower mass fluxes (e.g., $G=560$ kg/m²s) showed the wall temperature to suddenly increase (by about 30°C) and fall back a few times during the experiment but no characteristic CHF was observed. It might be possible that the flow transitions to an “inverted annular” type even at lower heat flux levels and the boiling takes place through the stable vapor film. The distinct boiling plateau was not seen during such tests. During this “film” type of boiling, the wall temperatures linearly increased as the heat flux was raised. More tests need to be conducted and further studies need to be done to confirm this phenomenon. Experiments performed at higher (179 kPa) and lower (25.3 kPa) exit pressures showed a similar trend but the wall temperature plots for these have been excluded for brevity. Roach et al. [10] made a similar observation of wall temperature behavior in some of their tests with single uniformly heated minitubes and attributed the disappearance of CHF to smooth transition of heat transfer from nucleate to film boiling. They found this to occur at mass fluxes as low as about 500 kg/m²s. Fukuyama and Hirata [26] reported similar findings in their studies with R-113 in a 1.2 mm inside diameter tube, but at relatively high mass fluxes ($>40,000$ kg/m²s) and high pressures (350–1500 kPa), and concluded that the traditional discontinuity in heat transfer coefficient between the nucleate and film boiling at the transition can be completely eliminated by the combined effects of mass flux, subcooling, and pressure. Similarly, Hosaka et al. [27] observed that compared to low mass flux flows, there was a smoother transition from nucleate to film boiling under the conditions of very high mass flux and high subcoolings in their tests with R-113 in tubes of 0.5 mm and 1 mm inside diameters.

For studies with the lower values of mass fluxes, a very high value of CHF was observed when inlet subcooling was very low resulting in exit qualities of about 0.2. But, for similar exit qualities in studies with higher mass fluxes, no CHF was observed. This is discussed in a later section describing the parametric effects on the CHF condition.

In all such tests at qualities slightly above zero when the characteristic CHF condition did not occur, the wall temperatures were much higher above the saturation temperature, and there was little variation in wall temperature from the inlet to the exit of the

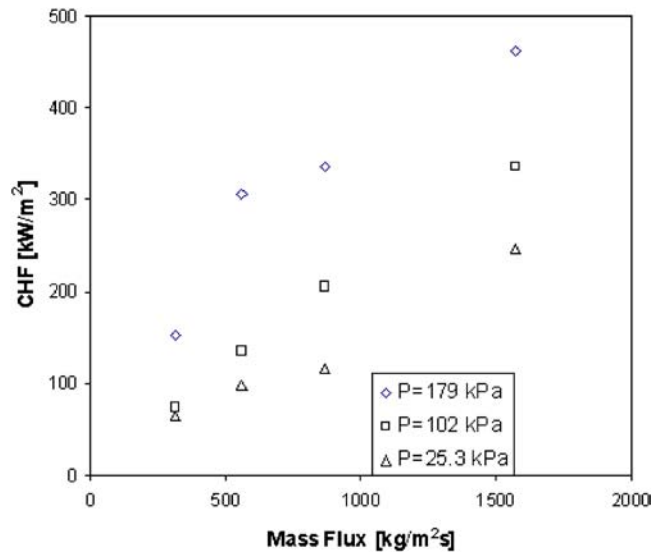


Fig. 8 Effect of mass flux on CHF for $\Delta T_{\text{sub}}\sim 46^\circ\text{C}$, $L_h=59$ mm

heated section as is depicted in Fig. 6 for the study at atmospheric pressure. Also, the wall temperature increased linearly as the heat flux was increased. For this reason, very few saturated CHF data points could be obtained and, in some tests, the experiment had to be terminated if wall superheats were above 60°C to save the test section even if no CHF was observed.

8.3 Parametric Effects on the Critical Heat Flux Condition

8.3.1 Effect of Mass Flux on Critical Heat Flux. Figure 8 depicts the dependence of CHF on mass flux for the three different exit pressures with inlet subcooling, $\Delta T_{\text{sub}}\sim 46^\circ\text{C}$. The subcooled CHF condition was observed in these data at the three pressures. The CHF increases with an increase in mass flux. The CHF increases with an increase in exit pressure for the same value of mass flux; the slope of the CHF-G curves increases with pressure. A similar observation was made at other values of inlet subcooling.

8.3.2 Effect of Inlet Subcooling on Critical Heat Flux. The effect of inlet subcooling on CHF is shown in Fig. 9 for all exit pressures for two mass fluxes. For the higher mass flux, it is seen that, at higher levels of inlet subcooling, CHF slightly decreased with a decrease in inlet subcooling. But, at lower subcoolings (water inlet temperature close to the saturation temperature), the CHF increased with a decrease in subcooling. The same trend was observed at the three different pressures; the value of CHF was higher for the higher exit pressure. A similar behavior is observed for the lower mass flux as well. For the cases where the CHF dramatically increased with reduction in inlet subcooling, the exit quality at CHF was close to zero.

8.3.3 Effect of Exit Quality on Critical Heat Flux. Detailed results for the effect of exit quality on CHF are presented in Figs. 10–12. Note that, in Fig. 10, the CHF first decreases with an increase in quality in the subcooled region, but with a further increase in quality (near zero quality and above), the CHF is found to have an increasing trend with quality. Much higher values of CHF are found in the region close to saturation when compared to the high subcooled region. With still further increases in heat flux/exit quality, the CHF condition did not occur even when the wall superheat ($\Delta T_{\text{sat}}=T_w-T_{\text{sat}}$) reached about $40\text{--}60^\circ\text{C}$; the wall temperature increased essentially linearly with increases in heat flux. At this point, the experiment was terminated to save the

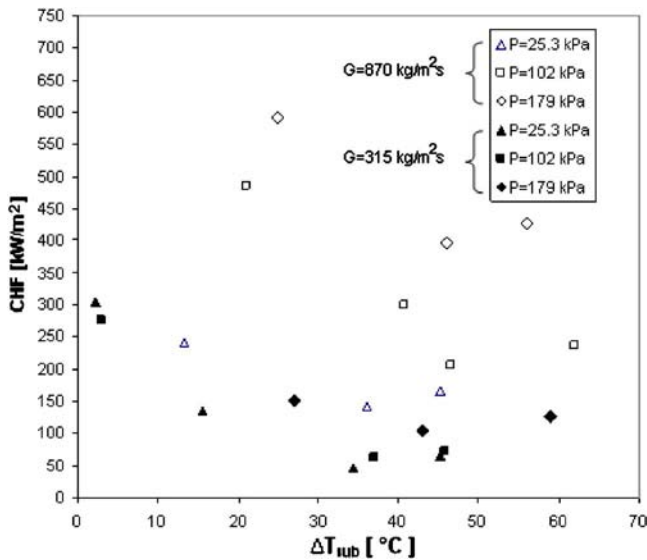


Fig. 9 Effect of inlet subcooling on CHF

test section, and the exit qualities and heat fluxes were $x=0.12$, $q''=825.2 \text{ kW/m}^2$, and $\Delta T_{\text{sat}}=52^\circ\text{C}$ for $G=1570 \text{ kg/m}^2 \text{ s}$; $x=0.19$, $q''=684.7 \text{ kW/m}^2$, and $\Delta T_{\text{sat}}=37^\circ\text{C}$ for $G=870 \text{ kg/m}^2 \text{ s}$;

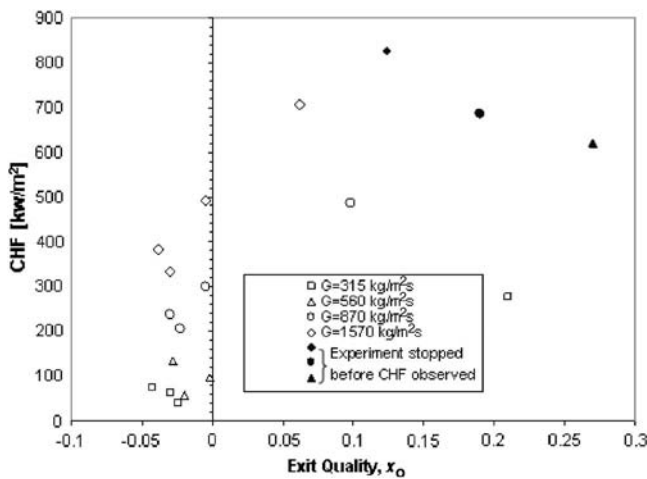


Fig. 10 Variation of CHF with quality for $P_{\text{exit}}=102 \text{ kPa}$ (abs)

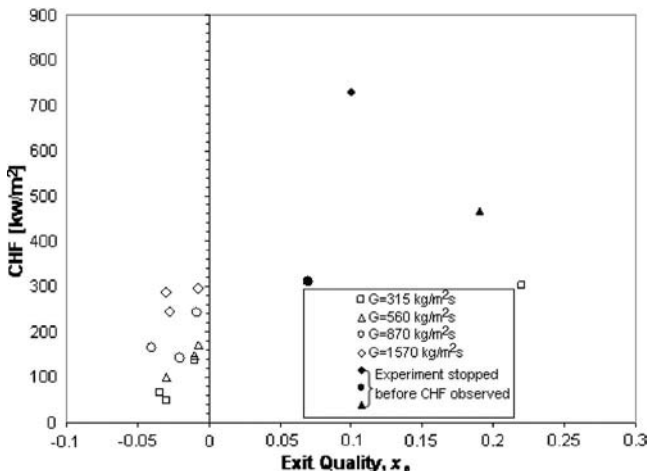


Fig. 11 Variation of CHF with quality for $P_{\text{exit}}=25 \text{ kPa}$ (abs)

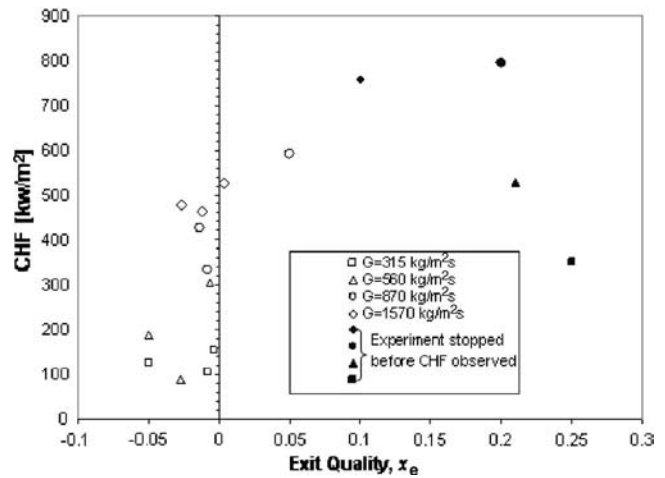


Fig. 12 Variation of CHF with quality for $P_{\text{exit}}=179 \text{ kPa}$ (abs)

and $x=0.27$, $q''=619 \text{ kW/m}^2$, and $\Delta T_{\text{sat}}=55^\circ\text{C}$ for $G=560 \text{ kg/m}^2 \text{ s}$. CHF was, however, observed at about $x=0.21$ for the mass flux of $G=315 \text{ kg/m}^2 \text{ s}$. The results for the exit quality are consistent with the trends observed for the variation of CHF with inlet subcooling.

The increase in CHF from the subcooled to the saturated region can be attributed to the void fraction change. In such a small diameter of the tube, the void fraction becomes significant enough to cause an increase in the velocity of flow through the tube, thereby causing an increase in the value of CHF. Nariai et al. [8] reported a similar observation in their studies on CHF in minitubes (1–3 mm inside diameter) but with much higher mass fluxes (7000–11,000 $\text{kg/m}^2 \text{ s}$). The maximum exit quality in their data was 0.05. Bergles and Rohsenow [9] reported similar findings for flow of water through a 2.38 mm tube with a mass flux of 3000 $\text{kg/m}^2 \text{ s}$.

Studies at subatmospheric pressure show a similar trend (Fig. 11). The CHF decreases with quality in the subcooled region, but as the quality advances toward zero, the CHF starts increasing again. No CHF was observed and the experiment was stopped when $x=0.1$ and $q''=727.6 \text{ kW/m}^2$ for $G=1570 \text{ kg/m}^2 \text{ s}$, $x=0.07$ and $q''=312.6 \text{ kW/m}^2$ for $G=870 \text{ kg/m}^2 \text{ s}$, and $x=0.19$ and $q''=465.5 \text{ kW/m}^2$ for $G=560 \text{ kg/m}^2 \text{ s}$ (for these cases, the inlet subcooling was about 3°C). For $\Delta T_{\text{sub}}=2.3^\circ\text{C}$ and $G=315 \text{ kg/m}^2 \text{ s}$, a value of $q''_{\text{CHF}}=303.5 \text{ kW/m}^2$, similar to that at an exit pressure of 102 kPa, was obtained.

Results for the variation of CHF with exit quality for the exit pressure of 179 kPa are reported in Fig. 12. Here, too, a similar trend to that observed in Figs. 10 and 11, is seen. For inlet subcoolings around $7\text{--}8^\circ\text{C}$, CHF was not observed for either of the mass fluxes. The wall superheats were quite high ($55\text{--}60^\circ\text{C}$) with exit qualities of $x=0.1, 0.2, 0.21$, and 0.25 for mass fluxes of 1570 $\text{kg/m}^2 \text{ s}$, 870 $\text{kg/m}^2 \text{ s}$, 560 $\text{kg/m}^2 \text{ s}$ and 315 $\text{kg/m}^2 \text{ s}$, respectively.

9 Comparison of Critical Heat Flux Data With Existing Correlations

All the CHF data obtained in this study, subcooled as well as saturated, were compared with the existing correlations. The CHF data in the subcooled region were compared with the Hall and Mudawar correlation [28]. This is represented in Fig. 13. Some of the deviation is because the Hall and Mudawar correlation overpredicts the data at very high inlet subcoolings and also it does not take into account the increased CHF behavior seen in this study as the qualities approach zero.

As previously seen, very few CHF data points could be obtained in the saturated region, because the wall temperatures kept

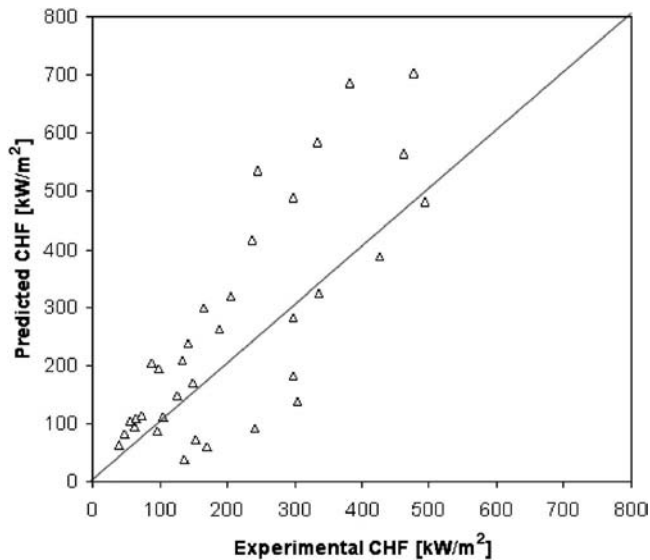


Fig. 13 Comparison of subcooled CHF data with the Hall and Mudawar correlation [28]

on linearly increasing with heat flux, and very high wall superheats were obtained even at significantly lower exit qualities. For most of the tests in the saturated region, the characteristic CHF was not observed and the experiment had to be terminated to save the test section. For the saturated CHF data, three correlations developed for mini/microchannels were considered for comparison: Wojtan et al. [19], Qu and Mudawar [29], and Zhang et al. [22]. The correlations from Refs. [19,29] do not consider the effect of inlet subcooling. However, the data presented in this study clearly show an effect of inlet subcooling on CHF. Hence, only one of these two correlations, by Qu and Mudawar [29], was used for comparison along with the correlation of Zhang et al. [22], which considers an inlet quality effect. The comparisons of the saturated CHF data with the correlations of Qu and Mudawar [29] and Zhang et al. [22] are shown in Fig. 14. The correlation of Zhang et al. highly overpredicts the data. It might be because this correlation was developed by doing a parametric trend analysis to the existing database of diameters in the range 0.33–6.22 mm. There are very few data that are available for the very small diameters, and they are almost all in the high mass flux range. The

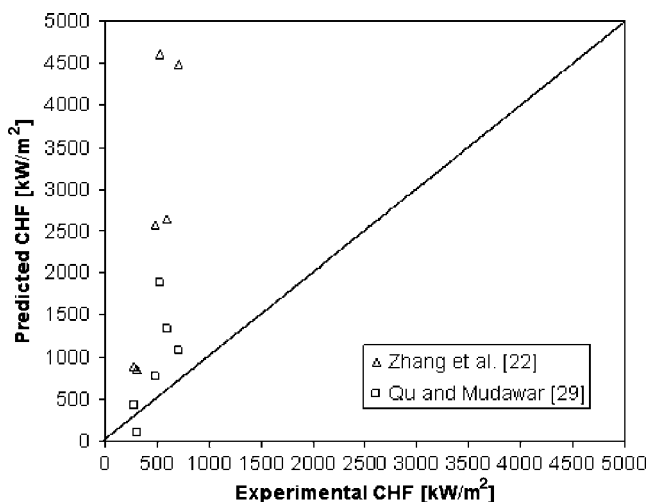


Fig. 14 Comparison of saturated CHF data with the Zhang et al. [22] and Qu and Mudawar correlations [29]

Qu and Mudawar correlation also does not predict the data well as it does not take into account the inlet subcooling effect.

Thus, there is a need for more data with smaller diameters for different mass fluxes, pressures, heated lengths, and type of fluids to develop a satisfactory CHF correlation, which can confidently predict CHF in the subcooled as well as the saturated region.

10 Conclusions

Experiments were performed to measure the CHF condition in the subcooled as well as the saturated region for a single micro-tube. The CHF increases with an increase in mass flux for all the three exit pressures considered in this study. For the same mass flux, CHF increased with an increase in exit pressure. Subcooling has a large impact on CHF at very low values of inlet subcooling. The effect of exit quality on CHF is found to be complicated. The CHF decreased with an increase in quality in the subcooled region, but suddenly increased to a high value around zero quality. With further increase in quality, CHF increased. The effects of other parameters on CHF, such as the fluid type, the diameter, and L/D ratio, need to be investigated. More experiments are being undertaken to fully understand the CHF phenomena in micro-tubes.

Acknowledgment

This work was supported by the National Science Foundation (NSF) under Grant No. CTS-0245642. Graduate student support from the Department of Mechanical, Aerospace and Nuclear Engineering at Rensselaer Polytechnic Institute is also gratefully acknowledged.

Nomenclature

- D = tube inside diameter, mm
- G = mass flux, $\text{kg/m}^2 \text{s}$
- H = heat gain, W
- I = current, A
- L = tube length, mm
- Nu = Nusselt number
- P = pressure, Pa
- Pr = Prandtl number
- PW = power, W
- Q = volumetric flow rate, m^3/s
- Re = Reynolds number
- T = temperature, $^{\circ}\text{C}$
- V = voltage, V
- c_p = specific heat of the fluid, J/kg K
- h = specific enthalpy, J/kg
- k = thermal conductivity, W/mK
- \dot{m} = mass flow rate, kg/s
- q'' = heat flux, kW/m^2
- x = quality

Greek Letters

- Δp = pressure difference, Pa
- ΔT = temperature difference, $^{\circ}\text{C}$
- ρ = density of fluid, kg/m^3

Subscripts

- CHF = critical heat flux
- TS = test section
- calc = calculated
- exit = at the exit
- expt = from experiment
- f = fluid
- fg = liquid vapor
- h = heated
- i = inlet
- o = outlet
- in = inner

out = outer
 sat = saturation
 sh = shunt
 sub = subcooled inlet
 t = total
 w = wall

References

- [1] Moore, G., 1965, "Cramming More Components Onto Integrated Circuits," *Electronics*, **38**(8), pp. 114–117.
- [2] Hannemann, R. J., 2003, "Thermal Control of Electronics: Perspectives and Prospects," *Rohsenow Symposium on Future Trends in Heat Transfer*, Warren M. Rohsenow Heat and Mass Transfer Laboratory, Massachusetts Institute of Technology, Cambridge, MA.
- [3] Kakac, S., and Liu, H., 1998, *Heat Exchangers: Selection, Rating and Thermal Design*, CRC, Boca Raton, FL, Chap. 9, pp. 903–904.
- [4] Kandlikar, S. G., and Grande, W. J., 2003, "Evolution of Microchannel Flow Passages—Thermohydraulic Performance and Fabrication Technology," *Heat Transfer Eng.*, **24**(1), pp. 3–17.
- [5] Vandervort, C. L., Bergles, A. E., and Jensen, M. K., 1994, "An Experimental Study of Critical Heat Flux in Very High Heat Flux Subcooled Boiling," *Int. J. Heat Mass Transfer*, **37**, pp. 161–173.
- [6] Celata, G. P., Cumo, M., and Mariani, A., 1993, "Burnout in Highly Subcooled Water Flow Boiling in Small Diameter Tubes," *Int. J. Heat Mass Transfer*, **36**(5), pp. 1269–1285.
- [7] Celata, G. P., Cumo, M., and Mariani, A., 1997, "Geometrical Effects on the Subcooled Flow Boiling Critical Heat Flux," *Rev. Gen. Therm.*, **36**, pp. 807–814.
- [8] Nariyai, H., Inasaka, F., and Uehara, K., 1989, "Critical Heat Flux in Narrow Tubes with Uniform Heating," *Heat Transfer-Jpn. Res.*, **18**, pp. 21–30.
- [9] Bergles, A. E., and Rohsenow, W. M., 1962, "Forced-Convection Surface-Boiling Heat Transfer and Burnout in Tubes of Small Diameter," Massachusetts Institute of Technology Report No. AF 19(604)-7344; U.S. Atomic Energy Commission DSR Report 8767-21.
- [10] Roach, G. M., Jr., Abdel-Khalik, S. I., Ghiaasiaan, S. M., Dowling, M. F., and Jeter, S. M., 1997, "Low Flow Critical Heat Flux in Heated Microchannels," *Nucl. Sci. Eng.*, **131**, pp. 411–425.
- [11] Oh, C. H., and Englert, S. B., 1993, "Critical Heat Flux for Low Flow Boiling in Vertical Uniformly Heated Thin Rectangular Channels," *Int. J. Heat Mass Transfer*, **36**(2), pp. 325–335.
- [12] Lowdermilk, W. H., Lanzo, C. D., and Siegel, B. L., 1958, "Investigation of Boiling Burnout and Flow Instability for Water Flowing in Tubes," Report No. NACA-TN-4382.
- [13] Lazarek, G. M., and Black, S. H., 1982, "Evaporative Heat Transfer, Pressure Drop and Critical Heat Flux in a Small Vertical Tube with R-113," *Int. J. Heat Mass Transfer*, **25**(7), pp. 945–960.
- [14] Bowers, M. B., and Mudawar, I., 1994, "High Flux Boiling in Low Flow Rate, Low Pressure Drop Mini-Channel and Micro-Channel Heat Sinks," *Int. J. Heat Mass Transfer*, **37**(2), pp. 321–332.
- [15] Yu, W., France, D. M., Wambsganss, M. W., and Hull, J. R., 2002, "Two-Phase Pressure Drop, Boiling Heat Transfer, and Critical Heat Flux to Water in a Small-Diameter Horizontal Tube," *Int. J. Multiphase Flow*, **28**, pp. 927–941.
- [16] Kamidis, D. E., and Ravigururajan, T. S., 1999, "Single and Two-Phase Refrigerant Flow in Mini-Channels," *Proceedings of NHTC2000: 33rd National Heat Transfer Conference*, Albuquerque, NM, pp. 1–8.
- [17] Lezzi, A. M., Niro, A., and Beretta, G. P., 1994, "Experimental Data on CHF for Forced Convection Water Boiling in Long Horizontal Capillary Tubes," *Proceedings of the Tenth International Heat Transfer Conference*, Rugby, UK, Vol. 7, pp. 491–496.
- [18] Jiang, L., Wong, M., and Zohar, Y., 1999, "Phase Change in Microchannel Heat Sinks with Integrated Temperature Sensors," *J. Microelectromech. Syst.*, **8**, pp. 358–365.
- [19] Wojtan, L., Revellin, R., and Thome, J. R., 2006, "Investigation of Saturated Critical Heat Flux in a Single Uniformly Heated Microchannel," *Exp. Therm. Fluid Sci.*, **30**, pp. 765–774.
- [20] Kuan, W. K., and Kandlikar, S. G., 2006, "Critical Heat Flux Measurement and Model for Refrigerant-123 Under Stabilized Flow Conditions in Microchannels," ASME Paper No. IMECE2006-13310.
- [21] Koşar, A., Kuo, C.-J., and Peles, Y., 2005, "Reduced Pressure Boiling Heat Transfer in Rectangular Microchannels With Interconnected Reentrant Cavities," *ASME J. Heat Transfer*, **127**, pp. 1106–1114.
- [22] Zhang, W., Hibiki, T., Mishima, K., and Mi, Y., 2006, "Correlation of Critical Heat Flux for Flow Boiling of Water in Mini-Channels," *Int. J. Heat Mass Transfer*, **49**, pp. 1058–1072.
- [23] Kline, S. J., and McClintock, F. A., 1953, "Describing Uncertainties in Single Sample Experiments," *Mech. Eng. (Am. Soc. Mech. Eng.)*, **75**, pp. 3–8.
- [24] Celata, G. P., Cumo, M., Guglielmi, M., and Zummo, G., 2002, "Experimental Investigation of Hydraulic and Single-Phase Heat Transfer in 0.13-mm Capillary Tube," *Microscale Thermophys. Eng.*, **6**, pp. 85–97.
- [25] Peng, X. F., and Peterson, G. P., 1996, "Convective Heat Transfer and Flow Friction for Water Flow in Microchannel Structures," *Int. J. Heat Mass Transfer*, **39**, pp. 2599–2608.
- [26] Fukuyama, Y., and Hirata, H., 1982, "Boiling Heat Transfer Characteristics With High Mass Flux and Disappearance of CHF Following to DNB," *Proceedings of the Seventh International Heat Transfer Conference*, Hemisphere, Washington, DC, Vol. 4, pp. 273–278.
- [27] Hosaka, H., Mirata, M., and Kasagi, N., 1990, "Forced Convective Subcooled Boiling Heat Transfer and CHF in Small Diameter Tubes," *Proceedings of the Ninth International Heat Transfer Conference*, Hemisphere, Washington, DC, Vol. 2, pp. 129–134.
- [28] Hall, D. D., and Mudawar, I., 2000, "Critical Heat Flux (CHF) for Water Flow in Tubes-II. Subcooled CHF Correlations," *Int. J. Heat Mass Transfer*, **43**, pp. 2605–2640.
- [29] Qu, W., and Mudawar, I., 2004, "Measurement and Correlation of Critical Heat Flux in Two-Phase Micro-Channel Heat Sinks," *Int. J. Heat Mass Transfer*, **47**, pp. 2045–2059.

Numerical Analysis of Wooden Porous Media Effects on Heat Transfer From a Staggered Tube Bundle

Mohammad Layeghi

Ph.D.

Department of Wood and Paper Science and Technology,
University of Tehran,

P.O. Box 3314-31585,

Tehran, Karaj, Iran

e-mail: mlayeghi@nrf.ut.ac.ir

A numerical analysis of forced convective heat transfer from a staggered tube bundle with various low conductivity wooden porous media inserts at maximum Reynolds numbers 100 and 300, Prandtl number 0.7, and Darcy number 0.25 is presented. The tubes are at constant temperature. The extended Darcy–Brinkman–Forchheimer equations and corresponding energy equation are solved numerically using finite volume approach. Parametric studies are done for the analysis of porous medium thermal conductivity and Reynolds number on the local Nusselt number distribution. Three different porous media with various solid to fluid thermal conductivity ratios 2.5, 5, and 7.5 are used in the numerical analysis. The results are compared with the numerical data for tube bundles without porous media insert and show that the presence of wooden porous media can increase the heat transfer from a tube bundle significantly (more than 50% in some cases). It is shown that high conductivity porous media are more effective than the others for the heat transfer enhancement from a staggered tube bundle. However, the presence of a porous medium increases the pressure drop. Therefore, careful attention is needed for the selection of a porous material with good heat transfer characteristics and acceptable pressure drop.

[DOI: 10.1115/1.2780184]

Keywords: laminar and incompressible fluid flow, forced convection, staggered tube bundle, wooden porous media, numerical analysis

1 Introduction

Heat transfer enhancement from a staggered tube bundle, using the idea of inserting a porous material between the tubes, has a great importance in many engineering applications including design and construction of compact heat exchangers, air preheaters, air conditioning units, etc. More recent studies of surfaces covered with porous materials have focused on the generation of reliable pressure drop and heat transfer information for low Reynolds number flow through a bundle of perpendicular or inclined cylindrical fibers [1]. There is a general need for data in the low Reynolds number range, and most of the existing results refer to heat exchanger applications at high Reynolds numbers [2]. Fowler and Bejan [3] studied numerically the heat transfer from a surface covered with flexible fibers, which bend under the influence of the interstitial flow and observed some heat transfer enhancement or decrement. Vafai and Kim [4] and Huang and Vafai [5,6] have shown that a porous coating can alter dramatically the friction and heat transfer characteristics of a surface. This effect has also been documented by Fowler and Bejan [3]. Depending on its properties

and dimensions, the porous layer can act as either as an insulator or as a heat transfer augmentation device. In many applications, it is very important to improve the efficiency of a tube bundle by increasing the local Nusselt number and regulating the pressure drop in a tube bundle. To the knowledge of the author, experimental and numerical studies are still needed to predict the effects of various porous media and tube bank arrangements on the local heat transfer coefficient and pressure drop in a staggered tube bundle.

Among the huge amount of works related to heat transfer from a staggered tube bundle, which are listed in Ref. [7], there are only a limited number of published works related to the heat transfer enhancement from a tube bundle using porous materials. Previous experiences have shown that all porous materials are not appropriate for this purpose [8–10]. In general, the efficiency of a porous medium in heat transfer enhancement from a solid substrate depends on porous medium structure, thermophysical properties, and fluid flow conditions. It has been found that fibrous materials and metal foams [10] saturated with a fluid can serve as an effective medium to augment forced convection heat transfer. Recently, Pavel and Mohamad [11,12] have numerically and experimentally studied the effects of metallic porous materials inserted in a pipe on the rate of heat transfer. The effects of porosity, porous material diameter, and thermal conductivity as well as Reynolds number on the heat transfer and pressure drop, have been investigated. The results have been compared with the clear flow case where no porous material is used. They have shown that higher heat transfer rates can be achieved when a porous insert is used at the expense of a reasonable pressure drop which depends on the permeability of the porous matrix. For a constant diameter of the porous medium, further improvement can be attained by using a porous insert with a smaller porosity and higher thermal conductivity. Care should be exercised since both pore Reynolds number Re_p and ϵ have a positive influence on heat transfer and a negative impact on pressure drop and consequently on the pumping power. The main mechanisms identified to be the basis for the heat transfer enhancement when using porous materials are flow redistribution or flow channeling, thermal conductivity modification, and enhancement of radiation heat transfer at high temperature or heat fluxes.

The other experimental and theoretical works related to forced convection heat transfer past an array of circular cylinders in the presence and absence of porous media have been carried out by Jubran et al. [13], Fand et al. [14], Bejan [15], Wang [16,17], and Layeghi and Nouri-Borujerdi [18]. However, there are a limited number of published works about wooden porous media inserts and their conductivity effects on heat transfer from a tube bundle.

The main objective of the present work is to numerically investigate the effects of various isotropic low conductivity wooden porous media inserts such as soft or hard wood on the heat transfer rate from a staggered tube bundle at maximum Reynolds numbers 100 and 300. The numerical results are obtained for a range of conductivities and compared with the available data in the literature for tube bundles with no porous media inserts. The differences between various cases are also discussed. The importance of this research is it shows that even low conductivity porous materials such as waste wooden materials can increase the heat transfer rate from a tube bundle.

2 Governing Equations

The conservation equations of mass, momentum, and energy for a two-dimensional laminar incompressible fluid flow around a tube bundle in an isotropic saturated porous medium with constant properties and local thermal equilibrium in a Cartesian coordinate system are described as (Fig. 1) [2] follows:
continuity

Contributed by the Heat Transfer Division of ASME for publication in the JOURNAL OF HEAT TRANSFER. Manuscript received October 25, 2005; final manuscript received June 19, 2007; published online January 25, 2008. Review conducted by Yogesh Jaluria.

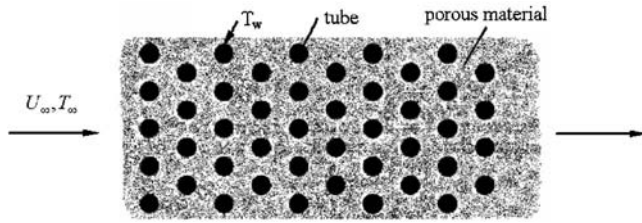


Fig. 1 Schematic of a staggered tube bundle with a porous material insert

$$\frac{\partial U}{\partial x} + \frac{\partial V}{\partial x} = 0 \quad (1)$$

momentum equations,

$$\begin{aligned} \frac{\rho_f \partial U}{\varepsilon \partial t} + \frac{\rho_f}{\varepsilon^2} \left[\frac{\partial}{\partial x}(UU) + \frac{\partial}{\partial y}(VU) \right] \\ = -\frac{\partial p}{\partial x} + \frac{\mu}{\varepsilon} \frac{\partial^2 U}{\partial x^2} - \frac{\mu}{K} U - \rho_f \frac{C_F}{K^{1/2}} |U|U \end{aligned} \quad (2)$$

$$\begin{aligned} \frac{\rho_f \partial V}{\varepsilon \partial t} + \frac{\rho_f}{\varepsilon^2} \left[\frac{\partial}{\partial x}(UV) + \frac{\partial}{\partial y}(VV) \right] \\ = -\frac{\partial p}{\partial y} + \frac{\mu}{\varepsilon} \frac{\partial^2 V}{\partial y^2} - \frac{\mu}{K} V - \rho_f \frac{C_F}{K^{1/2}} |V|V \end{aligned} \quad (3)$$

energy equation,

$$\begin{aligned} (\rho c)_m \frac{\partial T}{\partial t} + (\rho c)_f \left[\frac{\partial}{\partial x}(UT) + \frac{\partial}{\partial y}(VT) \right] \\ = \left[(k_{\text{eff}} + k_{D,x}) \frac{\partial^2 T}{\partial x^2} + (k_{\text{eff}} + k_{D,y}) \frac{\partial^2 T}{\partial y^2} \right] \end{aligned} \quad (4)$$

where (U, V) are the Darcy velocity components [2], C_F is a dimensionless form-drag constant, T is the temperature, and p is the static pressure, and $(\rho c)_m = (1 - \varepsilon)(\rho c)_s + \varepsilon(\rho c)_f$. Here, we assume $C_F = 0.1$, which is an average value for many porous types of foam.

ε and K are porosity and permeability of the porous medium. Indices s and f refer to solid and fluid parts of the porous medium, respectively. k_{eff} is the effective thermal conductivity in the porous medium. It is the volume average of the fluid medium and solid medium conductivities, $k_{\text{eff}} = \varepsilon k_f + (1 - \varepsilon)k_s$. $k_{D,x}$ and $k_{D,y}$ are the longitudinal and transverse thermal dispersion conductivities in the x and y directions, respectively. At high pore Reynolds numbers in nearly parallel flows, they can be correlated as a linear

function of Peclet number. Since the porous medium is assumed to be isotropic, we assume $k_{D,x} = k_{D,y} = k_D$. The thermal dispersion can then be obtained by the following equation:

$$\frac{k_D}{k_f} = C_T \text{Pe}_m = C_T U_m d_p / \alpha_f \quad (5)$$

where in the above equations, Pe_m is the Peclet number based on pore diameter d_p and mean velocity U_m . The coefficient C_T depends on the porous medium structure and distance from the solid walls [19,20]. $\alpha_f = k_f / (\rho c)_f$ is the thermal diffusivity of the fluid.

The time derivative terms have been retained in the governing equations only in order to introduce relaxation into the discretized algebraic equations during iteration toward a steady-state solution field.

3 Method of Solution

The typical solution domain and the tube bundle boundary definition and nomenclature used in this work are shown in Fig. 2 along with coordinate system and details of the mesh between two adjacent tubes. The inlet flow has a uniform velocity U_∞ . The solution domain is bounded by the inlet (line MK), the outlet (line NL), and by lines KL and MN in Fig. 2(a). Lines KL and MN will hereafter be referred to as the bottom and top boundaries, respectively. Those boundaries consist of arcs representing the surfaces of the tubes, with symmetry planes where there are no tubes. The full domain included ten longitudinal rows of tubes: five tubes on each of the bottom and top boundaries. In the numerical solution, we used $L_{us}/D = 30$ and $L_{ds}/D = 30$.

These lengths were judged to be sufficiently long so that any increase in the values of L_{us} and L_{ds} would not have a significant impact on the results. The staggered tube bundle arrangement is in the form of an equilateral triangle with $S_T/D = 0.75$, $S_L/D = 1.3$, and $S_D/D = 1.5$. The appropriate boundary conditions for the solution domain shown in Fig. 2(a) are given in Table 1.

Figure 2(b) shows typical computational grids between two adjacent tubes. Two types of control volumes, quadrilateral and triangular, are used in the numerical analysis. The quadrilateral control volumes are arranged near the tube boundaries and triangular control volumes are used everywhere between the tubes and quadrilateral control volumes, as shown in Fig. 2(b). The grids can be systematically refined in order to obtain grid independent results. Three different meshes with 25, 50, and 100 nodes on each tube are used in the present numerical analysis. The distances of the first node with respect to the wall are 0.002 m, 0.001 m, and 0.0005 m, respectively. The first 15 grids near walls are distributed with growth factor 1.02.

The governing equations are discretized using standard finite volume approach based on collocated grid system [21]. The QUICK scheme is used to compute a higher-order value of the

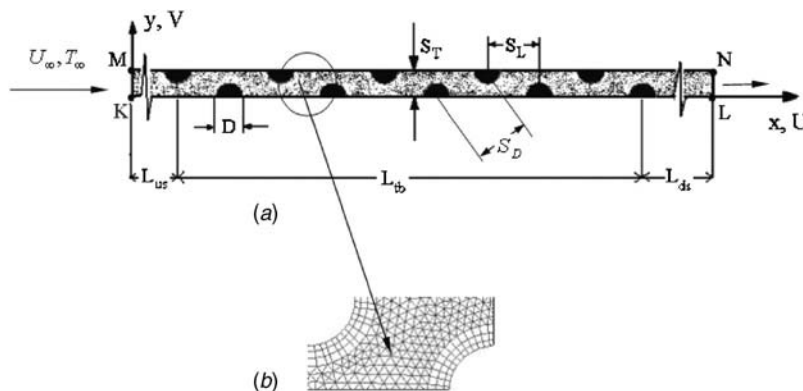


Fig. 2 (a) Solution domain and the tube bundle boundary definition and nomenclature and (b) details of the mesh between two adjacent tubes

Table 1 Summary of boundary conditions for U , V , and T

Boundary condition	U	V	T
Inlet ($x=0$)	$U=U_\infty$	$V=0$	$T=T_\infty$
Exit ($x=L_{us}+L_{tb}+L_{ds}$)	$\frac{\partial U}{\partial x}=0$	$V=0$	$\frac{\partial T}{\partial n}=0$
Symmetry (portions of lines KL and MN in Fig. 2)	$\frac{\partial U}{\partial y}=0$	$V=0$	$\frac{\partial T}{\partial x}=0$
Tube surface (portions of lines KL and MN in Fig. 2)	$U=0$	$V=0$	$T=T_w$

convected terms [22]. QUICK-type schemes [23] are based on a weighted average of second-order upwind and central interpolations of the variable. This results in a set of algebraic equations with a sparse coefficient matrix. For scalar equations, this linear system is solved using a point implicit (Gauss–Seidel) solver in conjunction with an algebraic multigrid (AMG) method [24]. The sequence of numerical steps is based on SIMPLE algorithm [24]. After solving the discretized equations for all nodes, the accuracy of the numerical solution is checked first by summation of the absolute value of the relative errors, which should be equal or less than 10^{-4} . Second, the spot value should approach a constant value. The relative error (RE) in the numerical procedure is defined as

$$RE = \sum_{\text{cells}} \left| \frac{\phi^{n+1} - \phi^n}{\phi^{n+1}} \right| \quad \phi = U, V, P, T \quad (6)$$

where superscript n refers to the previous iteration.

4 Results and Discussion

The average velocity at the minimum cross-sectional area V_{\max} and the inlet velocity U_∞ have the following relationship:

$$\frac{V_{\max}}{U_\infty} = \max \left\{ \frac{S_T/D}{S_T/D - 1}, \frac{0.5S_T/D}{[(0.5S_T/D)^2 + (S_L/D)^2]^{0.5} - 1} \right\} \quad (7)$$

The local Nusselt numbers based on freestream and bulk temperatures are defined as

$$Nu_D = \frac{q_w'' D}{(T_\infty - T_w) k_f} = - \frac{D}{T_w - T_\infty} \frac{\partial T}{\partial n} \Big|_w \quad (8a)$$

$$Nu_b = \frac{q_w'' D}{(T_b - T_w) k_f} = - \frac{D}{T_w - T_b} \frac{\partial T}{\partial n} \Big|_w \quad (8b)$$

where q_w'' is the wall heat flux and n is the outward normal on the tube surface at a given angle θ from the front of the tube. The bulk temperature T_b for each tube is calculated at the vertical plane passing through the centerline of the tube as follows. For odd- and even-numbered tube rows (bottom and top boundary tubes in Fig. 2(a), respectively),

$$T_b = \frac{\int_{y=D/2}^{y=S_T/2} \rho_f U T dy}{\rho_f (S_T/2) U_\infty} \quad (9a)$$

$$T_b = \frac{\int_{y=0}^{y=(S_T-D)/2} \rho_f U T dy}{\rho_f (S_T/2) U_\infty} \quad (9b)$$

Figure 3 shows the Nusselt number distribution on the first three rows in a staggered tube bundle surrounded by a porous medium at $Re_{\max}=100$ and $Pr=0.7$. The thermal conductivity of the porous medium is 2.5 times more than the fluid. The maximum Reynolds number Re_{\max} is defined as $Re_{\max} = \rho_f V_{\max} D / \mu = U_\infty / V_{\max} Re$. It can be seen that fully developed region is reached soon since the Nusselt number distributions on the second and third rows are very close together. As shown in Fig. 4, the Nusselt number distributions on the second and third rows are very close together at $Re_{\max}=300$ as well.

At higher Reynolds numbers, however, the fully developed region is reached further from the second row. Comparison between Figs. 3 and 4 shows that the porous medium increases the Nusselt

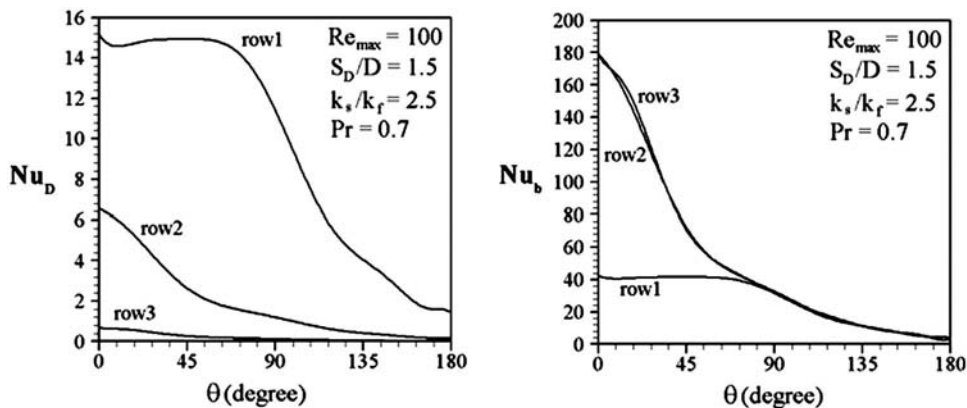


Fig. 3 Nusselt number distribution on the first three rows of a staggered tube bundle surrounded by a porous medium ($\epsilon=0.6$, $Da=0.25$) at $Re_{\max}=100$

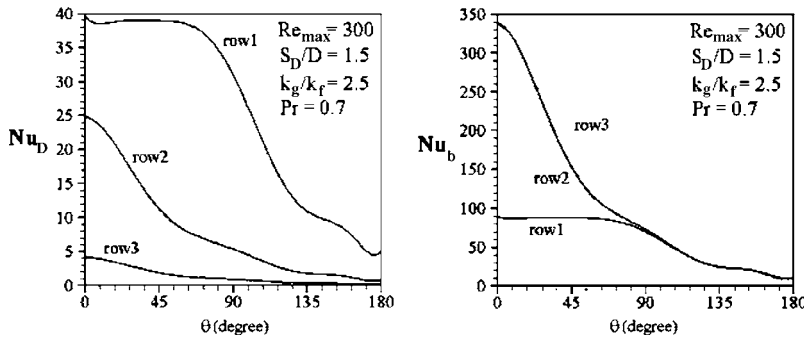


Fig. 4 Nusselt number distribution on the first three rows of a staggered tube bundle surrounded by a porous medium ($\epsilon=0.6$, $Da=0.25$) at $Re_{max}=300$

number based on bulk temperature on the second and third rows at $Re_{max}=300$ with respect to $Re_{max}=100$. The Nusselt number based on bulk temperature Nu_b provides a better realistic understanding about the effects of porous medium on the heat transfer rate from a tube bundle with respect to the Nusselt number based on freestream temperature Nu_D . On the other hand, the presence of the wooden porous medium increases the local Nusselt number on the second and third rows as the maximum Reynolds number increases from 100 to 300. This result may be related to the effect of porous medium in changing velocity gradients near the tube walls and the thermal dispersion phenomenon, which increases the Nusselt number as well.

Grid independency analysis has shown that a mesh with 101,776 nodes with first near wall grid distance equal to 0.0005 m is sufficient to obtain grid independent results. Figure 5 shows a comparison between local Nusselt numbers on the first three rows in a staggered tube bundle in the presence and absence of a porous medium with $\epsilon=0.6$ at $Re_{max}=100$.

It is obvious that for the same pitch-to-diameter ratio, the local Nusselt number based on bulk temperature Nu_b on first and third rows in a staggered tube bundle in the presence of porous medium is higher than that in the absence of porous medium. As shown in Fig. 6, the difference between these two cases will increase as the Reynolds number increases. This result seems to be related to the increase in velocity gradients and thermal dispersion due to the increase in Reynolds number.

Figures 5 and 6 show that the presence of wooden porous material around a staggered tube bundle can increase the local Nusselt number or heat transfer rate significantly. However, the amount of increase in heat transfer differs and depends on the Reynolds number.

Figure 7 shows the effect of wooden porous medium thermal conductivity ratio on the heat transfer rate from the first and third rows in a tube bundle at two maximum Reynolds numbers 100 and 300. It can be seen that as the thermal conductivity ratio increases, the Nusselt number based on bulk temperature in-

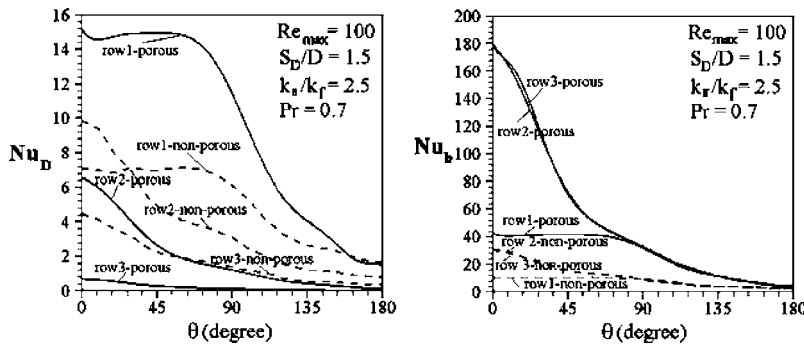


Fig. 5 Nusselt number distribution on the first three rows of a staggered tube bundle in the presence and absence of porous medium ($\epsilon=0.6$, $Da=0.25$)

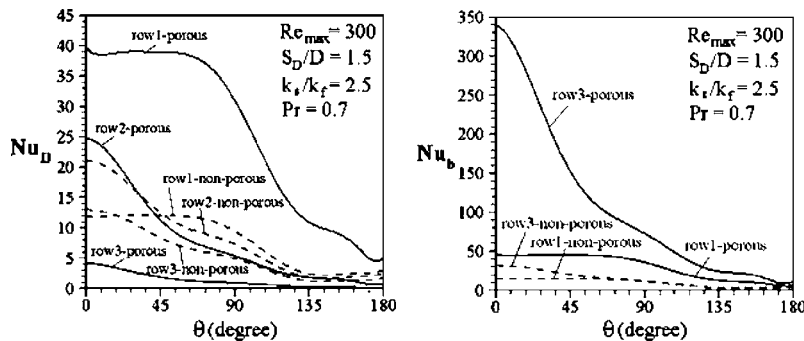


Fig. 6 Nusselt number distribution on the first three rows of a staggered tube bundle in the presence and absence of porous medium ($\epsilon=0.6$, $Da=0.25$)

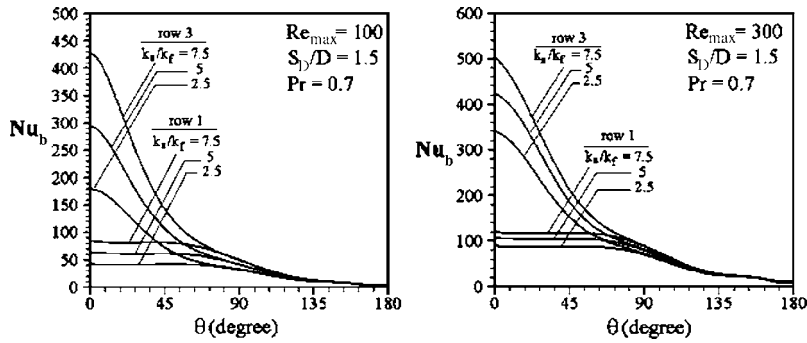


Fig. 7 The effect of solid to fluid thermal conductivity ratio on the Nusselt number distribution on the first and third rows ($\varepsilon=0.6$, $Da=0.25$)

creases on both first and third rows. It is important to note that due to the small value of Reynolds number, the heat transfer field becomes fully developed soon after the second row in both cases.

The total pressure drop along a staggered tube bundle with ten rows is obtained about 0.165 Pa and 0.8 Pa at $Re_{max}=100$, 300, respectively, when there is no porous medium around the tube bundle. The presence of a porous medium, however, increases the pressure drop along the tube bundle (0.28 Pa at $Re_{max}=100$ and 1.53 Pa at $Re_{max}=300$ for $\varepsilon=0.6$) about 50%.

In many applications, both heat transfer and pressure drop should be evaluated to obtain an optimum design. In Table 2, the ratio of fully developed Nusselt number and total pressure drop is given for various cases with or without wooden porous insert. This ratio is a characteristic parameter for the performance of a tube bundle with or without wooden porous insert and is defined as

$$r_h = \frac{\bar{Nu}_{FD}}{\Delta P_{tot}} \quad (10)$$

From the results in Table 2, it can be seen that in both cases: $Re_{max}=100$ and $Re_{max}=300$, the porous medium with conductivity ratio $k_s/k_f=7.5$ provides maximum heat transfer enhancement from the tube bundle. The increase in Nusselt number based on bulk temperature is more than 50% for the first row and is more than 50% for the second and third rows. However, the total pressure drop increases less than 50% in both cases: $Re_{max}=100$ and $Re_{max}=300$.

Finally, a comparison between the present work and the previous numerical data of Wang et al. [7] for Nusselt number distribution on the first and third rows of a tube bundle with the absence of wooden porous insert has shown that the agreement between the results is very good.

5 Conclusions

In this paper, forced convective heat transfer from a staggered tube bundle surrounded by wooden porous media at maximum Reynolds numbers 100 and 300, Prandtl number 0.7, and Darcy number 0.25 has been studied. The effects of wooden porous materials with different thermal conductivities on heat transfer enhancement from a staggered tube bundle have been discussed. The unsteady form of the extended Darcy–Brinkman–Forchheimer equations and corresponding energy equation have been solved numerically using finite volume approach. Parametric studies have been done for the study of the effects of porous structure conductivity and Reynolds number on the local Nusselt number distribution. Total pressure drop along the tube bundle is also calculated for the cases with or without wooden porous media inserts. Three different porous media with thermal conductivities 2.5, 5, and 7.5 times more than fluid conductivity have been used in the numerical analysis. The results show that the presence of wooden porous media has significant effect on the heat transfer enhancement from the tube bundle (more than 50% in some cases). Finally, the ratio of fully developed Nusselt number and total pressure drop is given for various cases with or without porous insert. It has been shown that the wooden porous medium with maximum thermal conductivity ($k_s/k_f=7.5$) is the best choice for the heat transfer enhancement in this study. However, it is important to note that the total pressure drop also increases when a porous medium inserted between the tubes in a tube bundle specifically at high Reynolds numbers. Finally, it should be noted that wooden porous materials are not the best choices for heat transfer enhancement applications in general. However, they are simple and relatively cheap waste materials available in many carpentry or factory yards and can be used in some local and specific applications

Table 2 Average Nusselt numbers and r_h for a tube bundle with or without a wooden porous insert with $k_s/k_f=7.5$ and $Da=0.25$ at two different Reynolds numbers

Re_{max}	Case	First row		Second row		Third row		Tube bundle total pressure drop, ΔP (Pa)	r_h
		\bar{Nu}_D	\bar{Nu}_b	\bar{Nu}_D	\bar{Nu}_b	\bar{Nu}_D	\bar{Nu}_b		
100	$k_s/k_f=7.5$, porous	10.8	47.0	0.997	103.7	0.041	104.1	0.28	371.8
100	k_f Nonporous	5.13	7.37	3.66	11.4	1.67	11.4	0.165	69.10
300	$k_s/k_f=7.5$, porous	28.5	76.1	6.22	146.5	0.707	145.9	1.53	95.34
300	k_f Nonporous	7.92	9.50	8.39	14.4	5.57	13.5	0.800	16.90

Nomenclature

A_t	= area
c	= heat capacity at constant pressure
C_f	= skin friction coefficient
D	= diameter
Da	= Darcy number, K/D^2
h	= heat transfer coefficient
\bar{h}	= average heat transfer coefficient
k	= thermal conductivity
K	= permeability
Nu	= Nusselt number, hD/k
\bar{Nu}	= average Nusselt number, $\bar{h}D/k$
P	= pressure
Pr	= Prandtl number
q	= total rate of heat transfer
q''	= heat flux
r_h	= ratio of Nusselt number to total pressure drop
Re	= Reynolds number, $\rho DU_\infty/\mu$
t	= time
S_D	= pitch
S_L	= longitudinal pitch
S_T	= transverse pitch
T	= temperature
U	= velocity in the x direction
V	= velocity in the y direction
x, y	= Cartesian coordinates

Greek Symbols

ε	= porosity
ϕ	= general variable
θ	= angle
μ	= fluid viscosity
ρ	= fluid density

Subscripts

D	= diameter, dispersion
eff	= effective
f	= fluid
m	= face value
r	= radial coordinate
s	= solid
t	= tube
tot	= total
w	= wall
∞	= freestream
max	= maximum
b	= bulk
FD	= fully developed

References

[1] Fowler, A. J., and Bejan, A., 1994, "Forced Convection in Banks of Inclined

Cylinders at Low Reynolds Numbers," *Int. J. Heat Fluid Flow*, **15**(2), pp. 90–99.

- [2] Nield, D. A., and Bejan, A., 1992, *Convection in Porous Media*, 2nd ed., Springer, New York.
- [3] Fowler, A. J., and Bejan, A., 1995, "Forced Convection From a Surface Covered With Flexible Fibers," *Int. J. Heat Mass Transfer*, **38**(5), pp. 767–777.
- [4] Vafai, K., and Kim, S. J., 1990, "Analysis of Surface Enhancement by a Porous Substrate," *ASME J. Heat Transfer*, **112**, pp. 700–706.
- [5] Huang, P. C., and Vafai, K., 1993, "Flow and Heat Transfer Control Over an External Surface Using a Porous Block Array Arrangement," *Int. J. Heat Mass Transfer*, **36**, pp. 4019–4032.
- [6] Huang, P. C., and Vafai, K., 1994a, "Passive Alteration and Control of Convective Heat Transfer Utilizing Alternate Porous Cavity-Block Wafers," *Int. J. Heat Fluid Flow*, **15**, pp. 48–61.
- [7] Wang, Y. Q., Penner, L. A., and Ormiston, M. J., 2000, "Analysis of Laminar Forced Convection of Air for Cross Flow in Tube Banks of Staggered Tubes," *Numer. Heat Transfer, Part A*, **38**(8), pp. 819–845.
- [8] Koh, J. C. Y., and Colony, R., 1974, "Analysis of Cooling Effectiveness for Porous Materials in a Coolant Passage," *ASME J. Heat Transfer*, **96**, pp. 324–330.
- [9] Koh, J. C. Y., and Stevens, R. L., 1975, "Enhancement of Cooling Effectiveness by Porous Materials in Coolant Passage," *ASME J. Heat Transfer*, **97**, pp. 309–311.
- [10] Phanikumar, M. S., and Mahajan, R. L., 2002, "Non-Darcy Natural Convection in High-Porosity Metal Foams," *Int. J. Heat Mass Transfer*, **45**(18), pp. 3781–3793.
- [11] Pavel, B. I., and Mohamad, A. A., 2004, "Experimental Investigation of the Potential of Metallic Porous Inserts in Enhancing Forced Convective Heat Transfer," *ASME J. Heat Transfer*, **126**(4), pp. 540–545.
- [12] Pavel, B. I., and Mohamad, A. A., 2004, "An Experimental and Numerical Study on Heat Transfer Enhancement for Gas Heat Exchangers Fitted With Porous Media," *Int. J. Heat Mass Transfer*, **47**(23), pp. 4939–4952.
- [13] Jubran, B. A., Hamdan, M. A., and Abdualh, R. M., 1993, "Enhanced Heat Transfer, Missing Pin, and Optimization of Cylindrical Pin Fin Arrays," *ASME J. Heat Transfer*, **115**, pp. 576–583.
- [14] Fand, R. M., Varahasamy, M., and Greer, L. S., 1993, "Empirical Correlation Equations for Heat Transfer by Forced Convection From Cylinders Embedded in Porous Media That Account for the Wall Effect and Dispersion," *Int. J. Heat Mass Transfer*, **36**(36), pp. 4407–4418.
- [15] Bejan, A., 1995, "The Optimal Spacing for Cylinders in Cross Flow Forced Convection," *ASME J. Heat Transfer*, **117**, pp. 767–770.
- [16] Wang, C. Y., 1999, "Longitudinal Flow Past Cylinders Arranged in a Triangular Array," *Appl. Math. Model.*, **23**(3), pp. 219–230.
- [17] Wang, C. Y., 2001, "Stokes Flow Through a Rectangular Array of Circular Cylinders," *Fluid Dyn. Res.*, **29**(2), pp. 65–80.
- [18] Layeghi, M., and Nouri-Borujerdi, A., 2004, "Fluid Flow and Heat Transfer Around Circular Cylinders in Presence and No-Presence of Porous Media," *J. Porous Media*, **7**(3), pp. 70–79.
- [19] Yagi, S., and Wakao, N., 1959, "Heat and Mass Transfer From Wall to Fluid in Packed Beds," *AIChE J.*, **5**(1), pp. 79–85.
- [20] Yagi, S., and Kunii, D., 1960, "Studies on Heat Transfer Near Wall Surface on Packed Tubes," *AIChE J.*, **6**(1), pp. 97–104.
- [21] Ferziger, J. H., and Peric, M., 1999, *Computational Methods for Fluid Dynamics*, Springer-Verlag, Berlin.
- [22] Barth, T. J., and Jespersen, D., 1989, "The Design and Application of Upwind Schemes on Unstructured Meshes," *AIAA 27th Aerospace Sciences Meeting, Reno, NV*, Paper No. AIAA-89-0366.
- [23] Leonard, B. P., 1995, "Order of Accuracy of Quick and Related Convection-Diffusion Schemes," *Appl. Math. Model.*, **19**, p. 640.
- [24] Patankar, S. V., 1980, *Numerical Heat Transfer and Fluid Flow*, Hemisphere, New York.

Impact of Interface Resistance on Pulsed Thermoelectric Cooling

Y. Sungtaek Ju

Mechanical and Aerospace Engineering Department,
University of California,
Los Angeles, CA 90095-1597;
Biomedical Engineering Interdepartmental Program,
University of California,
Los Angeles, CA 90095-1597
e-mail: just@seas.ucla.edu

Pulsed thermoelectric cooling is an attractive approach for the site specific thermal management of infrared sensors and other low-heat flux devices. Intense Joule heating caused by electrical interface resistance, however, can severely degrade pulsed cooling performance. Numerical simulations are used to quantify the impact of the interface resistance on pulsed thermoelectric cooling. The degradation in performance is most pronounced for microcoolers that have small bulk resistivity at high pulse amplitudes. Our work also forms a basis for new techniques to probe interfaces in TE devices for energy harvesting as well as cooling applications. [DOI: 10.1115/1.2780186]

Keywords: thermoelectric, interface effect, microscale heat transfer, cooling, energy harvesting

Recent efforts at enhancing the performance of thermoelectric coolers have focused heavily on improving the thermoelectric figure of merit of materials, which is defined as $ZT = S^2 T / \rho k$. Here, S is the Seebeck coefficient, k is the thermal conductivity, ρ is the electrical resistivity, and T is the absolute temperature. Significant improvement in ZT values has been reported for superlattices and other nanostructured materials, but their widespread use still awaits further innovation in materials engineering and manufacturing technology.

A complementary approach to enhancing the performance of thermoelectric coolers is to apply high-amplitude transient electrical pulses to the thermoelectric elements [1–4]. By inducing intense cooling only over a brief period of time, one can reduce the cold-junction temperature below the minimum achievable steady-state value. The deleterious effects of excess Joule heating within the bulk elements can be circumvented by intermittently breaking thermal contact between the thermoelectric elements and an object to be cooled [5].

In a more recent experimental study, Snyder et al. [6] reported various parameters of interest in pulsed cooling, such as the minimum temperature, the time to reach the minimum temperature. While numerical simulations based on the conventional continuum model captured general trends reasonably well, the minimum temperature observed, was appreciably higher than the theoretical prediction. Understanding a mechanism behind such discrepancy is important in assessing the limitation of pulsed thermoelectric cooling.

In the present article, we report a numerical simulation study to explain the experimentally observed anomaly in pulsed cooling performance. We find that the electrical interface resistance strongly influences the cold-junction temperature and its dependence on current amplitude. The interface resistance we extract by

comparing our numerical simulation results with the experimental data is consistent with the resistance typically reported for metal-semiconductor interfaces.

The impact of the electrical interface resistance on macroscale coolers was briefly examined in a previous study [3], but no definite conclusion was reached partly due to significant experimental uncertainties. The impact of the interface resistance is expected to be more pronounced for microthermoelectric coolers. Previous studies examined interfacial effects on thermal and electrical transport in microcoolers operating under steady states [7,8]. The interface resistance, however, was ignored in previous numerical studies of pulsed cooling in microcoolers [9].

We consider a configuration schematically illustrated in Fig. 1. The geometric and material properties of the element are taken from Snyder et al. [6] and Yang et al. [9] to facilitate comparison with the available experimental data and simulation results. The hot side of the element is assumed to be bonded to a heat spreader maintained at a constant temperature, and the cold side is attached to a thin foil of copper, which serves as an electrode.

We numerically solve the one-dimensional transient heat conduction equation using the finite volume method. The time derivative is handled using the explicit method. In the finite volume method, the thermoelectric element and copper foil are divided into small differential control volumes, and the energy conservation principle is applied to each control volume to obtain a discretized version of the heat conduction equation. The numerical code is first validated by comparing the predicted steady-state cold-junction temperature with the analytic solutions. The code is further validated by comparing the predicted temporal cold-junction temperature profiles with the recently reported simulation results [9]. The grid and time step size independence study is performed for each simulation case to ensure the accuracy of our results.

The interface is modeled as a fictitious homogeneous layer of an infinitesimal thickness. The thermal and electrical conductivities of this layer are specified to match the given thermal and electrical interface resistances, R''_t and R''_e , respectively. We note that our simplistic interface model does not fully capture complex thermoelectric phenomena at interfaces. More detailed studies of interface effects on thermoelectric cooler performance were reported earlier for steady-state operations [7,8]. These studies suggested that electron-phonon nonequilibrium and boundary Seebeck effects may not play a *major* role when the thermal interface resistance is much smaller than the thermal resistance of the element itself. Further studies are necessary to fully elucidate the impact of these other interface phenomena on pulsed thermoelectric cooling.

By applying the energy conservation principle to the differential control volume enclosed between the dotted lines in Fig. 1, we write

$$q''_L + j^2 R''_e + jST_i = q''_R \quad (1)$$

$$q''_L = \frac{T_L - T_i^-}{dx/2k_L} = -k_L \left. \frac{\partial T}{\partial x} \right|_{i^-} \quad (2)$$

$$q''_R = \frac{T_i^+ - T_R}{dx/2k_R} = -k_R \left. \frac{\partial T}{\partial x} \right|_{i^+} \quad (3)$$

By combining the above equations with a solution to the continuum heat conduction equation within the interface layer, we eliminate the intermediate variables T_i^+ and T_i^- and express the heat fluxes q''_L and q''_R in terms of T_L , T_R , and R''_t . Details of the implementation of the finite volume method are discussed in Ref. [10] and will not be repeated here.

Figure 2 shows the predicted temporal variations in the cold electrode temperature for three different values of the electrical interface resistance. The thermoelectric element is initially subjected to current $I_{\min,ss}$ over a time period of $3t_{\text{diff}}$ to achieve the

Contributed by the Heat Transfer Division of ASME for publication in the JOURNAL OF HEAT TRANSFER. Manuscript received December 20, 2006; final manuscript received June 18, 2007; published online January 28, 2008. Review conducted by Yogendra Joshi.

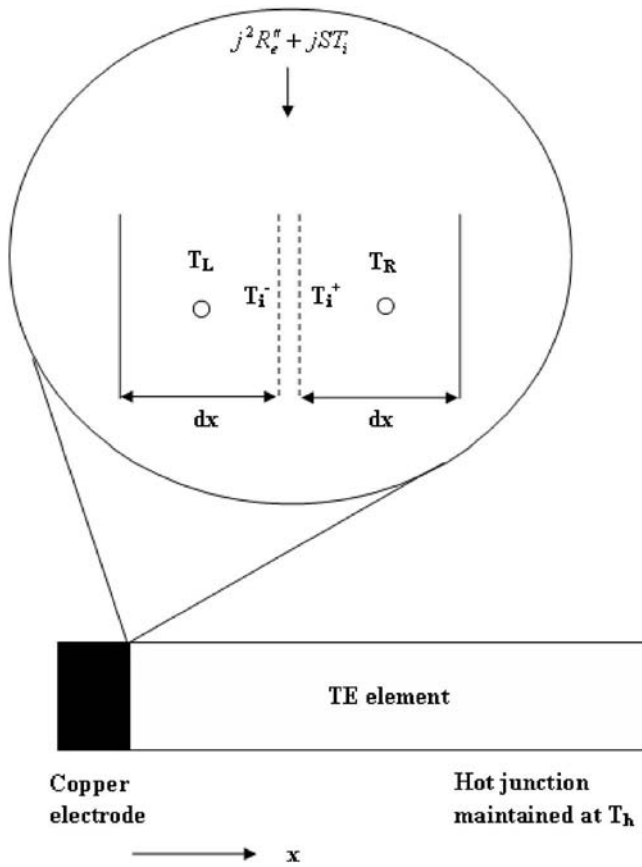


Fig. 1 Schematic diagram of a freestanding thermoelectric element subjected to a pulsed current. A region near the interface at the cold junction is enlarged to show differential elements used for the finite volume method.

minimum steady-state temperature $(T_c)_{\min,ss}$. Assuming that the material properties remain constant, one can calculate the minimum achievable cold-junction temperature in steady state as

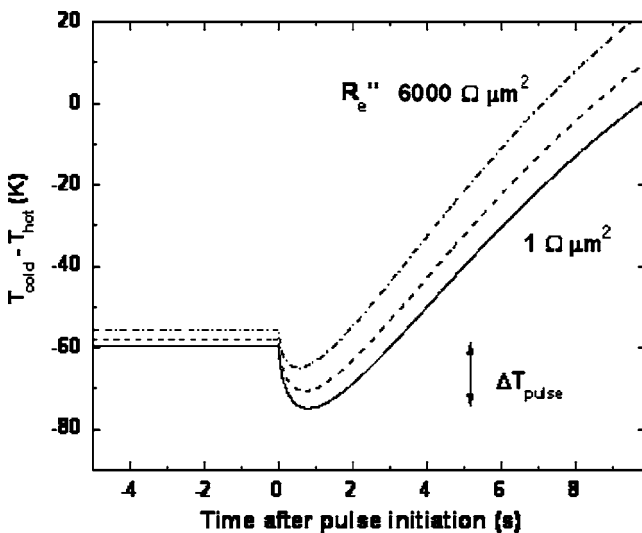


Fig. 2 Predicted temporal temperature profiles in the cold junction of the model macrocooler subjected to a current pulse of amplitude of $3.5I_{\min,ss}$. The simulation results are shown for three different values of the electrical interface resistance.

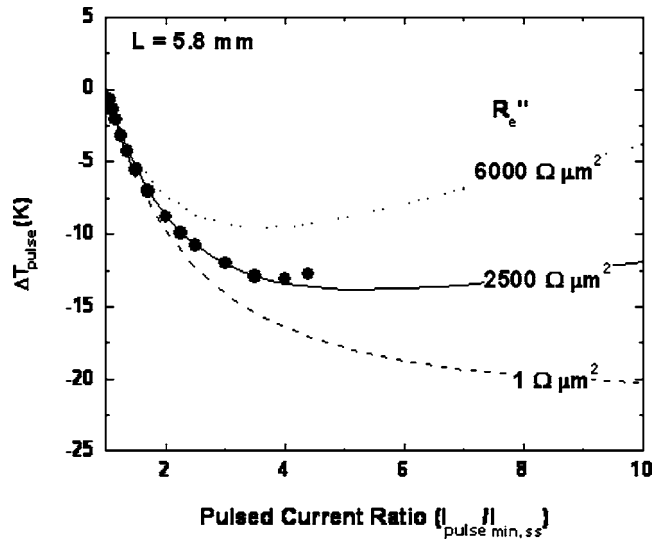


Fig. 3 Extra temperature drop due to pulsed cooling as a function of the current ratio. $I_{\min,ss}$ is the current necessary to achieve the minimum steady-state cold-junction temperature. The symbols are experimental data from Snyder et al. [6].

$$(T_c)_{\min,ss} = \frac{\sqrt{1 + 2zT_h} - 1}{z} \quad (4)$$

and the required current as $I_{\min,ss} = S(T_c)_{\min,ss} A / \rho L$. The thermal diffusion time t_{diff} is a measure of time required for heat to diffuse along the entire length L of the element and is calculated as $L^2 / (k / \rho c_p)$. A current pulse of amplitude of $3.5I_{\min,ss}$ is subsequently applied to the element.

Note that $(T_c)_{\min,ss}$ increases with increasing electrical interface resistance. The changes in $(T_c)_{\min,pulsed}$ are even bigger, consistent with the fact that highly localized Joule heating at the interface has a very strong impact on pulsed cooling. The time required to reach the minimum cold-junction temperature decreases with increasing electrical interface resistance. We have also varied the thermal interface resistance from values as small as $10^{-9} \text{ m}^2 \text{ K/W}$ to values as high as $10^{-7} \text{ m}^2 \text{ K/W}$ for each case, but these variations in R_{th}'' have much smaller influence on pulsed cooling.

The extra temperature drop achieved through pulsed cooling is defined as $\Delta T_{pulse} = (T_c)_{\min,pulsed} - (T_c)_{\min,ss}$. Figure 3 shows the predicted ΔT_{pulse} as a function of the ratio between the pulse amplitude and $I_{\min,ss}$. When the electrical interface resistance is sufficiently small, ΔT_{pulse} decreases monotonically with increasing current ratio, at least up to 10. In contrast, when $R_e'' = 6000 \text{ Ohm } \mu\text{m}^2$, ΔT_{pulse} reaches a minimum at a current amplitude ratio of ~ 3.5 . ΔT_{pulse} then increases with further increase in current as intense Joule heating at the interface counteracts Peltier cooling.

The experimental data of Snyder et al. [6] can be fitted with the present numerical simulation results if the electrical interface resistance is assumed to be approximately $2500 \text{ Ohm } \mu\text{m}^2$. For comparison, previous studies of thermoelectric and other semiconductor devices reported that the electrical interface resistance between semiconductors and metal electrodes is of the order of $10^3 - 10^4 \text{ Ohm } \mu\text{m}^2$ when standard techniques for making a junction (such as soldering or hot pressing) are employed [11,12]. Figure 4 shows that the predicted cold-junction electrode temperature profiles also compare well with the experimental data, giving further support to the interface resistance estimated above.

While the present simulations can explain the experimental data well, we note that there are other mechanisms that may also explain the observed degradation in pulsed cooling performance at

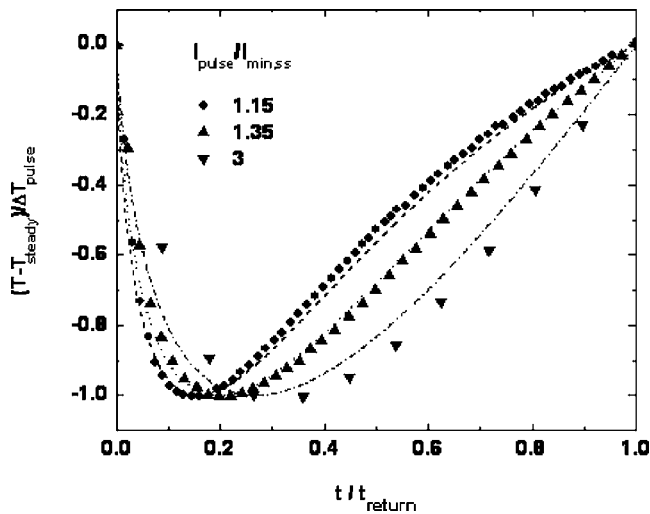


Fig. 4 Comparison between the temporal temperature profiles experimentally observed and predicted in the present study for the model macrocooler. t_{ret} is the time from the pulse initiation to return to the steady-state cold-junction temperature.

high current amplitudes. For example, the heat capacitance of the electrical leads and parasitic heat loss along the leads could have much more influence than was accounted for in our simulations.

The above numerical simulations are performed using the material properties and dimensions of a specific thermoelectric cooler. For other thermoelectric coolers, a first-order assessment of the importance of the electrical contact resistance can be made by comparing the interface resistance R_e'' with the electrical resistance of a segment L_{pulse} of the element. The length L_{pulse} can be estimated as the thermal diffusion length over the time interval it takes to reach the minimum cold-junction temperature, t_{min} . Using the semiempirical expression for t_{min} derived in a previous study, we write $L_{pulse} \sim L/[2(P+1)]$. Here, P is the current ratio $I_{pulse}/I_{min,ss}$ and L is the thermoelectric element length. The magnitude of electrical interface resistance that leads to significant interface effects is then predicted to decrease with increasing pulsed current amplitude and with decreasing thermoelectric element length and bulk resistivity.

Thermoelectric microcoolers of lengths of the order of $100 \mu\text{m}$ and smaller are interesting because they may enable highly reliable and compact systems for device and package level cooling of low-power cryogenic devices. Figure 5 shows the predicted values of ΔT_{pulse} for a thermoelectric element of length of $100 \mu\text{m}$ as a function of current ratio and electrical contact resistance. The element is first subjected to I_{ss} , which is reduced from $I_{min,ss}$ to compensate for a significant interface resistance. Once a steady-state is reached, a pulsed current is applied over 5 ms. For the electrical contact resistance of $1000 \Omega \mu\text{m}^2$, which is comparable to the value we have extracted for the macrocooler of Snyder et al. [6], ΔT_{pulse} is almost zero. This illustrates once again that the electrical contact resistance has much more pronounced effects for microcoolers. For thin-film microcoolers of lengths of the order of a few micrometers, even a contact resistance as small as $1 \Omega \mu\text{m}^2$ can have appreciable effects. As a reference, the resistance-area product of tunnel barriers formed by the natural oxidation of typical metals can be as high as a few thousand $\Omega \mu\text{m}^2$. Much smaller interface resistance ($<20 \Omega \mu\text{m}^2$) can be achieved but only under well-controlled conditions [8].

In summary, we report a numerical simulation study of the impact of the interface resistance between a thermoelectric ele-

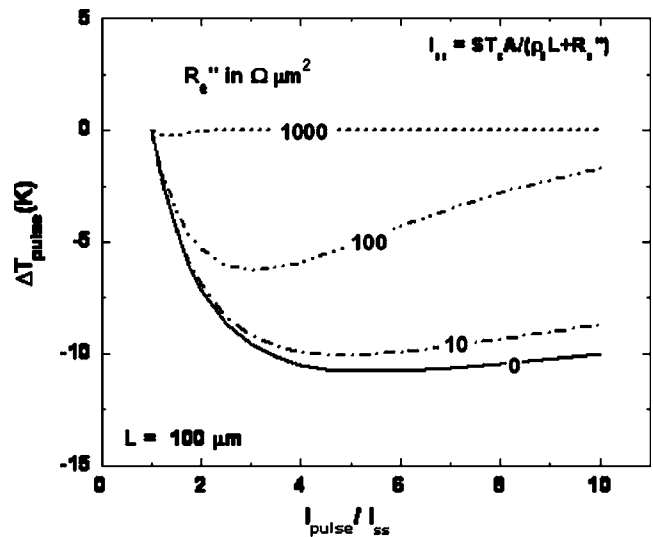


Fig. 5 The impact of the electrical interface resistance on the pulsed cooling performance of microthermoelectric coolers of length of $100 \mu\text{m}$

ment and its electrodes on pulsed cooling performance. The main idea behind pulsed thermoelectric cooling is to limit the diffusion of thermal energy generated within *bulk* elements by Joule heating. We find, however, that intense localized heating at the element-electrode interface strongly influences the minimum achievable cold-junction temperature and its dependence on current amplitude. The interface resistance we extract by comparing our numerical simulation results with recently reported experimental data is consistent with values reported for common metal-semiconductor interfaces. For microthermoelectric coolers of length of the order of $100 \mu\text{m}$ or smaller, the impact of electrical contact resistance can be much more pronounced.

This article is based in part on work supported by Grant No. FA9550-06-1-0326 from the Air Force Office of Scientific Research.

References

- [1] Parrott, J. E., 1960, "Interpretation of Stationary and Transient Behavior of Refrigerating Thermocouples," *Solid-State Electron.*, **1**, pp. 135–143.
- [2] Landecker, K., and Findlay, A. W., 1961, "Study of Fast Transient Behavior of Peltier Junctions," *Solid-State Electron.*, **3**, pp. 239–260.
- [3] Hoyos, G. E., Rao, K. R., and Jerger, D., 1977, "Numerical Analysis of Transient Behavior of Thermoelectric Coolers," *Energy Convers.*, **17**, pp. 45–54.
- [4] Field, R. L., and Blum, H. A., 1979, "Fast Transient Behavior of Thermoelectric Coolers with High Current Pulse and Finite Cold Junction," *Energy Convers.*, **19**, pp. 159–165.
- [5] Miner, A., Majumdar, A., and Ghoshal, U., 1999, "Thermoelectromechanical Refrigeration Based on Transient Thermoelectric Effects," *Appl. Phys. Lett.*, **75**, pp. 1176–1178.
- [6] Snyder, G. J., Fleurial, J.-P., Caillat, T., Yang, R. G., and Chen, G., 2002, "Supercooling of Peltier Cooler Using a Current Pulse," *J. Appl. Phys.*, **92**, pp. 1564–1569.
- [7] Ju, Y. S., and Ghoshal, U., 2000, "Study of Interface Effects in Thermoelectric Microrefrigerators," *J. Appl. Phys.*, **88**, pp. 4135–4139.
- [8] da Silva, L. W., and Kaviany, M., 2004, "Micro-Thermoelectric Cooler: Interfacial Effects on Thermal and Electrical Transport," *Int. J. Heat Mass Transfer*, **47**, pp. 2417–2435.
- [9] Yang, R., Chen, G., Kumar, A. R., Snyder, J., and Fleurial, J.-P., 2005, "Transient Cooling of Thermoelectric Coolers and Its Applications for Microdevices," *Energy Convers. Manage.*, **46**, pp. 1407–1421.
- [10] Patankar, S. V., 1980, *Numerical Heat Transfer and Fluid Flow*, Hemisphere, WA.
- [11] Goldsmid, H. J., 1986, *Electronic Refrigeration*, Plenum, New York.
- [12] Ilzycer, D., Sher, A., and Shiloh, M., 1980, "Electrical Contacts to Thermoelectric Bismuth Telluride Based Alloys," *Proceedings of the Third International Conference on Thermoelectric Energy Conversion*, pp. 200–202.

A Light Transmission Based Liquid Crystal Thermography System

Timothy B. Roth

Ann M. Anderson¹

e-mail: andersoa@union.edu

Department of Mechanical Engineering,
Union College,
Schenectady, NY 12308

This paper presents results from a study aimed at developing a novel thermochromic liquid crystal (TLC) temperature measurement system that uses light transmission instead of light reflection to measure surface temperature fields. In previous work, we reported on the effect of temperature on light transmission through TLCs as measured with a spectrophotometer [Roth, T. B., and Anderson, A. M., 2005, "Light Transmission Characteristics of Thermochromic Liquid Crystals," Proceedings of IMECE2005, Orlando, FL, Paper No. IMECE2005-81812; 2007, "The Effects of Film Thickness, Light Polarization and Light Intensity on the Light Transmission Characteristics of Thermochromic Liquid Crystals," ASME J. Heat Transfer, 129(3), pp. 372–378]. Here we report on results obtained using a charge coupled device (CCD) camera and polychromatic light setup that is similar to the type of equipment used in TLC reflection thermography. We tested three different light sources, a white electroluminescent light, a green electroluminescent light, and a halogen fiber optic light, using both direct and remote lighting techniques. We found that the green signal (as detected by the CCD camera) of the green electroluminescent light makes the best temperature sensor, because under remote lighting conditions it showed a 500% linear signal increase as the temperature of the R25C10W TLCs was raised from 30° to 48°C. We further found that the angle of the CCD camera relative to the light did not significantly affect the results for angles up to 10 deg for remote lighting and 15 deg for direct lighting. The effect of light intensity variation was not significant for intensities up to 40% of the original level when normalized on the intensity at 19°C (a temperature outside the active range of the TLCs). The use of light transmission results in a larger range of temperature over which the TLCs can be calibrated and offers opportunities for more uniform lighting conditions, which may help overcome some of the problems associated with light reflection. [DOI: 10.1115/1.2780187]

Keywords: thermochromic liquid crystals, temperature measurement, light transmission

Introduction

Thermochromic liquid crystals (TLCs) are used to measure surface temperature in a variety of applications. Correlating the color or hue of reflected light from TLC material with temperature is a standard technique [1–3]. A typical setup using light reflection from a TLC layer is shown in Fig. 1(a). The TLC material is

painted onto a black surface to maximize reflection and a camera and light source are located above (i.e., on the same side of) the liquid crystal layer.

The main disadvantage of using reflected light is that the correlating equation for temperature is sensitive to light intensity, lighting type, and viewing angle [4,5]. In addition, while the TLC material displays color over its entire active range, the reflection calibration generally utilizes only 25–50% of this range [2].

The light transmission properties of liquid crystals are used extensively in liquid crystal display technology [6], however, little work has been done to characterize the effect of temperature on the light transmission properties of TLCs. In previous work [7–9], we used a spectrophotometer and showed that light transmission characteristics through TLCs do change with temperature and that we can detect these changes. Here we extend that work by presenting light transmission data acquired using a charge coupled device (CCD) camera and a polychromatic light source (see Fig. 1(b)).

Methods and Materials

Thermochromic Liquid Crystal Materials. We used Hallcrest R25C10W sprayable TLCs. These materials are microencapsulated by a polymer coating that yields 10–15 μm diameter microcapsules. The resulting slurry is then combined with a water soluble aqueous binder to form a sprayable material. These particular TLCs have a published event (color start) temperature of 25°C and a bandwidth of 10°C, implying a clearing point (color end) temperature of approximately 45°C.

Experimental Setup and Procedure. We investigated the performance of the TLC material using two lighting configurations. One used "remote lighting," in which the light source was placed 1–20 cm from the liquid crystal layer. The second used "direct lighting," in which the TLC material was painted directly onto the light source. We used two types of electroluminescent lights (green and white, from Edmund Optics) and a halogen fiber optic light (Schott-Fostec).

For the remote lighting configuration, the TLC material was applied to the outer surface of a standard 1 cm path length polystyrene cuvette, which was modified to connect to a temperature controlled circulating water bath. We embedded calibrated thermocouples in one side of the cuvette and then carefully poured diluted, filtered TLC material over the thermocouples to form a TLC surface. We used two different surfaces in the study: a thick layer (0.40 mm \pm 0.03 mm) and a thin layer (0.24 mm \pm 0.03 mm). The temperature of the TLC surface was controlled by circulating water through the inside of the cuvette. We placed the light source below the cuvette by attaching electroluminescent lights directly to the bottom side of the cuvette. When using the halogen light source, we used a fiber optic cable, which was carefully mounted in line with the camera and placed approximately 20 cm below the cuvette.

For the direct lighting configuration, the TLC material was applied directly onto the electroluminescent lights using an airbrush. The surface was dried with a heat gun between the application of each coat to ensure drying of each layer of TLC material. We estimated the thickness of this surface to be 0.40 mm \pm 0.03 mm. The TLC coated electroluminescent light was then attached to a temperature controlled copper heating disk using thermal grease. A set of calibrated thermocouples, embedded in the disk, was used to measure temperature.

In each case, the Sony XC003 3CCD camera was placed approximately 20 cm above the TLC surface. Tests were conducted by slowly heating the TLC material at a rate of 1.5°C/min and acquiring images of the surface as it heated (these results were found to agree with steady state data). Each image was analyzed using the MATLAB image processing toolbox to determine the amount of red, green, and blue in a specified region of the image (generally consisting of \sim 5000 pixels). The output result for each

¹Corresponding author.

Contributed by the Heat Transfer Division of ASME for publication in the JOURNAL OF HEAT TRANSFER. Manuscript received August 29, 2006; final manuscript received April 23, 2007; published online January 28, 2008. Review conducted by Bengt Sundén. Paper presented at the 2006 AIAA/ASME Thermophysics Conference.

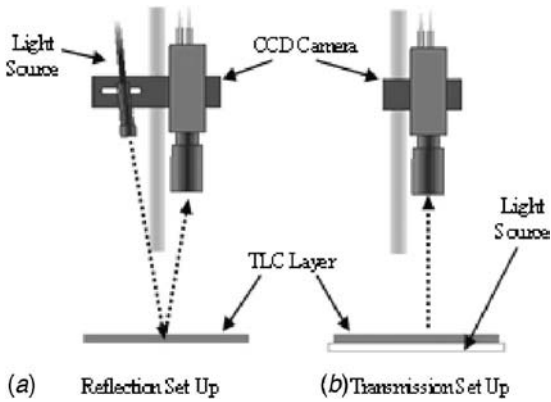


Fig. 1 Test setup for liquid crystal thermography in (a) reflection mode and (b) transmission mode. For the transmission tests, we used both direct lighting (as shown) and remote lighting, in which the light source was placed a distance below the TLC layer.

test is a temperature T versus RGB (red, green, blue) or I (intensity= $(R+B+G)/3$) calibration curve. We also studied the effects of lighting type, lighting angle, and light power level during testing.

Uncertainty Estimates. All temperature measurements used calibrated thermocouples with an uncertainty of $\pm 0.1^\circ\text{C}$. The Sony XC003 is an 8 bit camera, which yields a resolution of $1/256$ (in arbitrary units, (au)) on the measured RGB signals. Images acquired using the remote lighting setup had an average standard deviation in red of 7.6% (1 au), in green of 3.8% (2.5 au), and in blue of 8.2% (3 au). Images acquired using the direct lighting setup had an average standard deviation in red of approximately 6.2% (1.1 au), in green of 2.5% (2 au), and in blue of 10% (2 au). The standard deviation values were higher at lower temperatures.

To test the repeatability of the two lighting systems we performed ten tests on the same TLC surface over the period of 1 week. For both lighting configurations, we measured a maximum variation in the temperature calibration curve of $\pm 0.2^\circ\text{C}$.

We also measured the effect of temperature on the output of the electroluminescent lights used in the direct lighting setup by analyzing images of the bare light on the calibration disk as it was heated. We measured a 1.5% increase in the overall intensity and a 7.5% increase in the green signal as the temperature of the copper disk was increased from 30°C to 50°C .

Experimental Results

Figure 2 plots the results for remote lighting conditions with the green electroluminescent light source and the $0.4\text{ mm} \pm 0.03\text{ mm}$ surface. At temperatures below the event temperature (25°C), the RGB and I signal levels are constant. The signal levels increase slightly from 25°C to 27°C and then decrease from 27°C to 30°C . The green signal increases linearly for temperatures above 30°C , the blue signal remains flat until about 40°C , and the red signal is small and flat. The error bars represent ± 2 standard deviations in signal as computed over the 5000 pixel region. The green signal increases from 25 au to 120 au (out of 256) in this linear region.

Figure 3 plots the results for direct lighting conditions with the green electroluminescent light source and a $0.40\text{ mm} \pm 0.03\text{ mm}$ layer of TLC material. The general trends are the same as that seen with the remote lighting except that in this case, the overall intensity is more linear than the green signal and the sensitivity is

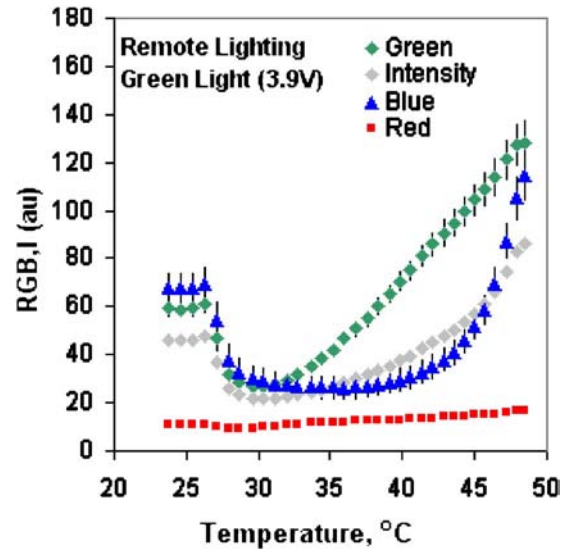


Fig. 2 The CCD RGB and I signals for light transmitted through the 0.4 mm TLC layer using the green electroluminescent light under remote lighting conditions

smaller. Over the range from 30°C to 48°C , the intensity increases from 27 au to 62 au and the green signal increases from 49 au to 119 au.

If we compare the data in Figs. 2 and 3, we see that the TLC material exhibits a larger change in signal with a more linear green signal when illuminated under remote lighting conditions. Direct lighting conditions result in a more linear variation of intensity with temperature. The sensitivity for direct lighting is about half of that for remote lighting. The standard deviation values are smaller for the direct lighting conditions as compared to remote lighting. Although the lower standard deviations are perhaps partially due to the lighting conditions, in this case, they may be more influenced by the surface quality. We used an airbrush to apply the TLCs in the direct lighting setup and were able to achieve a more uniform surface.

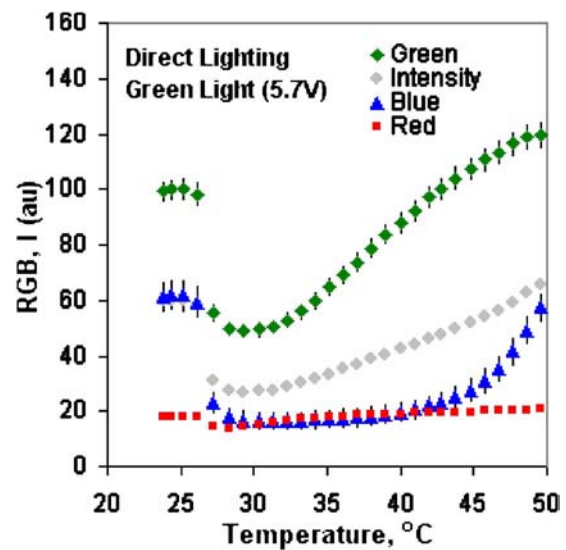


Fig. 3 The CCD RGB and I signals for light transmitted through the 0.4 mm TLC layer using the green electroluminescent light under direct lighting conditions

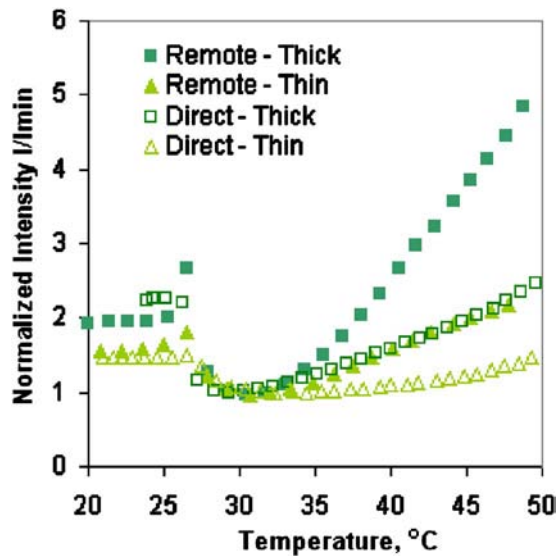


Fig. 4 Normalized intensity through a 0.40 mm and a 0.23 mm TLC layer with the green electroluminescent light source under remote and direct lighting conditions. The intensity values are normalized by the intensity value at 30°C.

Figure 4 compares the intensity of light transmitted through a thick layer of TLC material to that transmitted through a thin layer when illuminated by the green electroluminescent light. Results are plotted for both remote and direct lighting conditions. In order to compare the result, we have normalized the intensity on the value of the intensity at 30°C (a minimum). The results show that the signal change for the thick TLC layer is more than twice that for the thin layer under both lighting conditions.

Tests performed using the white electroluminescent and halogen lights showed that the most significant changes are for the green component of the white light and the red component of the halogen light. However, the halogen light resulted in higher standard deviations: either the halogen light itself is less uniform or, because of its placement (farther below the TLC surface), the divergence and scattering effects intensify the surface nonuniformities. Based on the experimental results, we determined that the green electroluminescent light source would be best for use as a temperature sensor because it is the most sensitive to temperature and the relation between the green signal and temperature is fairly linear. A set of additional tests was performed to assess the effects of light intensity and camera viewing angle on the calibration obtained with the green light.

We found that it is possible to correct for light source intensity level by normalizing the data on a signal value taken outside the active range of the crystals. Figure 5 shows results for illumination from the green electroluminescent light at a range from 38% to 100% of nominal light. The figure plots the green component of transmitted light divided by the green component at 19°C versus temperature. This temperature, 19°C, is outside the active range of the crystals and is used to account for the change in light source intensity. Analysis revealed that we could reduce the light power to 60% of nominal (from 3.9 V to 3 V) before the results start to vary by more than 0.2°C, which is within the repeatability of our system. However, when the voltage level to the light drops below this value (38%, 2.5 V), the effect is more significant and cannot be corrected by normalization. At this light level, the signal levels are too low to be accurately detected. Results of intensity normalization were similar for the direct lighting setup and other light sources.

The effect of camera viewing angle was measured from 0 deg to 20 deg angles. We found that under remote lighting conditions, the temperature calibration curve is not significantly af-

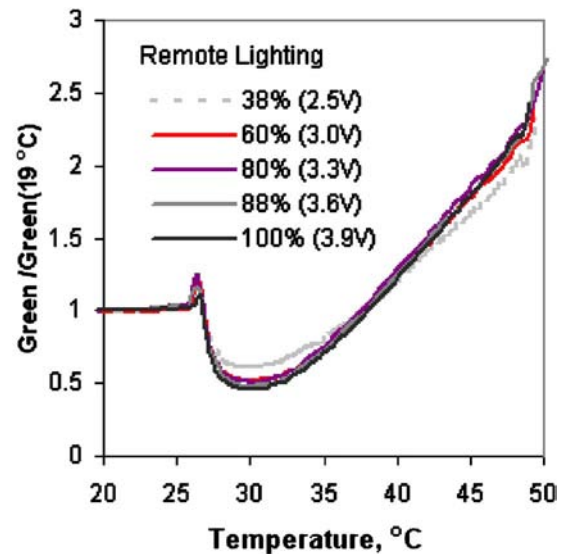


Fig. 5 The normalized green signal for a range of green light intensity levels. The green values are normalized by the green value at 19°C, which is a temperature outside the active range of the TLCs.

ected for angles up to 10 deg. Under direct lighting conditions, the temperature calibration is not significantly affected for angles up to 15 deg. Beyond those angles, the shift in the calibration curve is greater than the repeatability of 0.2°C.

Discussion

This work presents the first results for a light transmission based liquid crystal thermography system that uses a CCD camera for detection and a polychromatic light source for illumination. We have shown that light transmission utilizes a larger portion of the active range of the TLC material than does light reflection. We are able to use normalization to address nonuniformities in lighting conditions and the system can withstand 10–15 deg of misalignment in the camera/light source setup. In addition, the technique offers possibilities for alternate lighting setups that may be more convenient for measuring surface temperature. We have shown that both direct lighting, in which the light is an integral part of the actual TLC sensor, and indirect lighting, in which the surface is illuminated from behind, can be used.

We found that the remote lighting conditions resulted in greater temperature sensitivity than the direct lighting conditions. This is most likely due to the effects of light scattering. Under remote lighting conditions, the light spreads before reaching the TLC surface. The greater sensitivity could be due to directional preferences in the TLC material. However, it is possible to have the illumination source be part of the temperature sensor, as shown by the direct lighting configuration. Although the sensitivity decreased under this setup from 0.16°C/au to 0.26°C/au, the direct lighting surface showed less sensitivity to lighting angle.

Figure 4 illustrates that sensitivity increases with TLC layer thickness. This result is in agreement with the previous spectrophotometer results [7,8] and suggests that the use of more TLC material will improve the technique. However, this may lead to measurement errors if significant temperature gradients exist across the TLC layer.

The goal of the work presented here was to determine if light transmission could be used to measure temperature. We made no effort to optimize the quality of the TLC surface or the sensitivity of the CCD camera. Using a linear fit to correlate the green signal with temperature (Fig. 2), we get a resolution of 0.16°C per unit of green signal. The standard deviation ranges from 1.5 to 4 units

of green signal, which results in a measurement uncertainty value, due to calibration alone, from 0.5°C at the lower temperatures to 1.0°C (for 95% confidence). For the direct surface lighting conditions, the results are similar (0.26°C per unit of green signal with a 1.5–2.5 au standard deviation leading to 0.7°C–1.3°C uncertainty in temperature).

The next step in the development of an actual sensor is to improve the sensitivity and decrease the standard deviation to yield a lower uncertainty in measured temperature. We could improve sensitivity by optimizing the camera to make use of the entire 8 bits (256 levels) or by using a 12 bit CCD camera, which will give us much higher resolution (4096 levels). To decrease the standard deviation, we need to improve the surface quality and uniformity of the TLC layer. Although the direct surface lighting conditions yielded less sensitivity to temperature, it had a similar temperature uncertainty, which is most likely the result of the better surface quality achieved with an air brush.

The processing of the raw image recorded by the CCD camera could also be improved. The RGB signal values presented in this study were averaged over a region of the TLC surface. The use of more advanced image processing techniques that use pixel by pixel information may be needed. For example, when we used normalization to account for the effects of overall light intensity changes, we used average values and were successful in accounting for variations up to 60% of nominal power levels. Using normalization on a pixel by pixel basis, although more complicated, may help eliminate the variation in TLC material thickness across the surface.

Conclusion

We have shown that the use of light transmission instead of light reflection for liquid crystal thermography addresses some of the issues associated with lighting effects and increases the temperature range over which the liquid crystals can be calibrated. By normalizing the signal using data from an image taken outside of

the active range of the TLC material, we are able to collapse data taken at up to 60% of light source intensity with up to 10–15 deg of off axis lighting. Finally, we find that for the liquid crystals studied here (Hallcrest R25C10W), measuring the change in the amount of green light (~500–560 nm) transmitted through the TLCs offers the most sensitivity and linearity. We believe that an integrated light/TLC sensor may offer more flexibility and complement existing liquid crystal thermography techniques.

Acknowledgment

The authors would like to acknowledge the support of the National Science Foundation (CTS-0216153 RUI/MRI and ILI-9851096) for equipment used in this research and Smitesh Bakrania and Cory Spicer for initial work on the project.

References

- [1] Bakrania, S., and Anderson, A. M., 2002, "A Transient Technique for Calibrating Thermochromic Liquid Crystals: The Effects of Surface Preparation, Lighting and Overheat," *Proceedings of IMECE'02:2002 ASME International Mechanical Engineering Congress and Exposition*, New Orleans, LA.
- [2] Hay, J. L., and Hollingsworth, D. K., 1996, "A Comparison of Trichromatic Systems for Use in the Calibration of Polymer-Dispersed Thermochromic Liquid Crystals," *Exp. Therm. Fluid Sci.*, **12**(1), pp. 1–12.
- [3] Smith, C. R., Sabatino, D. R., and Praisner, T. J., 2001, "Temperature Sensing With Thermochromic Liquid Crystals," *Exp. Fluids*, **30**(2), pp. 190–201.
- [4] Farina, D. J., Hacker, J., Moffat, R. J., and Eaton, J. K., 1994, "Illuminant Invariant Liquid Calibration of Thermochromic Liquid Crystals," *Exp. Therm. Fluid Sci.*, **9**(1), pp. 1–12.
- [5] Wiberg, R., and Lior, N., 2004, "Errors in Thermochromic Liquid Crystal Thermometry," *Rev. Sci. Instrum.*, **75**(9), pp. 2985–2994.
- [6] Birecki, H., and Kahn, F. J., 1980, "The Optics of Twisted Nematic Liquid Crystal Displays," *J. Appl. Phys.*, **51**(4), pp. 1950–1954.
- [7] Roth, T. B., and Anderson, A. M., 2005, "Light Transmission Characteristics of Thermochromic Liquid Crystals," Paper No. IMECE2005-81812.
- [8] Roth, T. B., and Anderson, A. M., 2007, "The Effects of Film Thickness, Light Polarization and Light Intensity on the Light Transmission Characteristics of Thermochromic Liquid Crystals," *ASME J. Heat Transfer*, **129**(3), pp. 372–378.
- [9] Roth, T. B., and Anderson, A. M., 2006, "Liquid Crystal Thermography Using Light Transmission," Paper No. AIAA-2006-3097.

Discussion of Boundary Conditions of Transpiration Cooling Problems Using Analytical Solution of LTNE Model

Jianhua Wang

Professor Dr.-Ing.

Mem. ASME

e-mail: jhwang@ustc.edu.cn

Junxiang Shi

Graduate Student

e-mail: shijx@mail.ustc.edu.cn

Department of Thermal Science and Energy Engineering,
University of Science and Technology of China,
Jinzhai Road No. 96,
Hefei, Anhui 230027, P.R.C.

To compare five kinds of different boundary conditions (BCs), an analytical solution of a steady and one-dimensional problem of transpiration cooling described by a local thermal nonequilibrium (LTNE) model is presented in this work. The influence of the five BCs on temperature field and thermal effectiveness is discussed using the analytical solution. Two physical criteria, if the analytical solution of coolant temperature may be higher than hot gas temperature at steady state and if the variation trend of thermal effectiveness with coolant mass flow rate at hot surface is reasonable, are used to estimate the five BCs. Through the discussions, it is confirmed which BCs at all conditions are usable, which BCs under certain conditions are usable, and which BCs are thoroughly unreasonable. [DOI: 10.1115/1.2780188]

1 Introduction

There are a number of thermal processes in technology taking place in porous media. Transpiration cooling is a typical example. With the development of spaceflight and aviation technology, the transpiration cooling is widely used in various regions, such as hypersonic vehicle combustors, gas turbine blades, cryogenic liquid rocket engines, and others. A physical sketch of the transpiration cooling is shown in Fig. 1. Fluid coolant is injected into a porous plate with a mass flow rate of m at a reservoir temperature of T_c to protect the hot surface of the plate from high heat flux.

In most numerical studies of the transpiration cooling, the following two assumptions were used: (1) The fluid coolant is incompressible and without phase change within pores. (2) The thermal properties of the fluid coolant and solid matrix are constant. Under these assumptions, the transpiration cooling can be seen to be a steady and one-dimensional problem, and it is therefore not necessary to consider mass and momentum equations. Usually, there are two models to describe this problem. One is called local thermal equilibrium model, which is based on another additional assumption that the fluid coolant and the solid matrix have the same temperature. The error caused by this assumption was analyzed by Wang and Wang [1]. The other is called local thermal nonequilibrium (LTNE) model. The temperature difference and

heat exchange between the fluid coolant and solid matrix is considered in this model; thus, this is an accurate model. Alazmi and Vafai [2] presented the LTNE model: solid,

$$0 = k_{s,e} \frac{d^2 T_s}{dy^2} - h_v (T_s - T_f) \quad (1)$$

fluid,

$$mc_f \frac{dT_f}{dy} = k_{f,e} \frac{d^2 T_f}{dy^2} + h_v (T_s - T_f) \quad (2)$$

Here, h_v is the volumetric heat transfer coefficient, $k_{s,e} = k_s(1 - \varepsilon)$ is the effective heat conductivity of the solid matrix, and $k_{f,e} = \varepsilon k_f + k_{f,disp}$ is the effective heat conductivity of the fluid coolant. The effective heat conductivity of the coolant consists of thermal diffusion and dispersion. Calmidi and Mahajan [3] indicated that it is difficult to describe the dispersion with an accurate quantity. However, Wakao et al. [4] and Alazmi and Vafai [2] presented the following empirical formula to estimate the dispersive effect of packed beds:

$$k_{f,disp} = 0.5k_f \left(\frac{\rho_f v d_p}{\mu_f} \right) \text{Pr} = 0.5mc_f d_p \quad (3)$$

The LTNE model consists of two second-order differential equations, Eqs. (1) and (2). To solve the two equations, four boundary conditions (BCs) are required. Burch et al. [5] and Polezhaev and Seliverstov [6] used the following two equations as cold surface BCs:

$$y = 0 \quad k_{s,e} \frac{dT_s}{dy} = h_c (T_s - T_c) \quad (4)$$

$$y = 0 \quad mc_f (T_f - T_c) = h_c (T_s - T_c) \quad (5)$$

These cold surface BCs are widely received by most investigators of transpiration cooling. However, up to now, it is not clear what two BCs might be used at the hot surface to be protected. There have been five empirical BCs which were used to solve the LTNE model in various situations. The first three BCs were summarized by Alazmi and Vafai [7]

$$y = H \begin{cases} h_g (T_g - T_s) = q_s + q_f = k_{s,e} \frac{\partial T_s}{\partial y} + k_{f,e} \frac{\partial T_f}{\partial y} \\ \text{(first)} \quad \frac{q_f}{q_s} = \frac{\varepsilon}{1 - \varepsilon} \quad \text{(second)} \quad \frac{q_f}{q_s} = \frac{k_f}{k_s} \quad \text{(third)} \quad \frac{q_f}{q_s} = \frac{\varepsilon k_f}{(1 - \varepsilon) k_s} \end{cases} \quad (6)$$

Here, h_g is the heat transfer coefficient at the hot surface of the porous plate. This coefficient includes the integral effects of thermal convection, radiation, and coolant injection. The physical meaning of the three BCs is that the total heat flux at the hot surface should be partaken by the fluid coolant and the solid matrix in simple manners: according to the ratio of the volume, the heat conductivity, or effective heat conductivity, of the fluid coolant to the solid matrix.

The fourth BC is an overall energy balance equation, which means that at steady state, the total heat flux is absorbed by the coolant only at the hot interface through heat convection. This heat convection results in an increase of the coolant temperature from the reservoir temperature up to a hot surface temperature; contrarily, within the porous plate, the temperatures of the solid matrix and fluid coolant do not change with time. This BC was used by Kuznetsov [8], Wolfersdorf [9], and Jiang et al. [10]

$$\text{(fourth)} \quad y = H \begin{cases} h_g (T_g - T_s) = k_{s,e} \frac{\partial T_s}{\partial y} + k_{f,e} \frac{\partial T_f}{\partial y} \\ h_g (T_g - T_s) = mc_f (T_f - T_c) \end{cases} \quad (7)$$

Contributed by the Heat Transfer Division of ASME for publication in the JOURNAL OF HEAT TRANSFER. Manuscript received July 25, 2006; final manuscript received June 1, 2007; published online January 28, 2008. Review conducted by Jamal Seyed-Yagoobi.

The fifth BC was presented by Kovenskii and Teplitskii [11]. They deemed that the coolant does not absorb any heat energy at the hot interface, and the heat exchange between the coolant and matrix occurs only within the pores,

$$\text{(fifth) } y = H \begin{cases} h_g(T_g - T_s) = k_{s,e} \frac{dT_s}{dy} \\ k_{f,e} \frac{dT_f}{dy} = 0 \end{cases} \quad (8)$$

The BCs mentioned above have been employed to study transpiration cooling problems in different situations, but for the case of constant hot gas temperature and coolant flow opposite to the heat flux, which BCs are more suitable and reasonable? To answer this question, an analytical solution of steady and one-dimensional problems is presented. Through comparison and analysis of the analytical solution under the different BCs, it can be confirmed which BCs at all conditions are usable, which BCs under certain conditions are usable, and which BCs are thoroughly unreasonable. The main objective of this work is to provide the investigators of transpiration cooling problems with a relatively comprehensive reference to choose a suitable BC for the LTNE model.

2 Nondimensionalization of Models

Introducing the following dimensionless parameters:

$$Y = \frac{y}{H} \quad \theta_s = \frac{T_s - T_c}{qH/k_{s,e}} \quad \theta_f = \frac{T_f - T_c}{qH/k_{s,e}}$$

$$Y = 1 \begin{cases} \frac{d\theta_s}{dY} + \lambda \frac{d\theta_f}{dY} = \text{Bi}_g(1 - \theta_s) \\ \text{(first) } \frac{\partial \theta_f / \partial Y}{\partial \theta_s / \partial Y} = \frac{\varepsilon}{\lambda(1 - \varepsilon)} = \frac{k_s}{k_f} \quad \text{(second) } \frac{\partial \theta_f / \partial Y}{\partial \theta_s / \partial Y} = \frac{1 - \varepsilon}{\varepsilon} \quad \text{(third) } \frac{\partial \theta_f / \partial Y}{\partial \theta_s / \partial Y} = 1 \end{cases} \quad (14)$$

$$\text{(fourth) } Y = 1 \begin{cases} \frac{d\theta_s}{dY} + \lambda \frac{d\theta_f}{dY} = \text{Bi}_g(1 - \theta_s) \\ M\theta_f(1) = \text{Bi}_g[1 - \theta_s(1)] \end{cases} \quad (15)$$

$$\text{(fifth) } Y = 1 \begin{cases} \frac{d\theta_s}{dY} = \text{Bi}_g(1 - \theta_s) \\ \frac{d\theta_f}{dY} = 0 \end{cases} \quad (16)$$

3 Analytic Solutions and Result Discussions

The general analytic solutions of Eqs. (10) and (11) have the following forms:

$$\begin{aligned} \theta_s &= C_1 e^{k_1 Y} + C_2 e^{k_2 Y} + C_3 e^{k_3 Y} + C_4 \\ \theta_f &= K_1 C_1 e^{k_1 Y} + K_2 C_2 e^{k_2 Y} + K_3 C_3 e^{k_3 Y} + C_4 \end{aligned} \quad (17)$$

with

$$K_i = \left(1 - \frac{1}{\text{Bi}_v} k_i^2 \right) \quad i = 1, 2, 3$$

Here, k_i can be calculated by the Cardano rule [12], and integral constants, $C_i (i=1, 2, 3, 4)$, are dependent on the corresponding BCs. Through the analytical solutions obtained at the five BCs, calculations of the coolant and matrix temperatures can be carried out, and the rationalities of the BCs can be discussed and analyzed.

$$\begin{aligned} M &= \frac{mc_f H}{k_{s,e}} \quad \lambda = \frac{\varepsilon k_f}{(1 - \varepsilon) k_s} \quad \kappa = \frac{k_{s,e}}{k_{f,e}} \\ \text{Bi}_v &= \frac{h_v H^2}{k_{s,e}} \quad \text{Bi}_c = \frac{h_c H}{k_{s,e}} \quad \text{Bi}_g = \frac{h_g H}{k_{s,e}} \end{aligned} \quad (9)$$

Here, M is the dimensionless coolant mass flow rate, and Bi_v , Bi_c , and Bi_g are the Biot numbers within the pores, at the cold surface, and at the hot surface of the solid matrix, respectively. Using these parameters, Eqs. (1) and (2) can be written as

$$\frac{d^2 \theta_s}{dY^2} = \text{Bi}_v (\theta_s - \theta_f) \quad (10)$$

$$M\kappa \frac{d\theta_f}{dY} = \frac{d^2 \theta_f}{dY^2} + \text{Bi}_v \kappa (\theta_s - \theta_f) \quad (11)$$

At the cold surface of the porous plate, Eqs. (4) and (5) are transformed into

$$Y = 0 \quad \frac{d\theta_s}{dY} = \text{Bi}_c \theta_s \quad (12)$$

$$Y = 0 \quad M\theta_f = \text{Bi}_c \theta_s \quad (13)$$

At the hot surface, the corresponding dimensionless BCs are transformed into

At a certain flow rate of coolant mass injection $M=5$ and a certain heat conductivity ratio of the solid matrix to the fluid coolant $\kappa=75$, the temperature profiles of the fluid coolant and solid matrix within the porous plate can be obtained by the first BC and the analytic solutions (the results are shown in Fig. 2(a)). It is observed that near the cold surface, the coolant temperature is almost identical with the matrix temperature; in the range from $Y=0.8$ to $Y=0.98$, the matrix temperature is gently higher than the coolant temperature; in the last segment, the coolant temperature rises rapidly; at the hot interface, $Y=1$, is much higher than the matrix temperature. This phenomenon can be explained with the first formula of Eq. (14). The heat conductivity of the solid matrix is usually much higher than that of the fluid coolant; for example, the heat conductivity of superalloy is much higher than that of liquid hydrogen; this fact conduces to a larger temperature gradient of the coolant compared to that of the matrix at the hot interface. Finally, the coolant temperature exceeds the matrix temperature. This trend cannot be changed by a variation in coolant mass flow rate; as demonstrated in Fig. 2(b), at the hot surface, the coolant temperature is always higher than the matrix temperature, in the entire range of M from 1 to 80.

Figure 3(a) illustrates the coolant and matrix temperature profiles near the hot surface of the plate at a certain flow rate of $M=5$ and a certain heat conductivity ratio of the solid matrix to the fluid coolant $\kappa=75$ for the second and third BCs. Only in the last piece of the profiles, the difference between the second and third BCs can be observed. The coolant temperature of the second BC near the hot surface rises with a larger gradient and exceeds the matrix temperature at the hot surface, whereas the coolant and

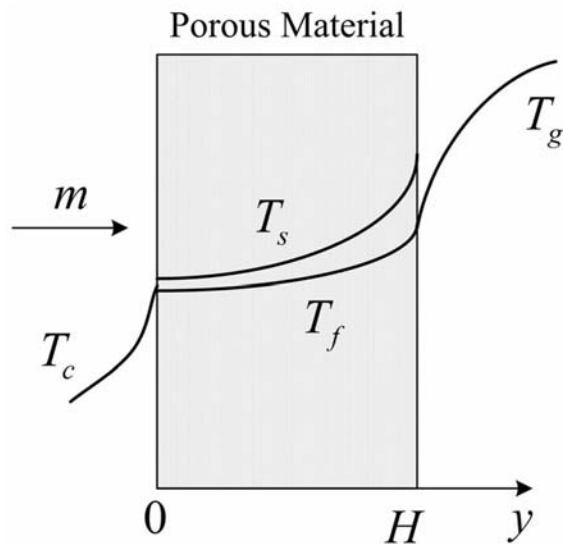


Fig. 1 Schematic diagram of transpiration cooling problem

matrix temperatures of the third BC rise with the same velocity. This phenomenon can be deciphered by the last two BCs in Eq. (14). For the second BC, the temperature gradient ratio of the fluid

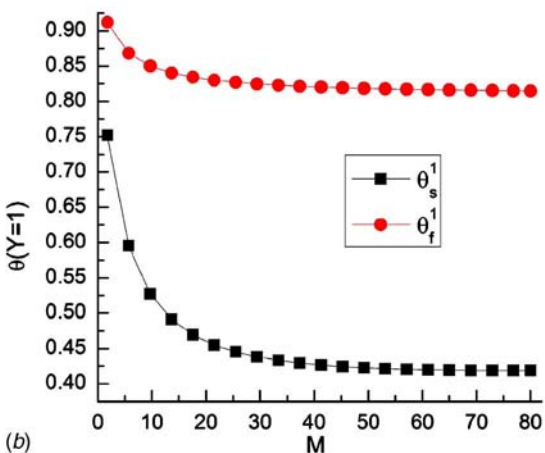
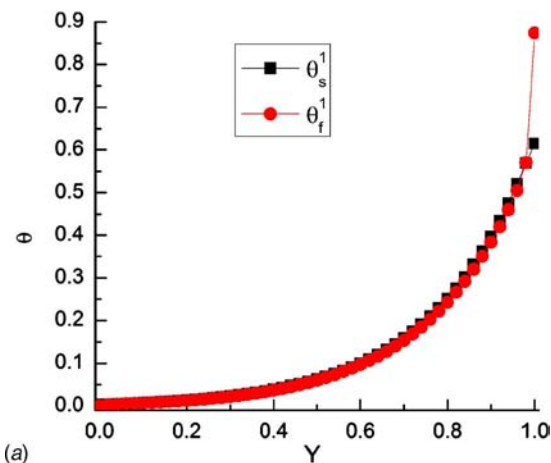


Fig. 2 (a) Temperature distribution within the plate at $M=5$ for the first BC; (b) temperature variation at the hot interface with coolant mass flow rate for the first BC

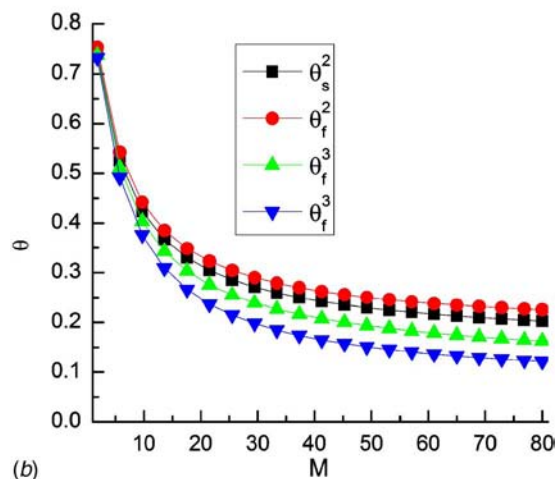
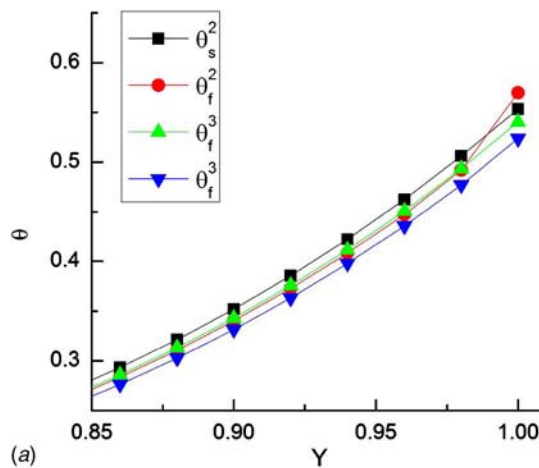


Fig. 3 (a) Temperature profile near the hot surface at $M=5$ for the second and third BCs; (b) temperature variation at the hot interface with coolant mass flow rate for the second and third BCs

coolant to the solid matrix is dependent on porosity. In this paper, the porosity is 0.25, the ratio is 3, and the coolant temperature at the hot surface is therefore slightly higher than the matrix temperature. For the case of the third BC, the temperature gradient ratio of the coolant to the matrix is 1; thus, the matrix temperature is always higher than the coolant temperature.

Figure 3(b) illustrates that at the hot interface, the coolant temperature obtained by the second BC is always higher than the matrix temperature; contrarily, that by the third BC is always lower than the matrix temperature; the coolant and matrix temperatures obtained by the second BC are all higher than those by the third BC. These two trends cannot be changed with the coolant mass flow rate. The reason is that these BCs describe only distributive relations of the total heat flux at the hot surface, and the relations are independent of the coolant mass flow rate; thus, the variation of the mass flow rate cannot change these trends.

For the fourth BC, at a constant coolant mass flow rate of $M=1$ and a certain heat conductivity ratio of the solid matrix to the fluid coolant $\kappa=75$, the temperature variation within the porous plate is shown in Fig. 4(a). Near the hot interface, the coolant temperature rises with a very large gradient, is then much higher than the matrix temperature, and even exceeds the hot gas temperature. This is inconsequential from the physical viewpoint. The coolant absorbs heat energy from the hot gas; it is therefore impossible that the coolant temperature exceeds the hot gas temperature. Which reason causes this error? Let us look at Eq. (15). The

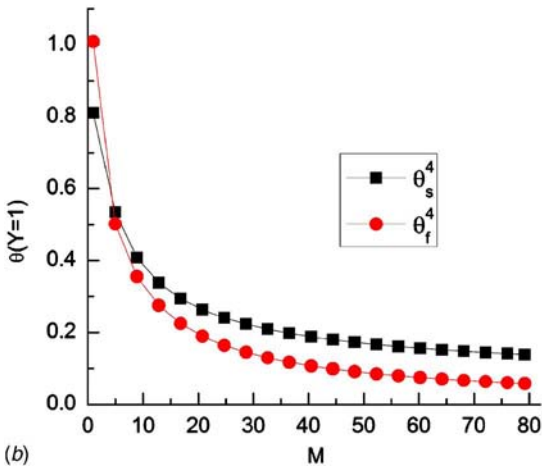
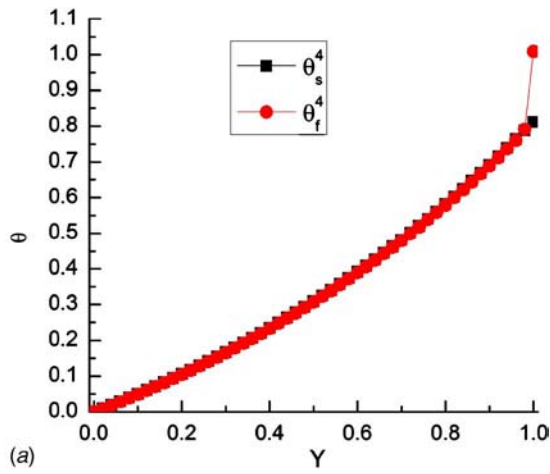


Fig. 4 (a) Temperature distribution within the plate at $M=1$ for the fourth BC; (b) temperature variation at the hot interface with coolant mass flow rate for the fourth BC

coolant mass flow rate M is used as a variable, the Biot number at the hot surface is constant, and the matrix temperature at the hot surface is limited by the first formula of Eq. (15) within $0 < \theta_s(1) < 1$. If M is a very small value, the coolant temperature $\theta_f(1)$ must be a very large value. Therefore, this inconsequential result may occur. Figure 4(b) shows the variation trend of the coolant and matrix temperatures with the mass flow rate M . When M is less than 5, the coolant temperature is higher than the matrix temperature, and the temperature difference increases with a decrease of the mass flow rate.

At the hot surface, the temperature profiles obtained by the fifth BC are shown in Fig. 5. The coolant temperature is always lower than the matrix temperature at all coolant mass flow rates. The reason is clear: The fifth BC is based on the assumption that the fluid coolant absorbs heat energy from the solid matrix and only within the pores; this means that at the hot interface, the coolant does not absorb any heat energy. Therefore, it is intelligible that the coolant temperature is always lower than the matrix temperature.

Transpiration cooling investigation focuses usually on the hot surface to be protected. Thus, the final temperatures at the hot surface are noteworthy. Figure 6 shows a comparison between the hot surface temperatures obtained by the five BCs. The temperatures of the second, third, and fifth BCs are relatively close. At larger coolant mass flow rates, the temperatures of the fourth BC are quite close to that of the fifth BC, but are inconsequential at lower flow rates. The coolant temperatures of the first and second

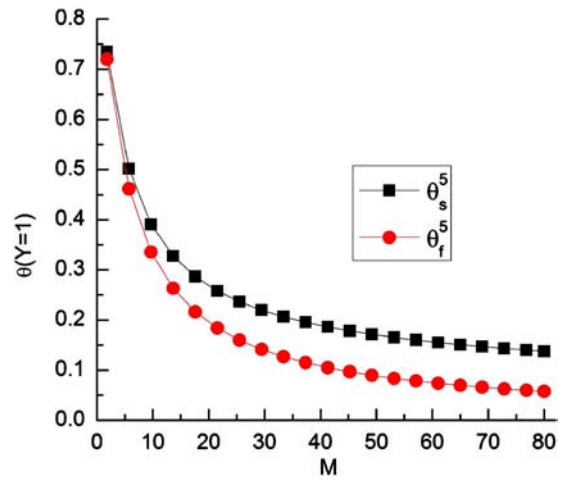


Fig. 5 Temperature variation at the hot interface with coolant mass flow rate for the fifth BC

BCs are higher than the matrix temperature at all coolant mass flow rates. This result is opposite to the cases of the third and fifth BCs. In most situations, the coolant and matrix temperatures obtained by the first BC are much higher than those by the other BCs.

To estimate the integrative effect of the heat exchange between the coolant and the matrix, another important parameter, thermal effectiveness, should be introduced. The following formula was used by Wolfersdorf [8] to describe the thermal effectiveness of transpiration cooling at the hot surface:

$$\eta = \frac{T_f|_{y=H} - T_c}{T_s|_{y=H} - T_c} = \frac{\theta_f(1)}{\theta_s(1)}$$

Figure 7 illustrates the thermal effectiveness distributions for the five cases at the hot surface. The variation trends of the third, fourth, and fifth BCs are identical; the thermal effectiveness decreases with an increase in the coolant mass flow rate. This phenomenon can be explained as follows: The increase in the coolant mass flow rate, the stay interval of the coolant within the pores reduces and the heat absorbed from the solid matrix decreases; therefore, the thermal effectiveness falls. It is noteworthy that with the increase of the coolant mass flow rate, the thermal effectiveness of the fourth and fifth BCs is almost consistent. The variation

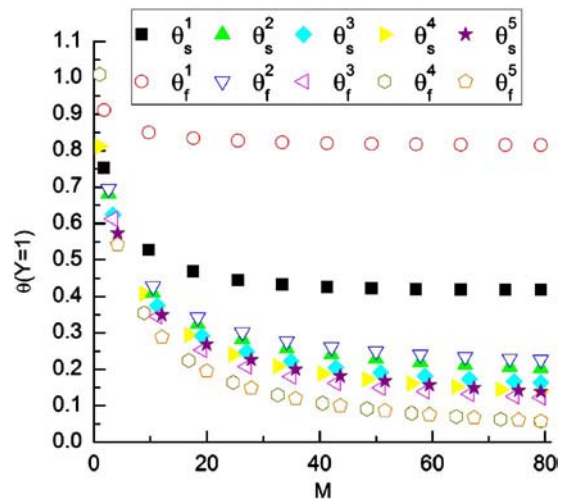


Fig. 6 Comparison of temperatures obtained by different BCs at the hot interface

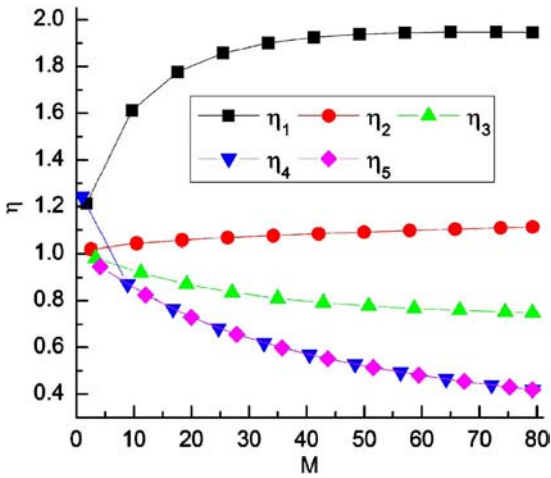


Fig. 7 Comparison of thermal effectiveness of different BCs at the hot interface

trends of the first and second BCs are opposite to the anterior cases; the thermal effectiveness increases with the coolant mass flow rate; therefore, this result seems to be unreasonable.

4 Conclusion

Under the conditions of constant hot gas temperature and the heat flux opposite to the coolant mass flow, an analytical solution of the LTNE model and a quite comprehensive investigation on five BCs of the LTNE model have been presented. Although the analytical solution of the LTNE model is obtained at constant thermal properties, this solution can be used to discuss the rationality of the BCs because the variation of the thermal properties cannot change the trends of temperatures. Through the discussion and analysis, the following six conclusions can be drawn.

- (1) It is evident that the different BCs may lead to substantial differences of the coolant and matrix temperatures at the hot surface. The coolant temperature obtained by the first BC is highest, by the fifth BC is lowest, by the first and second BCs are always higher than the matrix temperature at all coolant mass flow rates, and by the third and fifth BCs are always lower than the matrix temperature at all coolant mass flow rates.
- (2) Through the analytical solution of the thermal effectiveness, it is observed that the first and second BCs will lead to an increase in the thermal effectiveness with the coolant mass flow rate. This result seems to be illogical in the investigation of transpiration cooling problems.
- (3) The results calculated by the fifth BC are reasonable at all situations, but this BC is simplified; the effect of the hot gas on the coolant at the hot interface is neglected. Therefore, the coolant temperature of the fifth BC is always lower than the corresponding true value.
- (4) It has to be taken care to use the fourth BC. At lower coolant mass flow rates, this BC may lead to an inconsequential result. However, at larger coolant mass flow rates, this BC seems to be usable.
- (5) The temperature and thermal effectiveness of the third BC are reasonable at all situations; therefore, the use of the third BC is secure.
- (6) Only for the temperature calculation of the matrix and coolant, without the consideration of the thermal effectiveness, the results obtained by the second BC are close to that by the third BC.

Acknowledgment

The project is supported by the Natural Science Foundation of China (No. 90305006) and Education Administration Foundation of Anhui Province (No. 2004kj365zd). One of the authors (Jianhua Wang) is also grateful for the financial support provided by the Foundation of the Education Ministry of China for the Returned Overseas Scholars.

Nomenclature

- y, Y = coordinates
 H = thickness of solid matrix, m
 T = temperature, K
 k = thermal conductivity, W/m K
 h = interfacial convective coefficient, W/m² K
 \dot{m} = coolant mass flow rate, kg/m² s
 h_v = volumetric convective coefficient, W/m³ K
 d_p = characteristic size of porous matrix, m
 c_f = coolant specific heat capacity, J/kg K
 Bi_v = Biot number within pores
 Bi_c = Biot number at cold surface
 Bi_g = Biot number at hot surface
 M = dimensionless coolant mass flow rate
 Pr = Prandtl number

Greek Symbols

- ε = porosity
 κ, λ = effective conductivity ratio
 θ = dimensionless temperature

Subscripts

- s = solid
 f = fluid
 c = coolant reservoir
 g = hot gas
 d = dispersion
 e = effective

References

- [1] Wang, J. H., and Wang, H. N., 2006, "A Discussion of Transpiration Cooling Problems Through an Analytical Solution of Local Thermal Non-Equilibrium Model," *ASME J. Heat Transfer*, **128**, pp. 1093–1098.
- [2] Alazmi, B., and Vafai, K., 2000, "Analysis of Variants Within the Porous Media Transport Models," *ASME J. Heat Transfer*, **122**, pp. 303–326.
- [3] Calmidi, V. V., and Mahajan, R. L., 2000, "Forced Convection in High Porosity Metal Foams," *ASME J. Heat Transfer*, **122**, pp. 557–565.
- [4] Wakao, N., Kaguei, S., and Funazkri, T., 1979, "Effect of Fluid Dispersion Coefficients on Particle-to-Fluid Heat Transfer Coefficients in Packed Beds," *Chem. Eng. Sci.*, **34**, pp. 325–336.
- [5] Burch, D. M., Allen, R. W., and Peavy, B. A., 1976, "Transient Temperature Distributions Within Porous Slabs Subjected to Sudden Transpiration Heating," *ASME J. Heat Transfer*, **98**, pp. 221–225.
- [6] Polezhaev, Y. V., and Seliverstov, E. M., 2002, "A Universal Model of Heat Transfer in Systems With Penetration Cooling," *High Temp.*, **40**, pp. 856–864.
- [7] Alazmi, B., and Vafai, K., 2002, "Constant Wall Heat Flux Boundary Conditions in Porous Media Under Thermal Non-Equilibrium Conditions," *Int. J. Heat Mass Transfer*, **45**, pp. 3071–3087.
- [8] Kuznetsov, A. V., 1995, "Analytical Comparison and Criteria for Heat and Mass Transfer Models in Metal Hydride Packed Beds," *Int. J. Heat Mass Transfer*, **38**, pp. 2873–2884.
- [9] Wolfersdorf, J. V., 2005, "Effect of Coolant Side Heat Transfer on Transpiration Cooling," *Int. J. Heat Mass Transfer*, **41**, pp. 327–337.
- [10] Jiang, P. X., Yu, L., Sun, J. G., and Wang, J., 2004, "Experimental and Numerical Investigation of Convection Heat Transfer in Transpiration Cooling," *Appl. Therm. Eng.*, **24**, pp. 1271–1289.
- [11] Kovenskii, V. I., and Teplitskii, Y. S., 2006, "Modelling of Heat Transfer in an Infiltrated Granular Bed in View of the Difference of Phase Temperatures," *Int. J. Heat Mass Transfer*, **49**, pp. 359–365.
- [12] Pixley, A. F., 1980, *Applied Linear Algebra*, University Press of America, Lanham, MD.

Heat Transfer From a Rotating Disk to Fluids for a Wide Range of Prandtl Numbers Using the Asymptotic Model

M. M. Awad

Faculty of Engineering and Applied Science,
Memorial University of Newfoundland,
St. John's, NL, A1B 3X5, Canada
e-mail: awad@engr.mun.ca

*A simple method for calculating heat transfer from a rotating disk to fluids for a wide range of Prandtl numbers using asymptotic analysis is presented. Nusselt numbers for a heated rotating disk for different Prandtl numbers is expressed in terms of the asymptotic Nusselt numbers corresponding to a very small value of Prandtl numbers and Nusselt numbers corresponding to a very large value of Prandtl numbers. The proposed model uses a concave downward asymptotic correlation method to develop a robust compact model. Using the methods discussed by Churchill and Usagi (1972, "General Expression for the Correlation of Rates of Transfer and Other Phenomena," *AIChE J.*, **18**(6), pp. 1121–1128), the fitting parameter in the proposed model can be determined at Prandtl numbers corresponding to the intersection of the two asymptotes. [DOI: 10.1115/1.2780185]*

Keywords: heat transfer, rotating disk, wide range, Prandtl numbers, asymptotic model

Introduction

Fluid flow, heat, and mass transfer over a rotating disk are related to many practical applications such as disk driver, jet or spray cooling, rotating machinery, spin coating, etc. For example, heat transfer by convection from a heated rotating disk to the surrounding fluid is important in the thermal analysis of the rotating components of different machines, especially for the case of high temperature fluids. The boundary layer on the disk is laminar and of uniform thickness at $\omega D^2/\nu < 10^6$. At $\omega D^2/\nu > 10^6$, the flow becomes turbulent near the outer edge and the transition point moves radially inward as $\omega D^2/\nu$ is increased.

First, von Kármán [1] presented an analytical study of the flow field induced by the rotation of a large disk in an infinite incompressible fluid under laminar conditions in 1921. He took the pressure to be independent of radial position and presented an integral solution to the flow field. After the pioneering work of von Kármán [1], a tremendous amount of the studies can be found in the literature but only those closely related to the present study are to be mentioned. Cochran [2] improved the solution numerically. Hannah [3] gave the exact solution for the laminar forced flow against an infinite rotating disk. Ostrach and Thornton [4] extended the results of Refs. [1,2] to include the effect of variable physical properties for gases with $Pr=0.72$ for compressible flow about a rotating isothermal disk.

Wanger [5] studied the laminar heat transfer from an isothermal rotating disk to ambient air. Using theoretical calculations on the basis of von Kármán's calculation [1] of flow conditions, he found that $h(\nu/\omega)^{0.5}/k=0.335$. Millsap and Pohlhausen [6] gave an ex-

act solution of the heat transfer problem for the von Kármán example [1] of the laminar flow of a viscous fluid over a rotating plate in dimensionless form. The solution was explicitly given for an isothermal plate with viscous dissipation included. They gave the numerical results for a limited range of Prandtl number from 0.5 to 10. They found that $h(\nu/\omega)^{0.5}/k=C$ for $1 < Pr < 10$, where C increased with Prandtl number. Cobb and Saunders [7] presented an experimental investigation of the heat transfer for a range of conditions from entirely laminar flow to conditions when the outer 80% of the disk area was under turbulence. For laminar flow, they found that the heat transfer agreed with Wanger's results [5] but Millsap and Pohlhausen's theory [6] gave too low values. For turbulent flow, they gave some measurements of the velocity and temperature profiles at 9 in. (0.229 m) radius and 1235 rpm. They made an attempt to deduce the turbulent flow heat transfer theoretically by assuming a 1/7 power law of temperature distribution, but this attempt gave too low values. This might be explained by the existence of a laminar region close to the plate in which, as already found, the temperature dropped less rapidly than the velocity for $Pr=0.72$. The temperature boundary layer appeared to extend a little further from the plate than did the velocity layer. Kreith et al. [8] applied the analogy between heat, mass, and momentum transfer to a rotating disk. They measured experimentally the mass transfer rates from a disk rotating in an infinite environment under laminar and turbulent conditions. They related the measured mass transfer rates to the corresponding heat transfer process by means of an analogy method. The advantage of using the experimental analog was to eliminate difficulties associated with accurate measurements of heat transfer coefficients. They found that $h(\nu/\omega)^{0.5}/k=0.345$ for $Pr=0.72$ under laminar conditions. Sparrow and Gregg [9] studied the effect of Prandtl number on heat transfer from an isothermal disk. They removed the restriction on Prandtl number by obtaining similarity solution over a wide range of Prandtl number from 0.01 to 100. They found asymptotic relations between C and Pr at very low and very high Prandtl numbers as

$$h\left(\frac{\nu}{\omega}\right)^{1/2}/k = 0.88447 Pr \quad Pr \rightarrow 0 \quad (1)$$

$$h\left(\frac{\nu}{\omega}\right)^{1/2}/k = 0.62048 Pr^{1/3} \quad Pr \rightarrow \infty \quad (2)$$

Hartnett [10] studied the heat transfer from a nonisothermal disk rotating in still air using a power-law radial distribution. He neglected the radial conduction terms in his work. He found that $h(\nu/\omega)^{0.5}/k=C$ with the constant becoming larger with increasing the exponent of power-law temperature profile. Hartnett and Deland [11] reported additional solutions of the energy equation for the rotating nonisothermal disk or cone with power function surface temperature distribution covering a range of Prandtl number from 0.1 to 100 and the exponent values of power-law temperature profile from 0.1 to 10. Mabuchi et al. [12] studied theoretically the laminar heat transfer from a disk rotating in uniform forced stream for the fluid of any Prandtl number in the case when the surface temperature difference was expressed by the quadratic relation. Sano [13] obtained exact asymptotic expansions for heat transfer in laminar forced flow against a nonisothermal rotating disk for large and small Prandtl numbers using a perturbation method. He assumed that the surface temperature of the disk varies according to a power law with the radial distance. Popiel and Boguslawski [14] measured the local heat transfer coefficients on the rotating isothermal disk in still air. From the values of the local Nusselt number against the rotational Reynolds number, they found that there were three different regions: laminar, transition, and turbulent. Oehlbeck and Erian [15] investigated the heat transfer from axisymmetric heat sources at the surface of a rotating disk under laminar flow conditions for incompressible flow with constant physical properties. They solved the energy equation in-

Contributed by the Heat Transfer Division of ASME for publication in the *JOURNAL OF HEAT TRANSFER*. Manuscript received February 12, 2007; final manuscript received July 16, 2007; published online January 30, 2008. Review conducted by Louis C. Burmeister.

cluding radial conduction numerically assuming that both natural convection and viscous dissipation effects were negligible. A solution could be obtained for any specified radial surface distribution of either temperature or heat flux. They presented several boundary conditions, including two for which an exact solution exists. They found that the heat transfer coefficients obtained for an isothermal disk and for the case of a power-law temperature distribution were in excellent agreement with existing solutions. Muir et al. [16] studied the problem of laminar heat transfer from an isothermal rotating disk with mass injection at the wall varying from zero to a large value. They varied the Prandtl number of the quiescent fluid over a wide range starting from liquid metal region ($Pr \sim 0.001$) to highly viscous fluids ($Pr \sim 100$). Numerical results showed that for a given finite rate of blowing at the wall, the heat transfer rate first increased, reaching a maximum value before falling sharply, as the Prandtl number was increased. Lin and Lin [17] proposed a new similarity variable for the analysis of laminar boundary-layer heat transfer from a rotating cone or disk to fluids of any Prandtl number. They obtained very accurate similarity solutions for both the isothermal and uniform-flux cases over a very wide range of Prandtl number from 0.001 to ∞ . They found that dimensionless temperature profiles in this range of Prandtl number were very similar. They gave a heat transfer correlation equation of high accuracy for all Prandtl numbers as

$$h \left(\frac{\nu}{\omega} \right)^{1/2} / k = 0.6 Pr / (0.56 + 0.26 Pr^{1/2} + Pr)^{2/3} \quad (3)$$

The maximum error of $h(\nu/\omega)^{0.5}/k$ predicted by Eq. (3) is less than 5% for all Prandtl numbers. Wang and Kleinstreuer [18] developed a powerful similarity solution of the highly nonlinear, coupled boundary-layer equations for steady laminar mixed convection heat transfer between a rotating cone/disk and power-law fluids. They were interested in the effects of the power-law viscosity index, a generalized local Prandtl number, the buoyancy parameter, and the type of thermal wall condition on the velocity and temperature fields and hence the skin friction coefficient and the local Nusselt number. They found that the momentum boundary-layer thickness increased measurably with decreasing viscosity index, while the thermal boundary-layer thickness was less affected by changes in the viscosity index. The magnitude and direction of the buoyancy force influenced the upward velocity profile near the wall and the temperature profiles significantly. As a result, the validated computer simulation model could be used to calculate the velocity and thermal region of influence as a function of thermal wall condition, power-law viscosity index, fluid Prandtl numbers, and buoyancy parameter. For all generalized Prandtl numbers, the heat transfer group (HTG) was consistently lower for shear-thinning fluids when compared with shear-thickening fluids. On the other hand, the skin friction group (SFG) was higher for all Prandtl numbers for pseudoplastics when compared with dilatant fluids. Both Prandtl number and buoyancy parameter had a more pronounced effect on SFG than on HTG.

In the present study, a simple method for calculating heat transfer from a rotating disk to fluids for a wide range of Prandtl numbers using asymptotic analysis is presented.

Proposed Methodology

Figure 1 shows Nusselt numbers for a heated rotating disk for different Prandtl numbers [19] based on data from Sparrow and Gregg [9]. There is an asymptotic behavior in Fig. 1. As a result, heat transfer from a rotating disk to fluids at any Prandtl number can be predicted using the asymptotic model. In the asymptotic model, the dependent parameter Nu has two asymptotes. The first asymptote is $Nu_{Pr \rightarrow 0}$ that corresponds to a very small value of the independent parameter Pr. The second asymptote is $Nu_{Pr \rightarrow \infty}$, that corresponds to a very large value of the independent parameter Pr. For the case of heat transfer from a rotating disk to fluids for a wide range of Prandtl numbers, the two asymptotes $Nu_{Pr \rightarrow 0}$ and

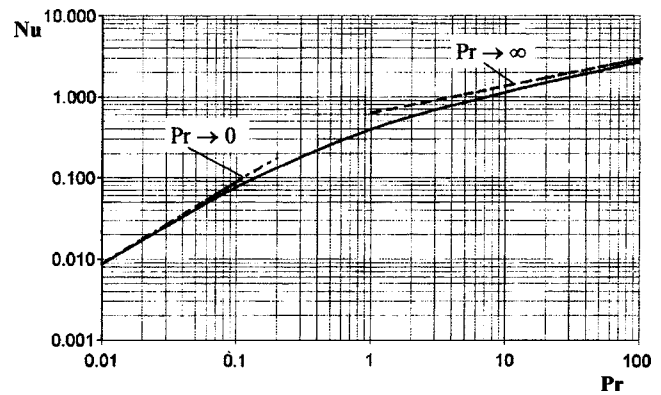


Fig. 1 Nusselt numbers for a heated rotating disk for different prandtl numbers [19]

$Nu_{Pr \rightarrow \infty}$ increase with increasing values of Pr, and the solution Nu is concave downward. This trend is also found in the case of internal forced and free convection within ducts and channels. In the present study, the two asymptotes $Nu_{Pr \rightarrow 0}$ and $Nu_{Pr \rightarrow \infty}$ can be expressed using Eqs. (1) and (2), respectively. Since $Nu_{Pr \rightarrow 0} < Nu_{Pr \rightarrow \infty}$ as $Pr \rightarrow 0$, so the solution Nu is concave downward, and the two asymptotes $Nu_{Pr \rightarrow 0}$ and $Nu_{Pr \rightarrow \infty}$ can be combined in the following method [20–23]:

$$\frac{1}{Nu} = \left[\left(\frac{1}{Nu_{Pr \rightarrow 0}} \right)^n + \left(\frac{1}{Nu_{Pr \rightarrow \infty}} \right)^n \right]^{1/n} \quad (4)$$

Equation (4) can be rearranged as

$$n = \frac{\ln[1 + (Nu_{Pr \rightarrow 0}/Nu_{Pr \rightarrow \infty})^n]}{\ln(Nu_{Pr \rightarrow 0}/Nu)} \quad (5)$$

Using Eqs. (1), (2), and (5), we obtain

$$n = \frac{\ln[1 + (0.88447 Pr / 0.62048 Pr^{1/3})^n]}{\ln(0.88447 Pr / Nu)} \quad (6)$$

The parameter n is a fitting or “blending” parameter whose value can be determined in a simple method. The effect of the parameter n in Eq. (6) is only important in the transition region. The results for small and large values of the independent parameter Pr remain unchanged with changing the parameter n .

To determine a value of n , there are a number of methods as discussed by Churchill and Usagi [20]. For example, an intermediate value of $Pr = Pr_{int}$ can be selected corresponding or near the intersection of the two asymptotes for which $Nu(Pr_{int})$ is known from analytical, experimental, or numerical methods. At the intersection of the two asymptotes, Eq. (6) reduces to

$$n = \frac{\ln[2]}{\ln(0.88447 Pr_{int}/Nu)} \quad (7)$$

At the intersection of the two asymptotes, $Nu_{Pr \rightarrow 0} = Nu_{Pr \rightarrow \infty}$. This leads to $Pr_{int} = 0.588$. From Fig. 1, at $Pr_{int} = 0.588$, $Nu = 0.273$. Substituting $Pr_{int} = 0.588$ and $Nu = 0.273$ into Eq. (7), we obtain that $n = 1.077$. Using Eqs. (1), (2), and (4) with $n = 1.077$, we obtain

$$\frac{1}{Nu} = \left[\left(\frac{1}{0.88447 Pr} \right)^{1.077} + \left(\frac{1}{0.62048 Pr^{1/3}} \right)^{1.077} \right]^{1/1.077} \quad (8)$$

Results and Discussion

Figure 2 shows Nusselt numbers for a heated rotating disk for different Prandtl numbers using the asymptotic model, Eq. (8), as well as the two asymptotes $Nu_{Pr \rightarrow 0}$ and $Nu_{Pr \rightarrow \infty}$ represented by Eqs. (1) and (2), respectively. Table 1 shows data comparison for an isothermal disk using the asymptotic model, Eq. (8), and dif-

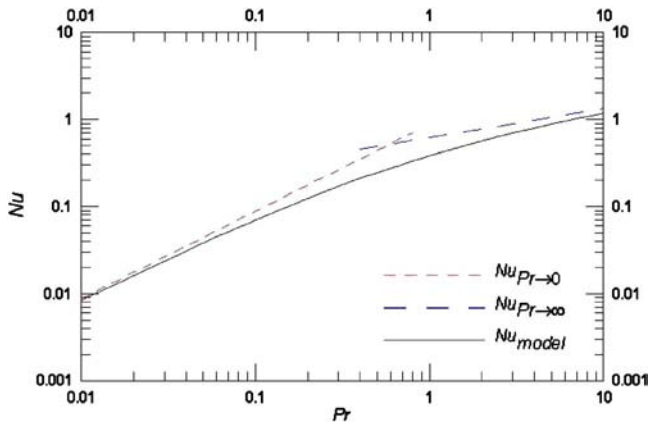


Fig. 2 Nusselt numbers for a heated rotating disk for different prandtl numbers using the asymptotic model

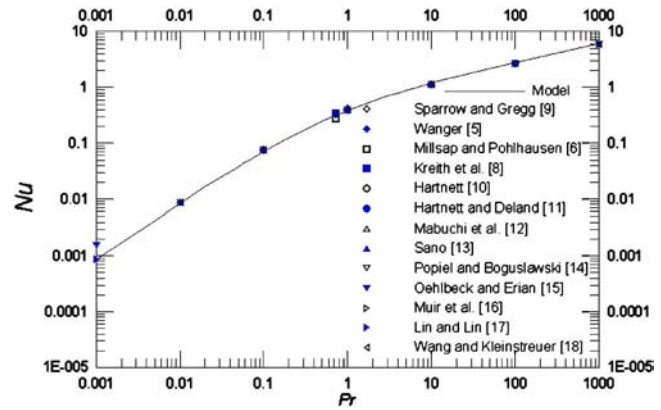


Fig. 3 Data comparison for an isothermal disk

Table 1 Data comparison for an isothermal disk

$h(\nu/\omega)^{0.5}/k$	Pr							
	0.001	0.01	0.1	0.72	1	10	100	1000
Present work	0.0008761	0.0084256	0.070308	0.31190	0.38273	1.1927	2.8147	6.177
Sparrow and Gregg [9]	0.0008845 ^a	0.0087051	0.076581		0.39625	1.1341	2.6871	6.205 ^a
Wanger [5]				0.335				
Millsap and Pohlhausen [6]				0.28 ^b				
Kreith et al. [8]				0.34				
Hartnett [10]				0.330				
Hartnett and Deland [11]			0.0766	0.330	0.396	1.13	2.69	
Mabuchi et al. [12]		0.00871	0.0767		0.3963	1.134	2.687	
Sano [13]		0.00872	0.0743		0.4447	1.161	2.704	
Popiel and Boguslawski [14]				0.33				
Oehlbeck and Erian [15]				0.341	0.394	1.131	2.684	6.002
Muir et al. [16] ^c	0.00152	0.00870	0.0763					
Lin and Lin [17]		0.0087051	0.076581		0.39625	1.1341	2.6871	
Wang and Kleinstreuer [18]	0.00088541	0.0087078	0.076590	0.32857	0.39626	1.1341	2.6872	6.0163
		0.008718	0.07667	0.3286	0.3962	1.1335	2.6885	6.0097

^aThese values are based on asymptotic solutions and are not exact.

^bThis value is due to the use of c_p in Pr instead of c_p .

^cThese values are computed for the case with no surface mass transfer.

ferent sets of data. From Table 1, it can be shown that the maximum relative error between $h(\nu/\omega)^{0.5}/k$ predicted by the present model using Eq. (8) and Sparrow and Gregg [9] data is 8.19% at $Pr=0.1$. The data points in Table 1 can be represented, as shown in Fig. 3. From Fig. 3, it is clearly apparent that the data points align well.

Summary and Conclusions

In the present study, a simple method for calculating heat transfer from a rotating disk to fluids for a wide range of Prandtl numbers using asymptotic analysis is presented. The method of combining asymptotes is based on the work of Churchill and Usagi [20]. The approximate solution of combining asymptotes is concave downward. A method of calculating the fitting or blending parameter at Prandtl numbers corresponding to the intersection of the two asymptotes was presented. The approximate solution for this problem was shown to be very accurate for a wide range of Prandtl numbers. The maximum relative error between $h(\nu/\omega)^{0.5}/k$ predicted by the present model using Eq. (8) and Sparrow and Gregg [9] data was 8.19% at $Pr=0.1$.

Acknowledgment

The author acknowledges the insightful comments and suggestions of the anonymous reviewers, Associate Editor Louis C. Burmeister and Editor Yogesh Jaluria, that have improved the quality of the paper.

Nomenclature

- C = constant
- D = disk diameter, m
- h = heat transfer coefficient, $W/m^2 K$
- k = fluid thermal conductivity, $W/m K$
- n = fitting parameter
- Nu = Nusselt number = $h(\nu/\omega)^{0.5}/k$
- Pr = Prandtl number

Greek Symbols

- ν = kinematic viscosity, m^2/s
- ω = disk angular velocity, rad/s

Subscripts

- 0 = corresponding to very small value
- ∞ = corresponding to very large value
- int = intermediate value

References

- [1] von Kármán, Th., 1921, "Über Laminare und Turbulente Reibung," ZAMM, **1**, pp. 233–252.
- [2] Cochran, W. G., 1934, "The Flow Due to a Rotating Disk," Proc. Cambridge Philos. Soc., **30**, pp. 365–375.
- [3] Hannah, D. M., 1947, "Forced Flow Against a Rotating Disk," British A. R. C. Report and Memo. No. 2772.
- [4] Ostrach, S., and Thornton, P. R., 1958, "Compressible Laminar Flow and Heat Transfer About a Rotating Isothermal Disk," NACA Report No. TN 4320.
- [5] Wanger, C., 1948, "Heat Transfer From a Rotating Disk to Ambient Air," J. Appl. Phys., **19**(9), pp. 837–839.

- [6] Millsap, K., and Pohlhausen, K., 1952, "Heat Transfer by Laminar Flow From a Rotating Plate," *J. Aeronaut. Sci.*, **19**(2), pp. 120–126.
- [7] Cobb, E. C., and Saunders, O. A., 1956, "Heat Transfer From a Rotating Disk," *Proc. R. Soc. London, Ser. A*, **236**, (1205), pp. 343–351.
- [8] Kreith, F., Taylor, J. H., and Chang, J. P., 1959, "Heat and Mass Transfer From a Rotating Disk," *ASME J. Heat Transfer*, **81**, pp. 95–105.
- [9] Sparrow, E. M., and Gregg, J. L., 1959, "Heat Transfer From a Rotating Disk to Fluids at Any Prandtl Number," *ASME J. Heat Transfer*, **81**, pp. 249–251.
- [10] Hartnett, J. P., 1959, "Heat Transfer From a Non-Isothermal Disk Rotating in Still Air," *ASME J. Appl. Mech.*, **81**, pp. 672–673.
- [11] Hartnett, J. P., and Deland, E. C., 1961, "The Influence of Prandtl Number on the Heat Transfer From Rotating Nonisothermal Disks and Cones," *ASME J. Heat Transfer*, **83**, pp. 95–96.
- [12] Mabuchi, I., Tanaka, T., and Sakakibara, Y., 1967, "Studies on the Convective Heat Transfer From Rotating Disk (2nd Report, The Effect of Prandtl Number on the Laminar Heat Transfer From a Disk Rotating in Uniform Forced Stream)," *Bull. JSME*, **10**(42), pp. 965–974.
- [13] Sano, T., 1973, "A Note on Asymptotic Solutions for Heat Transfer in Laminar Forced Flow Against a Non-Isothermal Rotating Disk," *Waerme-Stoffuebertrag./Thermo- and Fluid Dynamics*, **6**(2), pp. 108–113.
- [14] Popiel, Cz., O., and Boguslawski, L., 1975, "Local Heat-Transfer Coefficients on the Rotating Disk in Still Air," *Int. J. Heat Mass Transfer*, **18**(1), pp. 167–170.
- [15] Oehlbeck, D. L., and Erian, F. F., 1979, "Heat Transfer From Axisymmetric Sources at the Surface of a Rotating Disk," *Int. J. Heat Mass Transfer*, **22**(4), pp. 601–610.
- [16] Muir, P. H., Fairweather, G., and Vedha-Nayagam, M., 1983, "Effect of Prandtl Number on Heat Transfer From an Isothermal Rotating Disk With Blowing at the Wall," *Int. Commun. Heat Mass Transfer*, **10**(4), pp. 287–297.
- [17] Lin, H. T., and Lin, L. K., 1987, "Heat Transfer From a Rotating Cone or Disk to Fluids of Any Prandtl Number," *Int. Commun. Heat Mass Transfer*, **14**(3), pp. 323–332.
- [18] Wang, T. -Y., and Kleinstreuer, C., 1990, "Similarity Solution of Combined Convection Heat Transfer From a Rotating Cone or Disk to Non-Newtonian Fluids," *ASME J. Heat Transfer*, **112**(4), pp. 939–944.
- [19] Weigand, B., 2004, *Analytical Methods for Heat Transfer and Fluid Flow Problems*, Springer, New York, Chap. 6.
- [20] Churchill, S. W., and Usagi, R., 1972, "A General Expression for the Correlation of Rates of Transfer and Other Phenomena," *AIChE J.*, **18**(6), pp. 1121–1128.
- [21] Churchill, S. W., 1988, *Viscous Flows: The Practical Use of Theory*, Butterworths, Boston, MA.
- [22] Kraus, A. D., and Bar-Cohen, A., 1983, *Thermal Analysis and Control of Electronic Equipment*, Hemisphere, New York.
- [23] Yovanovich, M. M., 2003, "Asymptotes and Asymptotic Analysis for Development of Compact Models for Microelectronic Cooling," 19th Annual Semiconductor Thermal Measurement and Management Symposium and Exposition (SEMI-THERM), San Jose, CA.

Discussion “Pressure Drop During Refrigerant Condensation Inside Horizontal Smooth, Helical Microfin, and Herringbone Microfin Tubes” (Olivier, J. A., Liebenberg, L., Kedzierski, M. A., and Meyer, J. P., 2004, J. Heat Transfer, 126(5), pp. 687–696)

M. M. Awad

Faculty of Engineering and Applied Science,
Memorial University of Newfoundland,
St. John’s,
Newfoundland, A1B 3X5 Canada
e-mail: awad@engr.mun.ca

In the paper “Pressure Drop During Refrigerant Condensation Inside Horizontal Smooth, Helical Microfin, and Herringbone Microfin Tubes” (Olivier, J. A., Liebenberg, L., Kedzierski, M. A., and Meyer, J. P., 2004, J. Heat Transfer, 126(5), pp. 687–696), there are some errors in equations. The errors will be summarized first. After that, a general expression for the liquid-only friction factor f_{Lo} will be presented because the general form presented in this paper, Eq. (16), is not valid for helical microfin tubes.

Equation (4) for the momentum pressure drop Δp_m must be written as follows:

$$\Delta p_m = G^2 \left\{ \left[\frac{(1-x)^2}{\rho_L(1-\varepsilon)} + \frac{x^2}{\rho_V \varepsilon} \right]_{\text{out}} - \left[\frac{(1-x)^2}{\rho_L(1-\varepsilon)} + \frac{x^2}{\rho_V \varepsilon} \right]_{\text{in}} \right\} \quad (4)$$

The error in Eq. (4) is clearly a typographical error considering that the exponent a is not in the Nomenclature and the parameter a is not used elsewhere in the manuscript. In addition, the model will faithfully predict the measurements given in the original paper once all of the other corrections have been incorporated.

In Eq. (7), for the definition of the Froude rate, it is better to use the subscript V not v for vapor to use a consistent style of writing the parameters in the whole paper

$$Fr = \left[\frac{G^2 x^3}{(1-x)\rho_V^2 g D_i} \right]^{1/2} \quad (7)$$

Contributed by the Heat Transfer Division of ASME for publication in the JOURNAL OF HEAT TRANSFER. Manuscript received March 20, 2007; final manuscript received June 15, 2007; published online January 25, 2008. Review conducted by Anthony M. Jacobi.

The line after Eq. (9) must be written as “with the two-phase multiplier being that of Souza et al. [16].” Reference [16] is Souza, A. L., Chato, J. C., Wattelet, J. P., and Christoffersen, B. R., 1993, “Pressure Drop During Two-Phase Flow of Pure Refrigerants and Refrigerant-Oil Mixtures in Horizontal Smooth Tubes,” *ASME Heat Transfer With Alternate Refrigerants, HTD*, 243, pp. 35–41.

Equation (10) is applicable only for the range $Fr_L > 0.7$, where the Froude number is defined as

$$Fr_L = \frac{G^2}{\rho_L^2 g D_i}$$

Equation (12) for helical microfin tubes must be written as follows:

$$f_{Lo} = 0.046 Re_L^{-0.2} \left(\frac{D_i}{D_e} \right)^{-1} \left(\frac{A}{A_n} \right)^{-0.5} (\sec \beta)^{-0.75} \quad (12)$$

where

$$\frac{A}{A_n} = 1 - \frac{4ent}{\pi D_i^2 \cos \beta} \quad (13)$$

Equation (14) for herringbone microfin tubes must be written as follows:

$$f_{Lo} = 0.046 Re_L^{-0.2} \left(\frac{D_i}{D_e} \right)^{-1} \left(\frac{A}{A_n} \right)^{-0.5} (2 \sec \beta)^{-1.1} \quad (14)$$

where

$$\frac{A}{A_n} = 1 - \frac{2ent}{\pi D_i^2 \cos \beta} \quad (15)$$

The general form of Eq. (16) is not valid for helical microfin tubes because the term ent is multiplied by 1 in Eq. (16), while the term ent is multiplied by 4 in Eqs. (12) and (13).

Based on Eqs. (12)–(15), the following general form for helical microfin tubes and for herringbone microfin tubes is presented as

$$f_{Lo} = 0.046 Re_L^{-0.2} \left(\frac{D_i}{D_e} \right)^{-1} \left(1 - \frac{4ent}{\pi D_i^2 X \cos \beta} \right)^{-0.5} (X \sec \beta)^{-Y}$$

For helical microfin tubes,

$$X = 1$$

$$Y = 0.75$$

For herringbone microfin tubes,

$$X = 2$$

$$Y = 1.1$$

The term $4/X$ in the general form for helical microfin tubes and for herringbone microfin tubes can be written in different ways, such as 2^{3-X} , $6-2X$, or $3!-2^X$.